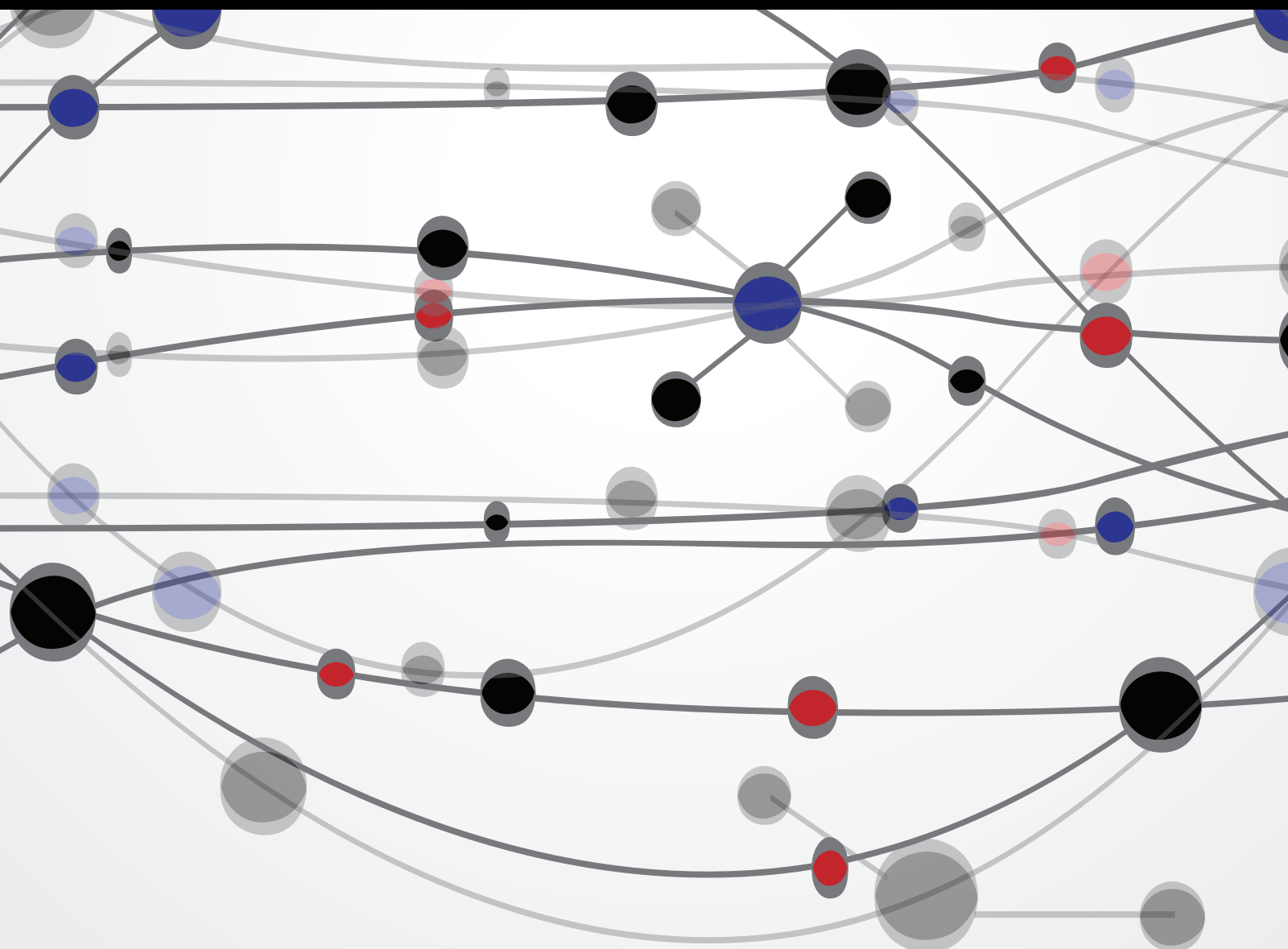


# Health Monitoring of Civil Infrastructure and Materials

Guest Editors: Dimitrios G. Aggelis, Ninel Alver, and Hwa Kian Chai



# **Health Monitoring of Civil Infrastructure and Materials**

The Scientific World Journal

---

## **Health Monitoring of Civil Infrastructure and Materials**

Guest Editors: Dimitrios G. Aggelis, Ninel Alver,  
and Hwa Kian Chai



Copyright © 2014 Hindawi Publishing Corporation. All rights reserved.

This is a special issue published in "The Scientific World Journal." All articles are open access articles distributed under the Creative Commons Attribution License, which permits unrestricted use, distribution, and reproduction in any medium, provided the original work is properly cited.

**Health Monitoring of Civil Infrastructure and Materials**, Dimitrios G. Aggelis, Ninel Alver, and Hwa Kian Chai  
Volume 2014, Article ID 435238, 2 pages

**Application of Acoustic Emission on the Characterization of Fracture in Textile Reinforced Cement Laminates**, J. Blom, J. Wastiels, and D. G. Aggelis  
Volume 2014, Article ID 178020, 7 pages

**Development of Hybrid Braided Composite Rods for Reinforcement and Health Monitoring of Structures**, Sohel Rana, Emilija Zdraveva, Cristiana Pereira, Raul Fangueiro, and A. Gomes Correia  
Volume 2014, Article ID 170187, 9 pages

**A Simple and Reliable Setup for Monitoring Corrosion Rate of Steel Rebars in Concrete**, Shamsad Ahmad, Mohammed Abdul Azeem Jibran, Abul Kalam Azad, and Mohammed Maslehuddin  
Volume 2014, Article ID 525678, 10 pages

**Identification of Historical Veziragasi Aqueduct Using the Operational Modal Analysis**, E. Ercan and A. Nuhoglu  
Volume 2014, Article ID 518608, 8 pages

**Online Bridge Crack Monitoring with Smart Film**, Benniu Zhang, Shuliang Wang, Xingxing Li, Zhixiang Zhou, Xu Zhang, Guang Yang, and Minfeng Qiu  
Volume 2013, Article ID 303656, 14 pages

**Development of Inspection Robots for Bridge Cables**, Hae-Bum Yun, Se-Hoon Kim, Liuliu Wu, and Jong-Jae Lee  
Volume 2013, Article ID 967508, 17 pages

**A Universal Fast Algorithm for Sensitivity-Based Structural Damage Detection**, Q. W. Yang, J. K. Liu, C.H. Li, and C.F. Liang  
Volume 2013, Article ID 235820, 8 pages

**Detecting the Activation of a Self-Healing Mechanism in Concrete by Acoustic Emission and Digital Image Correlation**, E. Tsangouri, D. G. Aggelis, K. Van Tittelboom, N. De Belie, and D. Van Hemelrijck  
Volume 2013, Article ID 424560, 10 pages

**The Sacred Mountain of Varallo in Italy: Seismic Risk Assessment by Acoustic Emission and Structural Numerical Models**, Alberto Carpinteri, Giuseppe Lacidogna, Stefano Invernizzi, and Federico Accornero  
Volume 2013, Article ID 170291, 10 pages

**Unsupervised Performance Evaluation Strategy for Bridge Superstructure Based on Fuzzy Clustering and Field Data**, Yubo Jiao, Hanbing Liu, Peng Zhang, Xianqiang Wang, and Haibin Wei  
Volume 2013, Article ID 427072, 6 pages

**Static Testing of a Bridge Using an Interferometric Radar: The Case Study of “Ponte degli Alpini,” Belluno, Italy**, Devis Dei, Daniele Mecatti, and Massimiliano Pieraccini  
Volume 2013, Article ID 504958, 7 pages

## Contents

---

**Ambient Vibration Testing for Story Stiffness Estimation of a Heritage Timber Building,**

Kyung-Won Min, Junhee Kim, Sung-Ah Park, and Chan-Soo Park

Volume 2013, Article ID 198483, 9 pages

**Investigation of Time Series Representations and Similarity Measures for Structural Damage Pattern**

**Recognition,** Wenjia Liu, Bo Chen, and R. Andrew Swartz

Volume 2013, Article ID 248349, 13 pages

**Monitoring of Civil Infrastructures by Interferometric Radar: A Review,** Massimiliano Pieraccini

Volume 2013, Article ID 786961, 8 pages

## *Editorial*

# **Health Monitoring of Civil Infrastructure and Materials**

**Dimitrios G. Aggelis,<sup>1</sup> Ninel Alver,<sup>2</sup> and Hwa Kian Chai<sup>3</sup>**

<sup>1</sup> Department of Mechanics of Materials and Constructions, Vrije Universiteit Brussel, Pleinlaan 2, 1050 Brussels, Belgium

<sup>2</sup> Department of Civil Engineering, Ege University, Bornova, 35100 Izmir, Turkey

<sup>3</sup> Department of Civil Engineering, University of Malaya, 50603 Kuala Lumpur, Malaysia

Correspondence should be addressed to Dimitrios G. Aggelis; daggelis@vub.ac.be

Received 12 January 2014; Accepted 12 January 2014; Published 18 February 2014

Copyright © 2014 Dimitrios G. Aggelis et al. This is an open access article distributed under the Creative Commons Attribution License, which permits unrestricted use, distribution, and reproduction in any medium, provided the original work is properly cited.

Despite the generally long life span of concrete structures, they cannot be considered maintenance-free. Several incidents of catastrophic failures remind the engineering world that monitoring of structures is imperative nowadays both for prevention of loss of life and property and also for effective infrastructure management based on a usually finite budget. Due to the variety of structural sizes, shapes, and uses, as well as the possible vulnerabilities of the different types of structures, different tools must be used, many times complementary, in order to lead to reliable assessment results. Indeed, the reliability of in situ implementation is a key issue for any health monitoring technique along with other characteristics such as testing speed and cost-effectiveness.

Several nondestructive testing (NDT) techniques have already been established, showing their suitability in certain aspects of material and structural characterization and behavior monitoring. As an example, the use of ultrasonic pulse velocity can be mentioned, the correlation of which with the quality of concrete is well documented. Other techniques based on elastic waves such as impact and impulse response, as well as the radar method, have proven their suitability in distinguishing delaminations and inhomogeneities. The assessment based on the above-mentioned methods as well as a number of others, like acoustic emission, radiography, vibration modal analysis, and slightly destructive surface strength methods in conjunction with visual inspection, provides a valuable platform for decision making concerning the maintenance, based on more robust engineering criteria than solely the experience of the engineer.

However, it is a common impression that most NDT techniques have not at all reached their full potential especially with regard to in situ implementation. Therefore, the current special issue intends to examine all possible tools for economic and timely infrastructure condition assessment, with emphasis on reliability and connection of the monitoring results with the proper maintenance action that should be taken. The challenges are even higher since new and innovative materials are being increasingly used. These materials include high performance concrete, textile reinforced concrete, and nanomodified and recycled materials, which offer better capabilities for sustainable structures; however their assessment through the same techniques used for conventional concrete should not be taken for granted.

In this special issue, the latest advances in different topics of civil structural health monitoring (SHM) are highlighted. More specifically, recent findings in elastic wave methods (acoustic emission, impact-echo, and ultrasonics) are reported. Vibration methodologies which are the most suitable for global bridge SHM are discussed, while the use of radar is reviewed and applied. Advancements in automated robotic inspection and online monitoring of bridge components are also discussed. The issue includes studies on corrosion detection, reinforcing and self-sensing elements for SHM. Algorithms incorporating pattern recognition clustering for the characterization of the location and degree of damage could not but be a strong part of the issue, while monitoring of self-healing and textile-reinforced materials is also discussed. The dual importance of monitoring of old

structures is stressed out: their structural safety as well as their cultural heritage significance. The methodologies are successfully tested in several case studies as reported herein.

We believe that the present special issue reflects on the recent advances in SHM and NDT for civil structures and materials complemented with insightful findings of various assessment techniques. We wish to thank all the authors for submitting their work in the issue and their patience during the review process.

*Dimitrios G. Aggelis  
Ninel Alver  
Hwa Kian Chai*

## Research Article

# Application of Acoustic Emission on the Characterization of Fracture in Textile Reinforced Cement Laminates

J. Blom, J. Wastiels, and D. G. Aggelis

Department of Mechanics of Materials and Constructions, Vrije Universiteit Brussel, Pleinlaan 2, 1050 Brussels, Belgium

Correspondence should be addressed to D. G. Aggelis; daggelis@vub.ac.be

Received 3 November 2013; Accepted 19 December 2013; Published 30 January 2014

Academic Editors: F. Ayuga and G. Turk

Copyright © 2014 J. Blom et al. This is an open access article distributed under the Creative Commons Attribution License, which permits unrestricted use, distribution, and reproduction in any medium, provided the original work is properly cited.

This work studies the acoustic emission (AE) behavior of textile reinforced cementitious (TRC) composites under flexural loading. The main objective is to link specific AE parameters to the fracture mechanisms that are successively dominating the failure of this laminated material. At relatively low load, fracture is initiated by matrix cracking while, at the moment of peak load and thereafter, the fiber pull-out stage is reached. Stress modeling of the material under bending reveals that initiation of shear phenomena can also be activated depending on the shape (curvature) of the plate specimens. Preliminary results show that AE waveform parameters like frequency and energy are changing during loading, following the shift of fracturing mechanisms. Additionally, the AE behavior of specimens with different curvature is very indicative of the stress mode confirming the results of modeling. Moreover, AE source location shows the extent of the fracture process zone and its development in relation to the load. It is seen that AE monitoring yields valuable real time information on the fracture of the material and at the same time supplies valuable feedback to the stress modeling.

## 1. Introduction to Acoustic Emission

Acoustic emission (AE) is the result of irreversible processes in a material: mainly crack propagation, material failure, and changes in the microstructure [1]. Any fracture incident releases energy in the form of elastic waves and is captured by piezoelectric sensors on the surface of the material. These waves are recorded as electric waveforms. The number of acquired signals is connected to the number of active sources, while the location of the source events can be calculated by the time delay between the recording of each signal by sensors at different positions [2–5]. Some important parameters of the waveforms are shown in Figure 1. Among others, amplitude (A) is the voltage of the maximum peak and is connected to the intensity of the cracking event. Rise time (RT) is the delay between the onset and the maximum peak, and RA is the inverse of the rise angle (RT/A) and is connected to the mode of fracture [1, 6]. Additionally, frequency is checked by the “average frequency” AF, defined as the number of threshold crossings over the waveform duration. Duration (Dur) is the time between the first and last threshold (Thr) crossings. The area under the rectified signal envelope is another

measure of the waveform’s intensity and is called MARSE (measured area under the rectified signal envelope) or simply “energy” [6]. The threshold is selected by the user and should be high enough to exclude recording of ambient noise but at the same time sensitive enough to allow recording of even small amplitude relevant waveforms.

In the present paper a case of AE monitoring during fracture of a novel engineering material is presented. The aim is to demonstrate the capacity of AE to characterize the damage development and provide important information in the modeling of materials by indicating the dominant fracture mode under specific loading patterns.

## 2. Monitoring of Textile Reinforced Mortar under Bending

With the increasing prevalence of composite materials, the structural and cost advantages of textile reinforced cements (TRC) are well established [7]. The mechanical properties and production costs of TRC are dependent on physical, chemical, and production properties and methods. TRCs differ from fiber reinforced cements (FRC) primarily in their fiber

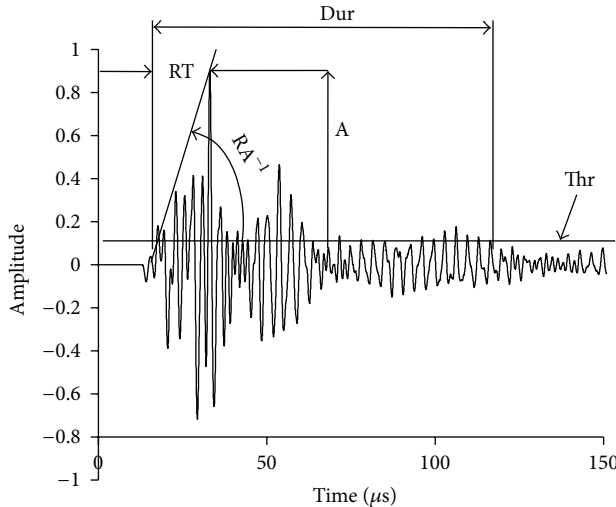


FIGURE 1: Typical AE waveform.

structure, which is continuous. In combination with a usually higher fiber volume fraction (above 5%), this leads to an increased tensile strength and ductility. Within TRC materials, the development of inorganic phosphate cement (IPC) composites at the Vrije Universiteit Brussel (VUB) has resulted in a novel material [8]. The cementitious material shows a neutral pH after hardening; thus reinforcing with E-glass fibers is possible without fiber protection. By using a high volume fraction of E-glass fiber a relatively cheap strain hardening textile reinforced cementitious composite can be produced. When designing construction elements it is important to predict the bending behaviour of this composite. In this work the behaviour of straight and curved beams is examined in bending. The hyperelasticity “Marlow” material model in Abaqus was calibrated using experimental data from tension and compression tests. The calibrated model was used to study the bending behaviour of a beam, without taking into account the effect shear. The first objective of this research is to evaluate the influence of geometrical properties on the failure mechanism of an IPC TRC beam. The validation of the FEM analysis and limitations due to the introduction of a more complex failure mechanism is the second goal. Acoustic emission procedures are employed to measure the change in the failure mechanism and Abaqus is used to perform the structural analysis.

**2.1. TRC in Tension and Compression.** According to the ACK theory [9], three distinct stages can be detected in the stress-strain curve of a unidirectionally reinforced brittle matrix composite. In the first stage the material behaves linearly elastically and a perfect elastic bond between matrix and fibers is assumed. Since the failure strain of the matrix is lower than that of the fibers, the matrix will crack. If the fiber volume fraction is higher than the critical fiber volume fraction, the fibers will be able to sustain the cracking load, and multiple cracking will occur. In the third “post cracking” stage the matrix is fully cracked, and the fibers will carry any additional load until they fail.

TABLE 1: Dimensions of straight and curved specimens tested in bending.

	Thickness (mm)	Width (mm)	Support span (mm)	Fibre volume fraction $V_f$ (%)	Number of layers
Straight	5.70	53.53	200.00	16.94	8
Curved	5.05	55.28	282.00	19.35	8

**2.2. TRC Beam in Bending.** A hyperelasticity “Marlow” material model was used for bending analysis in Abaqus [10], because it enables the user to define a different behaviour in compression and tension. The tensile stress-strain data was taken by averaging the experimental data obtained from 10 samples. The compressive behaviour is assumed linear with a composite Young’s modulus of 17.07 GPa, until collapse at 80 MPa. Results of modeling for a straight and a curved beam will be presented and discussed along with the experimental ones.

### 3. Experimental Part

**3.1. Materials and Loading.** The matrix is a mixture of a calcium silicate powder and a phosphoric acid based solution of metal oxides. The liquid to powder mass ratio is 1/0.8. Mixing is performed using a Heidolph RZR 2102 overhead mixer. First the liquid and the powder are mixed at 250 rpm until the powder is mixed into the fluid, after which the speed is increased to 2000 rpm. E-glass chopped glass fiber mats with a surface density of 300 g/m<sup>2</sup> (Owens Corning M705-300) are used as reinforcement. All IPC 8-layer laminates are made by hand lay-up with an average matrix consumption of 800 g/m<sup>2</sup> for each layer, which results in an average fiber volume fraction ( $V_f$ ) of 20%. Laminates are cured under ambient conditions for 24 hours. Postcuring is performed at 60°C for 24 hours while both sides are covered with plastic sheet to prevent early evaporation of water. Two sets of laminates are prepared: one flat and one curved with a base length of 282 mm and a vertex height of 138 mm. Basic parameters of the specimens are shown in Table 1.

**3.2. Tensile Test.** The stress-strain curve data was generated using flat coupons of the material on a universal testing machine (INSTRON 5885H) with a capacity of 100 kN. The rate of cross-head displacement was set to 1 mm/min. The strain was measured with a double clip extensometer. The stiffness in the first ( $E_{c_1} = 16$  GPa) and the third stage ( $E_{c_3} = 4$  GPa) is obtained from the experimental data by determination of the slope of the graphs.

**3.3. Bending Test.** The straight and curved specimens were loaded in a three-point bending test, as seen in Figure 2. The straight beam was simply supported. The span between the supports was 200 mm. The supports of the curved beam are pinned with a span of 282 mm. An INSTRON 5885H universal testing machine fitted with a load cell of 10 kN was

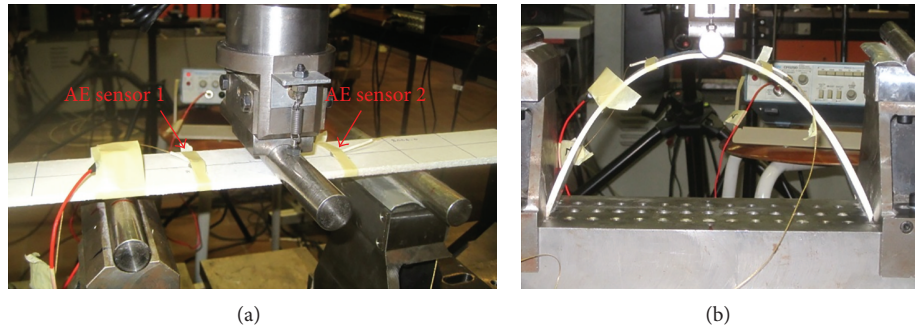


FIGURE 2: Three point bending set up for (a) straight beam, (b) arch beam.

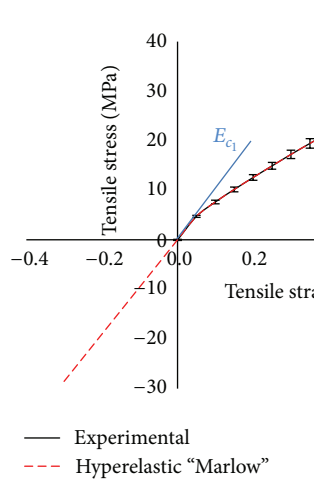


FIGURE 3: Stress-strain curves obtained from tensile tests on 8-layer TRC specimens.

used. The testing was displacement controlled, with a rate of 1 mm/min.

#### 4. Tensile and Bending Behaviour

The black continuous line in Figure 3 shows the average stress-strain curves obtained from 10 tested samples. The discontinuous red line represents the stress-strain curve computed with the calibrated hyperelastic "Marlow" model in Abaqus [11].

Concerning bending, the force-deflection curves obtained from the 3-point bending on a straight and curved beam are shown in Figure 4. The red discontinuous line represents the force deflection curves obtained from the Abaqus bending model while the solid lines stand for experimental results.

The agreement between the numerical and experimental results is excellent for the thin straight beam in bending even with a model which is not taking in account shear [12]. However, there is no agreement for the arch shaped specimen. This implies that interlaminar shear starts playing an important role and not taking it into account results in strong discrepancies between the predicted and the actual behaviour [13]. Figures 5(a) and 5(b) show the normal stress, at the bottom of the section, along the longitudinal axis of the straight

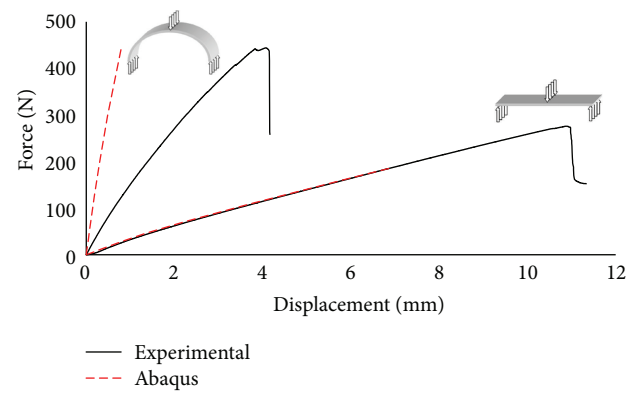


FIGURE 4: Force-deflection curves obtained from 3-point bending (curved and straight beams) and FEM simulation (solid lines stand for experimental curves, dashed lines for numerical).

and the curved beams, respectively. It is obvious that the straight beam in Figure 5(a) is characterized by positive stress (tension) at the bottom of the section over the entire length of the specimen. However, in a curved beam the load will be transversal to the textile reinforcement layers only in the midsection. When increasing the curvature the forces will become more in line with the reinforcement layers. Curving a beam will result in the shift of bending (force perpendicular to reinforcement) to compression-shear (force aligned with reinforcement), as has been seen in [13]. Figures 5(c) and 5(d) depict the vertical displacement. While the straight beam moves downwards for its whole length, the displacement is more complicated for the curved one. Near the midspan the displacement is downward while at the sides it becomes positive (upward) due to the change of shape of the arch which tends to "open" under the vertical load. These results will be discussed along with the AE monitoring that follows.

#### 5. Acoustic Emission Monitoring

For the specific experiment, two miniature AE sensors of the "pico" type (mistrasgroup) were used. They exhibit a broadband response and peak sensitivity at 450 kHz. They were attached by means of tape on the side surface of the components. A layer of Vaseline was used between the sensors and

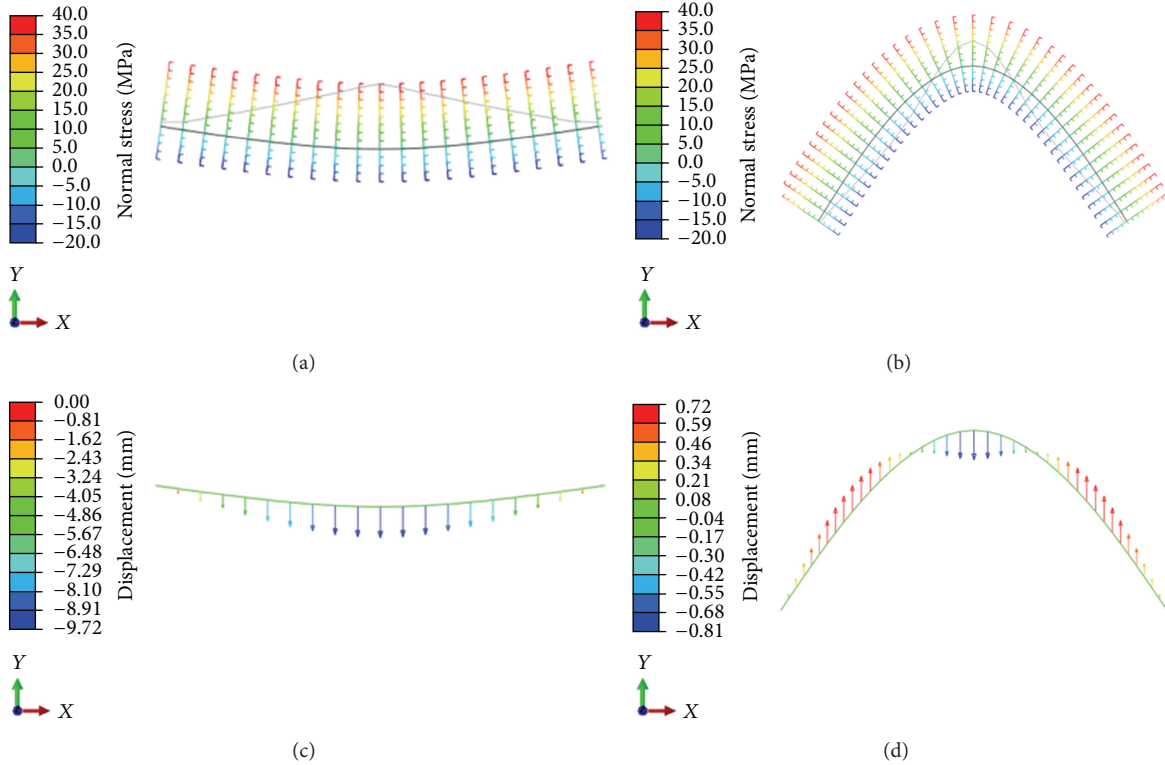


FIGURE 5: Normal stress (MPa) on the longitudinal axis of (a) straight and (b) curved beams. Vertical displacement of (c) straight and (d) curved beams.

the specimen's surface for acoustic coupling. The separation distance of the sensors was 100 mm, as they were placed 50 mm in either side of the centre load application point (see Figure 2). The signals that exceeded 35 dB were preamplified by 40 dB and acquired in a PAC micro-II 8-channel board. AE monitoring was active during the whole loading pattern of each specimen, while activities with "zero" energy were not recorded. The larger transducer seen on the left of the photographs of Figure 2 was for exciting signals for ultrasonic monitoring which is not presented herein. In order to increase the reliability of the analysis and exclude possible noises the information of the AE "events" is only used. AE event is the source of the emission and is connected to a crack propagation incident. In the specific case one event leads to acquisition of one "hit" on each of the sensors (two hits in total) in a short time window. By knowing the pulse velocity of the medium and the acquisition time on each sensor, linear location of the sources along the axis of the specimen is automatically conducted. The pulse velocity of the medium was measured along the longitudinal axis by pencil lead breaks before the experiment and was found equal to 2700 m/s in average.

## 6. AE Results and Discussion

In this study we will focus on the two extremes, namely, the straight and the arch with the maximum curvature, which are also shown in Figures 2(a) and 2(b). Figure 6 shows the AF

history for the AE hits for both the straight and curved (arch) plates. Each dot is the AF of one single AE signal while the time of acquisition is shown on the horizontal axis. A strong overlap is exhibited for the two populations straight and arch. The AF for the straight beam starts at an average of 300 kHz and smoothly decreases to approximately 220 kHz up to the moment of load drop (shown by an arrow on the horizontal axis). Until that moment matrix crack is reasonably active while after the serious cracking events that occur when the load bearing capacity of the beam is reached, fiber pull out and debonding between the successive layers are activated. This is why the AF drops to much lower values (moving average down to 50 kHz). The behaviour of the curved beam (arch) is similar but with distinct differences. Up to the fracture moment the AF decreases smoothly but it is constantly lower than the straight beam's AF. It starts at approximately 270 kHz and reaches 170 kHz just before load peak. This difference in average value of approximately 50 kHz indicates that the fracture mechanism in the arch includes more shear characteristics compared to the pure bending of the beam. Consequently, it clearly decreases at the moment of load drop indicating the activation of excessive debonding events. After the load drop points, the behaviour does not change much for the two beams since fracture of both is dominated by pull out and delaminations. However, the distinct differences in the first stage show that the shape of the beams actually influences the stress field and the dominant fracture mechanisms. The curved beam undertakes much more shear which is exhibited

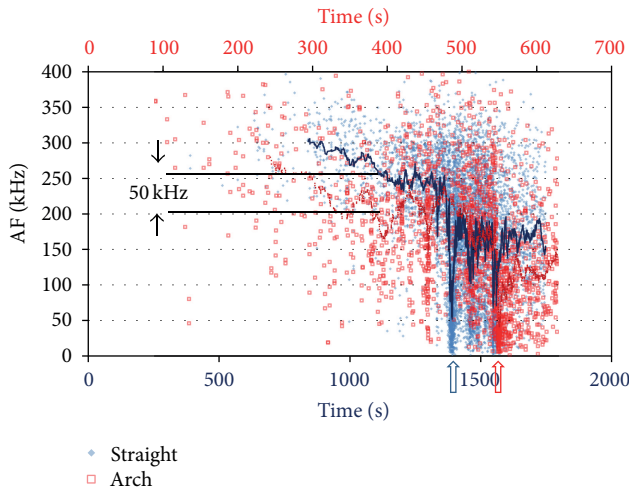


FIGURE 6: Average frequency (AF) for the straight and the curved plate (arch). The lines are the moving average of the recent 30 points.

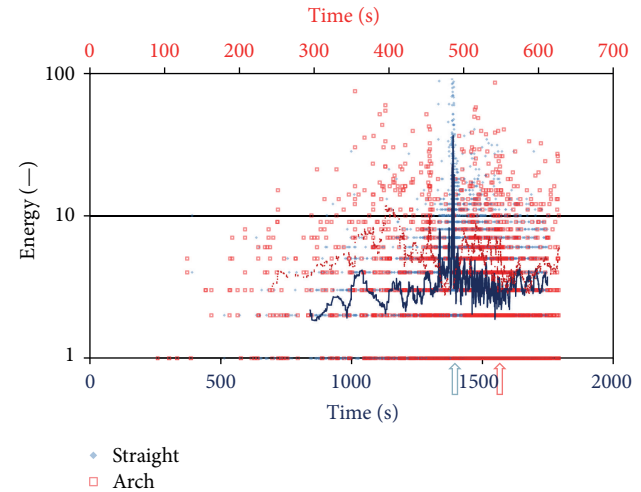


FIGURE 7: AE energy for the straight and the curved plate (arch). The lines are the moving average of the recent 30 points.

by lower frequency content of acoustic emissions. This confirms the conclusion of the modeling according to which for a straight beam neglecting the interlaminar shear is not crucial, while it becomes important for the modeling of the curved beam.

Focusing on the emitted energy for the two beams similar trends are noticed; see Figure 7. After the moments of load peak the behaviour is quite similar. However, at earlier stages of loading the energy emitted by a typical event of the arch is certainly higher (typically more than double) than the straight beam. This indicates that the events related to shear stresses are of higher intensity, compared to the pure matrix cracks that are characteristic of the straight beam.

In order to discuss on a more standard basis, the average values of these AE parameters along with AE durations are shown in Table 2. The AE activity of arch beams before the load peak is characterized by lower frequency, longer duration, and higher energy. After the peak the differences are much smaller; the average frequency is around 150 kHz for both specimens while the other parameters also seem to converge between the straight and arch geometries. This is due to the common damage mechanism of pull out and delaminations that is dominant after the matrix is fully cracked. Before that moment the data suggest that the straight beam sustains more normal stresses due to pure bending (short signals of higher frequency), while the curved undertakes stronger shear stresses due to the arch geometry. These significant changes before and after the maximum load have been observed previously in several fiber reinforced materials like ceramics [14], steel fiber reinforced concrete [15], and laminated composites [16]. Mainly it is the manifestation of fiber pull out and debonding, the shearing nature of which creates emissions with long duration and low frequency.

As already mentioned AE source location took place and the analysed data population belongs to the classified events

TABLE 2: Average values of AE descriptors for different loading stages of the beams.

	Av. freq. (kHz)	Energy (-)	Duration ( $\mu$ s)
Straight beam			
Prepeak	258	2.8	224
Postpeak	154	4.4	616
Arch beam			
Prepeak	215	6.0	383
Postpeak	148	5.0	560

in order to increase the reliability. Figure 8(a) shows the location results for the straight beam along with the cumulative number of events. Each dot is the calculated distance of the fracture source events from the first sensor (distance between the sensors is 100 mm). The slight black line is the moving average of the recent 30 points for clarity. The events initially are located very close to the centre of the beam as should be expected in three-point bending. There is a standard deviation,  $\sigma$ , of 10 mm around the mean value at the early stages of loading. However, later after the major fracture moment and load drop the mean value seems to shift away from the centre and the standard deviation considerably increases. This shows that although damage initiates at the centre due to the three-point bending setup, after the load drop, damage has the tendency to shift to one of the edges while the damaged area becomes wider ( $\sigma = 12.4$  mm).

Results concerning the arch geometry show again small but characteristic differences (Figure 8(b)). Although the moving average line of AE location is close to the centre, the values exhibit a higher standard deviation (11.7 mm compared to 10 mm for the straight beam). After the load drop, again the mean value seems to shift to one of the sides while the widespread of the emission as seen by the standard deviation is increased to 14.3 mm. Therefore, it is a common place that the width of the fracturing zone increases as delaminations become more frequent at the end. This is reasonable since

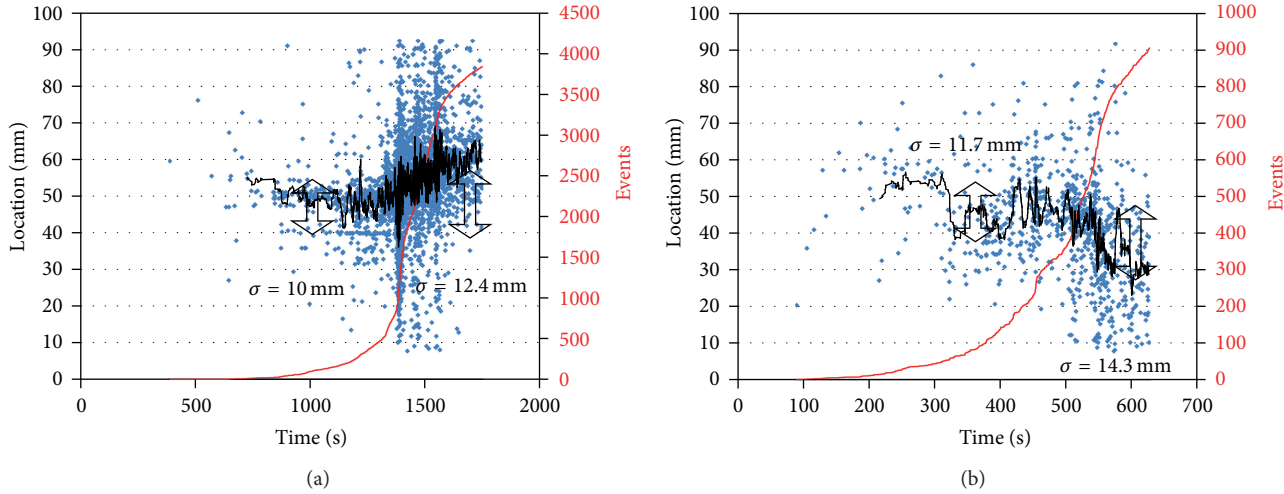


FIGURE 8: Location and cumulative number of AE events during loading of (a) the straight beam and (b) the arch beam.

initially the three-point bending dictates the start of cracking at the centre due to maximum bending moment while once the delaminations start to occur, the damage becomes more widespread to both directions.

In Figure 8 the cumulative number of events is also seen for both cases. The straight beam exhibited a much higher activity in terms of the population of events. This implies that matrix cracking occurs with more events but of smaller intensity compared to the case of an arch beam where the total number of events is one-fourth but the average intensity is more than double.

The above discussion shows that simple AE descriptors can be used to distinguish the different fracture stages in complex material like fiber reinforced cement. During loading, a succession of failure modes is usually exhibited: initially matrix cracking due to tensile loading and consequently shearing due to incidents like fiber pull out or debonding. AE can readily capture the differences and hence shed light into the ongoing fracture process in real time. Concerning the curved beam, the existence of shear stresses and shear-related damage is seen from the start of loading based on the performance of frequency and other AE waveform indicators. It is thus confirmed that, for the highly curved beam, modeling cannot be conducted based on normal stresses alone, since strong shearing is also active. One point that should be kept in mind in such analyses is related to the heterogeneity and shape of the monitored specimen/structure. In the specific case, the plate geometry induces plate wave dispersion, while the heterogeneous nature of the material induces strong scattering in addition to damping. Therefore, the elastic waveform is continuously changing from the point of the emission to the receiver position. Frequency characteristics are bound to decrease, while the waveform loses amplitude. Therefore, any specific AE value reported herein holds strictly for the specific test setup and sensor separation distance. In different cases (geometry, sensor type, and separation distance) similar trends are expected but the absolute values of the AE descriptors will not necessarily be the same.

## 7. Conclusions

The present study discusses the acoustic emission behaviour of TRC laminates under bending. The following important conclusions are drawn.

- (1) The acoustic emission activity changes during the fracture process indicating the shift from matrix cracking to debonding and fiber pull-out events. Specifically, AE frequency decreases while the duration of the waveforms increases after the major fracture that is accompanied by a clear load drop.
- (2) The change in the developed stress field induced by the curvature of the beams is confirmed by the AE behaviour. AE waveforms of the arch shaped beam exhibit more shear characteristics than the straight beam, namely, longer duration and lower frequency, even at early loading levels.
- (3) Fracture in the curved beams which include shear components comprises of fewer and stronger events.
- (4) AE study can supply valuable feedback to the numerical modeling in terms of the load at onset of fracture as well as the dominant mode of fracture, which cannot be assessed in real time by another conventional technique.
- (5) The bending behaviour of thin straight TRC beam with a IPC matrix can be predicted by using model in a FEM program “Abaqus.” Nevertheless, the choice and calibration of the material model “Marlow” will influence the prediction. Introducing curvature will introduce shear driven failure mechanisms. When neglecting this phenomenon in the FEM model strong discrepancies between the predicted and the actual behaviour will occur.

## Conflict of Interests

The authors declare that there is no conflict of interests regarding the publication of this paper.

## References

- [1] C. U. Grosse and M. Ohtsu, *Acoustic Emission Testing*, Springer, Heidelberg, Germany, 2008.
- [2] M. Ozawa, S. Uchida, T. Kamada, and H. Morimoto, "Study of mechanisms of explosive spalling in high-strength concrete at high temperatures using acoustic emission," *Construction and Building Materials*, vol. 37, pp. 621–628, 2012.
- [3] A. Farhidzadeh, S. Salamone, B. Luna, and A. Whittaker, "Acoustic emission monitoring of a reinforced concrete shear wall by b-value-based outlier analysis," *Structural Health Monitoring*, vol. 12, no. 1, pp. 3–13, 2013.
- [4] S. Shahidan, R. Pulin, N. M. Bunnori, and K. M. Holford, "Damage classification in reinforced concrete beam by acoustic emission signal analysis," *Construction and Building Materials*, vol. 45, pp. 78–86, 2013.
- [5] A. Carpinteri, M. Corrado, and G. Lacidogna, "Heterogeneous materials in compression: correlations between absorbed, released and acoustic emission energies," *Engineering Failure Analysis*, vol. 33, pp. 236–250, 2013.
- [6] M. Ohtsu, "Recommendation of RILEM TC 212-ACD: acoustic emission and related NDE techniques for crack detection and damage evaluation in concrete: test method for classification of active cracks in concrete structures by acoustic emission," *Materials and Structures*, vol. 43, no. 9, pp. 1187–1189, 2010.
- [7] W. Brameshuber, "Textile reinforced concrete state of the art report of RILEM technical committee," Tech. Rep. TC 201-TRC, Rilem, Aachen, Germany, 2006.
- [8] X. Wu and J. Gu, "Inorganic resin compositions, their preparation and use thereof," PCT Patent Application WO 97/19033, EP 0 861 216 B1 (MEMC-TW-VUB), Department Research & Development, Vrije Universiteit Brussel, Brussel, Belgium.
- [9] J. Aveston, G. A. Cooper, and A. Kelly, "Single and multiple fracture," in *Proceedings of the Conference on the Properties of Fibre Composites*, pp. 15–26, National Physical Laboratory, IPC Science & Technology Press, London, UK, 1971.
- [10] Dassault Systèmes, Abaqus Analysis User's Manual Version 6.10, 2010.
- [11] Marlow, Abaqus Analysis User's Manual Volume III, 2010.
- [12] J. Blom, H. Cuypers, P. van Itterbeeck, and J. Wastiels, "Modelling the behaviour of textile reinforced cementitious composites under bending," in *Proceedings of the 4th International Conference on Fibre Concrete*, pp. 205–210, Prague, Czech Republic, 2007.
- [13] E. Velazquez and J. B. Kosmatka, "Stresses in half elliptic curved beams subjected to transverse tip force," *Journal of Applied Mechanics*, vol. 80, no. 1, 7 pages, 2013.
- [14] K. G. Dassios, D. G. Aggelis, E. Z. Kordatos, and T. E. Matikas, "Cyclic loading of a SiC-fiber reinforced ceramic matrix composite reveals damage mechanisms and thermal residual stress state," *Composites A*, vol. 44, pp. 105–113, 2013.
- [15] D. G. Aggelis, D. V. Soulioti, E. A. Gatselou, N.-M. Barkoula, and T. E. Matikas, "Monitoring of the mechanical behavior of concrete with chemically treated steel fibers by acoustic emission," *Construction and Building Materials*, vol. 48, pp. 1255–1260, 2013.
- [16] D. G. Aggelis, N.-M. Barkoula, T. E. Matikas, and A. S. Paipetis, "Acoustic structural health monitoring of composite materials : damage identification and evaluation in cross ply laminates using acoustic emission and ultrasonics," *Composites Science and Technology*, vol. 72, no. 10, pp. 1127–1133, 2012.

## Research Article

# Development of Hybrid Braided Composite Rods for Reinforcement and Health Monitoring of Structures

**Sohel Rana,<sup>1</sup> Emilija Zdraveva,<sup>2</sup> Cristiana Pereira,<sup>2</sup>  
Raul Fangueiro,<sup>1,2</sup> and A. Gomes Correia<sup>2</sup>**

<sup>1</sup> Fibrous Materials Research Group (FMRG), School of Engineering, University of Minho, Azurém Campus, 4800-058 Guimaraes, Portugal

<sup>2</sup> Department of Civil Engineering, University of Minho, Azurém Campus, 4800-058 Guimaraes, Portugal

Correspondence should be addressed to Sohel Rana; soheliitd2005@gmail.com

Received 21 October 2013; Accepted 4 December 2013; Published 20 January 2014

Academic Editors: D. G. Aggelis and H. K. Chai

Copyright © 2014 Sohel Rana et al. This is an open access article distributed under the Creative Commons Attribution License, which permits unrestricted use, distribution, and reproduction in any medium, provided the original work is properly cited.

In the present study, core-reinforced braided composite rods (BCRs) were developed and characterized for strain sensing capability. A mixture of carbon and glass fibre was used in the core, which was surrounded by a braided cover of polyester fibres. Three compositions of core with different carbon fibre/glass fibre weight ratios (23/77, 47/53, and 100/0) were studied to find out the optimum composition for both strain sensitivity and mechanical performance. The influence of carbon fibre positioning in BCR cross-section on the strain sensing behaviour was also investigated. Strain sensing property of BCRs was characterized by measuring the change in electrical resistance with flexural strain. It was observed that BCRs exhibited increase (positive response) or decrease (negative response) in electrical resistance depending on carbon fibre positioning. The BCR with lowest amount of carbon fibre was found to give the best strain sensitivity as well as the highest tensile strength and breaking extension. The developed BCRs showed reversible strain sensing behaviour under cyclic flexural loading with a maximum gauge factor of 23.4 at very low strain level (0.55%). Concrete beams reinforced with the optimum BCR (23/77) also exhibited strain sensing under cyclic flexural strain, although the piezoresistive behaviour in this case was irreversible.

## 1. Introduction

Light weight combined with very good mechanical properties has opened up the possibility of using fibre reinforced plastics (FRPs) in several high end applications including reinforcement of concrete structures. The main disadvantage of steel bars commonly used for concrete reinforcement is the corrosion problem. The use of FRPs in civil structures as replacement of steel is gaining popularity due to their light weight and very good corrosion resistance. Moreover, FRPs offer huge flexibility in tailoring their properties by selecting different fibre/matrix systems and composite structures. Therefore, it is possible to introduce different functionalities into FRPs so that they can serve several purposes at the same time. Health monitoring of civil structures is very much essential in order to avoid accidents from sudden fractures. The approach of inserting various types of sensor (strain

gauges, piezoelectrics [1, 2], fibre optics [3, 4], etc.) into the structures for health monitoring is usually complex and expensive and requires highly skilled personnel for their application and use. These problems can be overcome by turning concrete structures intelligent, that is capable of sensing their own deformation and damage. FRPs are the ideal reinforcements for designing such concrete structures due to the possibility of imparting multifunctionality to FRPs by tailoring their composition or structure. Efforts have been directed towards designing FRPs with self-sensing capability by introducing into their structure a conductive component such as carbon fibres, which can change their electrical resistance with deformation and damage. Use of hybrid composites containing mixture of conductive reinforcements with other reinforcements such as glass and aramid proved helpful to introduce pseudoductility in order to detect

damage well before the structural collapse [5–7]. Several hybrid composite systems with different structures and compositions of glass and carbon fibres or powder have been investigated in order to develop either continuous monitoring system [7–9] or discontinuous warning system for structural health monitoring [10, 11]. Some researchers succeeded to develop hybrid carbon/glass fibre composites which are able to provide alarm signal well before the composite collapse [11]. However, a very small change in resistance at low strain level makes these hybrid composites unsuitable for designing continuous monitoring system [9]. Combination of glass fibre with carbon particle instead of continuous carbon fibre was found to improve the strain sensitivity at low strain level [12, 13]. Recently, attempts have also been made to develop hybrid composites with good sensitivity using carbon nanotubes (CNTs) [14–20]. However, dispersion of CNTs within the composite matrix is a critical issue, since improper dispersion can adversely affect the mechanical properties of composites [21]. Design of continuous monitoring system can also be based on the measurement of residual resistance caused due to deformation. However, it was observed that good sensitivity at low strain in terms of residual resistance is obtained only at the prestressed conditions [9]. Although prestressing of composites is a suitable condition for civil engineering structures, it may present problems in other applications.

Braiding process is gaining a lot of importance in recent times for the manufacturing of composites with complex structures due to its simplicity and low cost [22]. Core-reinforced braided composite rods (BCRs), which are comprised of unidirectional core fibres surrounded by a braided cover, have already been proposed for applications like concrete rebars and medical implants due to their very good mechanical performance [23, 24]. A simple and cost-effective process for continuous single step production of core-reinforced braided rods has been patented by the authors [25]. Superior adhesion of these braided rods with concrete as well as their applicability for concrete internal reinforcement as replacement of steel rebars has also been demonstrated by them [26, 27]. It was observed that BCRs containing carbon fibre core or hybrid cores containing mixture of carbon with glass or high tenacity polyethylene showed higher tensile strength and lower elastic modulus as compared to steel rebars [28]. Attempts are also being made currently to improve the modulus and ductility of BCR using certain proportion of steel fibres in the composition [29]. Potential of core-reinforced braided rods for structural health monitoring was also introduced in our previous studies [30, 31]. In these studies, BCRs with three core compositions (glass/carbon ratio of 23/77, 53/47, and 0/100) were characterized for piezoresistivity under cyclic flexural strain and the composition with lowest amount of carbon fibres (23/77) resulted in better strain sensing behaviour with a gauge factor as high as 23.4 [31]. The present paper reports the further continuation of this research work which also investigated the influence of core fibre positioning in the cross-section of composite rods on the strain sensing behaviour. Moreover, since reinforcement is also one of the primary tasks of BCRs, the effect of their composition on the

mechanical properties has also been reported and discussed. Also, the probable mechanism of the piezoresistivity of BCR under flexural deformation has been discussed. In addition to that, in order to investigate the sensing ability of developed BCRs within concrete structures, mortar beams reinforced with BCRs having optimum composition were fabricated and characterized for piezoresistive behaviour under cyclic flexural strain.

## 2. Experimental

**2.1. Materials and Methods.** BCRs were produced using polyester fibres for braided structure and a combination of glass fibre and carbon fibre as the core reinforcement. Braiding of polyester fibres and impregnation of core fibres with polyester resin/hardener mixture were done simultaneously in a single process using a vertical braiding machine with an incorporated impregnation system [25]. The take-up speed was kept at 0.01 m/s, which led to a breading angle of 23–24°. The composite rods were then cured at environmental temperature and moisture conditions ( $20 \pm 2^\circ\text{C}$  and  $50 \pm 5\%$ ). The properties of E-glass and carbon fibres used for core reinforcement are provided in Table 1 and the composition of different composites is listed in Table 2. The surface texture and cross-sections of the braided rods have been illustrated in Figure 1. The ribbed surface texture leads to superior adhesion of these composite rods with concrete [26]. It can be noticed that in the hybrid rods, the carbon fibres are present in one side of the cross-section and the other side is comprised of glass fibres. The placement of the fibres within the cross-section of the braided rods was controlled while feeding them in the braiding machine by passing the fibres through holes of metal plates placed before and after the resin bath [25]. Carbon and glass yarns were distributed in these holes according to their position in the cross-section of BCRs. However, the core fibres were not put under any tension during feeding. As a result, they lost their straightness to some extent due to the braiding of polyester fibres around them and took a misaligned arrangement decided by the braiding process parameters such as braiding angle, take-up speed, and pretensioning [27]. The extent of this core fibre misalignment can be estimated from the strain of toe region (where mainly orientation of core fibres occurs due to tension leading to very small increase in load with deformation) present in the tensile curves of BCRs tested without pretension.

BCR reinforced mortar samples were prepared by incorporating the BCRs within mortar paste (mixture of cement, sand, and water) according to 196\_1\_NPEN\_1996 standard. A water/cement ratio of 0.5 was used and mixing of cement/water/sand was performed in a standard mixer. Demolding was done after 24 hours and demoulded samples were kept in a condition room with maintained temperature of  $22^\circ\text{C}$  and relative humidity of 65% for 14 days for setting. Samples for piezoresistive testing had the dimension of 2.5 cm  $\times$  2.5 cm  $\times$  10.5 cm (shown in Figure 2) with the braided rods located at ~5.5 mm from the bottom surface. Based on the results of mechanical properties and piezoresistive behaviour of BCR, mortar samples for piezoresistive characterization were prepared only incorporating BCRI type of braided rod.

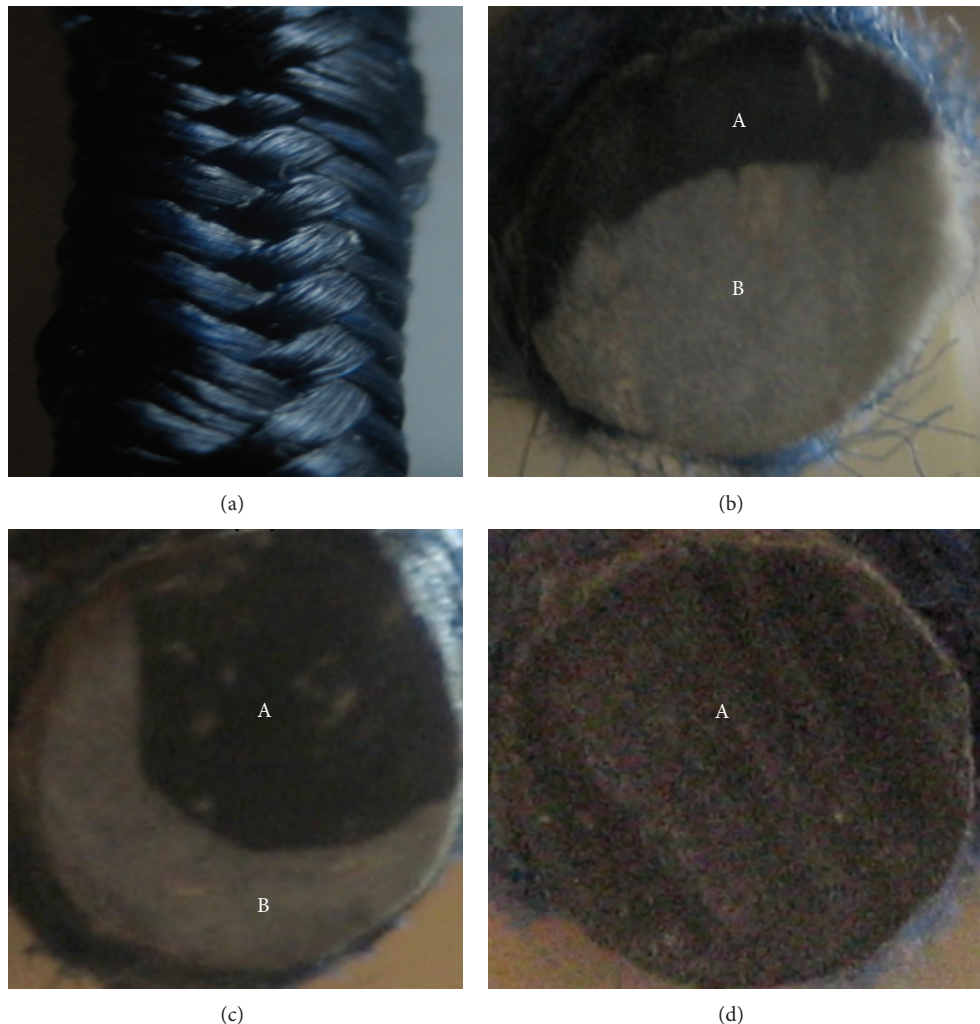


FIGURE 1: Surface texture of BCR (a) and distribution of carbon fibre (A) and glass fibre (B) within BCR1 (b), BCR2 (c), and BCR3 (d).



FIGURE 2: Mortar beams reinforced with BCRs.

TABLE 1: Properties of core reinforcement fibres.

Fibre type	Manufacturer	Elastic modulus (GPa)	Tensile strength (GPa)	Strain at break (%)
Carbon	Toho Tenax	240	4.3	1.8
E-glass	Saint-Gobain Vetrotex	73.5	3.5	4.8

TABLE 2: Composition of different braided composites.

Codes	Fibre weight fraction	Diameter (mm)	Core fibre type	Core composition (wt%)
BCR1	0.35	5.27	E-glass/carbon	77/23
BCR2	0.32	5.75	E-glass/carbon	53/47
BCR3	0.33	6.40	carbon	100

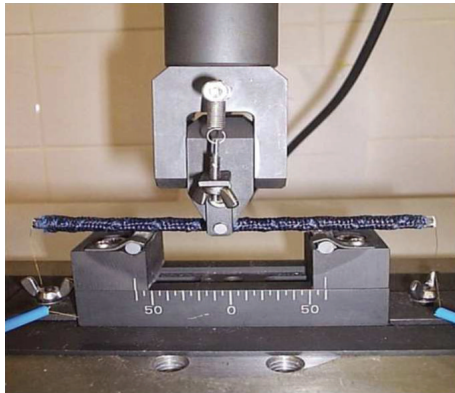


FIGURE 3: Measurement setup for piezoresistive characterization of BCR.



FIGURE 4: Measurement setup for piezoresistive characterization of BCR reinforced beams.

TABLE 3: Testing parameters for piezoresistive characterization of BCR.

Parameters	Values
No. of cycles	4
Span length (mm)	60
Sample length (mm)	138
Displacement limit (mm)	0.55
Crosshead speed (mm/min)	0.3

**2.2. Characterization.** The strain sensing behaviour of BCRs was characterized by measuring the change in electrical resistance between the sample ends using two-terminal dc method [28] under cyclic 3-point flexural loading. Hybrid composites studied previously [32] showed poor strain sensing behaviour in flexural loading as compared to tensile or compression mode due to the nullifying effect of resistance

TABLE 4: Testing parameters for piezoresistive characterization of BCR reinforced mortar.

Parameters	Values
No. of cycles	4
Span length (mm)	90
Sample length (mm)	105
Force limit (kN)	2.5
Crosshead speed (mm/min)	0.3

change in the tension and compression side. Therefore, attempts have also been made by some researchers to measure the resistance change in tension and compression side separately [33]. However, the two-terminal resistance measurement between the sample ends, as employed in this study, is more simple and suitable for practical applications. Cyclic tests were performed at low strain range (up to 0.55%) in order to investigate the performance of the BCRs in sensing very low deformation in continuous manner. The experimental setup for the characterization of piezoresistive behaviour is shown in Figure 3 and the testing parameters are provided in Table 3. Electrical resistance of the samples was continuously measured during the flexural test by making electrical connections between the two probes of a digital multimeter (Agilent 84401A) and sample ends through gold wires fixed to the samples using silver paste. Since under flexural loading one side of the specimen is subjected to tensile stresses and the other side to compressive stresses, each BCR was tested two times keeping the carbon fibre part in tension and compression side, respectively. The objective here was to investigate the effect of carbon fibre positioning on the piezoresistive behaviour.

The strain sensing capability of the composites was evaluated in terms of gauge factor (GF), which is defined as follows:

$$GF = \frac{\Delta R/R}{\varepsilon}, \quad (1)$$

where  $\Delta R$  is the change in electrical resistance,  $R$  is the initial resistance,  $\Delta R/R$  is the fractional change in resistance, and  $\varepsilon$  is the flexural strain at the outer surface of specimen at midspan, which was calculated from maximum deflection in the center of the rod ( $D$ ), diameter ( $d$ ), and support span ( $L$ ) using the following formulae:

$$\varepsilon = \frac{6Dd}{L^2}. \quad (2)$$

The fractional resistance change and gauge factor can be positive or negative depending on the type of response

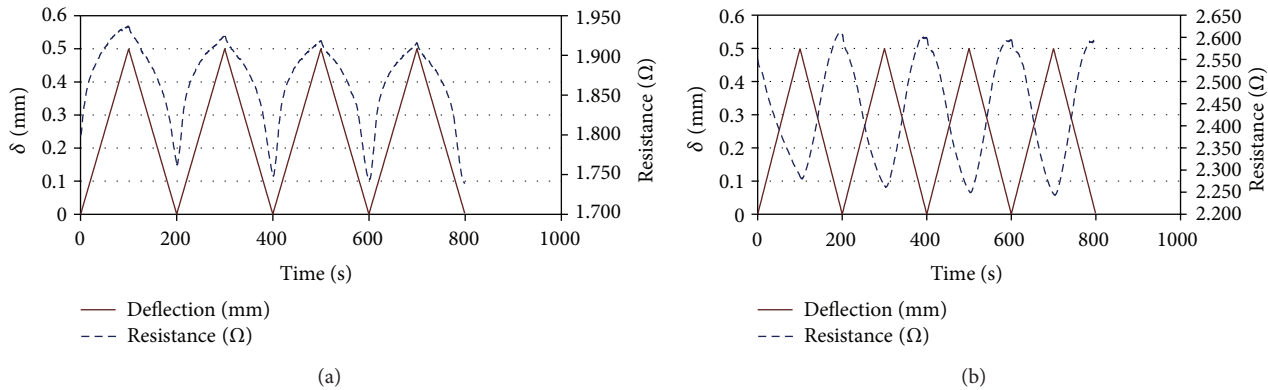


FIGURE 5: Piezoresistive behaviour of BCR1 in cyclic flexural loading: (a) positive response and (b) negative response.

TABLE 5: Fractional resistance change and average gauge factor of BCRs.

BCR type	Cycle no.	Response	1	2	3	4	Average GF	
			$\varepsilon (*10^{-2})$	$\Delta R/R$	$\varepsilon (*10^{-2})$	$\Delta R/R$		
BCR1	Positive	0.48	0.10	0.48	0.11	0.48	0.12	23.4
	Negative	0.47	0.08	0.47	0.07	0.47	0.07	14.9
BCR2	Positive	0.48	0.04	0.48	0.02	0.48	0.01	4.2
	Negative	0.48	0.06	0.48	0.07	0.48	0.07	14.1
BCR3	Positive	0.55	0.02	0.55	0.01	0.55	0.01	2.3
	Negative	0.52	0.04	0.52	0.04	0.52	0.05	8.6

(positive response in case of resistance increases with deformation or negative response in case of resistance decreases with deformation). However, to avoid confusion only the magnitude of fractional resistance change and gauge factor has been reported mentioning the type of response separately. The braided composites were characterized for tensile properties in a Universal Testing Machine (Hounsfield H100 KS) according to ASTM D3916-94 using a crosshead speed of 5 mm/min.

Piezoresistive behaviour of BCR reinforced mortar samples was characterized using a similar setup (Figure 4) as used for BCR characterization. The parameters for piezoresistive characterization of mortar samples are provided in Table 4. The mortar samples were characterized keeping the BCR in the tension side of the specimens. 3 samples from each category were tested to characterize the piezoresistive behaviour of BCR and reinforced mortar beams and the average value has been reported. In case of tensile testing of BCR, 5 samples were tested from each category.

### 3. Results and Discussion

**3.1. Piezoresistive Behaviour.** The developed BCRs showed two types of piezoresistive behaviour under flexural loading depending on the position of carbon fibres in the cross-section of braided composites. If the carbon fibres were located in the tension side of the samples, the positive response was observed whereas the negative response resulted from positing of carbon fibres in the compression side of the specimens. Figure 5 shows the type of response

observed with BCR1 depending on the placement of carbon fibres. It can be seen that the resistance change with deformation was quite reversible except for the initial 1 or 2 cycles where there was noticeable decrease in resistance. However, in the later cycles, this decrease in resistance became insignificant making the piezoresistive behaviour reversible. This fact can also be observed from the  $\Delta R/R$  values listed in Table 5. In the last two cycles,  $\Delta R/R$  values were the same in most of the cases. The other braided composites (BCR2 and BCR3) also showed similar positive and negative responses. However, the extent of resistance change with deformation was different for different BCRs due to difference in the composition. The fractional change in resistance in different cycles and the average gauge factors for different BCRs are listed in Table 5. It can be noticed that the highest strain sensitivity or gauge factor was obtained with BCR1 and the strain sensitivity decreased with the increase in carbon fibre percentage in the BCR composition. The influence of carbon fibre content and positioning on the piezoresistive behaviour has been explained in detail in the next section.

**3.2. Mechanism of Piezoresistivity.** As reported previously [7], the zero-frequency resistance change of carbon fibre composites may be due to (a) dimensional change as a result of elastic deformation of fibres, (b) change of resistivity resulting from change in interfibre contacts due to strain or change in fibre arrangements, and (d) fibre breakage. Since the composites were subjected to a low strain level in the present study and the piezoresistive behaviour was

TABLE 6: Tensile properties of BCRs.

BCR type	Modulus of elasticity (GPa)	Tensile strength (MPa)	Extension at failure (%)
BCR1	78.5	766.7	1.4
BCR2	74.5	740.4	1.2
BCR3	96.3	747.8	1.2

quite reversible, the effect of dimensional change and fibre breakage was expected to be negligible. The role of inter-fibre contacts was believed to be the dominating factor for resistance change in the studied braided composites. The change of inter fibre electrical contacts upon flexural loading was probably attributed mainly to two facts such as, first, (a) *separation of carbon fibres*. As, in the flexural loading, different sections of BCR cross-section were subjected to different level of tensile stresses (in the tension side of the specimen) according to their distance from the neutral axis, the fibres located in one section may try to separate from the next one due to shearing forces acting on them. This fact results in the decrease of number of electrical contacts leading to increase in the electrical resistance. The increase in electrical resistance of carbon fibre composites under flexural deformation was also observed in other studies; however, the mechanism was not explained [32]. In the compressive side of the specimens, however, compressive stresses probably lead to fibre bulking resulting in more touching of fibres and decrease in the electrical resistance. The second fact is (b) *fibre alignment*. Upon application of flexural loads, the misaligned carbon fibres in the tension side of the cross-section get oriented along the BCR axis. This fact may aggravate the fibre separation phenomena and lead to further increase in the electrical resistance. However, fibre alignment phenomena is absent in the compressive side of the specimens and, therefore, these misaligned fibres do not have much influence on the resistance change of the compressive side. Another important point that needs attention here is that when the carbon fibres are subjected to uniform tensile stresses throughout the cross-section of BCR, as in case of tensile loading, fibre alignment can help to increase the electrical contact points (as the uniform tensile stresses try to orient the carbon fibres and form a compact bundle of fibres) resulting in decrease in the electrical resistivity, as observed in the previous studies [34]. So, according to this mechanism, the change of electrical contact points is expected to be more with misaligned fibre arrangements due to the possibility of fibre alignment upon deformation. The misaligned arrangement of conductive carbon fibres, therefore, resulted in very good strain sensitivity of the studied BCRs. It can be noticed that the highest piezoresistive behaviour was obtained with BCRI and the strain sensibility decreases with the increase in the carbon fibre %. In the composites with higher amount of carbon fibres, there will be less change in electrical contacts during deformation due to more touching of fibres leading to a large number of electrical contact points throughout the composites. Previous researchers also found less strain sensitivity with higher percentage of carbon fibres in tensile loading due to the decrease in the “electrical ineffective length” [35] (average length between two adjacent contact

points of misaligned carbon fibres) with the increase in carbon fibre percentage [9]. Moreover, with higher amount of carbon fibres, it was not possible to restrain the position of carbon fibres only in one half of the cross-section and therefore the carbon fibres experienced both tensile and compressive stresses. As a result, the overall strain sensitivity decreased due to cancelling effect of positive and negative responses. The trend of fractional resistance change with strain in the first cycle has been presented in Figure 6. It is interesting to note that the curve for BCRI presents more nonlinearity than the other BCRs. The fractional resistance changes sharply and linearly up to 0.1% strain and then more gradually at higher strains due to saturation in the electrical contacts. This behaviour was also observed in continuous carbon fibre composites where resistance change was mainly attributed to the change in electrical contact points [35]. Another interesting point to note here is that the negative responses seem to be more linear than the positive responses. In case of positive response, as carbon fibres are mainly located in the tension side of the specimen, the change of electrical contact points due to alignment of disoriented fibres under tension is significant in very low strain and as the strain increases, this effect disappears when the fibres become oriented and the effect of fibre separation only plays the main role. Because of this, the change of resistance at low strain level is high and gradually the resistance changes levels off as the strain increases. However, in case of negative response, where the carbon fibres are subjected to compressive forces, the effect of fibre alignment is absent and due to this, resistance changes more uniformly throughout the strain cycle.

**3.3. Mechanical Performance.** The results of tensile testing of BCRs are listed in Table 6. It can be seen that the highest tensile strength and breaking stain were obtained in case of BCRI, that is, composites with 77% of E-glass and 23% carbon core fibres. As the glass fibres present in these composites are at higher quantity, they can bear the redistributed loads even after breakage of carbon fibres. Moreover, the loads can also be transferred back to the broken carbon fibres and partially sustained by means of a mechanism called positive hybrid effect [11] leading to higher breaking strength and extension. However, the breaking extension of BCRI is still lower than the carbon fibres (1.8%) indicating insufficient use of carbon fibres in the braided composites. This is due to the misalignment of core fibres under the influence of braiding process. Although pretensioning of core fibres helps to maintain their alignment and improves the mechanical performance of BCRs [27], this has been avoided in the present study since misalignment of core fibres was found

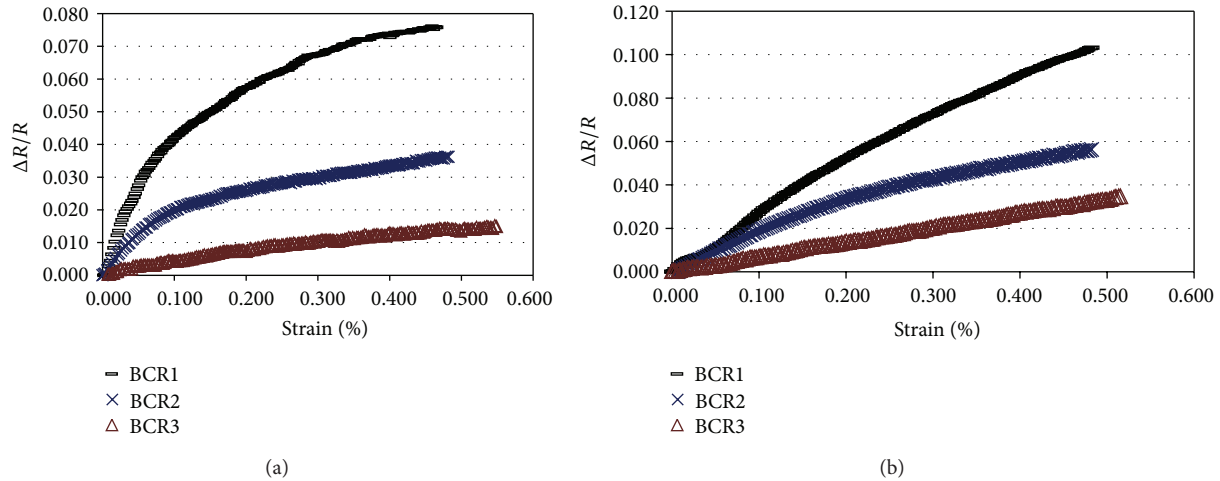


FIGURE 6: Change of fractional resistance with flexural strain for different BCRs: (a) positive response and (b) negative response.

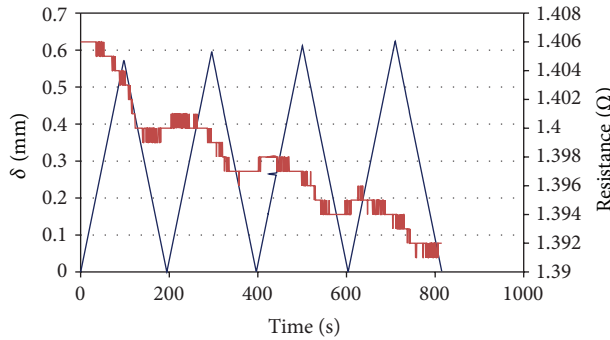


FIGURE 7: Piezo resistive behaviour of BCR reinforced mortar under cyclic flexural loading.

helpful for strain sensitivity. Due to the less amount of carbon fibres, BCRI, however, showed lower elastic modulus as compared to BCR3 comprised of 100% carbon fibres. The lowest tensile properties were obtained with BCR2 which was made of 53% E-glass and 47% carbon fibres. As the glass fibres that were present in these braided composites had almost equal quantity to that of the carbon fibres, it was not possible for them to bear the load sustained by the composites after the breakage of carbon fibres. This resulted in catastrophic failure and poor mechanical properties. Besides composition, the mechanical performance of BCRs can be further tailored by changing the grade or type of glass and carbon fibres used.

**3.4. Optimum Composition.** Therefore, the best piezo resistive behaviour was obtained with BCRI which was also found fairly well in terms of mechanical properties. The gauge factor obtained with this braided composite was either 23.4 or 14.9 (depending on positive or negative response), which is much higher than the other carbon fibre/glass fibre hybrid systems reported previously [5, 9, 32] and also comparable to continuous or short carbon fibres composites [34, 36]. The used braiding process was able to introduce a certain degree of misalignments into the core carbon fibres and also

position them in only one-half of the cross-section in order to subject them to either tensile or compressive stresses under flexural deformation. As a result, BCRI proved to be very effective in sensing very low flexural strain in continuous manner. Although the BCRs containing lower amount of carbon fibres than the one reported in this paper were found better in terms of strain sensitivity, they were not suitable for reinforcement of concrete due to lower mechanical properties as compared to steel rebars [28]. Since these BCRs were primarily developed for concrete reinforcement, both reinforcing and sensing capabilities were taken into account and BCRI has been considered as the optimum composition. However, for other applications, which allow to use BCRs with lower mechanical properties, compositions with lower amount of carbon fibres can be used to obtain better strain sensitivity. Studies are also underway to improve the strain sensitivity of BCR without reducing the amount of carbon fibres by dispersing short carbon fibres in the matrix [31].

**3.5. Piezo resistive Behaviour of BCR Reinforced Mortar.** The test results of piezo resistivity of BCRI reinforced mortar samples are provided in Table 7 and presented in Figure 7. It can be observed that the resistance decreases in the loading cycles and remains constant in the unloading cycles. Therefore, resistance change is not reversible and continuous loading and unloading cycles lead to the decrease in resistance of BCR reinforced mortar beams. This indicates the permanent changes in the electrical contact points in each cycle, probably due to permanent change in the structure of BCRs. This permanent change in BCR structure was possible due to the comparatively higher flexural strain (~1%) used in the piezo resistive characterization of BCR reinforced mortar beams. In this case, the resistance decreased as the BCR was placed in the tension side of concrete samples in a small section where tensile stresses were approximately uniform. This led to alignment of carbon fibres and increase in the electrical contact points, as discussed in “Mechanism of Piezo resistivity” section. Nevertheless, the decrease in electrical resistance, as observed up to this strain level, suggests only

TABLE 7: Results of piezoresistive characterization of BCR reinforced mortar.

Parameters	Cycles			
	1	2	3	4
$t$ (s)	97	296	500	710
$\delta$ (mm)	0.571	0.595	0.612	0.624
$R$ ( $\Omega$ )	1.403	1.399	1.397	1.394
$\Delta R/R$	0.002	0.005	0.006	0.009
$\epsilon$ ( $\times 10^{-2}$ )	1.057	1.102	1.133	1.156

minor structural changes and absence of breakage or major structural damage which can increase the electrical resistance significantly. Therefore, a slight increase in resistance can be considered as an alarm signal for possible structural damage in order to carry out the maintenance work on time. It can be also noticed that the BCR reinforced mortar beams showed much lower sensitivity to the change in flexural strain as compared to BCRs. Further study is underway to understand the piezoresistive behaviour of BCR reinforced mortar by estimating the actual stresses to which BCRs are subjected within the mortar beams. Also, studies are being carried out to investigate the piezoresistive behaviour of BCR reinforced mortar by placing the BCRs at different cross-sections of the mortar beams and also at different strain levels. However, it can be concluded from the present results that BCR reinforced beams can sense their own deformations and may be helpful to diagnose structural damage. However, further understanding and improvement are extremely necessary to successfully apply these materials in practical situations.

#### 4. Conclusions

This paper reported the potential of core-reinforced hybrid carbon fibre/glass fibre braided rods for continuous monitoring of very low flexural strain. The effect of carbon fibre/glass fibre weight ratio on both strain sensitivity and tensile properties was investigated. Also, the influence of carbon fibre positioning on strain sensitivity was studied. It was observed that the studied braided composites with lowest amount of carbon fibres (23%) led to best strain sensitivity and good mechanical properties. The change of resistance in the braided composites was mainly attributed to the resistivity change due to strain-dependent change in the electrical contacts either due to fibre separation or fibre alignment or both. The braided composites showed both positive and negative responses under flexural strain depending on the placement of carbon fibres in the cross-section. The much higher gauge factors obtained with the best composition at low strain level (23.4 for positive response and 14.9 for negative response at strain up to 0.55%) as compared to previously reported hybrid composites were due to the misaligned arrangement of carbon fibres caused by the braiding process. Mortar beams reinforced with the BCRs having optimum composition were also found to sense their flexural deformation. However, the piezoresistive behaviour of reinforced beams was irreversible and may be useful to detect the structural damage. Further studies are going on

to properly understand the piezoresistive behaviour of BCR reinforced mortar in order to successfully apply them in real situations.

#### Conflict of Interests

The authors declare that there is no conflict of interests regarding the publication of this paper.

#### Acknowledgment

The authors would like to acknowledge the Grant POCI/CTM/60856/2004 funded by Portuguese Foundation for Science and Technology (FCT) that helped in carrying out this research.

#### References

- [1] M. Tracy and F.-K. Chang, "Identifying impact load in composite plates based on distributed piezoelectric sensors," in *Smart Structures and Integrated Systems*, vol. 2717 of *Proceedings of SPIE*, pp. 231–236, February 1996.
- [2] N. P. Saint, Y. Jayet, and J. C. Baboux, "The Piezoelectric implant method: theoretical and experimental study of the influence of inherent geometrical and bonding defects," in *Smart Structures and Materials*, vol. 2779 of *Proceedings of SPIE*, pp. 152–157, June 1996.
- [3] B. Culshaw and W. C. Michie, "Optical fibre sensors and their role in smart structures," in *Smart Structures and Materials*, Proceedings of SPIE, pp. 432–443, December 1996.
- [4] S. Kabashima, T. Ozaki, and N. Takeda, "Damage detection of satellite structures by optical fiber with small diameter," in *Smart Structures and Materials*, Proceedings of SPIE, pp. 343–351, March 2000.
- [5] N. Muto, Y. Arai, S. G. Shin et al., "Hybrid composites with self-diagnosing function for preventing fatal fracture," *Composites Science and Technology*, vol. 61, no. 6, pp. 875–883, 2001.
- [6] N. Takada, S. Shin, H. Matsubara, and H. Yanagida, "Fracture detection of fiber reinforced composite using electrical conductivity," in *Proceedings of the 5th Symposium on Intelligent Materials*, 1996.
- [7] C. E. Bakis, A. Nanni, J. A. Terosky, and S. W. Koehler, "Self-monitoring, pseudo-ductile, hybrid FRP reinforcement rods for concrete applications," *Composites Science and Technology*, vol. 61, no. 6, pp. 815–823, 2001.
- [8] N. Muto, H. Yanagida, M. Miyayama, T. Nakatsuji, M. Sugita, and Y. Ohtsuka, "Foreseeing of fracture in CFGFRP composites by the measurement of residual change in electrical resistance," *Journal of the Ceramic Society of Japan*, vol. 100, no. 4, pp. 585–588, 1992.
- [9] Y. Okuhara and H. Matsubara, "Memorizing maximum strain in carbon-fiber-reinforced plastic composites by measuring electrical resistance under pre-tensile stress," *Composites Science and Technology*, vol. 65, no. 14, pp. 2148–2155, 2005.
- [10] F. Nanni, F. Auricchio, F. Sarchi, G. Forte, and G. Gusmano, "Self-sensing CF-GFRP rods as mechanical reinforcement and sensors of concrete beams," *Smart Materials and Structures*, vol. 15, no. 1, pp. 182–186, 2006.
- [11] F. Nanni, G. Ruscito, G. Forte, and G. Gusmano, "Design, manufacture and testing of self-sensing carbon fibre-glass fibre

- reinforced polymer rods," *Smart Materials and Structures*, vol. 16, no. 6, pp. 2368–2374, 2007.
- [12] G. Gusmano, F. Nanni, and F. Auricchio, "Evaluation of Conductive FRP sensors for potential monitoring of concrete structure soundness," in *Innovations and Developments in Concrete Materials and Constructions*, pp. 337–344, Thomas Thelford Publishing, London, UK.
- [13] F. Nanni, G. Gusmano, G. Forte, F. Auricchio, F. Sarchi, and F. Ramaoli, Italian Patent PV2003A000001, 2003.
- [14] B. Fiedler, F. H. Gojny, M. H. G. Wichmann, W. Bauhofer, and K. Schulte, "Can carbon nanotubes be used to sense damage in composites?" *Annales de Chimie*, vol. 29, no. 6, pp. 81–94, 2004.
- [15] E. T. Thostenson and T.-W. Chou, "Carbon nanotube networks: sensing of distributed strain and damage for life prediction and self healing," *Advanced Materials*, vol. 18, no. 21, pp. 2837–2841, 2006.
- [16] E. T. Thostenson and T.-W. Chou, "Real-time in situ sensing of damage evolution in advanced fiber composites using carbon nanotube networks," *Nanotechnology*, vol. 19, no. 21, Article ID 215713, 2008.
- [17] C. Li, E. T. Thostenson, and T.-W. Chou, "Sensors and actuators based on carbon nanotubes and their composites: a review," *Composites Science and Technology*, vol. 68, no. 6, pp. 1227–1249, 2008.
- [18] L. Gao, E. T. Thostenson, Z. Zhang, and T.-W. Chou, "Sensing of damage mechanisms in fiber-reinforced composites under cyclic loading using carbon nanotubes," *Advanced Functional Materials*, vol. 19, no. 1, pp. 123–130, 2009.
- [19] L. Böger, M. H. G. Wichmann, L. O. Meyer, and K. Schulte, "Load and health monitoring in glass fibre reinforced composites with an electrically conductive nanocomposite epoxy matrix," *Composites Science and Technology*, vol. 68, no. 7-8, pp. 1886–1894, 2008.
- [20] M. Nofar, S. V. Hoa, and M. D. Pugh, "Failure detection and monitoring in polymer matrix composites subjected to static and dynamic loads using carbon nanotube networks," *Composites Science and Technology*, vol. 69, no. 10, pp. 1599–1606, 2009.
- [21] B. Fiedler, F. H. Gojny, M. H. G. Wichmann, M. C. M. Nolte, and K. Schulte, "Fundamental aspects of nano-reinforced composites," *Composites Science and Technology*, vol. 66, no. 16, pp. 3115–3125, 2006.
- [22] W. Michaeli and D. Jürss, "Thermoplastic pull-braiding: pultrusion of profiles with braided fibre lay-up and thermoplastic matrix system (PP)," *Composites A*, vol. 27, no. 1, pp. 3–7, 1996.
- [23] H. G. Harris, W. Somboonsong, and F. K. Ko, "New ductile hybrid FRP reinforcing bar for concrete structures," *Journal of Composites for Construction*, vol. 2, no. 1, pp. 28–37, 1998.
- [24] T. Hiermer, K. G. Schmitt-Thomas, and Z.-G. Yang, "Mechanical properties and failure behaviour of cylindrical CFRP-implant-rods under torsion load," *Composites A*, vol. 29, no. 11, pp. 1453–1461, 1998.
- [25] R. Fangueiro, C. Pereira, M. Araujo, and S. Jalali, International Patent 103581, 2011.
- [26] G. Sousa, *Braided structural elements for concrete reinforcement [M.S. thesis]*, University of Minho, Portugal, 2004.
- [27] C. Gonilho Pereira, R. Fangueiro, S. Jalali, M. Araujo, and P. Marques, "Braided reinforced composite rods for the internal reinforcement of concrete," *Mechanics of Composite Materials*, vol. 44, no. 3, pp. 221–230, 2008.
- [28] C. Gonilho-Pereira, S. Jalali, R. Fangueiro, M. Araújo, and P. Pina Marques, "Hybrid composite rods for concrete reinforcement," in *Proceedings of the 1st International Conference on Structures and Architecture (ICSA '10)*, pp. 1651–1658, Guimaraes, Portugal, July 2010.
- [29] S. Patinha, F. Cunha, S. Rana, and R. Fangueiro, "Mechanical behavior of novel braided composite rods with steel wire in the core," in *Proceedings of the 11th International Symposium of Fiber Reinforced Concrete Structures (FRPRCS11 '13)*, pp. 26–28, Guimaraes, Portugal, June 2013.
- [30] Raul Fangueiro, Sohel Rana, and A. Gomes Correia, "Braided composite rods: innovative fibrous materials for geotechnical applications," *Geomechanics and Engineering*, vol. 5, no. 2, pp. 87–97, 2013.
- [31] K. P. Rosado, S. Rana, C. Pereira, and R. Fangueiro, "Self-sensing hybrid composite rod with braided reinforcement for strutural health monitoring," *Materials Science Forum*, vol. 730–732, pp. 379–384, 2013.
- [32] J. W. Cho, J. S. Choi, and Y. S. Yoon, "Electromechanical behavior of hybrid carbon/glass fiber composites with tension and bending," *Journal of Applied Polymer Science*, vol. 83, no. 11, pp. 2447–2453, 2002.
- [33] S. Wang and D. D. L. Chung, "Self-sensing of flexural strain and damage in carbon fiber polymer-matrix composite by electrical resistance measurement," *Carbon*, vol. 44, no. 13, pp. 2739–2751, 2006.
- [34] X. Wang and D. D. L. Chung, "Continuous carbon fibre epoxy-matrix composite as a sensor of its own strain," *Smart Materials and Structures*, vol. 5, no. 6, pp. 799–800, 1996.
- [35] J. B. Park, T. Okabe, D. Y. Song, N. Takeda, and A. Kitano, "In-situ health monitoring of CFRP composites using electrical characteristics," in *Smart Structures and Materials*, Proceedings of SPIE, pp. 323–331, March 2001.
- [36] X. W. Xiaojun Wang and D. D. L. Chung, "Short-carbon-fiber-reinforced epoxy as a piezoresistive strain sensor," *Smart Materials and Structures*, vol. 4, no. 4, article 017, pp. 363–367, 1995.

## Research Article

# A Simple and Reliable Setup for Monitoring Corrosion Rate of Steel Rebars in Concrete

**Shamsad Ahmad, Mohammed Abdul Azeem Jibran,  
Abul Kalam Azad, and Mohammed Maslehuddin**

Civil and Environmental Engineering Department, King Fahd University of Petroleum and Minerals, P.O. Box 1403, Dhahran 31261, Saudi Arabia

Correspondence should be addressed to Shamsad Ahmad; shamsad@kfupm.edu.sa

Received 24 August 2013; Accepted 16 October 2013; Published 12 January 2014

Academic Editors: D. G. Aggelis, N. Alver, and H. K. Chai

Copyright © 2014 Shamsad Ahmad et al. This is an open access article distributed under the Creative Commons Attribution License, which permits unrestricted use, distribution, and reproduction in any medium, provided the original work is properly cited.

The accuracy in the measurement of the rate of corrosion of steel in concrete depends on many factors. The high resistivity of concrete makes the polarization data erroneous due to the Ohmic drop. The other source of error is the use of an arbitrarily assumed value of the Stern-Geary constant for calculating corrosion current density. This paper presents the outcomes of a research work conducted to develop a reliable and low-cost experimental setup and a simple calculation procedure that can be utilised to calculate the corrosion current density considering the Ohmic drop compensation and the actual value of the Stern-Geary constants calculated using the polarization data. The measurements conducted on specimens corroded to different levels indicate the usefulness of the developed setup to determine the corrosion current density with and without Ohmic drop compensation.

## 1. Introduction

The rate of reinforcement corrosion, commonly expressed as corrosion current density,  $I_{corr}$ , is a quantitative indicator of the damage caused to the steel rebars due to their corrosion. Such information is of great importance for detecting corrosion initiation at early stages and for predicting the time to initiation of corrosion-induced cracking and residual strength of a corroding structure and hence its remaining service-life [1]. The nondestructive test methods generally utilised for measuring corrosion rate include Tafel plot, linear polarization resistance, electrochemical noise, A.C. impedance, and electrical resistance. The main advantages of electrochemical techniques include sensitivity to low corrosion rates, short experimental duration, and well-established theoretical understanding. On the other hand, the gravimetric weight loss measurement is a destructive technique for determining the average rate of corrosion [2].

The linear polarization resistance method (LPRM) is mostly used for measuring the  $I_{corr}$  of the rebar embedded in concrete, as it is nondestructive and nonperturbative.

Furthermore, the LPRM is suitable for use in the laboratory and in the field while other methods are only suitable for use in the laboratory. The setup used in LPRM consists of a working electrode, a counter-electrode, a reference electrode, and a DC power supply unit; usually a potentiostat or galvanostat is utilised for this purpose.

The potentiostat or galvanostat is connected to the rebar (the working electrode), counter-electrode, and the reference electrode. In the potentiostatic mode, the potential difference between the working and the counter-electrode is kept constant and the resulting current is measured. In the galvanostatic mode the current flowing between the counter-electrode and the working electrode is kept constant and the resulting potential of the working electrode is measured. For both modes the potential and current are plotted and the slope of this curve, denoted as the resistance to polarization,  $R_p$ , is calculated, and this value is used to calculate the  $I_{corr}$  utilising the well-known Stern-Geary equation [3]. The main difference in determining the  $R_p$  for big-size laboratory specimens or in situ measurements, compared to small-size laboratory specimens, is

the geometrical arrangement of the counter electrode. In laboratory studies, the concrete specimen containing the steel rebar as working electrode, the counter-electrode, and the reference electrode are immersed in a sodium chloride solution which promotes a uniform distribution of the polarizing current on the steel rebars. In the case of a big-size specimen or in the in situ measurement, a disk-shaped counter-electrode (having a central hole to accommodate the reference electrode) is placed on a water-soaked sponge kept on the surface of the concrete specimen/structure. The reference electrode is placed in the central hole of the counter-electrode.

The  $I_{\text{corr}}$  measurements in large-size laboratory concrete specimens or in in situ structures using the LPRM have been a challenging problem because of various practical difficulties encountered in the application of the available test methods and instruments resulting in a significant error in the estimation of the corrosion rate. The major sources of errors include failure to adequately correct for the Ohmic drop resulting from the relatively high electrical resistivity of concrete; lack of information on the area of the rebar that is actually being polarized; and the lack of precise value of the Stern-Geary constant used for the calculation of the corrosion rate. For an improved or better estimation of  $I_{\text{corr}}$ , the correct measurement of  $R_p$  taking into consideration the Ohmic drop compensation and the area of rebar actually polarized and also the determination of the actual value of the Stern-Geary constant,  $B$ , using the values of Tafel slopes are essential. For this purpose, the aspects that need to be considered are adequate compensation for Ohmic drop, verification of the range of linearity of the polarization around  $E_{\text{corr}}$ , selection of an optimum polarization response time, careful interpretation of the  $R_p$  value particularly when the steel is in a passive state, solving the problem of uncertainty of the rebar surface actually polarized by the applied electric signal using a suitable method, and the determination of the values of the Tafel slopes (for calculating the actual value of  $B$ ) using the polarization data [4–15].

A simple experimental setup and calculation procedure were reported earlier by Ahmad and Bhattacharjee [8] considering the accuracy by having a provision of Ohmic drop compensation and determination of the precise value of the Stern-Geary constant. However, the performance of the setup developed by Ahmad and Bhattacharjee [8] was not evaluated for its application for measuring a wide range of very low to very high  $I_{\text{corr}}$ . Commercial setups are also available in recent times for measuring reinforcement corrosion rate but the accuracy of the commercially available setups needs to be verified for their applications to reinforcement corrosion rate. Furthermore, the commercial setups have not been shown to be reliable when Ohmic drop compensation option was utilized. The objective of the present study was to develop a simple low-cost setup for measuring  $I_{\text{corr}}$  by making a minor modification in the original setup of Ahmad and Bhattacharjee [8]. The performance of the developed setup was evaluated for determining its capability to measure  $I_{\text{corr}}$  in all ranges with and without Ohmic drops compensation.

## 2. Development of a Setup and a Calculation Procedure to Estimate $I_{\text{corr}}$

**2.1. Circuitry of the Setup.** Slightly modified version of the circuitry proposed earlier by Ahmad and Bhattacharjee [8] is shown in Figure 1. The only modification made in the circuitry was the connection of the wire connecting rebar (working electrode) to the positive terminal of the voltmeter in addition to the connection through the ammeter. This change made it possible to have stable readings in ammeter during polarization, particularly at low current intensities. The circuitry is based on the linear polarization resistance method and it is integrated in a way that the data can be generated to calculate the Ohmic resistance of concrete and Tafel slopes required for calculating  $I_{\text{corr}}$  more accurately. The part of the integrated circuitry for measuring the half-cell potential using a Cu/CuSO<sub>4</sub> electrode (CSE) as a reference electrode is similar to that specified by ASTM C 876-99 [16]. The part of the integrated circuitry for determining the Ohmic resistance is based on the principle of determining the internal resistance of a cell [17]. The part of the integrated circuitry for the determination of the apparent polarization resistance is based on the galvanostatic technique [18]. The counter-electrode (C.E.) for applying the polarizing current was made of stainless steel having a width of 25 mm and thickness of 3 mm with a central hole to accommodate the reference electrode (R.E.). A photograph of the components of the developed setup is shown in Figure 2.

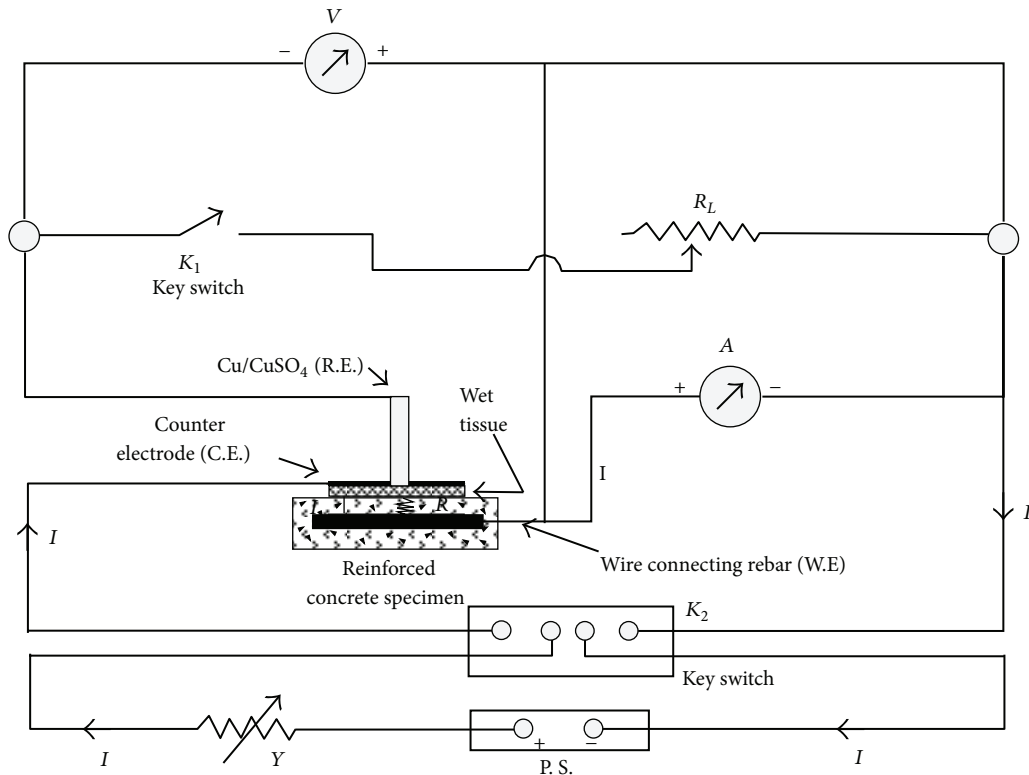
### 2.2. Data Generation Using the Developed Setup

**2.2.1. Preparation of the Test Points.** Before using the setup for carrying out measurements, there should be good physical contact between the reference electrode tip and the concrete surface to avoid poor electrolytic contact of the reference electrode with the specimen. For this purpose, the prewetting of the surface points under test is done through a tissue paper soaked with water and allowed to be there for 20–30 minutes so that the moisture can soak in before the initiation of the test.

Referring to Figure 1 and the earlier work published by Ahmad and Bhattacharjee [8], the procedure for measurement of half-cell potential, that is, corrosion potential ( $E_{\text{corr}}$ ) and generation of data required to determine Ohmic resistance ( $R$ ), and polarization resistance ( $R_p$ ) are as follows.

**2.2.2. Corrosion Potential ( $E_{\text{corr}}$ ).** Keeping key switches  $K_1$  and  $K_2$  off, the corrosion potential  $E_{\text{corr}}$  is recorded allowing a sufficient response time of 30–60 seconds for measurements to stabilize. If the corrosion potential is low, the voltmeter reading is not stable and fluctuates; consequently, the reading after 30–60 seconds waiting period should be considered as the representative value.

**2.2.3. Data for Ohmic Resistance ( $R$ ).** For determining the Ohmic resistance ( $R$ ), different value of resistances ( $R_L$ ) is set in the standard decade box resistor and  $R_L$  versus  $V_L$  data are generated keeping key switch  $K_{1\text{on}}$  and key



- $R_L$ : standard decade box resistor
- $V$ : voltmeter capable of reading 0-1.0 V with a least count of 0.1 mV
- $K_1$  &  $K_2$ : key switches
- R.E.: standard  $\text{Cu}/\text{CuSO}_4$  reference electrode as per ASTM C-876
- C.E.: counter electrode
- W.E.: working electrode (rebar)
- A: ammeter capable of reading 0-200  $\mu\text{A}$  with a least count of 0.1  $\mu\text{A}$
- R: Ohmic resistance of concrete
- E: E.M.F. of corrosion cell
- I: cathodic current applied to the rebar for polarization
- P.S.: constant voltage power supplier
- Y: variable resistance to keep circuit resistance high enough to maintain constant current

FIGURE 1: Experimental setup for generating the data pertaining to corrosion potential, Ohmic resistance, and polarization resistance (modified version of the setup proposed earlier by Ahmad and Bhattacharjee [8]).

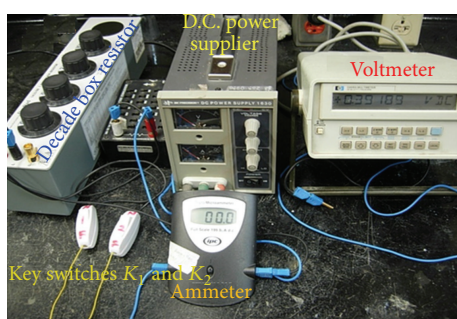


FIGURE 2: Photograph showing components of the developed setup.

switch  $K_2$  off. The switch  $K_1$  permits a standard decade box resistor to be connected momentarily, whenever a voltage reading is desired, thus avoiding excessive current drain over

a prolonged period of time. The terminal voltage of the cell, under load,  $V_L$ , is given by the voltmeter reading, when the key switch,  $K_1$ , is closed. At least 10 values of  $V_L$  are recorded by setting different values of  $R_L$  in increasing order with a gap of 10 to 15 s between two consecutive readings.

**2.2.4. Data for Polarization Resistance ( $R_p$ ).** For determining the polarization resistance ( $R_p$ ), a cathodic polarizing current,  $I$ , is applied and the resulting potential  $V$  (which is more negative than  $E_{\text{corr}}$ ) is recorded by keeping key switch  $K_1$  off throughout the experiment and key switch  $K_2$  on. The current is applied in steps until the maximum value of the overvoltage,  $\epsilon$  (value of potential by which  $E_{\text{corr}}$  is shifted as a result of polarization), is reached, which is usually 10 to 20 mV for the polarization curve to be in the linear range, with the help of a variable resistor,  $Y$ , which helps to keep the resistance of the circuit high enough to maintain a constant

current. Initially, a cathodic current of  $2 \mu\text{A}$  is applied and then the second current step is  $4 \mu\text{A}$ , the third  $6 \mu\text{A}$ , and so forth. After allowing a response time of 30 seconds at each current step the steady voltmeter reading is recorded. After polarizing, a significant fluctuation in the voltage of rebars with low corrosion is noted and hence a response time of 30 seconds is commonly used to note the voltmeter reading.

**2.3. Calculation Procedure for Corrosion Parameters.** The Ohmic resistance ( $R$ ), polarization resistance ( $R_p$ ), Tafel slopes ( $\beta_a$  and  $\beta_c$ ), Stern-Geary constant ( $B$ ), and corrosion current density ( $I_{\text{corr}}$ ) are determined, as follows.

**2.3.1. Determination of Ohmic Resistance ( $R$ ).** The  $1/R_L$  and  $1/V_L$  values are plotted keeping  $1/R_L$  on the  $x$ -axis and  $1/V_L$  on the  $y$ -axis. The slope and  $y$ -axis intercept of the best-fit straight line joining these points are noted down. The ratio of the value of the slope to the value of intercept gives the value of the Ohmic resistance,  $R$ . The value of the Ohmic resistance can be utilised for compensating the Ohmic drop mathematically.

**2.3.2. Determination of Polarization Resistance ( $R_p$ ).** With the help of the recorded polarization data ( $I$  versus  $V$  values), the polarized potential ( $E$ ) can be determined as  $E = V$  (without Ohmic drop compensation) or  $E' = V - I \cdot R$  (Ohmic drop compensation), where  $R$  is the Ohmic resistance obtained in the previous step. Using the value of  $E$ , the overvoltage ( $\epsilon$ ) can be determined as  $\epsilon = E - E_{\text{corr}}$ , where  $E_{\text{corr}}$  is the measured value of the corrosion potential (without applying polarization current). The  $I$  versus  $\epsilon$  values are plotted and a straight line is best-fitted. The slope of the best-fitted straight line is taken as  $R_p$ .

**2.3.3. Determination of Tafel Slopes ( $\beta_a$  and  $\beta_c$ ) and Stern-Geary Constant ( $B$ ).** Instead of assuming the value of the Stern-Geary constant,  $B$ , as 26 mV for actively corroding reinforcement and 52 mV for passive reinforcement [19], the Tafel slopes  $\beta_a$  and  $\beta_c$  should be determined utilising the polarization data for determining its accurate value. The values of  $\beta_a$  and  $\beta_c$  can be determined by best-fitting the polarization data into the polarization equation, as follows [20]:

$$2.3R_p I_i = \frac{\beta_a \beta_c}{\beta_a + \beta_c} \left[ \exp\left(\frac{2.3\epsilon_i}{\beta_a}\right) - \exp\left(-\frac{2.3\epsilon_i}{\beta_c}\right) \right]. \quad (1)$$

The search method can be used to determine  $\beta_a$  and  $\beta_c$ , in which several possible combinations of the values of  $\beta_a$  and  $\beta_c$  can be tried within their minimum and maximum values of 120 mV to 240 mV corresponding to  $B$ -value in the range of 26 mV to 52 mV [19]. The final value of  $\beta_a$  and  $\beta_c$  can be taken corresponding to the minimum value of the sum of squares of the differences of left-hand side and right-hand side values of (1) for  $i$  number of the  $I$  versus  $\epsilon$  values within the linear polarization range. The minimization of the sum of error squares can be carried out using *Excel-Solver* and the optimum values of  $\beta_a$  and  $\beta_c$  can be determined satisfying

the constraints:  $\beta_a$  and  $\beta_c$  should be between 120 and 240 mV. Once the values of  $\beta_a$  and  $\beta_c$  are determined, the Stern-Geary constant,  $B$ , can be determined using (2) [3]

$$B = \frac{\beta_a \beta_c}{2.3(\beta_a + \beta_c)}. \quad (2)$$

**2.3.4. Determination of Corrosion Current Density ( $I_{\text{corr}}$ ).**  $I_{\text{corr}}$  can be determined using the calculated values of  $R_p$ ,  $B$ , and surface area of the steel rebar,  $A_s$ , from (3) [3]

$$I_{\text{corr}} = \frac{B}{R_p A_s}. \quad (3)$$

### 3. Experimental Program

**3.1. Test Specimens.** Fifteen reinforced concrete specimens reinforced with three 12 mm diameter bars in each specimen were prepared to assess the efficacy of the developed setup in measuring reinforcement corrosion. The details of the concrete specimens are shown in Figure 3. In Figure 3, three steel bars embedded in concrete are represented by three thick horizontal lines. The three thin vertical lines represent the GFRP bars embedded in concrete to hold the steel bars in correct positions during casting. Steel rebars embedded in the slab specimens were corroded to varying degree using the impressed current technique. The positive terminal of a D.C. power supply was connected to the steel rebar and the negative terminal was connected to the stainless steel plates (25 mm wide and 3 mm thick strips used as counter electrodes), placed over the concrete surface corresponding to the line of steel rebars, each having a surface area of  $158.33 \text{ cm}^2$ , as shown in Figure 4. Different degrees of reinforcement corrosion were obtained by varying the duration of the impressed current in the range of 27 to 280 hours.

Since the slab specimens were corroded by low intensity impressed current for simulating natural corrosion, the maximum corrosion rate measured in such specimens was found to be less than  $1 \mu\text{A}/\text{cm}^2$ . In order to examine the usefulness of the developed setup for measuring varying intensities of corrosion (low, medium, and high), another different batch of 13 specimens, naturally corroded under chloride exposures for a period of about five years, was considered in which the  $I_{\text{corr}}$  was in the range of  $1 \mu\text{A}/\text{cm}^2$  to  $10 \mu\text{A}/\text{cm}^2$ .

**3.2.  $I_{\text{corr}}$  Measurements.** The developed setup was utilized to measure  $I_{\text{corr}}$  in the test specimens prepared and corroded in accelerative and natural manners. A photograph of the corrosion measurement using the developed setup is shown in Figure 5. The white layer under the steel plate is water-soaked tissue paper placed to improve the electrolytic contact of the reference electrode with the specimen. The  $I_{\text{corr}}$  values were calculated with and without  $IR$  compensation.

**3.3. Calculations for Determining  $I_{\text{corr}}$ .** Table 1 shows a set of typical data for calculating the Ohmic resistance,  $R$ . By plotting the  $1/R_L$  versus  $1/V_L$ , a best-fit straight line is obtained, as shown in Figure 6. The ratio of the slope (41.815) and intercept (0.0441) gives the value of  $R$  as 948 Ohm.

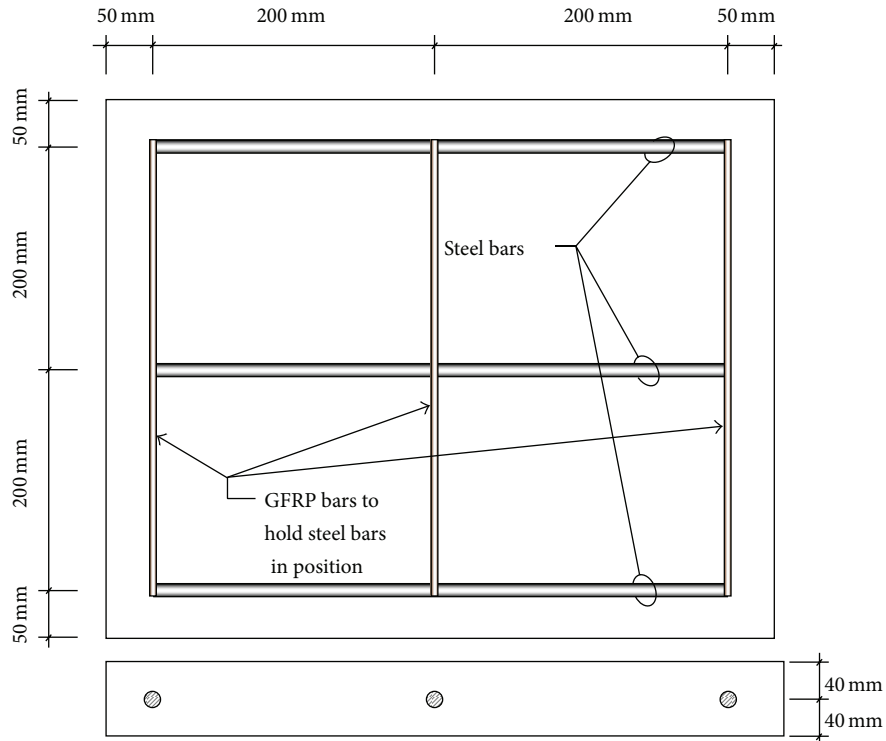


FIGURE 3: Details of reinforced concrete slab specimens.

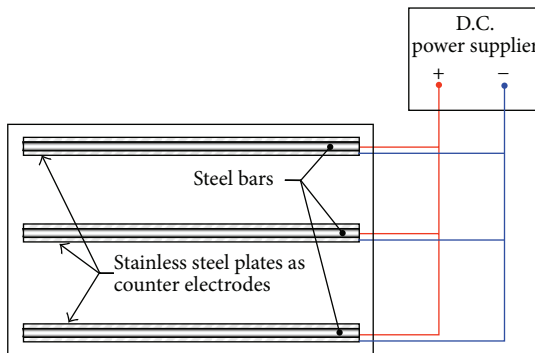
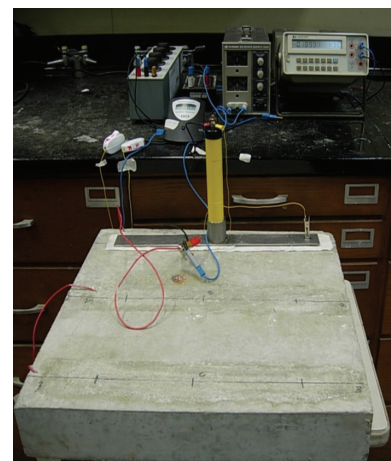


FIGURE 4: Setup for corroding the steel rebars.

FIGURE 5:  $I_{corr}$  measurement using developed setup.

A typical set of the polarization data along with the measured value of  $E_{corr}$  and calculated value of  $R$  are presented in Table 2. The values of over voltage  $\varepsilon$  and  $\varepsilon'$  for without and with Ohmic drop compensation, respectively, are also shown in Table 2. Using the  $I$  versus  $\varepsilon$  values, the best-fitted linear polarization curves for without and with Ohmic drop compensation are also plotted, as shown in Figure 7. The slopes of the best-fitted straight lines are taken as the polarization resistance values as  $R_p = 6473$  Ohm (without Ohmic drop compensation) and  $R'_p = 5525$  Ohm (with Ohmic drop compensation). After obtaining the values of polarization resistance, Tafel slopes can be calculated by best-fitting equation (1) using *Excel-Solver*. The calculations of the Tafel slopes as well as Stern-Geary constant are presented in

Table 2. Using the calculated values of polarization resistance, Stern-Geary constant, and surface area of the steel rebar ( $158.33 \text{ cm}^2$ ), the corrosion current density can be calculated using (3), as follows:  $I_{corr} = 46.57 \times 10^3 / (6473 \times 158.33) = 0.045 \mu\text{A}/\text{cm}^2$  (without  $IR$  drop compensation) and  $I_{corr} = 45.69 \times 10^3 / (5525 \times 158.33) = 0.052 \mu\text{A}/\text{cm}^2$  (with  $IR$  drop compensation).

Three sets of  $I_{corr}$  measurements were carried out on each of 15 slab specimens corroded in accelerative way and one set of  $I_{corr}$  measurement was conducted on each of 13 cylindrical specimens corroded naturally. In this way a total

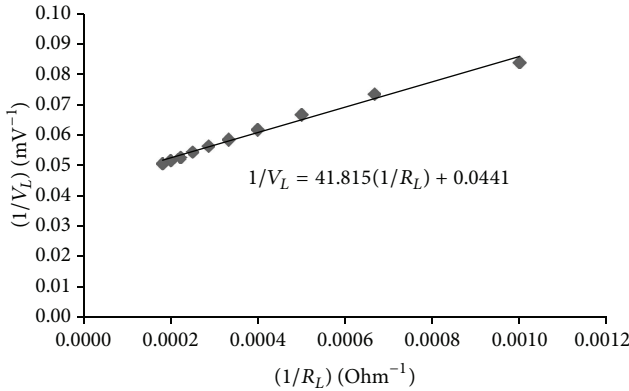


FIGURE 6: Plot of  $1/R_L$  versus  $1/V_L$  values for obtaining Ohmic resistance,  $R$ .

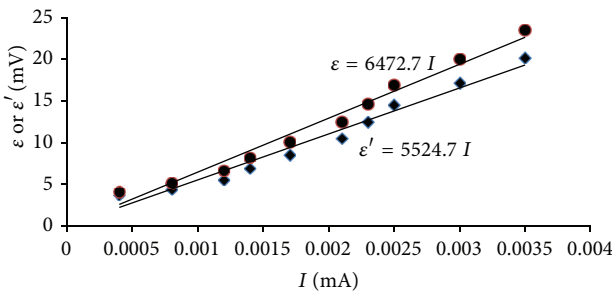


FIGURE 7: Plot of  $I$  versus  $\epsilon$  values for obtaining polarization resistance,  $R_p$  and  $R'_p$ .

TABLE 1: Sample calculation for  $R$ .

Specimen ID: AC-4 with $E_{corr} = 57$ mV; $R = 948$ Ohm			
$R_L$ (Ohm)	$V_L$ (mV)	$1/R_L$	$1/V_L$
1000	11.9	0.0010	0.08
1500	13.6	0.0007	0.07
2000	15.0	0.0005	0.07
2500	16.2	0.0004	0.06
3000	17.1	0.0003	0.06
3500	17.8	0.0003	0.06
4000	18.4	0.0003	0.05
4500	19.0	0.0002	0.05
5000	19.4	0.0002	0.05
5500	19.8	0.0002	0.05

of 58 sets of  $I_{corr}$  values were determined with and without  $IR$  drop compensation utilizing the developed setup and calculation procedure, as presented in Table 3. The measured values of  $I_{corr}$  were found to be in the range of  $0.026 \mu\text{A}/\text{cm}^2$  to  $3.38 \mu\text{A}/\text{cm}^2$  without Ohmic drop compensation and  $0.03 \mu\text{A}/\text{cm}^2$  to  $14.3 \mu\text{A}/\text{cm}^2$  with Ohmic drop compensation. The  $I_{corr}$  measurements in a wide range of very low to very high values, using the developed setup, have confirmed that the setup is capable of measuring corrosion rates of any degree, from very low to very high.

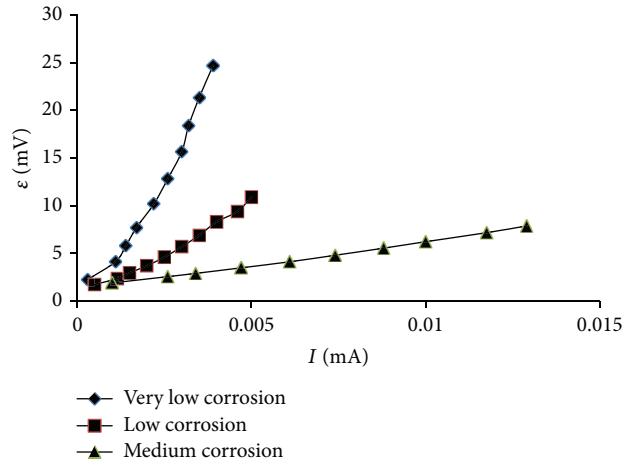


FIGURE 8: Polarization curves for specimens with very low, low, and medium corrosion.

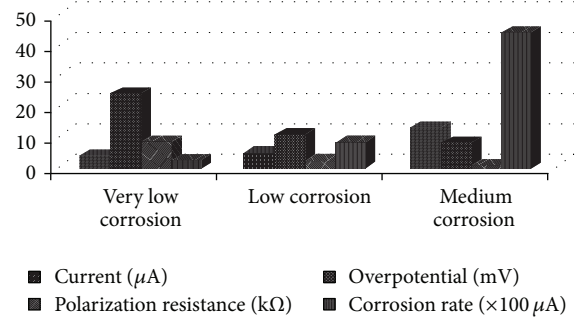


FIGURE 9: Comparison of  $I$ ,  $\epsilon$ ,  $R_p$ , and  $I_{corr}$  for very low, low, and medium corrosion.

## 4. Results and Discussions

**4.1. Variation of Polarization Trend with Degree of Corrosion.** In order to show the variation of the polarization trend with the variation in the  $I_{corr}$  from low to high, polarization data ( $I$  versus  $\epsilon$  values) obtained for three different specimens typically having very low, low, and medium degree of corrosion were plotted, as shown in Figure 8. It can be seen from the data in Figure 8 that the linearity of the polarization curves is more with an increase in the degree of corrosion. Further, in case of very low corrosion, the overpotential is very high at a very low value of the polarizing current. For a higher degree of corrosion, the requirement for polarizing current increases even for a relatively very small overpotential.

Figure 9 shows a comparison of  $I$ ,  $\epsilon$ ,  $R_p$ , and  $I_{corr}$  values for varying intensity of corrosion. It can be observed that the requirement for polarizing current  $I$  increases while the resulting overpotential,  $\epsilon$ , decreases with an increase in the degree of corrosion. Further, as expected, the polarization resistance,  $R_p$ , decreased while the corrosion rate,  $I_{corr}$ , increased with an increase in the degree of corrosion.

**4.2. Correlation between  $I_{corr}$  Values Measured with and without IR Drop Compensation.** The  $I_{corr}$  values presented

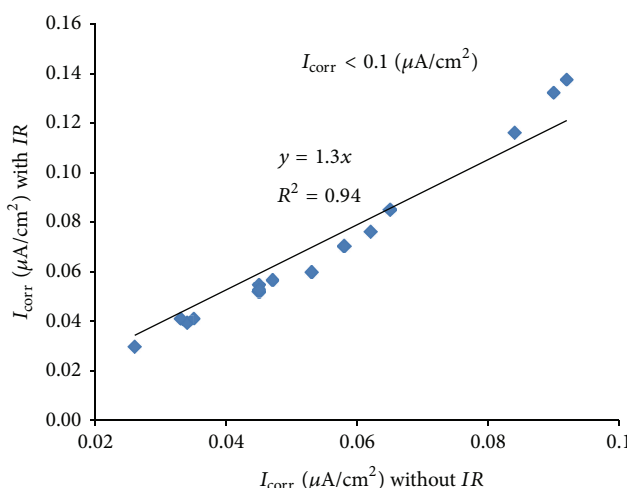
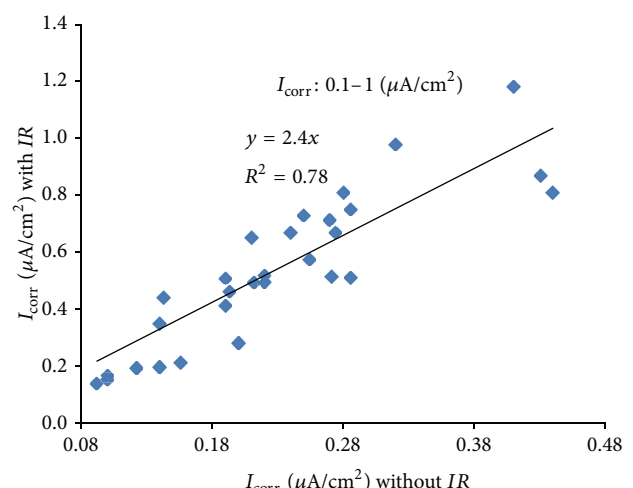
TABLE 2: Sample calculation for  $R_p$ ,  $\beta_a$ ,  $\beta_c$ , and  $B$ .

$I$ (mA)	$E = V$ (mV)	Specimen ID: AC-4 with $E_{corr} = 57$ mV (CSE) and $R = 948$ Ohm					Square of the error for (1) (without IR drop)	Square of the error for (1) (with IR drop)
		$E' = V - IR$ (mV)	$\varepsilon = E - E_{corr}$ (mV)	$\varepsilon' = E' - E_{corr}$ (mV)	$R_p$ and $R'_p$ (Ohm)			
0.0004	61.08	60.70	4.08	3.70			11.530	11.534
0.0008	62.12	61.36	5.12	4.36			0.034	0.031
0.0012	63.65	62.51	6.65	5.51			7.138	7.047
0.0014	65.20	63.87	8.20	6.87			4.551	4.460
0.0017	67.10	65.48	10.10	8.48	$R_p = 6473$		5.288	5.160
0.0021	69.47	67.47	12.47	10.47	$R'_p = 5525$		8.431	8.222
0.0023	71.62	69.43	14.62	12.43			1.076	1.007
0.0025	73.90	71.53	16.90	14.53			1.244	1.301
0.003	77.00	74.15	20.00	17.15			0.410	0.191
0.0035	80.50	77.18	23.50	20.18			1.135	1.128

Minimization of the sum of the squares of the error for best fitting (1) with the help of the Excel-Solver using constraints as follows:  $\beta_a$  and  $\beta_c \geq 120$  mV but  $\leq 240$  mV;  $B \geq 26$  mV but  $\leq 52$  mV.

Min. sum = 40.836 at  $\beta_a = 240$  mV and  $\beta_c = 193$  mV  
Therefore, from (2)  $B = 46.57$  mV

Min. sum = 40.085 at  $\beta_a = 240$  mV and  $\beta_c = 187$  mV  
Therefore, from (2)  $B = 45.69$  mV

FIGURE 10: Correlation between  $I_{corr}$  with and without IR compensation for  $I_{corr} < 0.1 \mu\text{A}/\text{cm}^2$ .FIGURE 11: Correlation between  $I_{corr}$  with and without IR compensation for  $I_{corr}$  0.1 to  $1.0 \mu\text{A}/\text{cm}^2$ .

in Table 3 were utilised for developing correlation between  $I_{corr}$  values measured with and without Ohmic drop compensation. For this purpose, the data were classified into three groups for different ranges of the degree of corrosion, as follows: (i) low corrosion ( $I_{corr} < 0.1 \mu\text{A}/\text{cm}^2$ ); (ii) medium corrosion ( $I_{corr} = 0.1$  to  $1.0 \mu\text{A}/\text{cm}^2$ ); and (iii) high corrosion ( $I_{corr} > 1 \mu\text{A}/\text{cm}^2$ ). The plots of  $I_{corr}$  with and without IR compensation for low, medium, and high corrosion are shown in Figures 10, 11, and 12, respectively. The equations correlating between  $I_{corr}$  with and without IR compensation are presented in Table 4. These data show that the effect of Ohmic drop increases with an increase in the intensity of corrosion. The error in  $I_{corr}$  due to Ohmic drop is only 30% in case of low degree of corrosion against an error of around 250% in case of medium degree of corrosion while it is 400% in the case of high degree of corrosion. The increase in the

effect of Ohmic drop is due to the higher requirement for polarizing current for the specimens having a higher degree of corrosion, as shown in Figure 9.

The data developed in this study have indicated that the  $I_{corr}$  can be determined without IR compensation with a fair degree of accuracy in specimens with low degree of corrosion ( $I_{corr} < 0.1 \mu\text{A}/\text{cm}^2$ ). However, IR compensation must be considered in determining medium to high  $I_{corr}$  ( $I_{corr} > 0.1 \mu\text{A}/\text{cm}^2$ ). Alternatively, the  $I_{corr}$  can be determined without IR compensation and the actual values can be obtained by multiplying with a coefficient of 2.4 for medium corrosion ( $I_{corr} = 0.1$  to  $1.0 \mu\text{A}/\text{cm}^2$ ) and 3.8 for high corrosion ( $I_{corr} > 1 \mu\text{A}/\text{cm}^2$ ). It should be noted that the experimental setup and calculation procedure developed in the present study are useful in situations where  $I_{corr}$  measurement with IR

TABLE 3:  $I_{corr}$  (with and without IR compensation) measured using developed setup.

Specimen ID	$I_{corr}$ without IR ( $\mu\text{A}/\text{cm}^2$ )	$I_{corr}$ with IR ( $\mu\text{A}/\text{cm}^2$ )
AC-1	0.026	0.030
AC-2	0.034	0.039
AC-3	0.033	0.041
AC-4	0.045	0.052
AC-5	0.084	0.116
AC-6	0.058	0.070
AC-7	0.035	0.041
AC-8	0.062	0.076
AC-9	0.053	0.060
AC-10	0.065	0.085
AC-11	0.100	0.165
AC-12	0.047	0.057
AC-13	0.045	0.052
AC-14	0.045	0.055
AC-15	0.045	0.053
AC-16	0.090	0.132
AC-17	0.140	0.196
AC-18	0.122	0.192
AC-19	0.286	0.509
AC-20	0.065	0.085
AC-21	0.156	0.212
AC-22	0.240	0.667
AC-23	0.143	0.441
AC-24	0.100	0.152
AC-25	0.090	0.111
AC-26	0.210	0.650
AC-27	0.190	0.508
AC-28	0.212	0.493
AC-29	0.440	0.809
AC-30	0.320	0.979
AC-31	0.286	0.751
AC-32	0.140	0.349
AC-33	0.092	0.138
AC-34	0.254	0.576
AC-35	0.220	0.495
AC-36	0.250	0.969
AC-37	0.280	0.809
AC-38	0.410	1.180
AC-39	0.193	0.461
AC-40	0.274	0.670
AC-41	0.190	0.411
AC-42	0.271	0.514
AC-43	0.250	0.730
AC-44	0.220	0.517
AC-45	0.270	0.712
NC-1	0.200	0.280
NC-2	0.250	0.350
NC-3	0.210	0.350
NC-4	0.240	0.380
NC-5	0.560	0.660
NC-6	0.431	0.870
NC-7	0.560	0.850
NC-8	2.250	9.700
NC-9	2.960	10.500

TABLE 3: Continued.

Specimen ID	$I_{corr}$ without IR ( $\mu\text{A}/\text{cm}^2$ )	$I_{corr}$ with IR ( $\mu\text{A}/\text{cm}^2$ )
NC-10	2.440	8.100
NC-11	3.380	14.300
NC-12	1.720	5.600
NC-13	1.082	3.180

AC: accelerated corrosion; NC: normal corrosion.

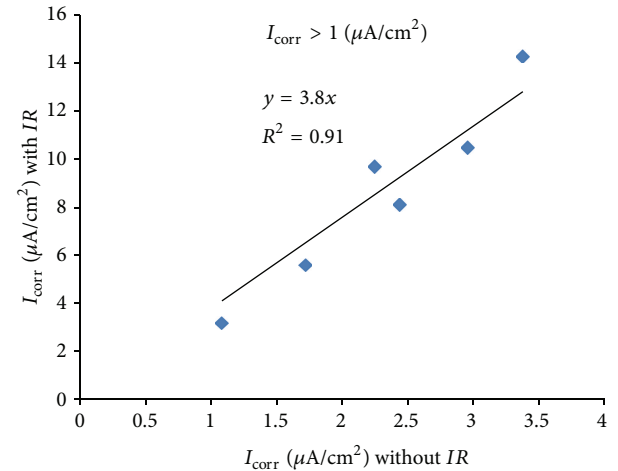


FIGURE 12: Correlation between  $I_{corr}$  with and without IR compensation for  $I_{corr} > 1 \mu\text{A}/\text{cm}^2$ .

TABLE 4: Relation between  $I_{corr}$  without and with Ohmic drop for various degrees of corrosion.

$I_{corr}$ ( $\mu\text{A}/\text{cm}^2$ )	Degree of corrosion	Relation between $I_{corr}$ measured without and with Ohmic drop
<0.1	Low	( $I_{corr}$ ) with IR = 1.3 ( $I_{corr}$ ) without IR
0.1 to 1	Medium	( $I_{corr}$ ) with IR = 2.4 ( $I_{corr}$ ) without IR
>1	High	( $I_{corr}$ ) with IR = 3.8 ( $I_{corr}$ ) without IR

compensation is not possible. Many of the  $I_{corr}$  measuring equipment commercially available in the market do not provide stable readings if the IR compensation is utilized.

The measurements using the proposed setup are possible for a normal thickness of concrete cover provided for reinforced concrete members. However, the effect of thickness of concrete cover on accuracy of the measurements should be considered in a separate study. The proposed setup and calculation procedure can be used in laboratory as well as in the field for measuring the corrosion current density of steel bars embedded in concrete with IR compensation. For the field applications, the rebars should be located using suitable equipment such as a cover meter for rightly placing the reference and counter electrodes and also for making connections with the rebars.

## 5. Conclusions

Based on the outcomes of the present study, the following conclusions are made.

- (1) A reliable experimental setup and a simple calculation procedure were developed that may be used to determine the  $I_{corr}$  over a wide range of values ( $0.1 \mu\text{A}/\text{cm}^2$  to more than  $10 \mu\text{A}/\text{cm}^2$ ). The  $I_{corr}$  values can be determined with and without *IR* compensation.
- (2) The  $I_{corr}$  measured with *IR* compensation was more than that measured without *IR* compensation. The effect of Ohmic drop was found to be low when the corrosion rate was low but its effect increased with an increase in the intensity of corrosion. The increase in Ohmic drop is due to higher requirement for polarizing current for the specimens with a high degree of corrosion.
- (3) The equations developed in this study can be utilized to correct the values of  $I_{corr}$  determined without Ohmic drop compensation to obtain the  $I_{corr}$  actual values.  $I_{corr}$  can be determined with a fair degree of accuracy in specimens with low intensity of corrosion ( $I_{corr} < 0.1 \mu\text{A}/\text{cm}^2$ ) without *IR* compensation. However, in specimens with medium to high corrosion a correction factor of 2.4 to 3.8 is required.

## Symbols

$A_s$ :	Surface area of the steel rebar exposed to corrosion
$B$ :	Stern-Geary constant
$E$ and $E'$ :	Polarized potential without and with Ohmic drop compensation, respectively
$E_{corr}$ :	Corrosion potential
$I$ :	Cathodic current applied to the rebar for polarization
$I_{corr}$ :	Corrosion current density
$IR$ :	Ohmic drop compensation
$R$ :	Ohmic resistance of concrete
$R_p$ and $R'_p$ :	Polarization resistance without and with Ohmic drop compensation, respectively
$V_L$ :	Potential drop corresponding to the resistance set in the standard decade box resistor, $R_L$
$\beta_a$ and $\beta_c$ :	Anodic and cathodic Tafel slopes, respectively
$\epsilon$ and $\epsilon'$ :	Overpotential without and with Ohmic drop compensation, respectively.

## Acknowledgments

The authors gratefully acknowledge the financial support received from the Center of Research Excellence in Corrosion (CoRE-C), King Fahd University of Petroleum and Minerals, Dhahran, Saudi Arabia, under the research Grant (CR-09-2010). The support of the Department of Civil & Environmental Engineering and the Research Institute is also acknowledged.

## Conflict of Interests

The authors declare that there is no conflict of interests regarding the publication of this paper.

## References

- [1] B. Pradhan and B. Bhattacharjee, "Performance evaluation of rebar in chloride contaminated concrete by corrosion rate," *Construction and Building Materials*, vol. 23, no. 6, pp. 2346–2356, 2009.
- [2] S. Sathiyanarayanan, P. Natarajan, K. Saravanan, S. Srinivasan, and G. Venkatachari, "Corrosion monitoring of steel in concrete by galvanostatic pulse technique," *Cement and Concrete Composites*, vol. 28, no. 7, pp. 630–637, 2006.
- [3] M. Stern and L. Geary, "Electrochemical polarization. I. A theoretical analysis of the shape of polarization curves," *Journal of Electrochemical Society*, vol. 104, no. 1, pp. 56–63, 1957.
- [4] G. W. Walter, "Problems arising in the determination of accurate corrosion rates from polarization resistance measurements," *Corrosion Science*, vol. 17, no. 11, pp. 983–993, 1977.
- [5] J. A. González, A. Molina, M. L. Escudero, and C. Andrade, "Errors in the electrochemical evaluation of very small corrosion rates—I. polarization resistance method applied to corrosion of steel in concrete," *Corrosion Science*, vol. 25, no. 10, pp. 917–930, 1985.
- [6] S. Feliu, J. A. Gonzalez, C. Andrade, and V. Feliu, "In-situ determination of the polarization resistance in a reinforced concrete beam," *Corrosion*, vol. 44, no. 10, pp. 761–765, 1988.
- [7] S. Feliu, J. A. González, M. C. Andrade, and V. Feliu, "Determining polarization resistance in reinforced concrete slabs," *Corrosion Science*, vol. 29, no. 1, pp. 105–113, 1989.
- [8] S. Ahmad and B. Bhattacharjee, "A simple arrangement and procedure for in-situ measurement of corrosion rate of rebar embedded in concrete," *Corrosion Science*, vol. 37, no. 5, pp. 781–791, 1995.
- [9] C. Andrade and C. Alonso, "On-site measurements of corrosion rate of reinforcements," *Construction and Building Materials*, vol. 15, no. 2–3, pp. 141–145, 2001.
- [10] C. Andrade, I. Martinez, M. Ramirez, and M. Garcia, "Non-destructive techniques for onsite measurements of reinforcement corrosion in concrete structures," in *Proceedings of the International Symposium on Non-Destructive Testing in Civil Engineering (NDT-CE '03)*, Berlin, Germany, September 2003.
- [11] R. Bäßler and A. Burkert, "GPM-portable equipment for determination of corrosion stage of concrete structures—laboratory and on-site experiences," in *Proceedings of the International Symposium on Non-Destructive Testing in Civil Engineering (NDT-CE '03)*, Berlin, Germany, September 2003.
- [12] C. Andrade, C. Alonso, J. Gulikers et al., "Test methods for on-site corrosion rate measurement of steel reinforcement in concrete by means of the polarization resistance method," *Materials and Structures/Materiaux et Constructions*, vol. 37, no. 273, pp. 623–643, 2004.
- [13] H. Wojtas, "Determination of corrosion rate of reinforcement with a modulated guard ring electrode; analysis of errors due to lateral current distribution," *Corrosion Science*, vol. 46, no. 7, pp. 1621–1632, 2004.
- [14] B. Elsener, "Corrosion rate of steel in concrete—measurements beyond the Tafel law," *Corrosion Science*, vol. 47, no. 12, pp. 3019–3033, 2005.

- [15] S. Feliu, J. A. González, J. M. Miranda, and V. Feliu, "Possibilities and problems of in situ techniques for measuring steel corrosion rates in large reinforced concrete structures," *Corrosion Science*, vol. 47, no. 1, pp. 217–238, 2005.
- [16] ASTM C876-99, Standard test method for half-cell potentials of uncoated reinforcing bars, 2011.
- [17] E. Frank, *Electrical Measurements Analysis*, McGraw Hills, New York, NY, USA, 1959.
- [18] D. A. Jones, "The advantages of galvanostatic polarization resistance measurements," *Corrosion*, vol. 39, no. 11, pp. 444–448, 1983.
- [19] J. A. Gonzalez and C. Andrade, "Effect of carbonation, chloride, and relative ambient humidity on the corrosion of galvanized rebars embedded in concrete," *The British Corrosion Journal*, vol. 17, no. 1, pp. 21–28, 1982.
- [20] F. Mansfeld, "Tafel slopes and corrosion rates from polarization resistance measurements," *Corrosion*, vol. 29, no. 10, pp. 397–402, 1973.

## Research Article

# Identification of Historical Veziragasi Aqueduct Using the Operational Modal Analysis

**E. Ercan and A. Nuhoglu**

*Department of Civil Engineering, Ege University, 35100 Izmir, Turkey*

Correspondence should be addressed to E. Ercan; emre.ercan@ege.edu.tr

Received 30 August 2013; Accepted 17 October 2013; Published 8 January 2014

Academic Editors: D. G. Aggelis and N. Alver

Copyright © 2014 E. Ercan and A. Nuhoglu. This is an open access article distributed under the Creative Commons Attribution License, which permits unrestricted use, distribution, and reproduction in any medium, provided the original work is properly cited.

This paper describes the results of a model updating study conducted on a historical aqueduct, called Veziragasi, in Turkey. The output-only modal identification results obtained from ambient vibration measurements of the structure were used to update a finite element model of the structure. For the purposes of developing a solid model of the structure, the dimensions of the structure, defects, and material degradations in the structure were determined in detail by making a measurement survey. For evaluation of the material properties of the structure, nondestructive and destructive testing methods were applied. The modal analysis of the structure was calculated by FEM. Then, a nondestructive dynamic test as well as operational modal analysis was carried out and dynamic properties were extracted. The natural frequencies and corresponding mode shapes were determined from both theoretical and experimental modal analyses and compared with each other. A good harmony was attained between mode shapes, but there were some differences between natural frequencies. The sources of the differences were introduced and the FEM model was updated by changing material parameters and boundary conditions. Finally, the real analytical model of the aqueduct was put forward and the results were discussed.

## 1. Introduction

The variety and natural availability of the materials needed for masonry and the choice of laying pieces of stones or bricks on top of each other with or without mortar have made this technique easy and common. Additionally, masonry has important characteristics such as aesthetics, solidity, durability, easy maintenance, versatility, and fire protection as discussed by Lourenço [1]. However the lack of insight and models for the complex behavior of units, mortar, joints, and masonry as a composite material has made analysis of masonry difficult. Existing calculation methods are mainly of an empirical and traditional nature and the use of numerical tools for the analysis or design of masonry structures is rather incipient as discussed by Lourenço [2]. Historical masonry structures have been particularly vulnerable to earthquakes and winds for thousands of years. The preservation of historical structures is considered to be a fundamental issue in the cultural life of modern societies as a consequence of the failure of preventing some of them from collapsing

in past decades [3]. For this reason, the conservation and the structural safety assessment of historical structures have become an increasing concern. There are many studies concerning this topic in the literature including both analytical and experimental investigations of these structures.

Bayraktar et al. [4] described the results of an ambient vibration test and operational modal analysis carried out on the historical masonry bell-tower of the Hagia Sophia church in Trabzon, Turkey. Bernardeschi et al. [5] described the numerical techniques implemented in the finite element code for structural analysis of Buti's masonry bell-tower, a medieval structure located on the Pisa mountains. Two different load conditions were taken into consideration in the numerical analysis of the tower: the first was its own weight, and the second was an earthquake load in addition to its own weight. Bayraktar et al. [6] investigated the nonlinear seismic performance of the Mikron arch bridge, a nineteenth century Ottoman-era structure built over the Firtina river near Rize, Turkey, using ambient vibrations. Firstly, a finite element analysis of the Mikron arch bridge was conducted,

then the bridge was subjected to ambient vibration testing, and the vibratory response was obtained. The investigators then used enhanced frequency domain decomposition and stochastic subspace identification techniques to extract the experimental natural frequencies, mode shapes, and damping ratios from these measurements. The experimental results were compared with those obtained by the linear finite element analysis of the bridge. A good agreement between the mode shapes was observed during this comparison, though this was not the case for natural frequencies. The boundary conditions and material properties of the linear finite element model of the Mikron arch bridge were readjusted using the vibration test results and the analytical model was updated.

It is seen that the ambient vibration test has been preferred in many attempts to determine the dynamic characteristics of structures. The method is especially preferred for testing of historical structures because no excitation equipment is needed. As environmental excitations such as wind, traffic, and human influences are always present, the test implies a minimum interference with the normal use of the structures. Furthermore, the ambient vibration test does not have any negative effect on the structures.

In this study, an Ottoman aqueduct, Veziragasi, (Figure 1) was investigated. An aqueduct is a water supply or navigable channel constructed to convey water. Although particularly associated with the Romans, aqueducts were devised much earlier in Greece, in the Near East, and on the Indian subcontinent, where peoples such as the Egyptians and Harappans built sophisticated irrigation systems. Like most other structures, aqueducts were built using the masonry technique.

The Ottoman “Vezir System,” conveying the waters of springs near Buca, Southeast of Izmir, and crossing Melez creek via a high aqueduct is called Veziragasi or Vezir. The Vezir aqueduct was constructed in 1678 by the order of Grand Vizier Köprülü Fazıl Ahmet Paşa. The stone used in the construction of the structure is roughly cut andesite, except for the arches, which are made from clay brick with a thick mortar. In the study, firstly, the dimensions of the structure, defects such as cracks and material degradations on the structure, and the materials used in different parts were determined in detail by making a measurement survey. Secondly, the material properties of the components of the masonry were determined for the finite element method (FEM) using uniaxial compressive and indirect tension tests. Nondestructive testing (NDT) methods such as impact-echo, ultrasonic-echo, and ultrasonic pulse velocity testing methods were also used for evaluation of material properties. The SIBIE (stack imaging of spectral amplitudes based on impact-echo) technique was applied to evaluate the inner structure of the aqueduct. The solid model of the structure was then developed and the modal analysis of the structure was calculated by FEM. A nondestructive dynamic test and operational modal analysis (OMA) were then administered and the dynamic properties of the aqueduct were extracted. The results from OMA and the results from FEM were compared and according to the feedback, the FEM model was updated by changing the material parameters and boundary

conditions. Finally, the real material properties were determined.

## 2. Descriptions of the Structure, History Investigation, and Measurement Survey

The Vezir aqueduct system brings water to the fountains of the city of Izmir. The Vezir aqueduct was constructed in 1678 by the order of Grand Vizier Köprülü Fazıl Ahmet Paşa. Grand Vizier Köprülü Fazıl Ahmet Paşa funded the construction of this water system by himself so the system was called Vezir Water System, as discussed by Aktepe [7]. Today Vezir aqueduct is located from North to East along Yeşildere Street and on the hillside of the Kadifekale. The walls of the structure are stone masonry with grey and pink andesite and mortar joints. The span arches are brick masonry with thick mortar. The three arches of the North section have extensive cracks.

The aqueduct was previously 150 meters in length but 45 meters of the Vezir aqueduct collapsed and today 85 meters with 4 spans at one side of the North section and a 20-meter section with one span at the other side of the South section remain. The North section has a length of 85 meters, a width of 3.5 meters, and a height of 8 meters. The span lengths from North to South are 5.20 m, 5.33 m, 6.00 m, and 3.5 m, respectively.

**2.1. Material Tests on Stone, Brick, and Mortar.** In order to determine the parameters needed for finite element modeling, material nondestructive and destructive tests were administered on the constituents of the masonry. Stones and bricks from the structure were taken and destructive tests were carried out. Samples strong enough from which to cut out core samples of diameter 54 mm for stone and diameter 25 mm for bricks were selected. Indirect tension tests (Brazilian test) and uniaxial compression (UAC) tests were carried out as discussed in TS 699 and Ulusay et al. [8, 9] (Figure 2). The average results are shown in Table 1.

For the nondestructive tests, before taking the samples to the laboratory, L and LB type Proceq Schmidt hammers were used to find the surface hardness values (rebound value) of the stone and clay brick samples, respectively. The Schmidt hammer test was also applied to the stones and clay bricks of the whole structure (Figure 3). The compressive strength was calculated from the “rebound (R) value-compressive strength scheme” of Ulusay et al. [9]. In the laboratory, before indirect and uniaxial compression tests were applied to the stone and clay brick samples, ultrasonic wave velocity tests had been conducted using puntit type equipment (Figure 3). The modulus of elasticity values of the stone samples was also determined by (1) given in ASTM [10]:

$$E = V^2 \rho (1 + m) \times \frac{(1 - 2m)}{(1 - m)}, \quad (1)$$

where  $V$ ,  $\rho$ , and  $m$  are ultrasonic pulse velocity, density, and Poisson's ratio, respectively. The Poisson's ratio is taken to be 0.21 for the andesite stone. The estimated modulus of



FIGURE 1: Vezirağası aqueduct.



FIGURE 2: Drilling out core samples, cutting edges, uniaxial compression, and Brazilian test.

elasticity values from ultravelocity tests is higher than the values obtained through destructive tests (Table 1).

The mortar samples were weak and too small for drilling so only point load tests could be applied on arbitrary-shaped samples. By use of the point load index, the uniaxial compressive strengths of mortars were estimated. The average estimated uniaxial strength of mortars was calculated to be 6.25 MPa from point load tests. Tensile strength and modulus of elasticity of mortar were also estimated from the literature with the aid of point load test results. The tensile strength and modulus of elasticity  $\sigma_t$ , 0.79 MPa, and  $E$ , 150 MPa, were taken, respectively. The density of the mortar was calculated to be  $\rho = 1.70 \text{ gr/cm}^3$ .

### **3. Determination of Material Parameters for Analytical Model**

Masonry is a composite and this composite material consists of two or more different constituent materials. By the use of the homogenization approach, the behaviors of mortar and stone/brick were assumed to act together so the overall behavior of the composite media has been taken into account. While determining the elastic parameters of the masonry

aqueduct, the homogenization equations which depend on the strength parameters of constituents were used. The aqueduct has two types of masonry: stone masonry MS and brick masonry BS.

*3.1. Determination of Material Parameters of MS and BS from Destructive Test Results.* The compressive strength of masonry is determined by (2) as described by Eurocode 6 [11]:

$$f_k = K \cdot f_b^{0.65} \cdot f_m^{0.25}, \quad (2)$$

where  $K$  is a constant,  $f_b$  is the compressive strength of stone or brick, and  $f_m$  is compressive strength of mortar.  $K$  is in the range from 0.4 to 0.6 and depends on the morphology of the masonry as described by Eurocode 6 [11].  $K$  was taken to be 0.5 in this study.

The modulus of elasticity of masonry was determined by the use of (3) as described by Lourenço [2]:

$$E = \frac{t_m + t_m}{(t_m/E_m) + (t_u/E_u)} \rho, \quad (3)$$

where  $t_m$ ,  $t_u$ ,  $E_m$ , and  $E_u$  are the thickness of mortar and height of the unit (stone or clay brick); the coefficient  $\rho$  varies

TABLE 1: Test results of stone and clay brick.

Sample	Number of samples	Density $\rho$ (g/cm <sup>3</sup> )	Rebound value, $R$	Compressive strength from $R$ (Mpa)	Compressive strength from UAC (Mpa)	$E$ from UAC (Gpa)	Tensile strength from Brazilian test (Mpa)	Ultrav. (m/sec)	$E$ from U.V. (Gpa)
Stone (standard deviation)	25	2.43 (0.8)	53.49 (2.7)	82	53.35 (3.4)	11.59 (0.4)	6.09 (1.81)	4030 (220)	16.24
Brick (standard deviation)	11	1.79 (0.1)	30.74 (4.4)	24	10.41 (2.1)	0.81 (0.06)	1.43 (0.08)	2739 (180)	—

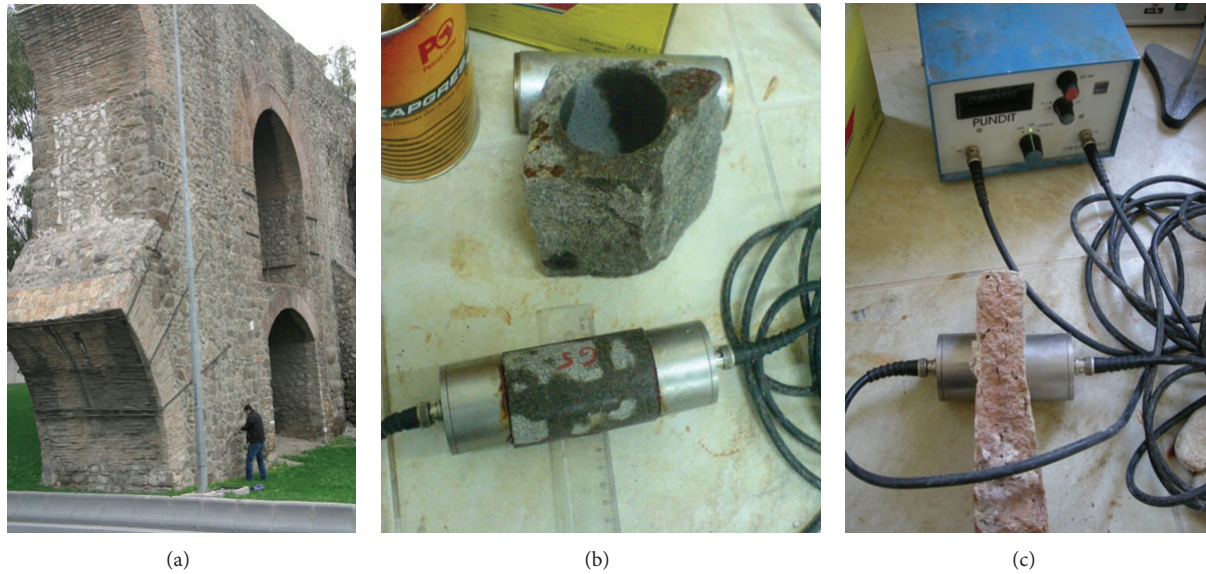
FIGURE 3: *In situ* Schmidt test and ultrasonic wave velocity test on stone and brick.

TABLE 2: Material parameters of masonry for FE model.

Material parameter	Stone masonry	Brick masonry
Compressive strength (MPa)	10.49	3.62
Tensile strength (MPa)	1.05	0.36
Modulus of elasticity (MPa)	871	201
Shear modulus	326	80.4
Density (kg/m <sup>3</sup> )	2100	1750
Poisson ratio	0.17	0.17

with the bond between mortar and unit and was taken to be 0.5 for this study as described by Lourenço [2].

The shear modulus can be taken to be 40% of the modulus of elasticity as described by Eurocode 6 [11]. The tensile strength of masonry can be taken to be 10% of compressive strength as described by Koçak [12].

The densities of BM and SM were calculated to be 2.1 kg/cm<sup>3</sup> and 1.75 kg/cm<sup>3</sup>, respectively. The Poisson ratio was taken to be 0.17 for masonry as described by Koçak [12]. The elastic material parameters of SM and BM for the finite element model are shown in Table 2.

**3.2. Impact-Echo Tests.** Impact-echo is one of the nondestructive testing methods for concrete based on multiple reflections of an acoustical wave between the test surface of concrete and an interface between materials with different mechanical impedances. An impact load is applied at the surface of the concrete and the vibrations caused by this impact are recorded by a receiver. As a result, a waveform is built up in the time domain. In the traditional impact-echo analysis, this waveform is transformed into the frequency domain by applying FFT. Peak frequencies are identified in the frequency spectrum and corresponding depth is calculated by the given formula in (4), where  $C_p$  is longitudinal wave velocity,  $f$  is the measured frequency, and  $d$  is the corresponding depth as described by Sansolone [13] and Ata et al. [14]:

$$d = \frac{C_p}{2f} \quad (4)$$

However, in most of the practical applications, due to the complex information existing in the data, it is difficult to interpret the frequency spectrum. Consequently, the SIBIE (stack imaging of spectral amplitudes based on impact-echo) procedure has been developed to improve the impact-echo method. The impact-echo method has been utilised for the

TABLE 3: Comparison of analytical and experimental modal parameters.

Frequency number	Analytical modal parameters (Hz)	PP method (Hz)		SSI method (Hz)		Damping ratios (%)	
		Test 1	Test 2	Test 1	Test 2	Test 1	Test 2
1	2.877	2.769	2.778	2.758	2.758	1.896	1.896
2	4.205	4.513	4.542	4.556	4.52	3.304	3.304
3	5.555	5.413	5.405	5.39	5.375	3.846	3.846
4	5.83	6.198	6.149	6.08	6.099	2.723	2.723
5	7.3699	Not extracted	7.035	Not extracted	7.015	Not extracted	2.105



(a)



(a)



(b)

FIGURE 4: Impact-echo test on aqueduct and digital storage oscilloscope.

evaluation of masonry structures. In this study, a stone masonry bridge was tested by carrying out the impact-echo and SIBIE procedures.

**3.2.1. SIBIE Procedure.** Based on the inverse scattering theory in elastodynamics as described by Nakahara and Kitahara [15], the SIBIE procedure was developed at Kumamoto University by Ohtsu and Watanabe [16] and Ata et al. [14]. This is an imaging technique for detecting waveforms in the frequency domain. In this study, the theory of SIBIE will not be mentioned.

**3.2.2. Impact-Echo Tests Results.** The clay masonry arch tested is shown in Figure 4. The tests were carried out at

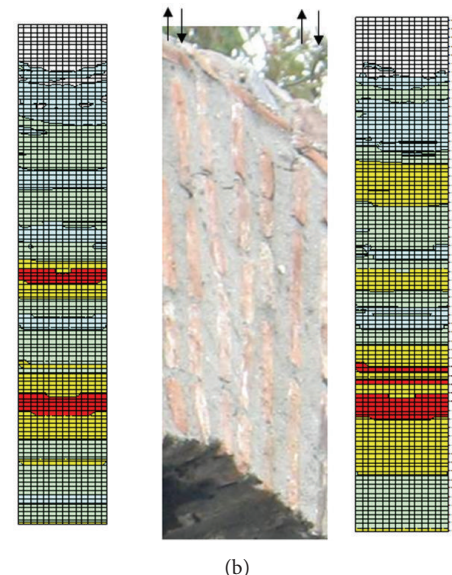


FIGURE 5: Two impact-echo test results on arc.

several locations on the arches and walls of aqueduct. A hammer with spherical hitting edge was used in the tests to generate elastic waves. Since the depth of the section to be tested was large, a hammer was used instead of a steel sphere to generate a high impact energy. A digital storage oscilloscope (Tektronix TDS 2014) and an accelerometer (Figure 4) were used to detect surface displacements caused by reflections of the elastic waves. The frequency range of the accelerometer system was from DC to 50 kHz. The Fourier



FIGURE 6: 3D FE model of Vezir aqueduct.

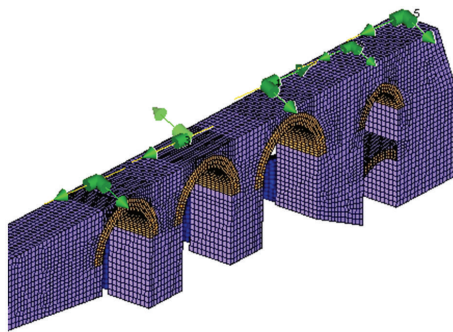


FIGURE 7: Uniaxial accelerometers placed to the top of the aqueduct alongside.

spectra of accelerations were analyzed by FFT (Fast Fourier Transform). Sampling time was  $4 \mu\text{sec}$  and the number of digitized data for each waveform was 2048. The cross-section of the bridge part tested was divided into square elements to perform SIBIE analysis. In this study, the size of square mesh for SIBIE analysis was set to 10 mm.

The results of the SIBIE analysis of the impact applied above the center of the arch are depicted in Figure 5. The SIBIE figure corresponds to the cross-section of the element that is tested. Here, the red color zones indicate the higher reflection due to the interface between materials with different mechanical impedances. In the figure, impact and detection locations are indicated with arrows. The distance between impact and detection was selected to be 5 cm. The depth of the section tested was 110 cm. The back wall reflection of the yellow color zone cannot be clearly observed in the SIBIE figure. The red color regions are clearly observed corresponding to the material interfaces. These reflections are due to extensive cracks in the arch which must be considered in the analytical model of the aqueduct.

According to the test results, the discontinuities in the structure appeared in the SIBIE results as relevant regions (red zones in this case). By evaluating the results, it can be said that there are some flaws between layers. Some flaws could be seen by side but SIBIE results show that there were others inside the structure as well. The size of these flaws was estimated to be about 3-4 cm and occurred because of delamination of unit and mortar. These flaws decrease the strength of the material and thus affect the durability of the structure and these factors are considered in the FEM model of the structure.

#### 4. Eigen Values and Mode Shapes of Vezir Aqueduct

For the Eigen values and mode shapes of the structure, a commercial finite element program SAP 2000 [17] was used. First of all, with the help of the measurement survey data, the 3D geometry of the Veziragasi aqueduct was defined by 37376 solid elements (Figure 6) and the calculated material parameters of SM (stone masonry) and BM (brick masonry) were defined to the program and the FE model was created. After the analysis was completed, the theoretical modal shapes of the structure were gathered. The results are shown in Table 3.

#### 5. Operational Modal Analysis of Vezir Aqueduct

The dynamic behavior of structures is related to their modal characteristics such as natural frequencies, mode shapes, and damping ratios. This dynamic behavior is a combination of many factors including assumptions in the design criteria and construction and uncertainties in the geometrical and material properties. Modal testing is a method to estimate the natural frequencies and mode shapes. Various methods, including both time and frequency domain-based procedures, are available for extracting modal information from the dynamic response of a structure and the corresponding input excitation. The process of establishing the dynamic characteristics of a system from an experimental model is called "system identification." In this study operational modal analysis (OMA) is used for system identification. In OMA, accelerometers are placed on the structure and the structure is excited by an unknown input force such as traffic, wind, and seismic loads caused by ambience and the responses of the structure are measured by these accelerometers.

The operational modal analysis ambient excitation does not lend itself to frequency response functions (FRFs) or impulse response function calculations because the input force is not measured. Therefore, a modal identification procedure will need to base itself on output-only data. Some modal parameter identification methods have been developed. In this study, the peak picking (PP) method from the power spectral densities (PSDs) and SSI methods were used for OMAs. The physics background of all these methods is quite similar, but a few implementation aspects such as data reduction, type of equation solvers, and sequence of matrix operations are different. In this study, the theory of OMA will not be mentioned.

Two ambient vibration tests were conducted for reliability on the aqueduct to determine its dynamic characteristics. 10 uniaxial accelerometers were used in OMA and these were placed on the top of the aqueduct alongside and the model was prepared for OMA (Figure 7). Signals acquired from accelerometers were gathered in the 17-channel data acquisition system (Brüel and Kjaer 3560) and were sent to Pulse software for further processing (Figure 8). Modal parameters were then extracted using OMA software [18].

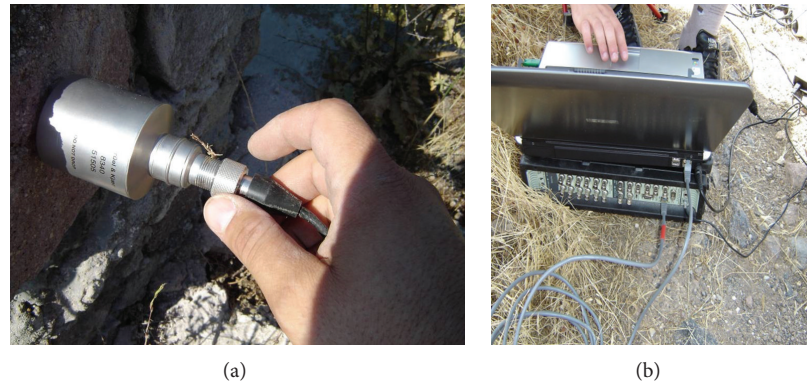


FIGURE 8: Uniaxial accelerometers and 17-channel data acquisition system.

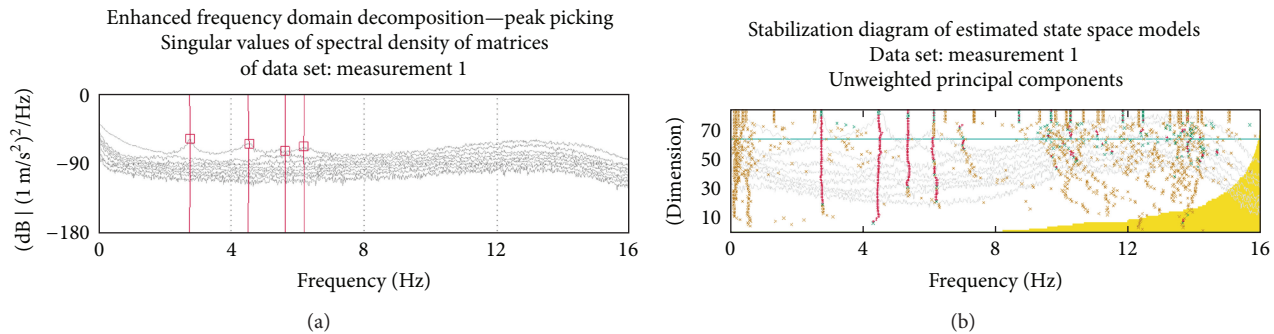


FIGURE 9: The frequency response function (PP method) and stabilization diagram of the measurement (SSI method).

TABLE 4: Updated and experimental modal frequencies.

Frequency	Analytical (SAP 2000)	Updated frequencies (SAP 2000)	Experimental frequencies (PP)	Experimental frequencies (SSI)
1	2.877	2.755	2.758	2.759
2	4.2050	4.521	4.556	4.515
3	5.555	5.410	5.391	5.398
4	5.831	5.971	6.089	6.219

The ambient vibration tests were conducted under environmental loads such as wind effects and traffic. The OMA, PP, and SSI methods (Figure 9) were used to determine the natural frequencies, mode shapes, and damping ratios of the aqueduct. The results from test 1 and test 2 are shown in Table 3. Frequencies obtained with the SSI method are nearly the same with those found in the PP method but a little bit different from the FEM results. Differences between the analytical and experimental results come from some uncertain parameters of the masonry.

## 6. Evaluation of Analytical and Experimental Results

The modal analyses results indicated that the initial theoretical frequencies were greater than the experimental frequencies, while the mode shapes had a good harmony. The possible reasons for this are the unknown mechanical properties of the masonry, cracks, and boundary conditions of the base. By changing some boundaries and the elasticity modulus of the

foundation of the aqueduct, the FEM model was updated and frequency values from FEM had become nearly the same as the experimental values as shown in Table 4.

The study also clearly showed that the ambient vibration test is a very effective method for determining the dynamic characteristics of historical structures under operational conditions. In this study, the natural frequencies, mode shapes, and modal damping ratios of the Vezir aqueduct were obtained using the ambient vibrations produced by traffic and wind. This was a nondestructive test for the aqueduct. Structural health can be assessed depending on the changes in dynamic characteristics of the aqueduct. If the natural frequencies and mode shapes of the aqueduct are measured again later, structural health can be evaluated by considering the changes.

## 7. Conclusions

The conventional testing methods and empirical formulas given in codes and standards for determining the material

parameters of the masonry structures can be considered sufficient. On the other hand, by using the OMA results, the material properties and boundary conditions assigned in the FE model can be modified to have real structural behavior. At first, the modal shapes extracted from FEA and OMA were in good agreement with each other but there was a little bit of difference in the frequency values. By changing the boundary conditions and modulus of elasticity using the OMA results, this difference was reduced and the 3D FE model of the structure was modified. With the help of the updated FE model, the structure can be tested for different earthquakes which have happened in the past and the structural health of the aqueduct can be understood.

## Conflict of Interests

The authors declare that there is no conflict of interests regarding the publication of this paper.

## Acknowledgments

The authors gratefully acknowledge the valuable contributions of Ahmet Can Altunışık, Barış Sevim, Temel Türker, and Alemdar Bayraktar to this study.

## References

- [1] P. B. Lourenço, *Computational strategies for masonry structures* [Ph.D. thesis], Delft University Press, Delft, The Netherlands, 1996.
- [2] P. B. Lourenço, *Assessment of the Stability Conditions of Cistercian Cloister*, 2, International congress on Studies in Ancient Structures, Istanbul, Turkey, 2001.
- [3] L. Binda, G. Gatti, G. Mangano, C. Poggi, and L. G. Sacchi, "The collapse of the Civic Tower of Pavia: a survey of the materials and structure," *Mason International*, vol. 20, no. 6, pp. 11–20, 1992.
- [4] A. Bayraktar, T. Türker, B. Sevim, A. C. Altunışık, and F. Yıldırım, "Modal parameter identification of Hagia Sophia bell-tower via ambient vibration test," *Journal of Nondestructive Evaluation*, vol. 28, no. 1, pp. 37–47, 2009.
- [5] K. Bernardeschi, C. Padovani, and G. Pasquinelli, "Numerical modelling of the structural behaviour of Buti's bell tower," *Journal of Cultural Heritage*, vol. 5, no. 4, pp. 371–378, 2004.
- [6] A. Bayraktar, B. Sevim, A. C. Altunışık, S. Atamtürkür, and F. Birinci, "Assessment of nonlinear seismic performance of a restored historical arch bridge using ambient vibrations," *Nonlinear Dynamics*, vol. 63, no. 4, pp. 755–770, 2011.
- [7] M. M. Aktepe, *İzmir Yazılıları: Camiler, Hanlar, Medreseler, Sebiller, Hazırlayan Yayınları*, Fikret Yılmaz, İzmir BB Kültür, İzmir, Turkey, 2003.
- [8] TS 699, *Methods of Testing Natural Building Stones*, Institute of Turkish Standards, Ankara, Turkey, 1987.
- [9] R. Ulusay, C. Gökcəoğlu, and A. Binal, *Rock Mechanics Laboratory Experiments*, Turkish Chambers of Geology Engineers, Ankara, Turkey, 2001.
- [10] ASTM, *Standard Method for Laboratory Determination of Pulse Velocities and Ultrasonic Elastic Constants of Rock*, 1996, D2845-97, 1969.
- [11] "European Committee for Standardization," Eurocode 6, Brussels, Belgium, 1996.
- [12] A. Koçak, *Linear and nonlinear analysis of historical masonry structures under static and dynamic loads case study: Küçük Ayasofya mosque* [Ph.D. thesis], Yıldız Technical University, İstanbul, Turkey, 1999.
- [13] M. Sansalone, "Impact-echo: the complete story," *ACI Structural Journal*, vol. 94, no. 6, pp. 777–786, 1997.
- [14] N. Ata, S. Mihara, and M. Ohtsu, "Imaging of ungrouted tendon ducts in prestressed concrete by improved SIBIE," *NDT and E International*, vol. 40, no. 3, pp. 258–264, 2007.
- [15] K. Nakahara and M. Kitahara, "Inversion of defects by linearized inverse scattering methods with measured waveforms," in *Proceedings International Symposium on Inverse Problems in Engineering Mechanics (ISIP '00)*, pp. 9–18, Springer, Berlin, Germany, 2002.
- [16] M. Ohtsu and T. Watanabe, "Stack imaging of spectral amplitudes based on impact-echo for flaw detection," *NDT and E International*, vol. 35, no. 3, pp. 189–196, 2002.
- [17] SAP2000, *Integrated Finite Element Analysis and Design of Structures*, Computers and Structures, Berkeley, Calif, USA, 2005.
- [18] OMA, *Operational Modal Analysis, Release 4. 0, Structural Vibration Solution A/S*, Aalborg East, Denmark, 2006.

## Research Article

# Online Bridge Crack Monitoring with Smart Film

**Benniu Zhang, Shuliang Wang, Xingxing Li, Zhixiang Zhou, Xu Zhang, Guang Yang, and Minfeng Qiu**

*Department of Information Science and Engineering, Chongqing Jiaotong University, Chongqing 400074, China*

Correspondence should be addressed to Benniu Zhang; benniuzhang@gmail.com

Received 30 August 2013; Accepted 17 October 2013

Academic Editors: D. G. Aggelis and N. Alver

Copyright © 2013 Benniu Zhang et al. This is an open access article distributed under the Creative Commons Attribution License, which permits unrestricted use, distribution, and reproduction in any medium, provided the original work is properly cited.

Smart film crack monitoring method, which can be used for detecting initiation, length, width, shape, location, and propagation of cracks on real bridges, is proposed. Firstly, the fabrication of the smart film is developed. Then the feasibility of the method is analyzed and verified by the mechanical sensing character of the smart film under the two conditions of normal strain and crack initiation. Meanwhile, the coupling interference between parallel enameled wires of the smart film is discussed, and then low-frequency detecting signal and the custom communication protocol are used to decrease interference. On this basis, crack monitoring system with smart film is designed, where the collected crack data is sent to the remote monitoring center and the cracks are simulated and recurred. Finally, the monitoring system is applied to six bridges, and the effects are discussed.

## 1. Introduction

Bridges play a significant role in the economic development for the conveniences to the traffic and transportation. However, owing to the complexity of the force condition as well as the uncertainty of the surrounding environment, lots of unstable factors have been forced to the bridge after the construction, such that it is difficult to grasp the mechanical prosperities and behaviors during the operation. The frequently collapsed accidents of bridges endanger social well-being and stabilization. In view of the importance of bridge security, bridge health monitoring, especially in the field of crack monitoring, has made a rapid progress and become a hot topic in the current research.

Crack is a macroreflection of deterioration and lesion of concrete structures. Due to crack propagation [1], secondary diseases can be caused, such as leakage, corrosion of steel bars, and concrete carbonization, further affecting normal usage and the safety of the structures.

The crack monitoring methods usually used for concrete bridges include point monitoring, distributed monitoring and image recognition monitoring method. The point monitoring method [2, 3] places sensors individually at certain critical points on the structures to monitor crack. It can only be feasible when the critical points are predicted accurately.

Unfortunately, in engineering practice, cracks do not always appear on the critical points owing to material-heterogeneity and calculation errors.

Recently, distributed monitoring method, which based on the optical fiber sensor, has been introduced in structural crack monitoring [4–9]. It has the characteristics of large information transmission capacity, high transmission speed, and high sensitivity. However, brittle optical materials with the order of several meters in length and only micrometer in diameter are difficult to be glued on or embedded into structures. Meanwhile, coaxial cable distributed sensor with electrical time domain reflectometry (ETDR) technology is buried in structures to collect strain and crack signals [10–12]. Still, this method has potential defects in installation, reliability, and stability of signals.

High-resolution camera lens make it available to monitor cracks by collecting real-time images of structures [13–15]. This method has a higher feasibility for short-term crack monitoring in a given small area, but it has difficulty in monitoring tiny crack.

Smart film monitoring method is proposed by the authors from empirical analysis and engineering practice. Smart film, in which a great number of insulated enameled copper wires are embedded to form a coordinate grid, is glued

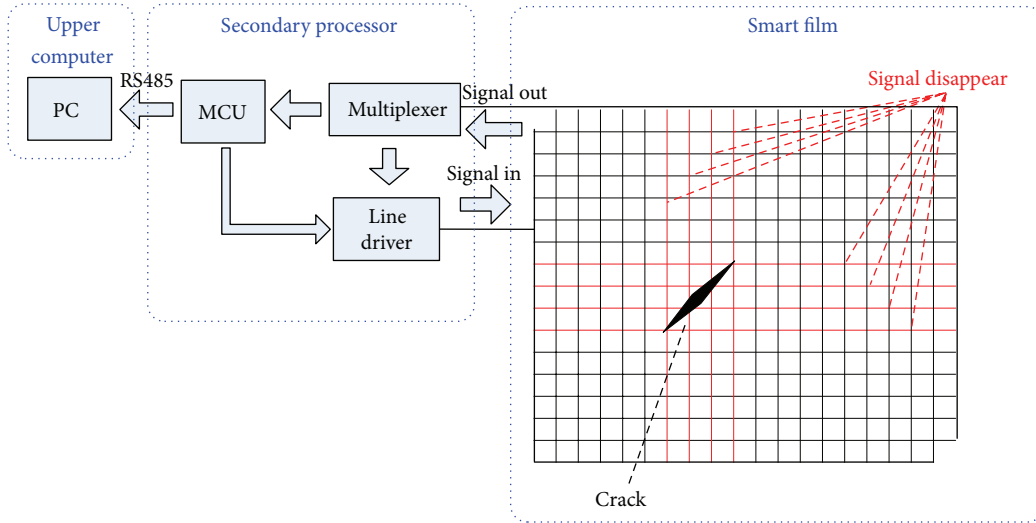


FIGURE 1: Schematic of smart film monitoring technique.

on the surface of the structure. Electrical signal is sent from one terminal of each wire, and the signal at the other hand is simultaneously detected. When a crack initiates, the conducting wires will break correspondingly. Therefore the signals will not get through those broken wires. By analyzing the conducting and breaking wires, initiation, length, shape, propagation, and the location of cracks can be identified. At the same time, crack width can be monitored by using the corresponding relationship between the diameter and crack width [16–18].

The crack sensing system built by this technique mainly consists of smart film, secondary processor, and upper computer. The smart film can be used for crack sensing. The secondary processor determines the location and the length of the crack according to the signal of the smart film and communicates with the upper computer for sending crack data. The upper computer processes and sends crack data to the remote monitoring center [16] (see Figure 1).

According to the above principles, the following problems may be encountered in the practical application. One of them is misjudgment of the crack owing to different reasons. Firstly, the smart film is glued on surface of the structure with epoxy resin and normal strain of the structure may break the enameled wire, thus resulting in misjudgment. Secondly tiny crack on the structure may not be detected because of no breakage of the wire. In addition the coupling effects between the wires can lead to the misjudgment, since all the wires of the smart film are parallel with each other and form a bunch of bus. Finally, the smart film, the secondary processor, and the upper computer can only be used for sensing and collecting the crack information. Therefore, to reach the intelligent monitoring of the concrete structure and accurate evaluation of the crack data, the system of data analysis and processing needs to be further developed.

To deal with the problems discussed above, a methodological approach on bridge crack monitoring with smart film is developed in this paper. Processing techniques are

considered and the logic structure is illustrated in Figure 2. Firstly, the fabrication of the smart film is firstly proposed for engineering practice. Secondly, by means of the mechanical sensing character of the smart film under the two conditions of normal strain and crack initiation, the feasibility of crack monitoring is analyzed and verified. At the same time, it is found that the enameled wires will not break under the normal strain condition, but when a crack passes through the wires, the wires will break accordingly. Then the phenomenon of coupling interference between parallel enameled wires of the smart film is revealed, and then low-frequency detecting signal and the custom communication protocol are adopted to reduce interference. On this basis, a crack monitoring system composed of the local monitoring center and the remote monitoring center is designed. The collected data of the local monitoring center is sent to the remote monitoring center, and then the crack will be simulated by the plug-ins of the interactive 3D scene and analysis of the crack data. Finally, the monitoring system is applied to six bridges including Masangxi Yangtze River Bridge and Tukan Wujiang River Bridge, and the effects are discussed. At the same time, the effectiveness of the results is testified by the comparison between the result of the man-operated periodic detection and that of monitoring.

This paper is structured as follows. Section 2 describes the fabrication of the smart film in detail. Section 3 analyzes the mechanical and electrical character of the smart film, attests the feasibility of crack monitoring under the two conditions of normal strain and crack initiation, and proposes the effective measures to prevent the signal interference between the wires. Then in Section 4, a description of the remote monitoring system used for the intelligent monitoring and the plug-ins of analysis and recurrence of crack data is given. Nextly, Section 5 discusses the applications of the remote crack monitoring system on six bridges including Masangxi Yangtze River Bridge. Finally, conclusions are presented in Section 6.

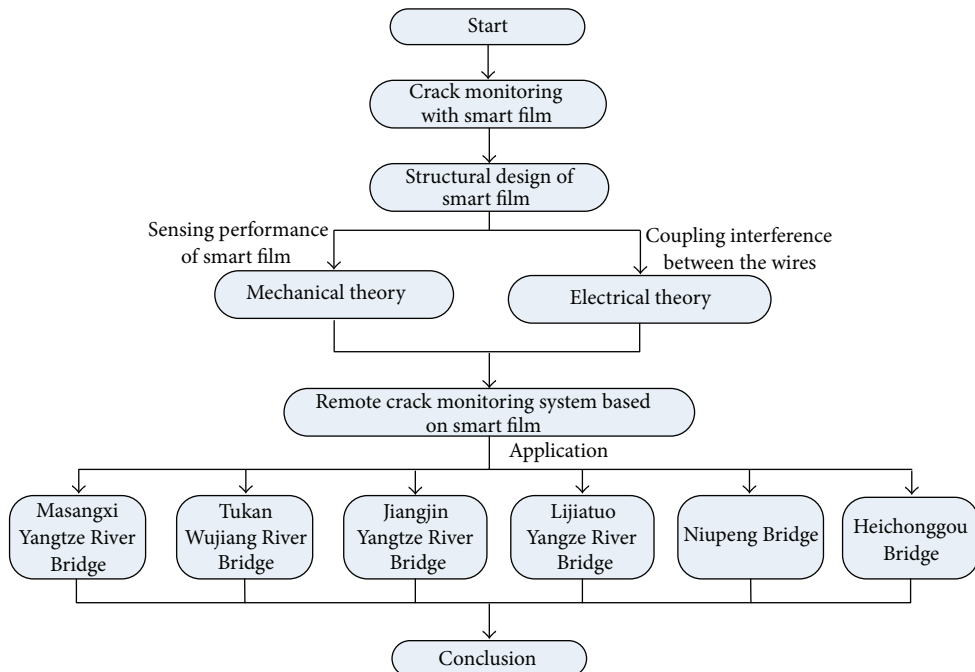


FIGURE 2: Diagram of the logic structure of this paper.

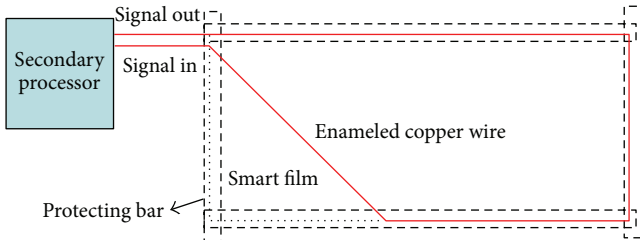


FIGURE 3: Road for one wire.

## 2. The Structural Design of Smart Film

According to the crack monitoring technique based on smart film, enamelled wires form the smart film regularly. Due to the small diameter of the wires, they are not easy to be fixed during the fabrication but easy to be broken. Therefore, plastic film with adhesive is used as substrate and glossy paper as the protection framework; then each wire is adhered on substrate as well as the bus protection framework and forms a grid as shown in Figure 3.

Different diameter has different ultimate strain. Therefore, a group of different diameter wires are placed transversely to monitor crack width. It is shown in Figure 4.

## 3. The Mechanical and Electrical Theory of the Enamelled Wires

**3.1. Mechanical Analysis [17].** Aimed to guarantee that the wires pasted on structures remain intact when no cracks appear on the structures, the wires must have larger failure strain than that of the concrete material. Here the ultimate

strain of several kinds of enamelled copper wire and epoxy are proofed and they are compared with the ultimate strain of common concrete material. According to the proof results, the ultimate strain of the wires is not less than  $90000 \mu\epsilon$ , and the strain of the epoxy resin is not less than  $20000 \mu\epsilon$ . Hence enamelled copper wires will not be broken under normal strain conditions of concrete structure.

Considering that the structures being monitored are much larger than diameter of enamelled wires, and the cracks will pierce through transverse direction of the wires, then the crack problem can be regarded as a 2D plane strain problem, as illustrated in Figure 5.

Assume that the crack appearing on concrete structure has pierced enamelled wire to generate a crack tip (Figure 6); the stress field in the vicinity of crack tip can be obtained. Then strain field nearby the crack tip (the singular) will be much greater than the ultimate strain. Hence, as long as the crack pierces the enamelled copper wire, it will be broken [17].

**3.2. Antiinterference Analysis.** It can be seen from the structure of smart film that enamelled wires are forming parallel lines at regular intervals (see Figure 7). During the period of sending detecting signal to judge wires' condition, the voltage of interference coupling is so easy to be generated due to parasitic capacitance that conditions are judged wrongly. Hence it is necessary to analyze coupling interference among the bus of smart film and find the suitable detecting signals and detection ways, aimed to reduce coupling interference and enhance the accuracy of condition judgments of wires.

Selecting two wires from the bus in Figure 7, a model can be formulated to analyze and infer the relationship between the voltage  $U_B$  of coupling interference and the frequency  $\omega$  of detecting signal, as demonstrated in Figure 8.

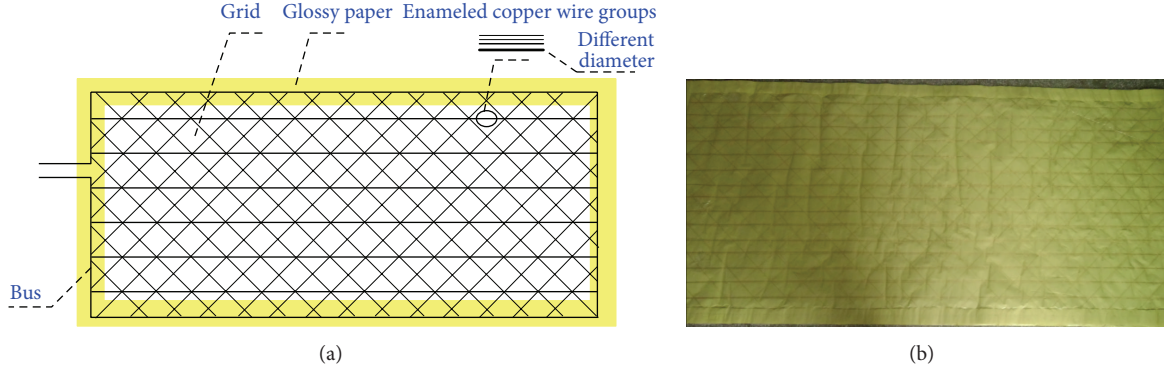


FIGURE 4: Smart film: (a) schematic and (b) photograph.

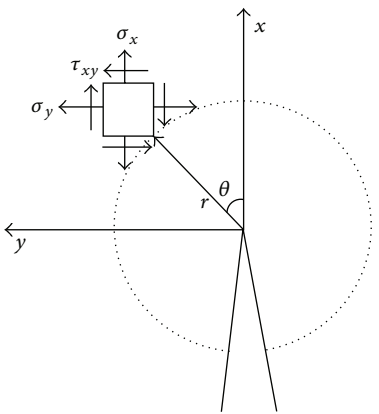


FIGURE 5: 2D plane strain of a crack.

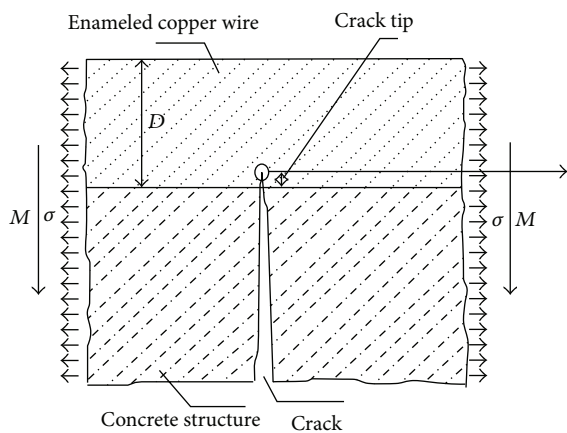


FIGURE 6: Concrete crack pierces to enameled wires.

It can be seen from the figure that interference still exists. Only by lowering the frequency of detecting signal, coupling interference generated by parasitic capacitance can be effectively reduced. However, the speed of detection will be affected if the detecting frequency is very low. Therefore, 1 kHz is used as the frequency of the detecting signal in



FIGURE 7: Bus of smart film.

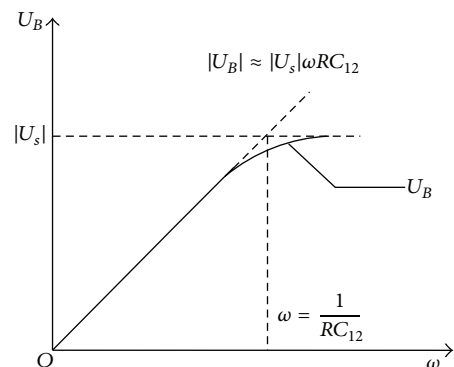


FIGURE 8: Relationship between coupling voltage and the frequency of detecting signal.

engineering practice. At the same time, in order to further improve the accuracy of condition judgments of the enameled wires, the custom communication protocol is also adopted. That is, after choosing a single wire, signal detection is sent 8 times circularly with high and low levels. Only when the levels are detected accurately by the output port, the enameled wire is thought to be intact.

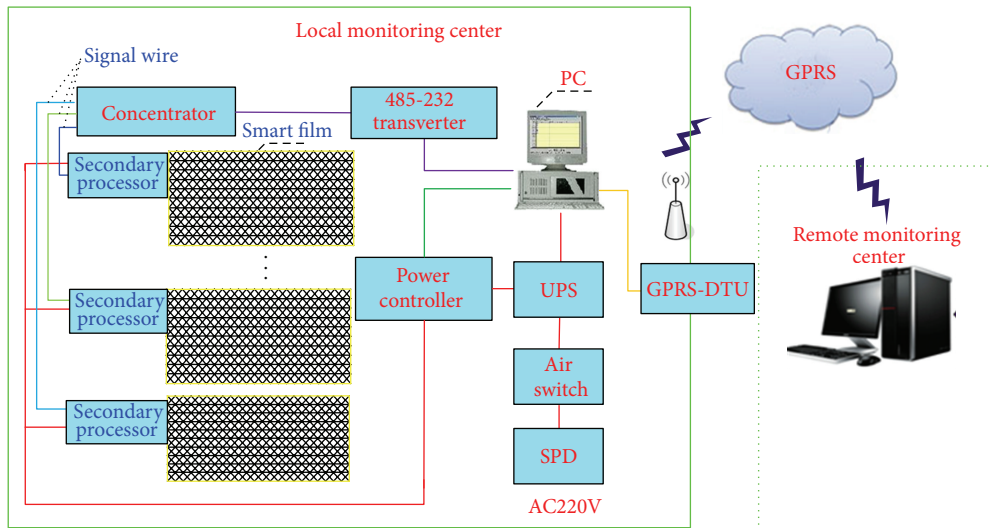


FIGURE 9: Hardware schematic of the remote crack monitoring system based on smart film.

#### 4. The Remote Crack Monitoring System Based on Smart Film

In practical monitoring, the smart film can be only used for sensing of crack information; the secondary processor can collect and send the data to the upper computer. In order to monitor concrete structures intelligently, master the real-time and accurate crack information, and improve the readability of crack data, the data in the upper computer need to be sent to the remote monitoring center timely, accurately, and stably. The remote monitoring center will analyze and process the data to judge whether the crack will lead to damage of the structure. Therefore the remote system for transmitting, storing, and analyzing the crack data is needed for the smart film to monitor concrete structures. According to the characteristics of the remote monitoring, the system is divided into two parts, that is, the local and the remote monitoring center (see Figure 9).

The hardware of the system is mainly composed of smart film crack sensors, communication lines, power managements, wireless transmission equipments, industrial personal computer (IPC), the protection devices of power supply, and the server of the remote monitoring center. Here GPRS-DTU is used as the wireless transmission equipment. Hence the server of the remote monitoring center must have access to the Internet.

The remote monitoring center is based on the plug-in 3D visualization design, including database management, scene interaction, data analysis and recurrence, 3D animation design in structure, report generation, and interface design. To deal with the problem of data analysis and recurrence, the least squares B-spline curve algorithm, which is usually used for drawing curve from points, is adopted to compose the broken points into a virtual crack. Then, the readability of the data can be improved. Figure 10 illustrates the 3D system.

#### 5. Applications on Real Bridges

**5.1. Masangxi Yangtze River Bridge.** Masangxi Yangtze River Bridge, located in Dadukou district of Chongqing municipality, China, is a prestressed concrete cable-stayed bridge with the main bridge of 179 m + 360 m + 179 m. Its total length is 1104.23 m and its deck's width is 30.6 m. It is divided into two independent bridges and consists of a west platform at one end, 9 approach bridges at the other end, and a main bridge between them. The main bridge and the approach bridge have 12 spans. The west platform has a length of 5 m. One of the approach bridges is 44 m and the others are 40 m. The main bridge has the structure of double-tower and double-cable-plane, the section of the girder has the structure of prestressed concrete separate triangle-box, and a half cubic curve camber is sited between middle span and side span.

**5.1.1. Sensor Distribution.** Before the installation of the monitoring system, a large number of cracks have existed in the Masangxi Yangtze River Bridge, and reinforcement of the durability and the structure has been implemented on two main towers according to the cracked condition. In order to ensure the safe operation of the bridge, the bridge crack monitoring system is installed on two towers, monitoring cracks including new and preexisting ones in real-time.

For the upstream side of tower no. 1, 3 pieces of smart films (no. 1-no. 3) are pasted on the connection part between the upper part and the middle part of the tower, 12 pieces of films (no. 4-no. 15) on the middle part, and 4 pieces of films (no. 16-no. 19) on the lower part. For the downstream side of the tower, 12 pieces of smart films (no. 20-no. 31) are pasted on the inner part of the middle tower, as shown in Figure 11(a).

For the downstream side of tower no. 2, 12 pieces of smart films (no. 1-no. 12) are pasted on the middle part of the tower. For the upstream side of the tower, 6 pieces of smart films

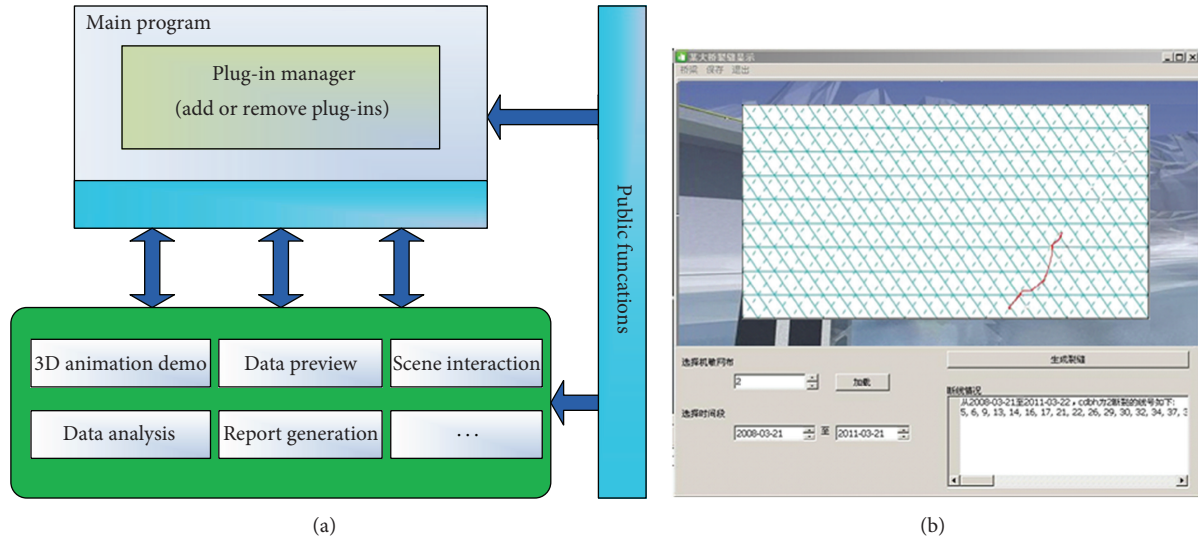


FIGURE 10: 3D visualization system: (a) system framework and (b) the plug-ins of analysis and recurrence of crack data.

(no. 13–no. 18) are pasted on the lower tower and 12 pieces of films (no. 19–no. 30) on the inner part of the middle tower, as shown in Figure 11(b). According to the force condition and the pre-existing cracks of the tower, it is found that the cracks are mainly vertical. Therefore, the pasted smart films are only transverse; the smart film on the outer surface of the tower consists of 12 transverse enameled wires, but the film on the inner tower consists of 15 transverse wires.

**5.1.2. The Interactive 3D Scene.** Since the 3D scene of Masangxi Yangtze River Bridge is formulated using 3DS MAX, the real geographic environment, bridge structure, and the distribution of the monitoring equipments can be simulated visually. After the running of plug-in of the interactive 3D scene, a single tower is used as the entrance and the scene interacts down layer by layer. In the main screen of each tower, a button of each smart film is created from different perspectives. When clicking the button, the crack will be recurred by the smart film (see Figure 12).

**5.1.3. Analysis and Recurrence of Crack Data.** The monitoring time is from March 2008 to November 2009. During this period, it can be found that part of cracks (new and old ones) spread to a certain degree according to analysis of the collected data through the server of the remote monitoring center.

In tower no. 1, cracks were found in December 2008, which appeared on the smart films with sequence number of 3, 4, 6, 7, 9, 10, 24, 26, 29, 30, and 31. In addition, all the wires in the smart films with the sequence numbers of 4, 6, 9, 10, and 26 broke due to the penetration of cracks. The width of the smart film is 30 cm. Therefore, the lengths of the cracks are more than 30 cm.

According to data analysis, it can be known that: during December 2008, the breakage ratio of sensor 24 was 27%, the ratio of sensor 26 was 87%, the ratio of sensor 27 was 47%, and the ratio of sensor 29 was 27%. Till November 2009,

TABLE 1: Data of the smart films of tower no. 1.

Sensor number	3	4	6	7	9	10
The total breakage ratio during December 2008	42%	100%	100%	92%	100%	100%
The total breakage ratio during November 2009	42%	100%	100%	92%	100%	100%
Sensor number	24	26	27	29	30	31
The total breakage ratio during December 2008	27%	87%	47%	27%	60%	67%
The total breakage ratio during November 2009	100%	100%	60%	67%	60%	67%

the newly added breakage ratio of sensor 24 was 73% and the total breakage ratio was 100%. The newly added ratio of sensor 26 was 13% and the total ratio was 100%. The newly added ratio of sensor 27 was 13% and the total ratio was 60%. The newly added ratio of sensor 29 was 40% and the total ratio was 67%. Hence, during December 2008 and November 2009, the cracks on the locations of the smart films with the sequence numbers of 24, 26, 27, and 29 continued to extend, and the cracks pierced through the whole smart films with the sequence numbers of 24 and 26. Figure 13 shows the visual recurrence of the real crack in 29th and 31st smart film of tower no. 1. Table 1 presents data of the smart films of tower no. 1.

In tower no. 2, cracks were also found in December 2008, which appeared on the smart films with the sequence numbers of 4, 5, 6, 9, 17, 19, 21, 22, 23, 24, 25, 27, 28, 29, and 30. In addition, all the wires in the smart films with the sequence numbers of 6, 17, 19, 21, and 27 broke due to the penetration

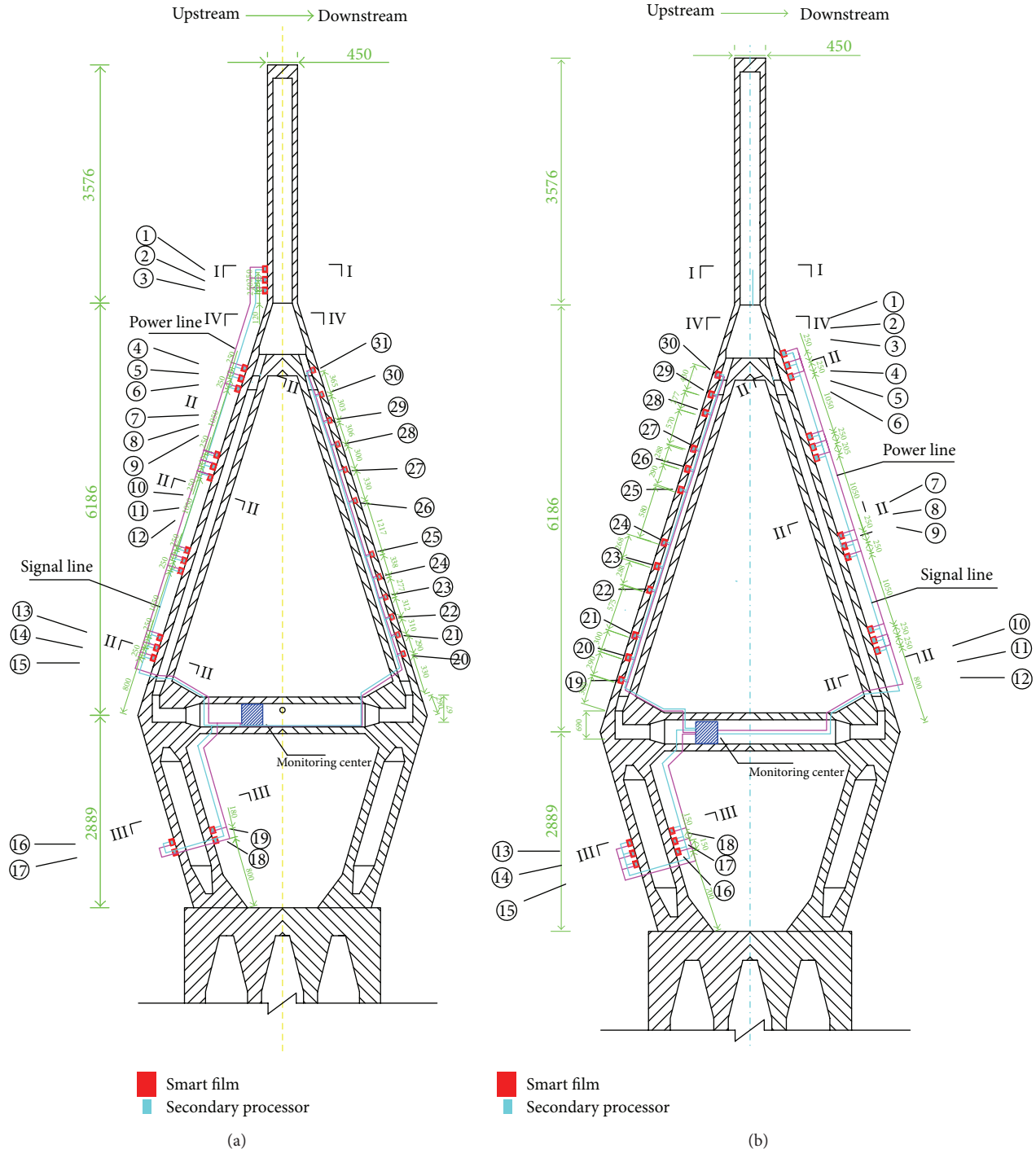


FIGURE 11: Illustration of sensor installation of tower crack monitoring system: (a) layout of the smart film and the secondary processor in tower no. 1 and (b) layout of the smart film and the secondary processor in tower no. 2.

of cracks. Similarly, the lengths of the cracks are more than 30 cm.

According to data analysis, it can be known that, during December 2008, the breakage ratio of sensor 4 was 8%, the ratio of sensor 5 was 17%, the ratio of sensor 9 was 83%, the ratio of sensor 22 was 66%, the ratio of sensor 23 was 87%, the ratio of sensor 24 was 80%, the ratio of sensor 25 was

40%, the ratio of sensor 28 was 53%, the ratio of sensor 29 was 87%, the ratio of sensor 30 was 60%, and the ratio of sensor 31 was 73%. Till November 2009, the newly added breakage ratio of sensor 4 was 75% and the total breakage ratio was 83%. The newly added ratio of sensor 5 was 67% and the total ratio was 84%. The newly added ratio of sensor 9 was 17% and the total ratio was 100%. The newly added ratio of sensor 22

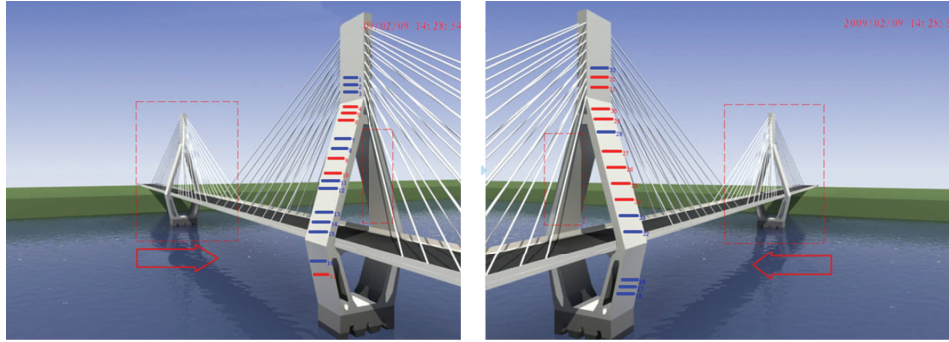


FIGURE 12: 3D scene of Masangxi Yangtze River Bridge.

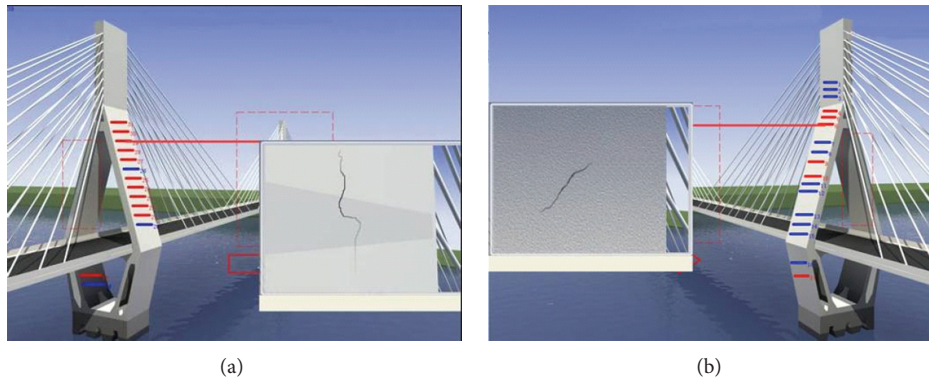


FIGURE 13: Visual recurrence of the real crack: (a) 29th smart film of tower no. 1 and (b) 31st smart film of tower no. 1.

was 27% and the total ratio was 93%. The newly added ratio of sensor 24 was 7% and the total ratio was 87%. The newly added ratio of sensor 25 was 26% and the total ratio was 66%. The newly added ratio of sensor 28 was 47% and the total ratio was 100%. The newly added ratio of sensor 29 was 13% and the total ratio was 100%. The newly added ratio of sensor 30 was 40% and the total ratio was 100%. The newly added ratio of sensor 31 was 27% and the total ratio was 100%. Hence, during December 2008 and November 2009, the cracks on the locations of the smart films with the sequence numbers of 4, 5, 9, 22, 24, 25, 28, 29, 30, and 31 continued to extend, and the cracks pierced through the whole smart films with the sequence numbers of 9, 28, 29, 30, and 31. The crack on the location of the smart film with the sequence number of 23 did not extend. Figure 14 shows the visual recurrence of the real crack in 4th and 30th smart film of tower no. 2. Table 2 presents data of the smart films of tower no. 2.

**5.1.4. Comparison of Data.** In order to verify the validity of monitoring data and grasp the propagation conditions of the cracks, professionals had been repeatedly sent to the scene to observe the problem. Figure 15 shows the comparison charts of tower no. 1 between man-operated detection and monitoring using the plug-in of recurrence of crack. And it can be drawn that the result of remote recurrence of crack is basically consistent with that of the local detection.

**5.1.5. Monitoring Result.** Before December 2008, new cracks were not found. And new cracks were not detected by the local detections of the professionals, especially after the Wenchuan earthquake in May. During December 2008, it could be found by the system that the structural cracks came to emerge. During December 2008 and October 2009, the structural cracks continued to extend. According to analysis of breakage time of the enameled wires, the results showed that the propagation of cracks on the towers experienced the process of relative stability, crack propagation, and relative stability. Currently, some cracks tend to extend, but in a relatively slow speed.

**5.2. Tukan Wujiang River Bridge.** Tukan Wujiang River Bridge, located in Yu-Xiang expressway connecting Chongqing Municipality and Hunan Province, China, is a prestressed continuous steel bridge with the main bridge of 110 m + 200 m + 110 m. It is divided into two independent bridges (the right bridge and the left bridge). The right bridge consists of a T-beam at one end, three T-beams at the other end, and a main bridge between them. The left bridge consists of the main bridge and three T-beams. The length of a T-beam is 30 m. A single cell and single box section is used in the box girder of the main bridge, whose width of roof is 12 m, width of base plate is 6 m, and width of unilateral cantilever is 3 m.

TABLE 2: Data of the smart films of tower no. 2.

Sensor number	4	5	6	9	17	19	21	22
The total breakage ratio during December 2008	8%	17%	100%	83%	100%	100%	100%	66%
The total breakage ratio during November 2009	83%	84%	100%	100%	100%	100%	100%	93%
Sensor number	23	24	25	27	28	29	30	31
The total breakage ratio during December 2008	87%	80%	40%	100%	53%	87%	60%	73%
The total breakage ratio during November 2009	87%	87%	66%	100%	100%	100%	100%	100%

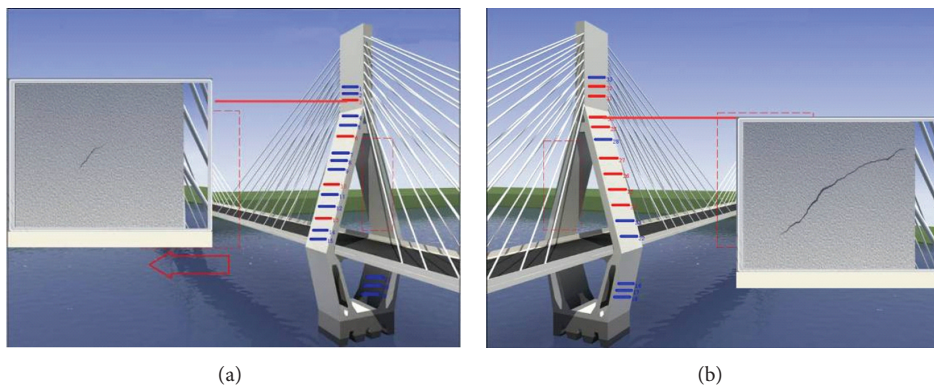


FIGURE 14: Visual recurrence of the real crack: (a) 4th smart film of tower no. 2 and (b) 30th smart film of tower no. 2.

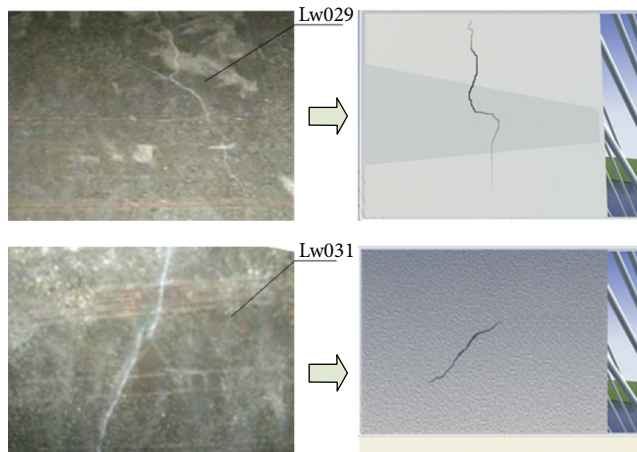


FIGURE 15: Comparison of tower no. 1 between man-operated detection and monitoring using the plug-in of recurrence of crack.

**5.2.1. Sensor Distribution.** The smart films are mainly pasted on pier, 1/4-segment of main span, the mid-segment of main span (the closure segment), which is shown in Figure 16. 26 pieces of smart films that have 80 enameled wires are pasted on each bridge. 3 pieces of films (no. 23–no. 25) are pasted on the plate of box girder of pier and 1 piece of film (no. 26) on the roof of box girder of pier. Six pieces of films (no. 17–no. 22) are pasted on the plate of box girder from 1/4-segment of main span. Four pieces of films (no. 13–no. 16) are pasted on

the plate of box girder from the mid-segment of main span. 12 pieces of films (no. 1–no. 12) are pasted on the base plate of box girder from the mid-segment of main span. The smart films on the two bridges are symmetric with each other.

**5.2.2. The Interactive 3D Scene.** Since the 3D scene of Tukan Wujiang River Bridge is formulated using 3DS MAX, the real geographic environment, bridge structure, and the distribution of the monitoring equipments can be simulated visually. After running of the plug-in of the interactive 3D scene, a single tower is used as the entrance and the scene interacts down layer by layer. In the main screen of each tower, buttons of each smart film are created from different perspectives. When clicking the buttons, the corresponding scenes will be recurred (see Figure 17).

**5.2.3. Analysis and Recurrence of Crack Data.** The monitoring begins with December 2008, and the system runs normally until now. It can be found from data collected by the server of the remote monitoring center that some cracks emerged on the two bridges.

Through the plug-in of analysis and recurrence of crack data, a vertical crack with a length about 15 cm could be found by sensor 11 (Lw011) which was arranged in the base plate of box girder from the mid-segment of main span of the right bridge, and it emerged in early November 2009, as shown in Figure 18(a). Three vertical cracks with the lengths ranging from 13 cm to 28 cm could be found by sensor 26 which was arranged close to the roof of box girder of pier 0 on the

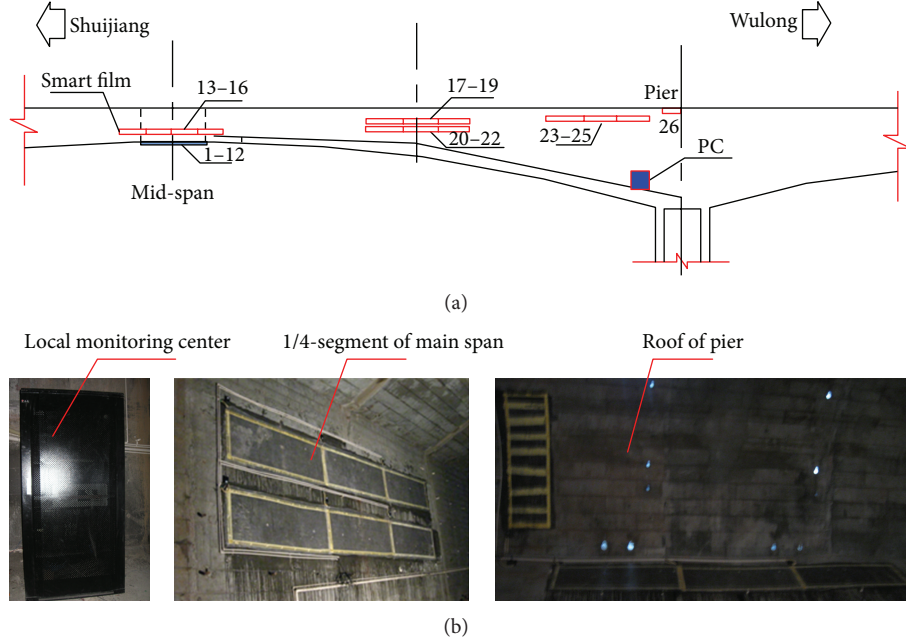


FIGURE 16: (a) Layout of smart film sensors and (b) the local monitoring center and smart film sensors.

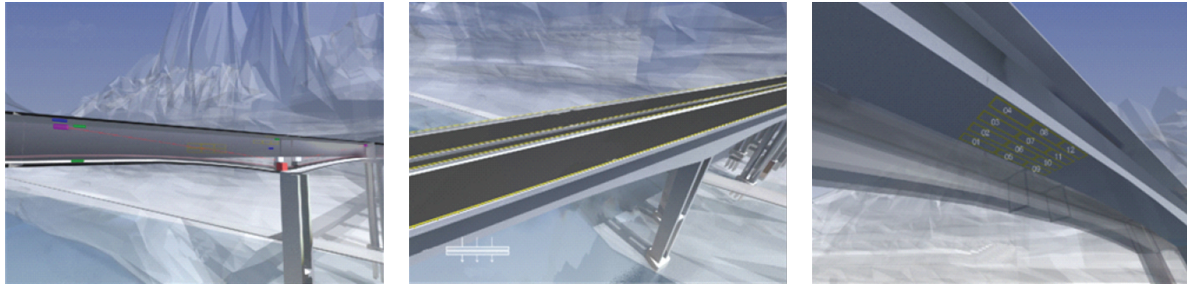


FIGURE 17: Effect of the interactive 3D scene.

right bridge, and they appeared in early September 2009, as shown in Figure 18(b). Two vertical cracks with the lengths from 7 cm to 15 cm could be found by sensor 1 (Lw001) which was arranged in the base plate of box girder from the mid-segment of main span of the left bridge, and they occurred in mid February 2009, as shown in Figure 18(c). Two vertical cracks with the lengths from 24 cm to 35 cm could be found by sensor 26 (Lw026) which was arranged in the roof of box girder of pier 0 on the left bridge, and their initiation time was mid November 2009, as shown in Figure 18(d).

**5.2.4. Comparison of Data.** During the monitoring period, the result of the plug-in of recurrence of crack was compared with that of man-operated periodic detection (see Figure 19). The locations which needed to be compared were Lw011 of the mid-segment of main span on the right bridge and Lw001 of the mid-segment of main span on the left bridge. The man-operated detection data is 16.8 cm and 12.3 cm, respectively. And the data is basically consistent with the result of the remote monitoring center.

**5.2.5. Monitoring Result.** According to the data of the enameled wires of the smart film from February 2009 to November 2010, it can be inferred that several vertical cracks exist on the base plate of the mid-segment of main span and close to the base plate of box girder of pier. On the basis of the locations and the directions, these cracks mostly belong to nonstructural cracks due to concrete shrinkage and temperature variation.

Moreover, through the load test during the completion period (September 1-2, 2009), a few enameled wires of the smart films on the base plate of the mid-segment of main span were found broken for a short time then returned to normal later. This phenomenon could be explained as follows. During the load test period, force was loaded on the mid-segment of main span temporarily which led to the appearance of cracks, and then the wires were broken. When the load was released, crack would disappear and the wires went back into contact. This phenomenon could not be found by man-operated detection. In summary, no obvious structural cracks had been found on Tukan Wujiang River Bridge yet.

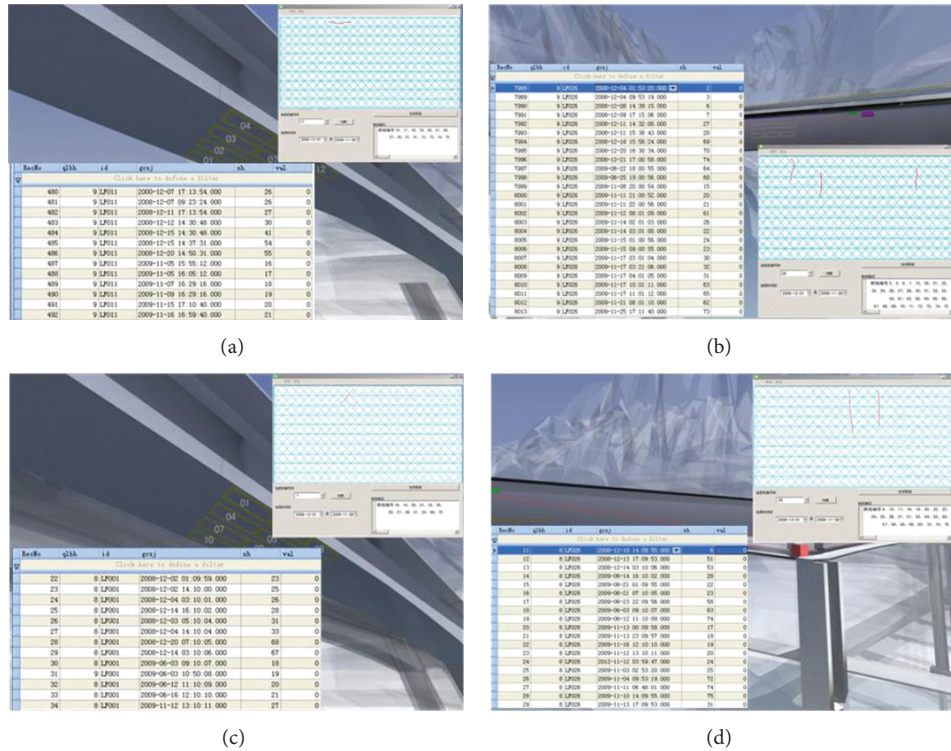


FIGURE 18: Recurrence of crack on Tukan Wujiang River Bridge.

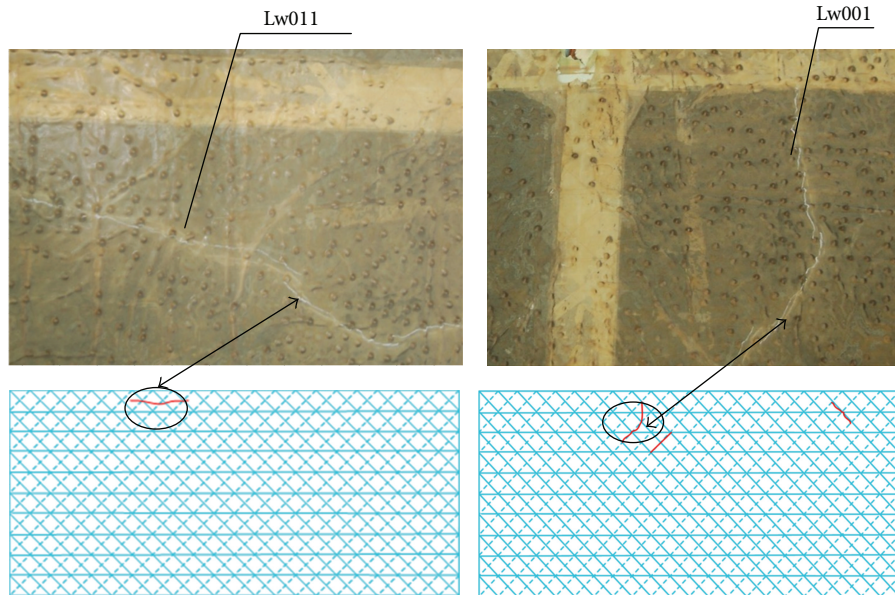


FIGURE 19: Data comparison.

**5.3. The Other Bridges.** At present, the bridges equipped with the remote monitoring system based on smart film include Jiangjin Yangtze River Highway Bridge, Lijiatuo Yangtze River Bridge, Niupeng Bridge, and Heichonggou Bridge.

Jiangjin Yangtze River Highway Bridge, a prestressed continuous steel bridge with the main bridge 140 m + 240 m + 140 m, is located in Chongqing municipality, China. Its

total length is 1360 m. A single cell and single box section is used in the box girder of the main bridge. The smart films are fabricated into crack sensors, which are installed on the mid-segment of main span, 1/4-segment of main span, and side span in Degan direction, respectively. The monitoring system was installed in April 2012, and it is still in use now (see Figure 20).



(a)

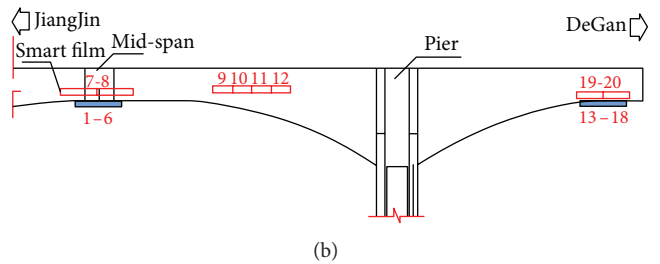


FIGURE 20: Jiangjin Yangtze River Highway Bridge and its sensor layout.

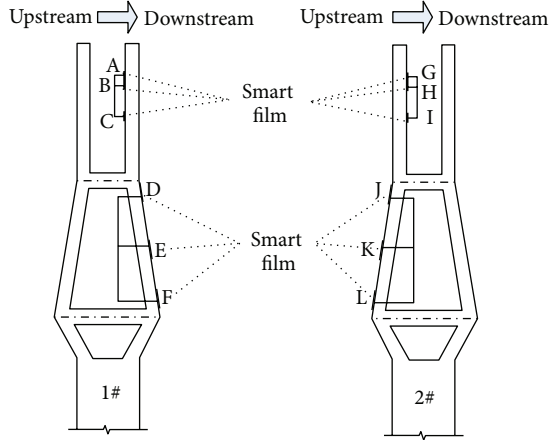


FIGURE 21: Lijiatuo Yangtze River Bridge and its sensor layout.

Lijiatuo Yangtze River Bridge, located in Chongqing Municipality, China, is a prestressed concrete cable-stayed bridge with the main bridge of 169 m + 444 m + 169 m. Its total length is 1288 m. The bridge has a structure of double-tower and double-cable-plane and consists of two transitional holes, eight approach bridges, and a main bridge. Each transitional hole has a length of 53 m. The length of each approach bridge is 50 m. Two sets of smart film crack monitoring systems are installed on two towers, respectively. For each tower, sensors are installed on two connection parts. For the girder, sensors are installed on 1/4-segment of two side spans, the mid-segment of main span, and 1/4-segment of main span. The monitoring system was installed in September 2012. So far, the systems are running well (see Figure 21).

Niupeng Bridge, located in Lvshui River area of Meng-Xin expressway connecting Mengzi and Xinjie, Yunnan province, China, is into a continuous steel bridge with the main bridge of 77 m + 140 m + 77 m. Its total length is 365 m. It is divided two independent bridges. A single cell and single box section is used in the box girder of the main bridge. Crack sensors are installed on the roof of pier of Mengzi Direction, the roof of pier of Xinjie Direction, and the mid-segment of main span. The monitoring system was installed in December 2012 and is still in use until now (see Figure 22).

Heichonggou Bridge, located in Zhamakong of Meng-Xin expressway connecting Mengzi and Xinjie, Yunnan province, China, is into a prestressed concrete continuous bridge with the main bridge of 98 m + 180 m + 98 m. It is divided two

independent bridges. A single cell and single box section is used in the box girder of the main bridge. Crack sensors are installed on the roof of pier of Mengzi Direction, the roof of pier of Xinjie Direction, the mid-segment of main span, and plate of 1/8-span of the left bridge. The monitoring system was installed in December 2012. So far, the system is running normally (see Figure 23).

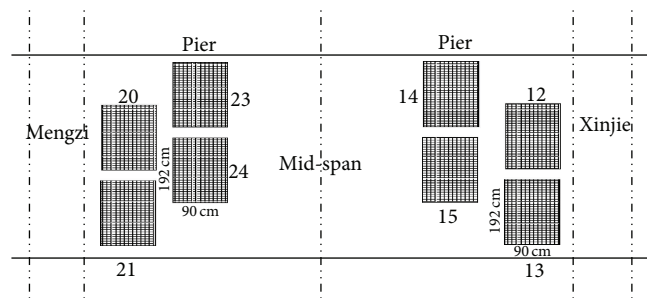
As discussed above, apart from the unique damage location due to bridge crack, sensors are mainly installed on the upper part of the tower, the middle part, the lower part, and two connection parts of the tower for the cable-stayed bridge. For the main girder, sensors are mainly installed on the locations where cracks are easy to initiate, including the base plate and the plate of the main bridge as well as the plate of 1/4-segment of main span. For the continuous steel bridge, sensors are mainly installed on the following locations: the base plate and the plate of the mid-segment of main span, the plate of 1/4-segment of main span, the plate of 1/8-segment of main span, the roof of pier, the base plate, and the plate of the closure segment in side span.

## 6. Conclusion

Smart film crack monitoring method, proposed by the authors, is a good choice for detecting initiation, length, width, shape, location, and propagation of cracks on concrete bridges. In this paper, a methodological approach on bridge crack monitoring with smart film has been developed. Firstly,



(a)

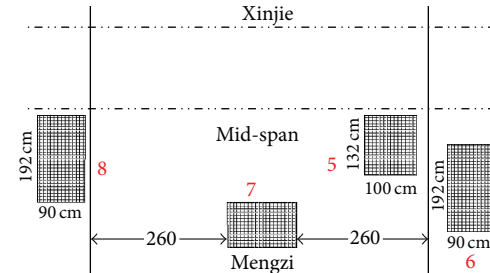


(b)

FIGURE 22: Niupeng Bridge and its sensor layout.



(a)



(b)

FIGURE 23: Heichonggou Bridge and its sensor layout.

this paper examines a new fabrication technique of the smart film based on structural characteristics which overcomes the difficulties found in other measures. Then the feasibility of crack monitoring is analyzed and verified by the mechanical sensing character of the smart film under the two conditions of normal strain and crack initiation. The result shows a good sensing performance under the two conditions. At the same time, the coupling effect between parallel enameled wires of the smart film is discussed, and then it is reduced by use of low-frequency detecting signal along with the custom communication protocol. On this basis, the remote crack monitoring system with smart film, consisting of the local monitoring center and the remote monitoring center, is designed. Then crack data collected by the local monitoring center is sent to the remote monitoring center and the cracks are simulated and recurred by the plug-ins of the interactive 3D scene and analysis of crack data, improving the readability of data.

Finally, the monitoring system has been applied to six bridges, including Masangxi Yangtze River Bridge, Tukan Wujiang River Bridge, Jiangjin Yangtze River Bridge, Lijiatuo Yangtze River Bridge, Niupeng Bridge, and Heichonggou Bridge. The monitoring effect has been discussed. The monitoring conditions on Masangxi Yangtze River Bridge and Tukan Wujiang River Bridge are demonstrated in detail. At the same time, the accuracy of the monitoring result is verified by the comparison between man-operated periodic detection and the system monitoring. Through the long-term operation of the system, the system concludes with a good stability (the running time of the system on Tukan Wujiang

River Bridge is over 5 years), reliability, and instantaneity. It is useful for evaluation of structural security of bridges.

## Conflict of Interests

The authors declare that there is no conflict of interests regarding the publication of this article.

## Acknowledgments

This work is jointly supported by Program for Innovation Team Building at Institutions of Higher Education in Chongqing (KJTD201306), Natural Science Foundation Project of CQ CSTC (cstc2013jcyjA0893 and jA30016), Scientific and Technological Research Program of Chongqing Municipal Education Commission (Grant no. KJZH11203), State Key Laboratory Breeding Base of Mountain Bridge and Tunnel Engineering (CQSLBF-Y12-6), National Engineering Research Center for Inland Waterway Regulation (SLK2014B05).

## References

- [1] Z. Kral, W. Horn, and J. Steck, "Crack propagation analysis using acoustic emission sensors for structural health monitoring systems," *The Scientific World Journal*, vol. 2013, Article ID 823603, 13 pages, 2013.
- [2] G. Heo, M. L. Wang, and D. Satpathi, "Optimal transducer placement for health monitoring of long span bridge," *Soil*

- Dynamics and Earthquake Engineering*, vol. 16, no. 7-8, pp. 495–502, 1997.
- [3] J. M. Ko and Y. Q. Ni, “Technology developments in structural health monitoring of large-scale bridges,” *Engineering Structures*, vol. 27, no. 12, pp. 1715–1725, 2005.
  - [4] D. Uttam and B. Culshaw, “Precision time domain reflectometry in optical fiber systems using a frequency modulated continuous wave ranging technique,” *Journal of Lightwave Technology*, vol. LT-3, no. 5, pp. 971–977, 1985.
  - [5] G. Jiang, P. Van Vickle, K. Peters, and V. Knight, “Oscillator interrogated time-of-flight optical fiber interferometer for global strain measurements,” *Sensors and Actuators A*, vol. 135, no. 2, pp. 443–450, 2007.
  - [6] F. Ravet, F. Briffod, B. Glisic, M. Nikles, and D. Inaudi, “Submillimeter crack detection with Brillouin-based fiber-optic sensors,” *IEEE Sensors Journal*, vol. 9, no. 11, pp. 1391–1396, 2009.
  - [7] L. D. Lu, Y. J. Song, F. Zhu, and X. P. Zhang, “Coherent optical time domain reflectometry using three frequency multiplexing probe,” *Optics and Lasers in Engineering*, vol. 50, no. 12, pp. 1735–1739, 2012.
  - [8] S. Villalba and J. R. Casas, “Application of optical fiber distributed sensing to health monitoring of concrete structures,” *Mechanical Systems and Signal Processing*, vol. 39, no. 1-2, pp. 441–451, 2012.
  - [9] M. H. Motamed, X. Feng, X. T. Zhang, C. S. Sun, and F. Ansari, “Quantitative investigation in distributed sensing of structural defects with Brillouin optical time domain reflectometry,” *Journal of Intelligent Material Systems and Structures*, vol. 24, no. 10, pp. 1187–1196, 2013.
  - [10] S. Sun, D. J. Pommerenke, J. L. Drewniak et al., “A novel TDR-based coaxial cable sensor for crack/strain sensing in reinforced concrete structures,” *IEEE Transactions on Instrumentation and Measurement*, vol. 58, no. 8, pp. 2714–2725, 2009.
  - [11] G. Pandey, M. Wolters, E. T. Thostenson, and D. Heider, “Localized functionally modified glass fibers with carbon nanotube networks for crack sensing in composites using time domain reflectometry,” *Carbon*, vol. 50, no. 10, pp. 3816–3825, 2012.
  - [12] G. Pandey, E. T. Thostenson, and D. Heider, “Electric time domain reflectometry sensors for non-invasive structural health monitoring of glass fiber composites,” *Progress in Electromagnetics Research*, vol. 137, pp. 551–564, 2013.
  - [13] I. M. Nazmul and T. Matsumoto, “High resolution COD image analysis for health monitoring of reinforced concrete structures through inverse analysis,” *International Journal of Solids and Structures*, vol. 45, no. 1, pp. 159–174, 2008.
  - [14] M. R. Jahanshahi, S. F. Masri, and G. S. Sukhatme, “Multi-image stitching and scene reconstruction for evaluating defect evolution in structures,” *Structural Health Monitoring*, vol. 10, no. 6, pp. 643–657, 2011.
  - [15] M. A. Caminero, M. Lopez-Pedrosa, C. Pinna, and C. Soutis, “Damage monitoring and analysis of composite laminates with an open hole and adhesively bonded repairs using digital image correlation,” *Composites B*, vol. 53, pp. 76–91, 2013.
  - [16] B. Zhang, Z. Zhou, K. Zhang, G. Yan, and Z. Xu, “Sensitive skin and the relative sensing system for real-time surface monitoring of crack in civil infrastructure,” *Journal of Intelligent Material Systems and Structures*, vol. 17, no. 10, pp. 907–917, 2006.
  - [17] Z. Zhou, B. Zhang, K. Xia, X. Li, G. Yan, and K. Zhang, “Smart film for crack monitoring of concrete bridges,” *Structural Health Monitoring*, vol. 10, no. 3, pp. 275–289, 2011.
  - [18] B. N. Zhang, S. L. Wang, X. X. Li, X. Zhang, G. Yang, and M. F. Qiu, “Crack width monitoring of concrete structures based on smart film,” *Smart Materials and Structures*. In press.

## Review Article

# Development of Inspection Robots for Bridge Cables

**Hae-Bum Yun,<sup>1</sup> Se-Hoon Kim,<sup>2</sup> Liiliu Wu,<sup>1</sup> and Jong-Jae Lee<sup>2</sup>**

<sup>1</sup> Department of Civil, Environmental and Construction Engineering, University of Central Florida, Orlando, FL 32816, USA

<sup>2</sup> Department of Civil and Environmental Engineering, Sejong University, Seoul 143-747, Republic of Korea

Correspondence should be addressed to Jong-Jae Lee; jongjae@sejong.ac.kr

Received 3 August 2013; Accepted 30 September 2013

Academic Editors: D. G. Aggelis, N. Alver, and H. K. Chai

Copyright © 2013 Hae-Bum Yun et al. This is an open access article distributed under the Creative Commons Attribution License, which permits unrestricted use, distribution, and reproduction in any medium, provided the original work is properly cited.

This paper presents the bridge cable inspection robot developed in Korea. Two types of the cable inspection robots were developed for cable-suspension bridges and cable-stayed bridge. The design of the robot system and performance of the NDT techniques associated with the cable inspection robot are discussed. A review on recent advances in emerging robot-based inspection technologies for bridge cables and current bridge cable inspection methods is also presented.

## 1. Introduction

Bridges are important national assets that should be properly maintained to ensure public safety. Recent advances in bridge engineering have allowed bridges to be designed and constructed longer and slender than ever. In particular, long-span cable-supported bridges require high maintenance associated with reliable and efficient inspection methods.

Cable-supported bridges, including cable-suspension and cable-stayed bridges, consist of numerous subsystems, including pylons, anchorages, cables, stiffening girders, and slabs. A bridge cable system is an important subsystem that consists of main cables, hanger ropes, and stay cables. The cable rope is usually made of high-strength carbon steel that is five to ten times stronger than regular structural steels [1].

In maintenance of bridge cables, only few components are considered to be repairable, such as high-density polyethylene (HDPE) cable sheathings, neoprene boots, and elastomeric rings. In the presence of corrosion or fatigue damage in main tension elements (MTEs) near anchorages or in free spans, repairing damaged MTEs is practically impossible. Thus, preventative maintenance is vital to ensure the safety of cable systems. To accomplish this, the development of reliable inspection methods is imperative to assess material and structural conditions of cable systems [2].

In the United States, highway bridges should be visually inspected every two years [3]. Structural Health Monitoring (SHM) technologies have also been used for bridge condition

assessment. Current bridge condition assessment methods, however, have some technical limitations. For example, near anchorages, cables at supports are often not visible since these cables are sealed with grout. In free spans, trolley and rolling devices are used to access cables, which is not the safest way to inspectors [4, 5]. Limitations of the current cable inspection methods can be overcome using emerging robotics technologies. The robotics technologies are usually combined with powerful nondestructive testing (NDT) techniques for bridge cable systems that are hardly accessible with current inspection practices. This paper reviews recent advances in robot-based inspection technologies for bridge cables. This paper also introduces a unique cable inspection robot that has been developed in Korea since 2010 as a part of the Super Long-Span Bridge R&D project led by Korea Ministry of Land, Infrastructure and Transport (MOLIT). Design of the cable robot system and performance test results of different NDT techniques associated with the robot will be presented.

This paper consists of two parts: (i) overview on current cable inspection methods (Sections 2 and 3) and (ii) introduction to the cable inspection robot developed in Korea (Section 4). In Section 2, an overview on current cable inspection methods will be described. In Section 3, commercially available cable-inspection systems will be described. Detailed description of the cable-inspection robot newly developed in Korea is presented in Section 5.



FIGURE 1: World-landmark cable bridges. The parenthesis shows the main span length, country, and constructed year.

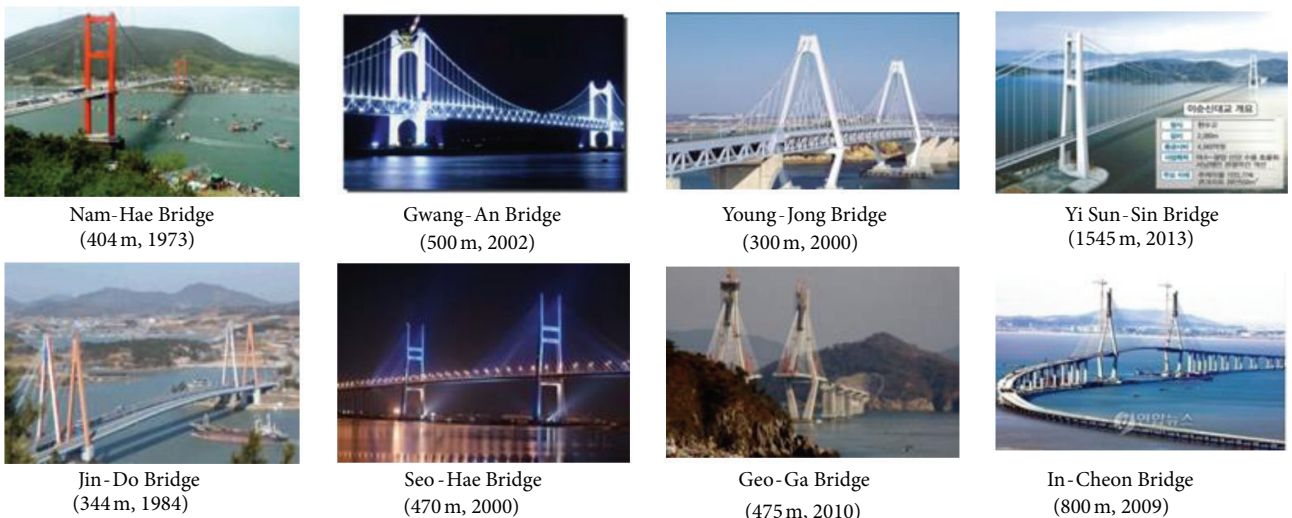


FIGURE 2: Cable-supported bridges in Korea. Numbers in parenthesis show the main span length and constructed year.

## 2. Current Practices for Bridge Cable Inspection

**2.1. Trends in Construction and Maintenance of Cable-Supported Bridges.** An increasing number of cable-supported bridges are being constructed over the world, especially in the developing countries (see Figure 1). Construction technologies of cable-suspension and cable-stayed bridges were originally developed in the USA and Germany and then in Japan through the major construction projects of the Akashi-Kaikyo Bridge, a cable-suspension bridge, and the Tatara Bridge, a cable-stayed bridge. More recently, a number of cable-supported bridges have been constructed in China, including the Tsing Ma Bridge in 1997, the Sutong Bridge in 2008, and the Xihoumen Bridge in 2009. The construction of the Stonecutters Bridge is considered as a technological

monument in bridge construction due to its unique design in composite towers and twin aerodynamic decks. The market size of cable-supported bridge construction is rapidly growing in Southeast Asian countries, including Thailand, Malaysia, Singapore, Vietnam, Philippines, Cambodia, and Bangladesh.

In Korea, the Nam-Hae Grand Bridge was constructed in 1973 as the first cable-suspension bridge, and the Jin-Do Grand Bridge was constructed in 1984 as the first cable-stayed bridge. The longest cable-suspension bridge in Korea is the Yi-Sun-Shin Bridge constructed in 2013, and the longest cable-stayed bridge in Korea is the Incheon Bridge constructed in 2010 (see Figure 2). Since Korean peninsula has many islands, the construction of long-span bridges is demanded to connect islands to the main land. Currently, a total of 64 bridges construction are planned in coastal areas.

TABLE 1: Bridge inspection standards in the United States and Korea. The table is modified from [6].

The United States	Korea
(i) AASHTO LRFD Bridge Design Specifications, 5th Ed. (2010)	(i) MOLIT <sup>1</sup> Infrastructure Maintenance Guide (1995)
(ii) AASHTO Manual for Bridge Evaluation, Second Ed. (2011)	(ii) MOLIT (Bridge and Tunnel) Inspection and Diagnosis Guiding Principle of Details (1996)
(iii) AASHTO Guide Manual for Bridge Element Inspection, First Ed. (2011)	(iii) KISTEC <sup>2</sup> The Bridge Inspection Handbook (1999)
(iv) AASHTO Guide for Commonly Recognized Structural Elements (1998)	(iv) MOLIT The Bridge Maintenance Manual (1999)
(v) AASHTO Manual for Condition Evaluation of Bridges (1994)	(v) MOLIT Concrete Structure Specifications (1999, 2003, 2007, and 2012)
(vi) AASHTO Manual for Maintenance Inspection of Bridges (1974, 1978, 1983, and 1993)	(vi) MOLIT Bridge Design Specifications (2000, 2005, 2008, 2010, and 2012)
(vii) AASHO Manual for Maintenance Inspection of Bridges (1970)	(vii) MOLIT Steel Structure Specifications (2003 and 2009)
(viii) FHWA Bridge Inspector's Reference Manual (2002 and 2006)	(viii) MOLIT The Bridge Maintenance Manual (2001)
(ix) FHWA, Bridge Inspector's Training Manual 90, 1991	(ix) MOLIT Maintenance Manual for Corrosion Protection of Steel Bridge (2003)
(x) FHWA Hydraulic Engineering Circular No. 18 (about 1988)	(x) KISTEC Manual for Bridge LCC Evaluation (2006)
(xi) FHWA "Scour at Bridges," a technical advisory (1988)	(xi) MOLIT Bridge-Tunnel Inspection and Diagnosis (2007)
(xii) FHWA Inspection of Fracture Critical Bridge Members (1986)	(xii) KISTEC Know-how of Bridge Inspection: Ordinary Bridge and Cable Bridge (2008)
(xiii) FHWA Bridge Inspector's Training Manual 70 (1979)	(xiii) MOLIT Inspection and Diagnosis Guiding Principle of Details (2009)
(xiv) FHWA Culvert Inspection Manual (about 1979)	(xiv) MOLIT Inspection and Diagnosis Guiding Principle of Details Manual (2012)
(xv) FHWA The Bridge Inspector's Manual for Movable Bridges (1977)	
(xvi) FHWA Recording and Coding Guide for the Structure Inventory and Appraisal of the Nation's Bridges (1972, 1979, 1988, 1991, and 1995)	
(xvii) FHWA National Bridge Inspection Standards (1971, 1979, and 1988)	
(xviii) Code of Federal Regulations, 23 Highways Part 650, Subpart C—National Bridge Inspection Standards	

<sup>1</sup>MOLIT: Ministry of Land, Infrastructure and Transport. <sup>2</sup>KISTEC: Korea Infrastructure Safety Corporation.

The market size of bridge construction is estimated over 1.2 billion U.S. dollars in next 20 years [7].

## 2.2. Current Maintenance Methods for Cable-Supported Bridges

**2.2.1. Maintenance of Cable-Supported Bridges.** Reliable inspection methods are vital to ensure structural and service safety of cable-supported bridges. Bridge maintenance agencies employ different levels of inspection, including routine, periodic, emergent, and in-depth inspection. Table 1 summarizes major bridge inspection manuals in the United States and Korea.

According to [8], bridges should be inspected every two years. In Korea, bridge agencies should perform regular inspection every 2 years and in-depth inspection every 5 years. In bridge inspection, it is important to observe excessive wear, broken wires, corrosion and pitting, state of lubrication, core condition, and so forth. Causes of defects and deteriorations must be understood using appropriate

diagnosis methods. Frequent cable defects include surface rust, section loss, fatigue cracking, and collision damage.

**2.2.2. Cable Inspection Using NDT Methods.** Challenges in bridge cable inspection are mainly due to limited accessibility to cable systems. MTEs within cable bundles are often hardly visible to inspectors. Cables grouted in anchorage areas are very difficult to be inspected. Visual inspection and NDT methods for bridge cables in free spans are challenging due to inaccessibility of the cable. Early detection of internal damage is vital in preventive inspection. However, internal deterioration of bridge cables is hardly detectable using visual inspection methods. For example, Figure 3 illustrates the importance of early detection of internal defects. During the project of rewrapping main cables of the Nam-Hae Bridge in Korea, corrosion was found at the bottom of main cables at midspan and near anchorage zones of side spans. Breakage of wires was found at cable bands, which could cause serious structural failure if it was not found during the cable retrofit project. Some NDT methods, such as magnetic, ultrasonic, X-ray tests, have been used to detect such internal deterioration.

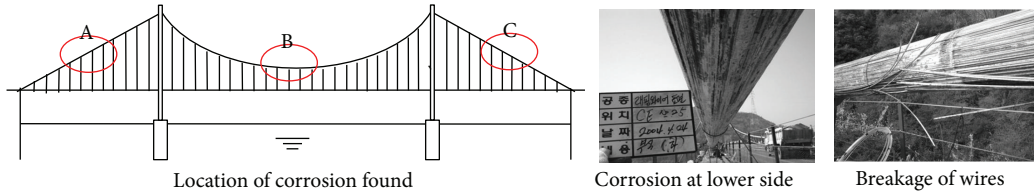


FIGURE 3: Inspection of the main suspension cables of the Nam-Hae Bridge [9].

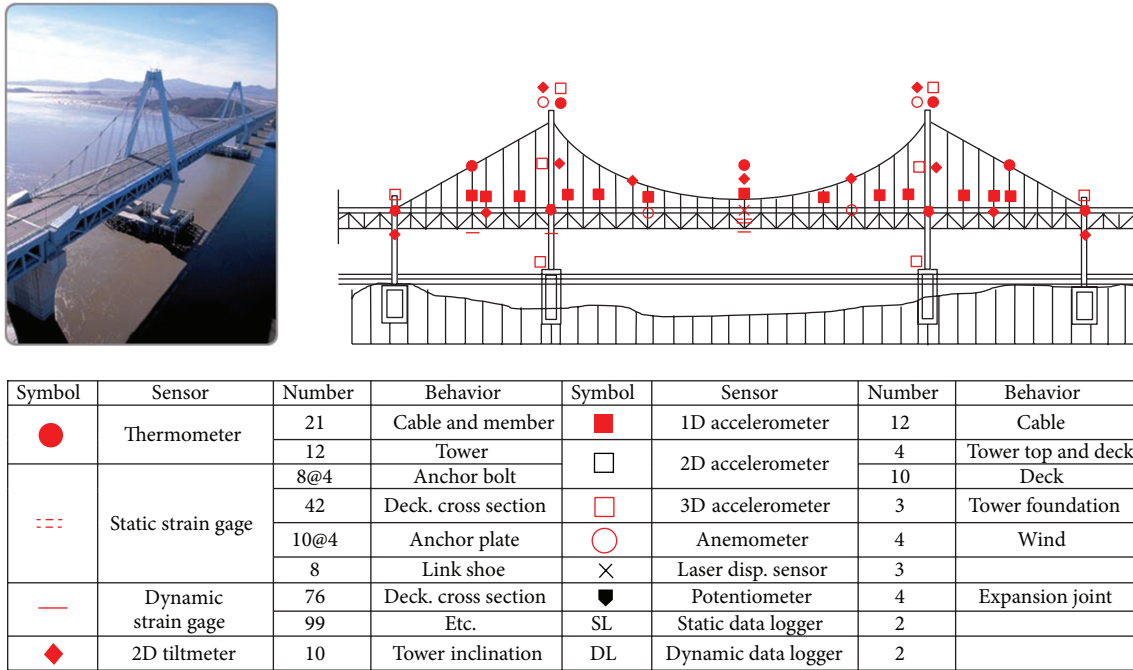


FIGURE 4: Structural health monitoring system of the Yeong-Jong Bridge in Korea.

**2.2.3. Cable Condition Assessment Using SHM Methods.** SHM technologies are widely employed to assess the structural conditions of cable bridges to ensure bridge safety and serviceability. The purposes of SHM are to diagnose and prognosis a bridge's structural safety based on the measurement of structural behaviors. A SHM system consists of three subsystems, including sensing, data communication, and data processing. The sensing subsystem can continuously collect sensor data, such as service stresses, environmental stresses, and bridge deformation. The data communication subsystem transfers sensor data from a remote field-monitoring site to a data repository site and archives them. The data processing subsystem extracts meaningful information for bridge maintenance from raw sensor data.

A number of SHM systems have been employed for condition assessment of cable-supported bridges. An example is the Wind and Structural Health Monitoring System (WASHMS) for the Tsing Ma Bridge, Ting Kau Bridge, and Kap Shui Mun Bridge, developed by the Hong Kong Highways Department [10]. The sensing system consists of approximately a total of 900 sensors including accelerometers, strain gauges, displacement transducers, inclinometer,

anemometers, temperature sensors, and dynamic weight-in-motion sensors: about 350 sensors on the Tsing Ma Bridge, 350 on Ting Kau Bridge, and 200 on Kap Shui Mun Bridge.

In Korea, SHM technologies have been actively employed for cable-supported bridges. Figure 4 shows the SHM system for the Yeong-Jong Bridge, which includes thermometers, strain gauges, tiltmeters, accelerometers, anemometers, displacement transducers, and potentiometers. Twelve accelerometers are installed throughout the bridge's cable system to monitor cable tension forces.

For condition assessment of bridge cables, measuring cable tension force is an important concern to assess structural safety. According to Tabatabai [2], although vibration-based force measurement is commonly used to estimate internal stress levels of bridge cables, the accuracy is arguable in many field applications. However, internal damage of cables, such as corrosion and inner wire breakage, can hardly be detected using the vibration-based method.

**2.3. Cable Inspection Methods.** Bridge cables are subject to various service and environmental stresses that could cause different modes of material and structural deterioration. Consequently, combinations of multiple NDT methods and

TABLE 2: Accelerometer-based cable monitoring systems in different countries [11].

Bridge	Nation	Main span (m)	Total number of cables ( <i>a</i> )	Number of cables installed with accelerometer ( <i>b</i> )	Ratio ( <i>b/a</i> , %)
Seo-Hae	Republic of Korea	470	144	24	16.7
Jin-Do	Republic of Korea	344	60	18	30.0
Tatara	Japan	890	168	4	2.4
Jintang	China	620	168	20	11.9
Rion-Antirion	Greek	560	368	13	3.5
Oresund	Denmark	490	160	16	10.0
Fred Hartman	USA	381	192	19	9.9

instruments are used in cable inspection [12]. Current cable inspection methods are reviewed in this section.

**2.3.1. Visual Inspection.** Human visual inspection is considered the primary cable inspection method over other NDT methods although human inspection relies heavily on subjective judgments of individual inspectors [2, 9]. In this method, first entire cable surface should be visually inspected from a close distance; then the inspection of neoprene boots, neoprene rings, visible guide pipes, and accessible anchorage surfaces is followed [2]. Visual inspections are often carried out using a cable inspection trolley that travels along cables at a low speed, which can be considered inconvenient and time consuming. Since the performance of an inspection trolley is largely affected by the existence of obstacles in cable paths, some part of cable systems, such as free cable spans with corrosion protection and anchorage areas, would be not accessible using this method [7].

**2.3.2. Image Processing-Based Inspection.** Image processing-based cable inspection originates from a more general field of signal processing, including various image-processing techniques, such as image smoothing, image enhancing, segmentation, and edge detection [13]. Cable surface images are usually captured by a camera in a form of digital images as a two-dimensional numeric matrix. Image processing techniques are used to process these numeric matrices associated with pattern recognition algorithms to extract useful damage-related information [14]. Mandal and Atherton applied image-processing techniques to evaluate the severity of cable surface damage [15]. Ho et al. developed damage detection algorithms for cable inspection purposes [16]. These algorithms were designed to smooth and enhance the contrast of the original images and to classify damage patterns based on principal component analysis techniques.

**2.3.3. Vibration-Based Cable Force Measurement.** Cable tension force can be calculated from vibration signatures of bridge cables using the following equation:

$$T = 4L^2 f^2 m, \quad (1)$$

where  $T$  is the cable tension;  $L$  is the cable length;  $m$  is the cable mass per unit;  $f$  is the natural frequency of the cable. Therefore, the cable tension force can be determined based

on the measurements of those cable's physical properties [17]. This method, however, is not strictly applicable to bridge cable inspection due to oversimplification ignoring bending stiffness, sag under dead weight, and other complicating factors such as neoprene rings, viscous dampers, and variable stiffness along length.

Numerous vibration-based cable force measurement techniques have been developed. For example, Zui et al. developed a vibration-based method to measure cable forces, considering both the flexural rigidity and sag inherent to the inclined cable [18]. Cho et al. implemented Zui's method using wireless sensor networks [19]. Table 2 summarizes some accelerometer-based cable monitoring systems in different countries.

**2.3.4. Ultrasonic Inspection.** Ultrasonic inspection techniques are also widely used in bridge cable inspection applications. An ultrasonic device consists of a transmitter sending high frequency sound waves through a specimen and a receiver to capture the reflected signal, while acoustic emission technique can detect breakage of a wire in a passive mode. Material defects as a discontinuity in a solid medium reflect the transmitted signal to a receiver as a signature of the presence of defects. Recently, long-range guided waves can be used as a transmitting signal [20]. Although the size and location of defects could be characterized based on the magnitude and delay time of the reflected signal [21], it requires calibrations through extensive laboratory experiments. The interpretation of ultrasonic test results could be subjective to the inspector's experiences and judgment.

Desimone et al. [22] conducted experimental study about the ultrasonic technique using a pulse wave for a wire with notches and grooves at different depth. Ultrasonic technique is applicable to inspecting cables connected to parallel wires in anchorage areas to detect wire fractures and corrosion [12]. This technique was applied to seven-wire cable strands at 12 anchorages of the Conhrane Bridge in Alabama, the United States [23, 24].

**2.3.5. Magnetic Methods.** Magnetic sensors can be used to measure tensile stress in a cable, loss of metallic area (LMA), and local fault (LF), such as wire breakage. The mechanism of magnetic sensors is based on the sensitivity of a magnetic field to the presence of impairments, such as corrosion and

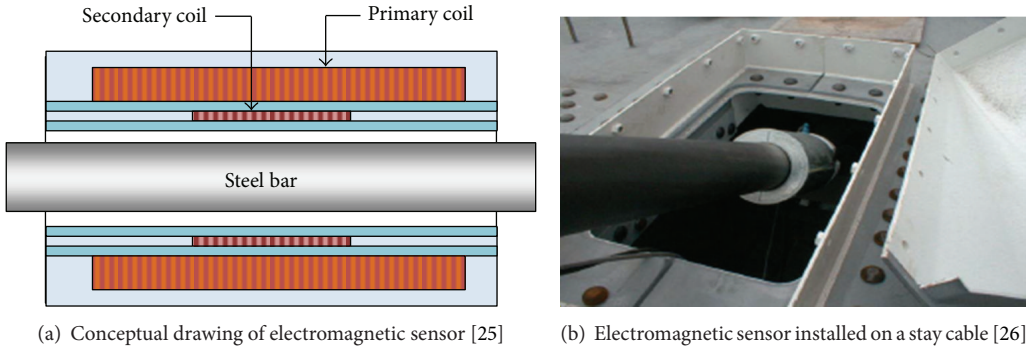


FIGURE 5: Electromagnetic sensors in bridge cable inspection applications.

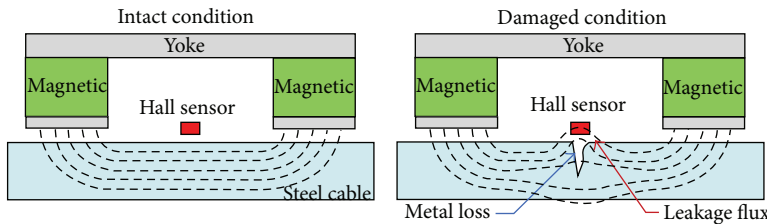


FIGURE 6: Mechanism of MFL-based damage detection [27].

fractures. Therefore, the change of a magnetic field along a cable indicates the presence of defects.

A conceptual drawing of an electromagnetic (EM) sensor is shown in Figure 5. The EM sensor consists of a primary coil and a secondary coil to measure the apparent relative permeability and formalize EM characteristics of a steel rod (i.e., specimen). When a pulsed current flows in the primary coil, a ferromagnetic material is magnetized, and a pulsed magnetic field is introduced along the specimen. The relative permeability is a function of cable tension. The relative permeability ( $\mu_r$ ) can be calculated as

$$\mu_r = \frac{\mu_0 \Delta B}{\Delta H}, \quad (2)$$

where  $\Delta B$  and  $\Delta H$  are the change in the induction and magnetic fields, respectively, and  $\mu_0$  is the permeability of the free space [25].

Magnetic flux leakage (MFL) devices are often used to assess the severity of corrosion and detect local faults (LF) due to outer and inner wire fractures by measuring the loss of metallic cross-sectional area (LMA) [12]. The mechanism of MFL devices is illustrated in Figure 6. In an intact condition, the magnetic flux field generated using magnets remains uniform. In a damaged condition, metal loss due to wire corrosion or fractures disturbs the magnetic field, which results in inhomogeneous magnetic fluxes. The disturbance in the magnetic field can be detected using a Hall sensor placed between the poles of magnets. The magnitude of the Hall sensor signal is proportional to the magnetic flux leakage [15]. Therefore, the accuracy of LMA measurement is largely influenced with the homogeneity of magnetic flux around a steel cable. A strong permanent or an electromagnet is commonly used.

This technique is considered as a promising cable inspection method since LMA can be measured precisely under protective coating on cables nondestructively in relatively short time [12]. Typical applications of MFL devices include the steel cable inspection of aerial tramways, mining elevators, and offshore pipelines [13, 28, 29]. The MFL inspection technique also has been employed to different cable-stayed bridges [30, 31]. Figure 5(b) shows a MFL system applied in hanger cable inspection for the Yeong-Jong Bridge, Korea [32] (see Figure 7).

There are a number of commercially available magnet sensors for steel wire ropes that can be used in bridge cable inspection. DMT GmbH developed magnetoinductive testing equipment for bridge cables (see Figure 8(a)). The equipment has strong permanent magnet heads for rope diameters of up to 150 mm. Brandt developed a rope testing head designed for inspection of steel cables with the diameter of up to 160 mm [37]. Kündig AG manufactures three PMK-series magnetic systems for wire rope diameters up to 125 mm [38]. Ropescan was developed by the British Coal Research Laboratory (now owned by Lloyds Beal Ltd.) to inspect mine-hoist locked coil wire ropes [39]. Canada Centre for Mineral and Energy Technology (CANMET) and the Noranda Technology Centre jointly developed Magnograph II, computer controlled wire rope testing equipment [34] (see Figure 8(b)). Magnograph can operate solely on Hall effect sensors which produce a signal independent of speed and are therefore able to operate at very low speeds. Intron Plus [32] and Laboratory LRM [40] manufacture testing heads that can inspect both flat and round steel wire ropes. These devices are typically applied in mine hoist ropes, on offshore platforms, cableways, cranes, lifts, and bridge cables [41].

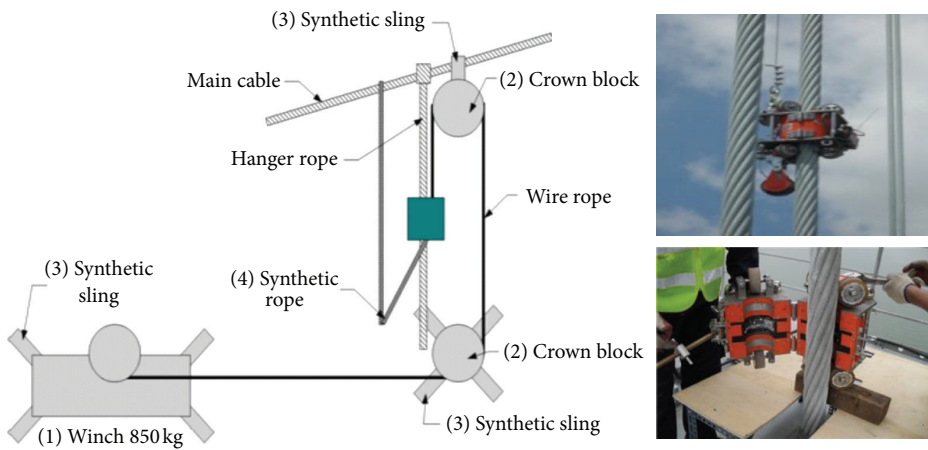


FIGURE 7: MFL system applied in hanger cable inspection for Yeong-Jong Bridge in Korea [32].

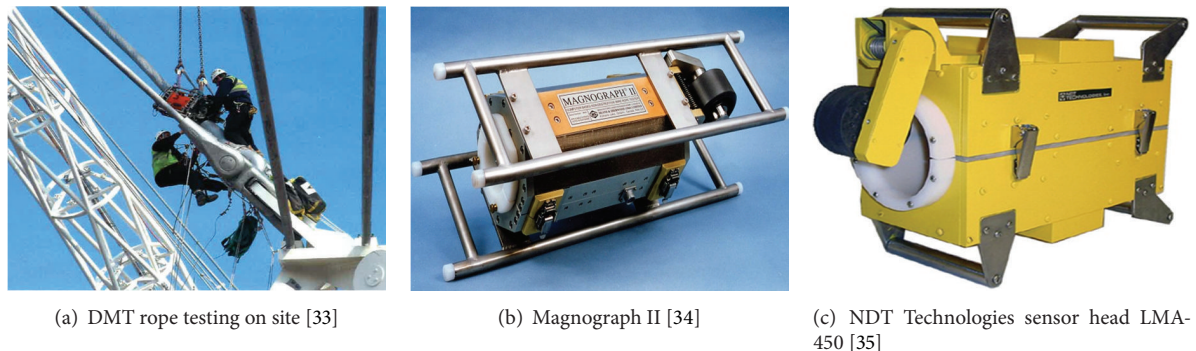


FIGURE 8: Commercially available magnetic sensor for bridge cable inspection.

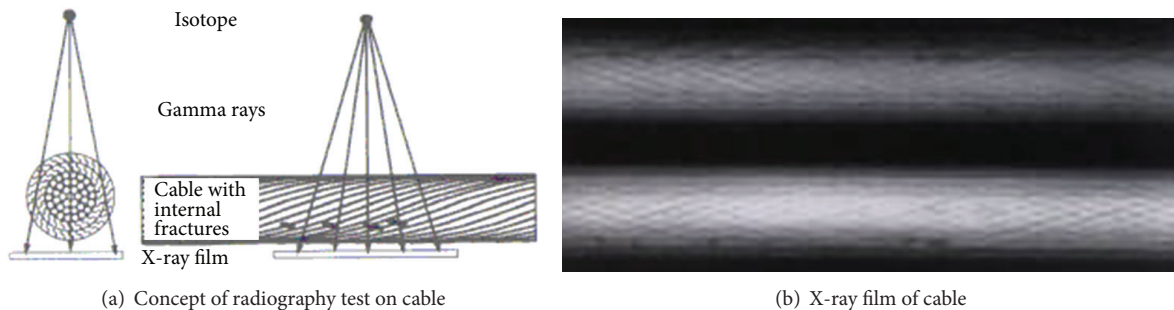


FIGURE 9: Radiography inspection for bridge cable inspection [36].

NDT Technologies produces MFL magnetic sensor heads. The device can measure LF and LMA of wire ropes up to 120 mm in diameter. The device weight is less than 75 kg (Figure 8(c)). University of Stuttgart in Germany developed magnet sensors associated with an annular array of two sets of 30 Hall effect sensors for the applications of aerial ropeways, bridge suspension cables, ship lifts, and cranes [42].

**2.3.6. Radiography.** Radiography is used for subsurface imaging to detect cable defects using either X-rays or gamma rays. X-rays are produced using a high-voltage X-ray tube,

and gamma rays are produced using a radioisotope (see Figure 9(a)). A summary of subsurface imaging technologies for reinforced concrete can be found in [43]. Radiography generally provides two-dimensional tomography for cross-sectional images of the three-dimensional object (see Figure 9(b)).

Xu et al. reported that the X-ray radiography can be applied to find cable defects in free spans, but not applicable for anchorages [48]. The application of radiography in bridge cable inspection is also limited due to possibility of radioactive hazards to working personnel while during inspection particularly at a high elevation of cable stay [1].

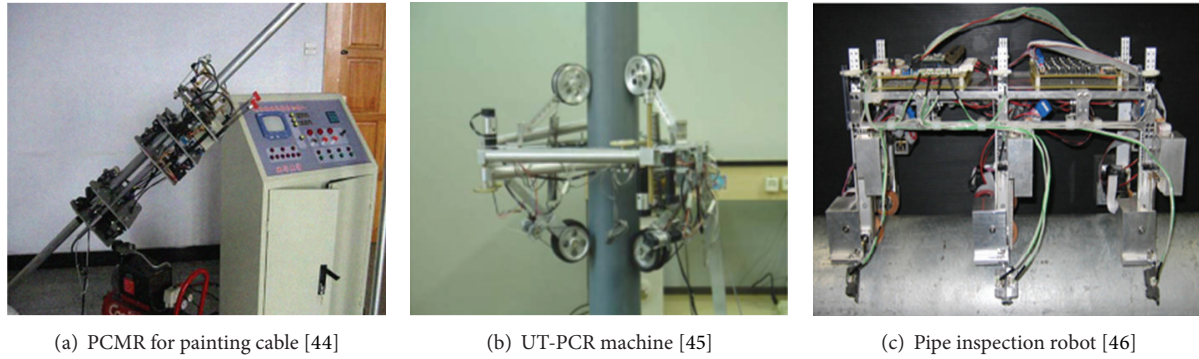


FIGURE 10: Pole and pipe inspection robots.



FIGURE 11: ATIS cable robot developed by Alpin Technik Leipzig [47].

### 3. Cable Inspection Robots

Robotic systems can move along bridge cable systems, such as bridge cables, pipes, steel wires, and circular poles for repair and maintenance as well as inspection. This section introduces several robotic systems that can be used for the inspection of bridge cable systems.

**3.1. Pipe Inspection Robots.** Li et al. developed a cable pneumatic climbing maintenance robot (PCMR) for coating and painting pipe structures (see Figure 10(a)) [44]. A pole climbing robot (UT-PCR) was developed by the University of Tehran, Iran, with pole grasping and vertical movement capability (see Figure 10(b)) [45]. The robot consists of a trilateral-symmetric body in a triangular shape with six limbs connected at its corner points through separate extension springs. The mechanical limbs are employed to grasp a pole. The wheels on the lower limbs are actuated by DC motors, while the wheels on the top limbs only guide the robot's movement. The robot has a self-locking mechanism to prevent sliding down on a pole.

A pipe-surface inspection robot was developed by Akita Prefectural University in Japan for pipe inspection (Figure 10(c)). This robot can traverse flanges, climb vertical flanges, and move along the bottom side of a pipe using six magnetic leg wheels.

A pole climbing and manipulating robot, developed by Sharif University, Iran, can pass bends and branches of a pole [49]. The robot consists of three main body parts, including

3-DOF planar substructure,  $z$ -axis rotating substructure, and grippers. The robot is actuated by three DC motors controlled by a central computer through control drivers.

**3.2. Cable Inspection Robots.** ATIS Cable Robot, a cable-climbing robot developed by Alpin Technik Leipzig, was designed to mount different modules to meet various purposes of cable inspection and maintenance, including visual inspection and MFL modules for inspection and taping and welding modules for maintenance (see Figure 11). The climbing robot is designed for different cable diameters from 24 mm to 350 mm. A relatively short installation time of 5 to 15 minutes is an advantage of this system.

Mavis ReCreator is another cable climbing robot developed by Tiefenbach GmbH (see Figure 12). This robot has five modules for cable coating maintenance, including coating removal, cleaning, repair, coating, and moving. Visual inspection instruments can be also mounted to the robot for surface inspection of bridge cables.

Luo et al. (2005) developed a robotic system that can inspect, clean, and paint bridge cables (see Figure 13) [50]. The inner frame connected to the climbing module can move along the cable in spiral motion. The outer frame connected to the maintenance module balances the robot while it moves controlling hanging weights of the painting bucket and battery.

A mobile robotic system for inspection of power transmission lines, developed by Tokyo Electric Power and Toshiba, consists of vehicle assembly, guide rail, guide rail

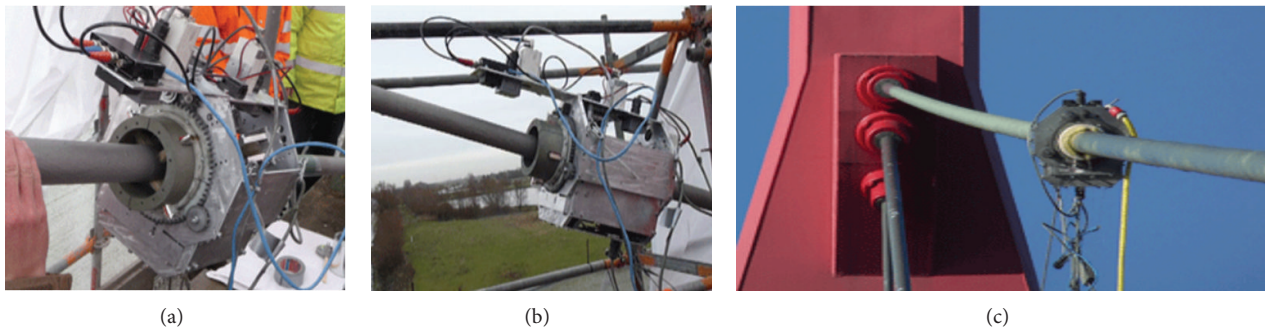


FIGURE 12: Mavis ReCreator and visual inspection [51].



FIGURE 13: In situ painting experiment of cable maintenance robot [50].

manipulator assembly, and balancer [52]. The robot can navigate a ground wire and maneuver over obstacles on ground wires. When the robot encounters a tower, a foldable arc-shaped arm that acts as a guide rail is unfolded to attach the arm to a ground wire placed on the opposite side of the tower.

#### 4. Development of Cable Inspection Robot in Korea

A research initiative has been supported by Korea Ministry of Land, Transportation, and Maritime Affairs (MLTM) since 2010 to develop a bridge cable inspection robot system. Although there are many commercially available systems as addressed in the previous chapters, challenges still remain to improve the performance of the inspection robot system (e.g., inspection speed, physical size, adaptability, controllability, etc.). The robotic system consists of three main subsystems, including (i) the climbing robot subsystem, (ii) the NDT subsystem, and (iii) the control and analysis subsystem (see Figure 14).

The climbing robot subsystem allows the robot unit to move on a bridge cable. The robot is controlled wirelessly by inspectors and can transmit sensor data collected from the sensing modules to the control and analysis subsystem. The NDT subsystem consists of two sensing modules, including (i) the magnetic sensing module using MFL devices to detect inner wire defects, such as LF due to wire fractures and

LMA due to wire corrosion, and (ii) the image processing-based sensing module to detect defects on cable surface. Figure 15 shows the design and specifications of the climbing robot subsystem and NDT subsystem. Two types of the climbing robot system were developed for cable-suspension bridges and cable-stayed bridges. This is necessary since cable-stayed bridges have inclined cables with larger gauges (up to 300 mm), and cable-suspension bridges have vertical hanger cables with smaller gauges (up to 90 mm). Detailed description of each subsystem will be presented in the subsequent subsections.

**4.1. Climbing Robot and Control Subsystems.** Three climbing mechanisms are usually employed for cable inspection robots, including magnetic, pneumatic, and electric methods [53, 54]. Electric method was chosen in this study for easy control and constant climbing force. Wireless communication is available between the climbing robot unit and the control and analysis subsystem to the robot control and sensor data transfer. The robot unit can be controlled by inspectors in distance of up to 600 m using a control software program shown in Figure 16.

**4.1.1. Cable-Suspension Bridge Robot.** An important design objective of the cable-suspension bridge robot was that the robot should be applicable to various gauge sizes of hanger cables. Another important design objective was that the robot should have enough climbing force to inspect vertical hanger

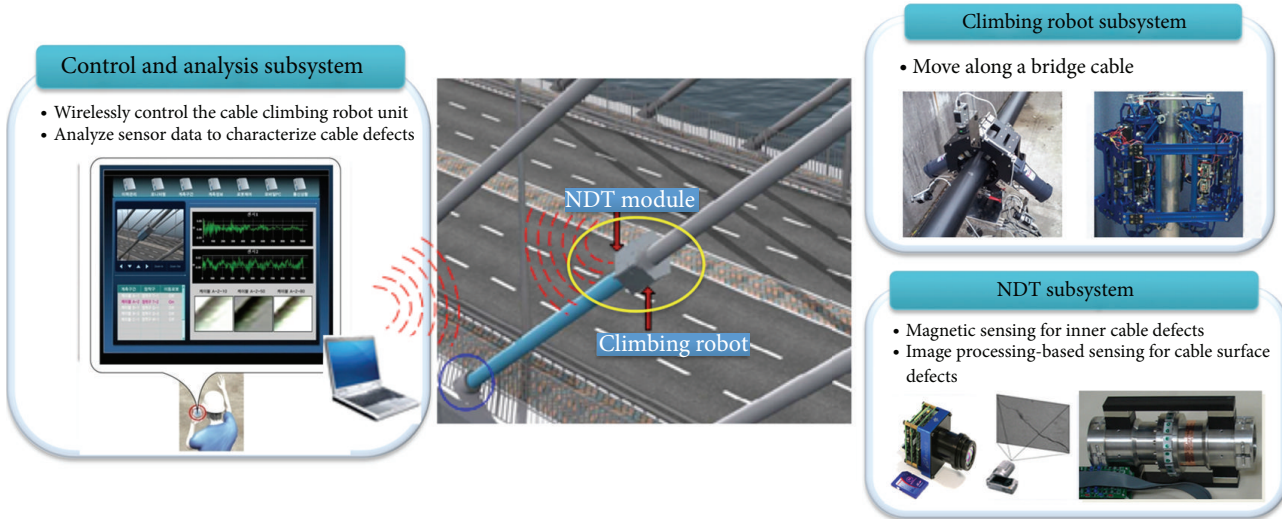


FIGURE 14: System components of cable inspection robot developed in Korea.

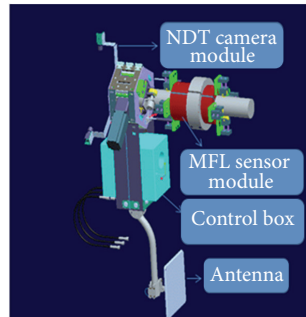


FIGURE 15: Design and specifications of cable inspection robot unit with the climbing robot subsystem and NDT subsystem.



- Functions of robot control software
- ① Robot status (velocity, location, and inclination)
  - ② Measuring range
  - ③ Moving speed
  - ④ Target location to move
  - ⑤ Number of cycles to be inspected
  - ⑥ Manual operation of robot
  - ⑦ Reset the moving distance

FIGURE 16: The climbing robot control software.

cables, and, for unpredictable power outage, the gravity force due to the robot dead weight should be effectively counteracted to avoid freefall. To accomplish these design objectives, electrical DC motors are used to actuate the robot system on hanger cables. The robot system employed pantograph mechanism for various cables gauges and self-locking mechanism for power outage (see Figure 17). The self-locking system was designed to prevent reverse force on the motor and to reduce falling acceleration during power outage. A simple gear system is used, which consists of differential gears including worm and pinion gears and worm wheels attached to disk dampers [55, 56].

**4.1.2. Cable-Stayed Bridge Robot.** For cable-stayed bridges, the climbing robot subsystem was designed for two important design objectives. First, the robot should have enough climbing force to climb inclined stay cables. The other is that the climbing robot should be able to excite a stay cable to test cable dampers, whose dynamic response is separately measured with accelerometers installed on stay cables. Therefore, the actuation system of the climbing robot consists of two modules: (i) climbing actuation module and

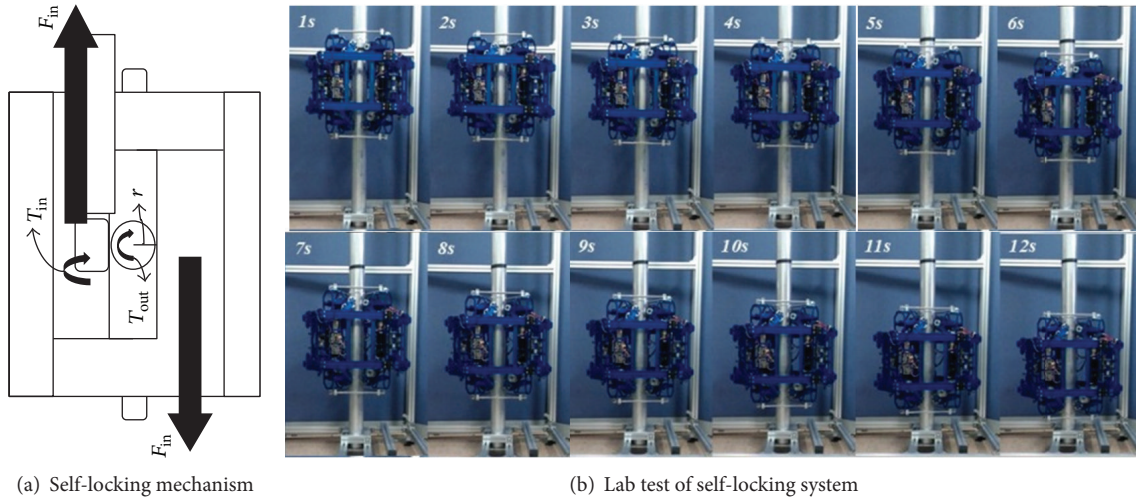


FIGURE 17: The climbing robot unit and self-locking mechanism for vertical hanger cables in suspension bridges [55].

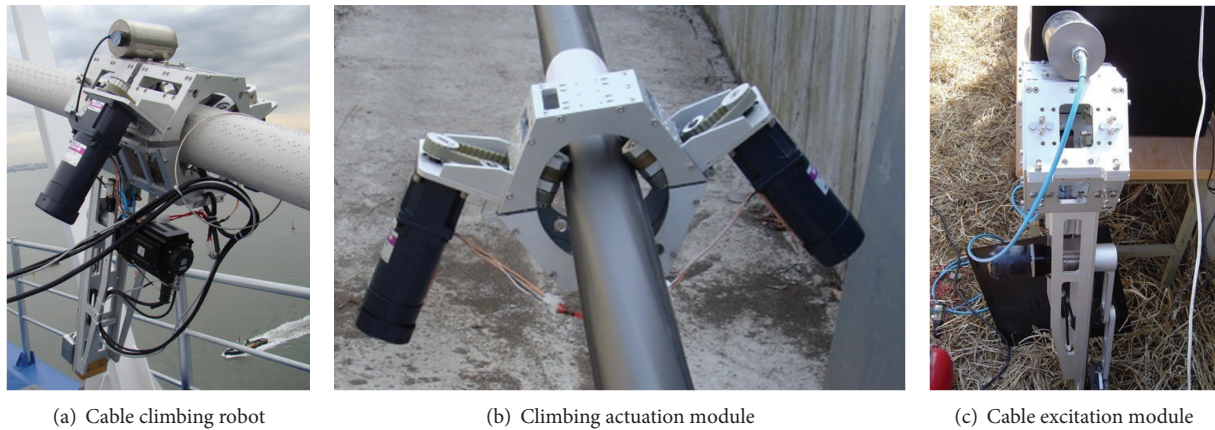


FIGURE 18: Cable climbing robot for stay cable inspection.

(ii) cable excitation module (see Figure 18(a)) [57]. The climbing actuation module has two electric motors to climb the robot unit on stay cables (see Figure 18(b)). The cable excitation module consists of a cable exciter associated with a pneumatic fixation device for the secure grip of the robot unit during cable vibration (see Figure 18(c)).

Urethane wheels are used for fast movement on stay cables with improving friction and reducing cable surface damage during inspection (see Figure 19(a)). The wheel assembly consists of the wheels attached to springs and spacers inside the outer frame for adaptation to various cable gauges. A control box is located at the bottom of the robot for posture stability during movement (see Figure 19(b)).

**4.2. Magnetic Sensing Module of NDT Subsystem.** The magnetic sensor head in the NDT subsystem consists of two modules, including (i) the magnetization module to generate a magnetic flux field and (ii) the sensing module to measure magnetic flux leakage caused by the presence of inner wire defects. The magnetic head is contained in an aluminum

case with the dimensions of  $W 195 \text{ mm} \times H 195 \text{ mm} \times L 320 \text{ mm}$ . The inner diameter of the casing is designed for steel cables with up to 85 mm diameter (see Figure 20(a)). The magnetization module generates a uniform magnetic field around a cable with a pair of yokes consisting of four high strength Nd-Fe-B permanent magnets (neodymium 35) and a plate of carbon steel (see Figures 20(b) and 20(c)).

The sensing module has two types of sensors, including Hall effect sensors and coil sensors (see Figure 21). The Hall effect sensors have 14 channels arranged around a bridge cable to detect LF, such as inner wire breakage. The coil sensors have 2 channels to measure a total magnetic flux that is necessary information to calculate LMA. These sensors are connected to an on-board data acquisition system in the control box.

A series of laboratory tests were carried out to verify the magnetic sensor performance. Cable specimens with the diameter of 76 mm and length of 2 m had nineteen 7-wire strands contained in a PVC pipe (see Figure 22).

Five damaged cases were tested by cutting strands at different locations to simulate LF. Figure 23 shows magnetic flux signals measured using seven Hall effect sensors. The

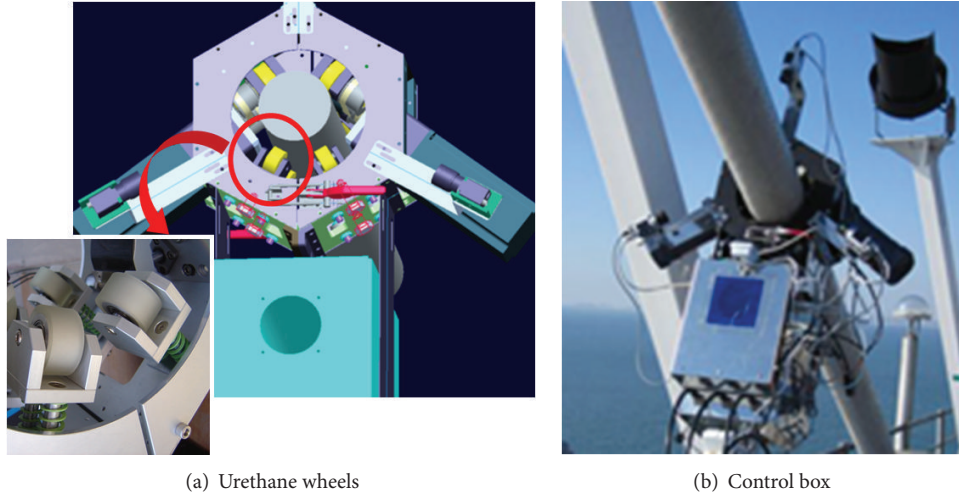


FIGURE 19: The cable climbing robot for stay cables in cable-stayed bridges.

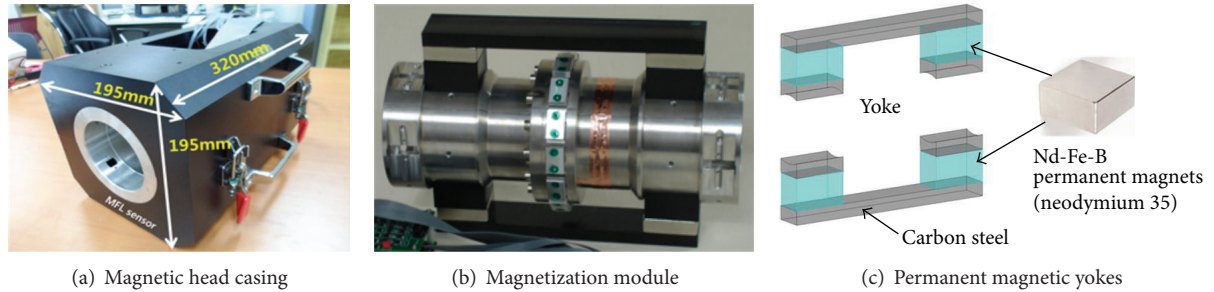


FIGURE 20: Magnetization module of the magnetic sensor.

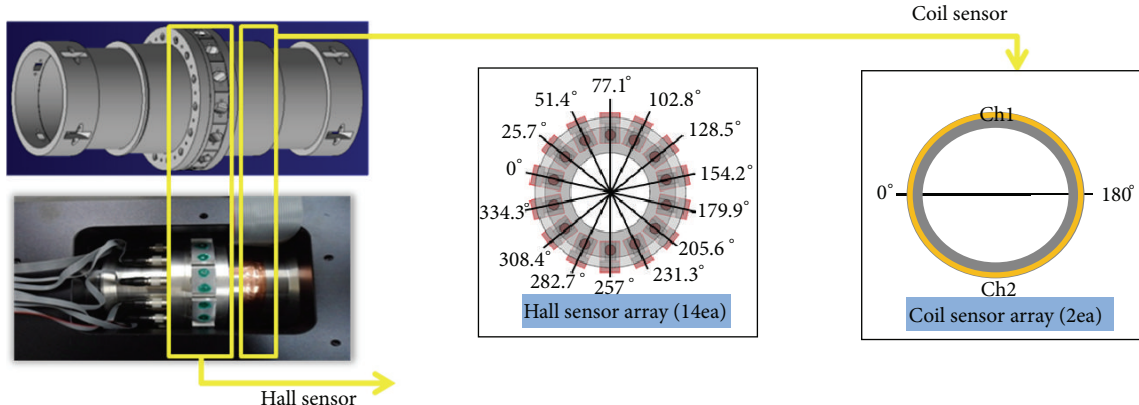


FIGURE 21: Sensing module of the magnetic sensor.

test result shows that the sensor magnitude is proportional to the proximity to damage location. Once the raw data were collected using the MFL sensors, the data were processed in the following procedures: (i) low pass filtering was applied to remove high frequency contents; (ii) a threshold was determined for the signal magnitude of Hall effect sensors through calibration using a laboratory mock-up test setup; (iii) LF locations were identified through visualization of contour mapping of the processed MFL data with respect

to the threshold on the cable cross section (see Figure 24). Once the laboratory tests were conducted, the MFL sensor was applied to field tests on the Seohae Grand Bridge in Korea. The measured magnetic flux along the cables showed no significant fluctuation, and this means there is no abrupt change in the test cables.

**4.3. Image Processing-Based Sensing Module of NDT Subsystem.** The image processing-based sensing module consists of

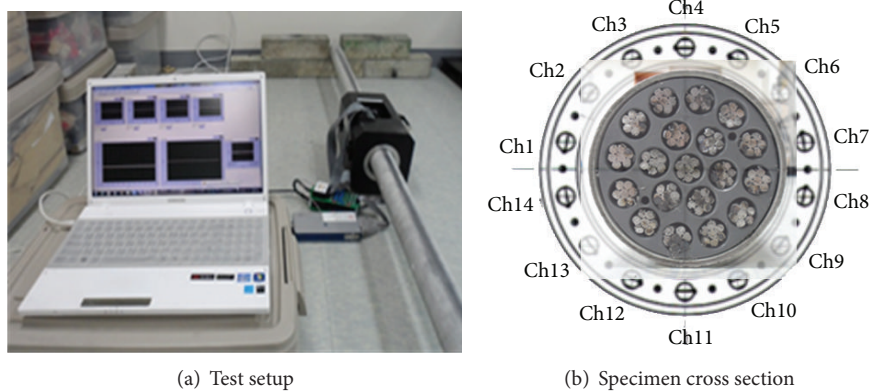


FIGURE 22: Laboratory tests of the magnetic sensor performance.

TABLE 3: Parameters used in the image-processing tests.

Parameters	Type I	Type II	Type III
Structuring element shape	Line	Line	Line
Structuring element size	5 (pixels)	10 (pixels)	5 (pixels)
Structuring element orientation	[0° 45° 90° 135°]	[0° 45° 90° 135°]	[0° 45° 90° 135°]
Binary threshold	—	—	Otsu's filter
Crack connection (pixel)	20	20	20
Length threshold before connection (pixel)	40	70	—
Length threshold after connection (pixel)	60	70	—
Area threshold before connection (pixel)	30	100	10
Area threshold after connection (pixel)	40	100	—
Eccentricity threshold (pixel)	—	—	0.958

three ruggedized cameras around a cable to collect digital images on cable surface (see Figure 25). The module collects raw cable surface images as the climbing robot moves on a bridge cable. The module has a high-speed wireless modem to transmit collected digital images to the server computer with the control and analysis subsystem.

A morphological technique-based image-processing algorithm was developed to detect crack-like defects on cable surface. The algorithm has several steps, including (i) morphological operation, (ii) image binarization, (iii) image segmentation, and (iv) noise filtering. The procedures of the image-processing algorithm are shown in Figure 26.

To detect crack-like cable surface defects, the morphological operation developed by Jahanshahi et al. was employed [58]:

$$T = \max [(I \circ S_{\{0^\circ, 45^\circ, 90^\circ, 135^\circ\}}) \cdot S_{\{0^\circ, 45^\circ, 90^\circ, 135^\circ\}}, I] - I, \quad (3)$$

where  $I$  is the original grayscale image of the cable surface;  $S$  is the structuring element that defines which neighboring pixels to be included in each morphological operation;  $\circ$  is the morphological opening;  $\cdot$  is the morphological closing;  $T$  is the grayscale processed image. To detect linear defects (i.e., cracks), a line pixel element was chosen as the structural element [58]. Since cracks on cable surface can have any orientation, the line-shape structuring element with four angles of 0°, 45°, 90°, and 135° was used during the morphological operation.

After the morphological operation, the output grayscale image was processed to binarize into black (i.e., cracks) and

white (i.e., background). The Otsu threshold method was applied in the binarization process based on pixel interclass variance maximal [59].

After the binarization, the cable image is separated into crack pixels and background pixels. In this binarization image, however, no topological connectivity is established among the pixels. Thus, segmentation was conducted based on the connectivity of eight neighboring pixels of a crack pixel to determine which crack pixels belong to which cracks.

After the segmentation, noisy cracks were filtered out based on the three geometrical properties of segmented cracks, including crack area, maximum crack length, and crack eccentricity. Here, the crack eccentricity is 0 for a circle and 1 for a straight line.

A series of laboratory tests were conducted using three types of bridge cables to evaluate applicability of the image-processing algorithm for various cable inspection conditions: regular cable (type I), cable wound with a spiral wire (type II), and dimpled cable (type III) (see Figure 27). Lines were marked with a black pen at various orientations to simulate crack-like defects on a mock-up test cable.

The image-processing algorithm was applied to the test images. Crack-like marks on different cable types were accurately identified, and sample test results are shown in Figure 28. The detected defects are shown in red pixels in green boxes. The parameters used in the image processing-based crack detection algorithm are summarized in Table 3. Tests on the real bridge cables are being carried out currently.

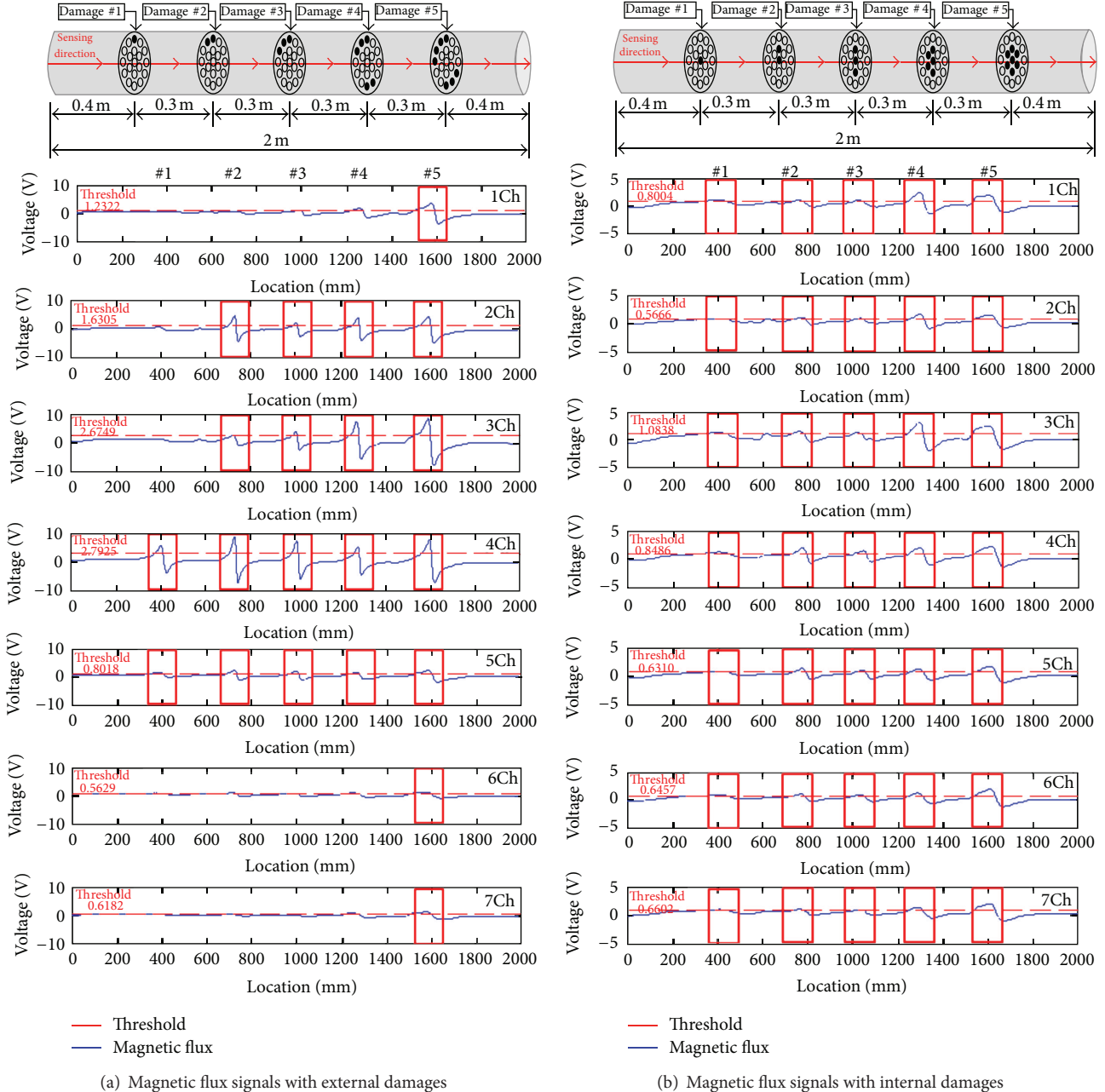


FIGURE 23: Test results of magnetic flux signals collected with the Hall effect sensors.

## 5. Conclusion

This paper presented an overview on current bridge cable inspection practices and the cable inspection robot developed in Korea. Two types of robot systems have been developed for inclined cables in cable-stayed bridges and vertical hanger ropes in suspension bridges. The hardware of the cable inspection robots has the following unique features.

- (i) The maximum cable diameters are 90 mm and 300 mm, and the maximum payloads are 25 kg and 45 kg for hanger ropes and stay cables, respectively.

- (ii) The robot is controlled with and transmits sensor data to the control system through wireless communication.
- (iii) Self-locking system is designed to prevent reverse force on the motor and dissipate freefalling force for unpredicted power outage.

The cable inspection robot system was tested in laboratory and field experiments to detect inner wire defects using a magnetic sensor and surface cable defects of bridge cables

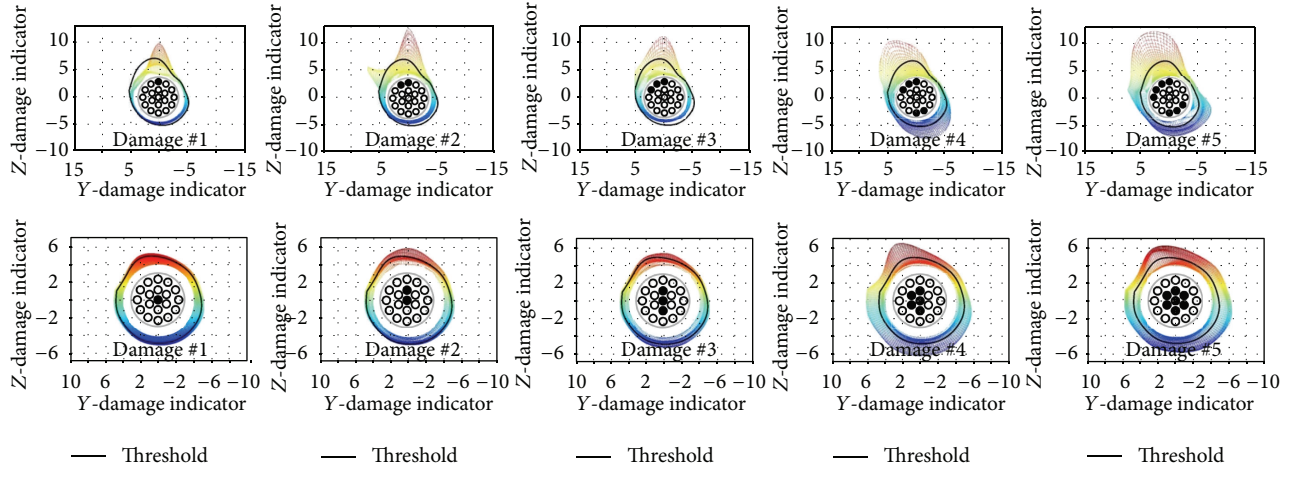


FIGURE 24: Visualized cross sections with threshold level.

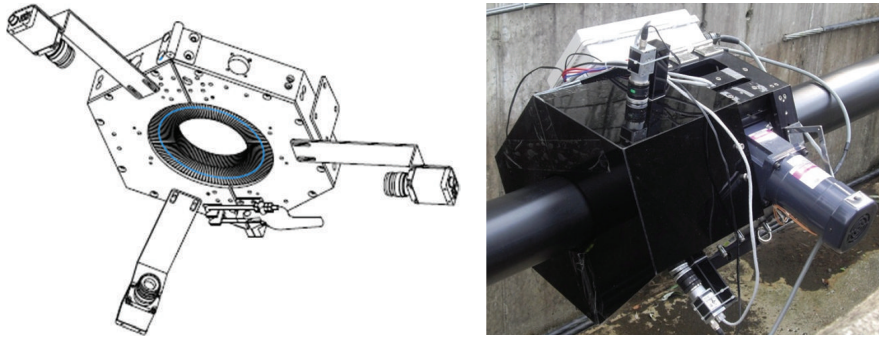
(a) Three cameras in the image processing-based sensing module  
(b) Image processing-based sensing unit mounted to the climbing robot

FIGURE 25: Image processing-based sensing module.

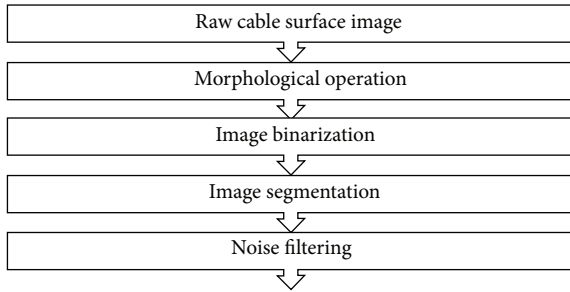


FIGURE 26: Morphological technique-based crack detection algorithm on cable surface.

using an image processing-based sensing. The following results were observed from NDT tests.

- (i) The magnetic sensors can be used to detect inner wire breakage by measuring magnetic flux change using the combination of two sensors, including 14-channel Hall effect sensors and two-channel coil sensors.
- (ii) The magnetic sensor module was packaged in a ruggedized aluminum case of  $W\ 195\text{ mm} \times H\ 195\text{ mm} \times L\ 320\text{ mm}$ . The total weight of the magnetic sensor was less than 20 kg.



FIGURE 27: Three types of cables for lab tests: regular cable (type I), cable wound with a spiral wire (type II), and dimpled cable (type III) [16].

- (iii) The image processing-based sensors can be used to detect crack-like surface defects with various orientations on cable surface. The crack detection algorithm was experimentally validated using three cable types, including regular cables, cables wound with spiral wires, and cable with dimples.

The robotic system is currently evaluated in realistic field conditions for robot mobility, defect detectability, and field applicability. Mobility is an important design concern for fast cable inspection with irregular surface conditions with obstacles on bridge cables. Detectability of various types of inner and outer defects on bridge cables should be validated

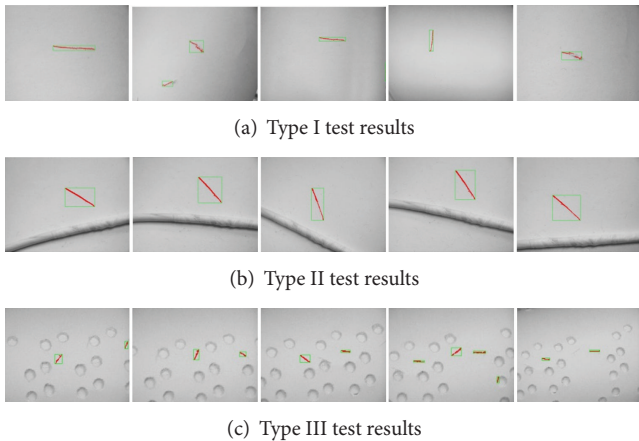


FIGURE 28: Image-processing test results to detect crack-like defects on different cable types.

under realistic field conditions. The bridge inspection robot should be applicable to various field conditions.

## Acknowledgments

This study was supported by the Korea Ministry of Land, Infrastructure and Transport (MOLIT) through Core Research Project 4 of the Super Long Span Bridge R&D Center (08 CTIP-E01). This study was also partially supported by U.S. National Science Foundation (no. 16206032). The authors declare that there is no conflict of interests regarding the publication of this paper.

## References

- [1] Emirates Authority for Standards and Metrology, “Cranes and lifting appliances. Selection of wire ropes—part 1: general,” UAE.S GSO ISO, 4308-1:2007, 2007.
- [2] H. Tabatabai, *Inspection and Maintenance of Bridge Stay Cable Systems: A Synthesis of Highway Practice*, vol. 353 of NCHRP Synthesis, Transportation Research Board, Washington, DC, USA, 2005.
- [3] American Association of State Highway and Transportation Officials, *AASHTO Manual for Bridge Evaluation*, AASHTO, 2011.
- [4] M. E. Elliott and E. Heymsfield, “Inspection of luling bridge cable stays: case study,” *Journal of Construction Engineering and Management*, vol. 129, no. 2, pp. 226–230, 2003.
- [5] Burgess & Nippe, *Creates Custom Device for Florida Cable-Stay Inspection*, Burgess & Nippe, Columbus, Ohio, USA, 2005.
- [6] Texas Department of Transportation, *Bridge Inspection Manual*, 2012.
- [7] Daewoo Institute of Construction Technology, “Trend of super long-span bridge,” *Technical Magazine*, vol. 498, 2008.
- [8] American Association of State Highway and Transportation Officials, *AASHTO Manual for Maintenance Inspection of Bridges*, AASHTO, Washington, DC, USA, 1970.
- [9] K. Kim, S. Lee, and H. Kim, “A case study of damage, fix and reinforcement about bridge cable,” *KISTEC*, vol. 31, pp. 6–67, 2008.
- [10] K.-Y. Wong, “Design of a structural health monitoring system for long-span bridges,” *Structure and Infrastructure Engineering*, vol. 3, no. 2, pp. 169–185, 2007.
- [11] Express and Transportation Research Institution, “Development of Monitoring-Based Maintenance Systems for Cable-Supported Bridges,” 2011.
- [12] V. Sukhorukov, D. Sukhorukov, D. Slesarev, and A. Mironenko, “Nondestructive testing of bridge stay cables,” in *Proceedings of the NDE-NDT for Highways and Bridges: Structural Materials Technology Conference*, pp. 347–352, 2012.
- [13] G. S. Park and E. S. Park, “Improvement of the sensor system in magnetic flux leakage-type nondestructive testing (NDT),” *IEEE Transactions on Magnetics*, vol. 38, no. 2, pp. 1277–1280, 2002.
- [14] F. Xu, X. Wang, and L. Wang, “Cable inspection robot for cable-stayed bridges: design, analysis, and application,” *Journal of Field Robotics*, vol. 28, no. 3, pp. 441–459, 2011.
- [15] K. Mandal and D. L. Atherton, “A study of magnetic flux-leakage signals,” *Journal of Physics D*, vol. 31, no. 22, pp. 3211–3217, 1998.
- [16] H. N. Ho, K. D. Kim, Y. S. Park, and J. J. Lee, “An efficient image-based damage detection for cable surface in cable-stayed bridges,” *NDT & E International*, vol. 58, pp. 18–23, 2013.
- [17] J. R. Casas, “A combined method for measuring cable forces: the cable-stayed alamillo bridge, Spain,” *Structural Engineering International*, vol. 4, no. 4, pp. 235–240, 1994.
- [18] H. Zui, T. Shinke, and Y. Namita, “Practical formulas for estimation of cable tension by vibration method,” *Journal of Structural Engineering*, vol. 122, no. 6, pp. 651–656, 1996.
- [19] S. Cho, J. P. Lynch, J.-J. Lee, and C.-B. Yun, “Development of an automated wireless tension force estimation system for cable-stayed bridges,” *Journal of Intelligent Material Systems and Structures*, vol. 21, no. 3, pp. 361–376, 2010.
- [20] WINS, <http://www.wins-ndt.com/>.
- [21] R. A. Hartle, T. W. Ryan, J. E. Mann, L. J. Danovich, W. B. Sosko, and J. W. Bouscher, *Bridge Inspector’s Reference Manual*, U.S. Department of Transportation Federal Highway Administration, 2002.
- [22] C. Desimone, P. Katchadjian, M. Tacchia, and R. Giacchetta, “Damage detection on wires of ropes applying ultrasonic waves,” in *Proceedings of the 10th Asia-Pacific Conference on Non-Destructive Testing*, 2001.
- [23] H. Tabatabai, A. Mehrabi, and A. G. Davis, “Field testing of stay cables for the cochrane bridge in Mobile, Alabama,” Tech. Rep., A.G. Lichtenstein, Inc., 1998.
- [24] A. T. Ciolko and W. P. Yen, “An immediate payoff from FHWA’s NDE initiative,” *Public Roads*, vol. 62, no. 6, pp. 10–17, 1999.
- [25] J. W. Kim, J. H. Lee, C. Lee, S. Park, D. J. Kim, and J. J. Lee, “Local damage evaluation technique using elasto-magnetic sensors operated on a cable climbing robot,” *Advanced Science Letters*, vol. 13, no. 1, pp. 105–109, 2012.
- [26] M. L. Wang, G. Wang, and Y. Zhao, “Application of EM stress sensors in large steel cables,” in *Sensing Issues in Civil Structural Health Monitoring*, pp. 145–154, Springer, Dordrecht, The Netherlands, 2005.
- [27] S. Park, J. W. Kim, M. J. Nam, and J. J. Lee, “Magnetic flux leakage sensing-based steel cable NDE technique incorporated on a cable climbing robot for bridge structures,” *Advances in Science and Technology*, vol. 83, pp. 217–222, 2013.
- [28] J. Tao, Q. Peiwen, and T. Zhengsu, “Magnetic flux leakage device for offshore oil pipeline defect inspection,” *Materials Performance*, vol. 44, no. 10, pp. 48–51, 2005.

- [29] K. Miya, "Recent advancement of electromagnetic nondestructive inspection technology in Japan," *IEEE Transactions on Magnetics*, vol. 38, no. 2, pp. 321–326, 2002.
- [30] R. Christen, A. Bergamini, and M. Motavalli, "Three-dimensional localization of defects in stay cables using magnetic flux leakage methods," *Journal of Nondestructive Evaluation*, vol. 22, no. 3, pp. 93–101, 2003.
- [31] R. Maldonado-Lopez and R. Christen, "Position-controlled data acquisition embedded system for magnetic NDE of bridge stay cables," *Sensors*, vol. 11, no. 1, pp. 162–179, 2011.
- [32] INTRON PLUS, Ltd., <http://www.intron-plus.com/>.
- [33] DMT, 2013, <http://www.dmt.de/>.
- [34] HEATH & SHERWOOD, 2013, <http://www.heathandsherwood64.com/>.
- [35] NDT Technologies, 2013, <http://www.ndttech.com/>.
- [36] A. Haller, "Wire cable testing using high resolution magnetic induction August Haller," *NDTnet*, vol. 3, no. 2, 1998.
- [37] G. Brandt, Dr. Brandt GmbH, 2013, <http://www.dr-brandt-gmbh.de/>.
- [38] E. Kündig AG, 2013, <http://www.en.kuendigag.ch/>.
- [39] LLOYDS BEAL, 2013, <http://www.lloydsbeal.co.uk/>.
- [40] Laboratory LRM dr eng. Roman Martyna, 2013, <http://www.lrm-nde.com/>.
- [41] V. Sukhorukov, "Steel wire rope inspection: new instruments," in *Proceedings of the 7th European Conference on Non-Destructive Testing*, 1998.
- [42] J. M. Nussbaum, "Detection of broken wires using a high resolution magnetic test method," in *Proceedings of the OIPEEC Technical Meeting "The Non-Destructive Testing of Rope"*, vol. 80, pp. 129–141, 1999, ODN 0688.
- [43] G. F. Pla-Rucki and M. O. Eberhard, "Imaging of reinforced concrete: state-of-the-art review," *Journal of Infrastructure Systems*, vol. 1, no. 2, pp. 134–141, 1995.
- [44] J. Li, X. Liu, S. Jiang, R. Li, and L. Ren, "Design of continuous climbing pneumatic cable maintenance robot," in *Proceedings of the IEEE International Conference on Mechatronics and Automation (ICMA '09)*, pp. 4633–4637, August 2009.
- [45] B. Yazdani, M. N. Ahmadabadi, A. Harati, H. Moaveni, and N. Soltani, "Design and development of a pole climbing robot mechanism," in *Proceedings of the IEEE International Conference on Mechatronics and Robotics*, pp. 575–580, 2004.
- [46] T. Yukawa, M. Suzuki, Y. Satoh, and H. Okano, "Magnetic part design of pipe-surface inspection robot," in *Proceedings of the 32nd Annual Conference on IEEE Industrial Electronics (IECON '06)*, pp. 3957–3962, November 2006.
- [47] ALPIN TECHNIK LEIPZIG, 2013, <http://www.alpinteknik.de/>.
- [48] J. Xu, X. Wu, and Y. Kang, "An instrument for detecting corrosion in anchorage zones of parallel wire cables using guided waves," in *Proceedings of the 18th World Conference on Non-destructive Testing*, pp. 16–20, April 2012.
- [49] M. Tavakoli, M. R. Zakerzadeh, G. R. Vossoughi, and S. Bagheri, "A hybrid pole climbing and manipulating robot with minimum DOFs for construction and service applications," *Industrial Robot*, vol. 32, no. 2, pp. 171–178, 2005.
- [50] J. Luo, S. Xie, and Z. Gong, "Cable maintenance robot and its dynamic response moving on the horizontal cable," in *Proceedings of the 12th International Conference on Advanced Robotics (ICAR '05)*, pp. 514–517, July 2005.
- [51] Hans Tiefenbach GmbH, 2013, <http://www.hanstiefenbach.de/>.
- [52] J. Sawada, K. Kusumoto, Y. Maikawa, T. Munakata, and Y. Ishikawa, "A mobile robot for inspection of power transmission lines," *IEEE Transactions on Power Delivery*, vol. 6, no. 1, pp. 309–315, 1991.
- [53] F. Xu and X. Wang, "Design and experiments on a new wheel-based cable climbing robot," in *Proceedings of the IEEE/ASME International Conference on Advanced Intelligent Mechatronics (AIM '08)*, pp. 418–423, August 2008.
- [54] J. Yuan, X. Wu, Y. Kang, and A. Ben, "Research on reconfigurable robot technology for cable maintenance of cable-stayed bridges in-service," in *Proceedings of the International Conference on Mechanic Automation and Control Engineering (MACE '10)*, pp. 1019–1022, June 2010.
- [55] H. M. Kim, K. H. Cho, F. Liu, and H. Choi, "development of cable climbing robotic system for inspection of suspension bridge," in *Proceedings of the International Symposium on Automation and Robotic in Construction*, pp. 1422–1423, 2011.
- [56] H. M. Kim, K. H. Cho, Y. H. Jin, F. Liu, and H. R. Choi, "Development of a climbing robot for inspection of bridge cable," *Korea Robotics Society*, vol. 7, no. 2, pp. 83–91, 2012.
- [57] J. Lee, K. Kim, H. H. Nam, and S. Park, "A non-destructive inspection system for cables in cable bridges," *KSCE*, pp. 49–454, 2012.
- [58] M. R. Jahanshahi, S. F. Masri, C. W. Padgett, and G. S. Sukhatme, "An innovative methodology for detection and quantification of cracks through incorporation of depth perception," *Machine Vision and Applications*, vol. 24, no. 2, pp. 227–241, 2011.
- [59] N. Otsu, "A threshold selection method from gray-level histograms," *Automatica*, vol. 11, no. 285–296, pp. 23–27, 1975.

## Research Article

# A Universal Fast Algorithm for Sensitivity-Based Structural Damage Detection

**Q. W. Yang,<sup>1</sup> J. K. Liu,<sup>2</sup> C.H. Li,<sup>1</sup> and C.F. Liang<sup>1</sup>**

<sup>1</sup> Department of Civil Engineering, Shaoxing University, Shaoxing 312000, China

<sup>2</sup> Department of Mechanics, Sun Yat-Sen University, Guangzhou 510275, China

Correspondence should be addressed to Q. W. Yang; yangqiuwei79@gmail.com

Received 3 August 2013; Accepted 1 October 2013

Academic Editors: D. G. Aggelis and H. K. Chai

Copyright © 2013 Q. W. Yang et al. This is an open access article distributed under the Creative Commons Attribution License, which permits unrestricted use, distribution, and reproduction in any medium, provided the original work is properly cited.

Structural damage detection using measured response data has emerged as a new research area in civil, mechanical, and aerospace engineering communities in recent years. In this paper, a universal fast algorithm is presented for sensitivity-based structural damage detection, which can quickly improve the calculation accuracy of the existing sensitivity-based technique without any high-order sensitivity analysis or multi-iterations. The key formula of the universal fast algorithm is derived from the stiffness and flexibility matrix spectral decomposition theory. With the introduction of the key formula, the proposed method is able to quickly achieve more accurate results than that obtained by the original sensitivity-based methods, regardless of whether the damage is small or large. Three examples are used to demonstrate the feasibility and superiority of the proposed method. It has been shown that the universal fast algorithm is simple to implement and quickly gains higher accuracy over the existing sensitivity-based damage detection methods.

## 1. Introduction

Recently, many methods have been presented to identify structural damage using the changes of modal parameters, specifically, the natural frequencies (or the square root of eigenvalues) and the mode shapes (i.e., the eigenvectors). In engineering practice, only a few eigenvalues and partial mode shapes can be obtained by a modal survey for large flexible structure. Then these existing damage identification methods can be categorized by solving the incomplete measurement problem. One group includes these methods in which mode shape expansion or model reduction cannot be avoided in damage identification. Many usual methods belong to this group, such as the finite element model (FEM), updated techniques based on the residual force vector [1–6], modal strain energy change methods [7, 8], and so forth. Methods of this sort will introduce additional errors into damage detection results, because the eigenvector expansion process would introduce errors in the “expanded” eigenvectors and the model reduction process would introduce errors in the FEM. The other group involves those methods that can detect structural damage by directly using the incomplete

modal parameters without any eigenvector expansion or model reduction. The sensitivity-based techniques belong to this group, such as the eigenvalue sensitivity [9–12], the eigenvector sensitivity [13], the flexibility sensitivity [14–17], or the combined sensitivity [18–20]. These methods make use of the derivatives of modal parameters with respect to physical design variables. These sensitivity coefficients are then used to calculate changes in the parameters that would force the analysis frequencies and modes to match those measured in the test. Messina et al. proposed a damage detection method termed the multiple damage location assurance criterion (MDLAC) by using the eigenvalue sensitivity analysis [9]. Wong et al. developed an iterative method based on the general-order perturbation theory and optimization method for multiple structural damage detection [10]. Yu et al. make use of eigenvalue perturbation theory and artificial neural network to detect small structural damage [11]. Yang and Liu defined a damage localization criterion to locate structural damage firstly and then used the eigenvalue sensitivity method to obtain the damage extent [12]. Shi et al. used the eigenvector sensitivity analysis to determine the damage location firstly and then used the eigenvalue

sensitivity method to obtain the damage extent [13]. Wu and Law studied the truncated modal flexibility sensitivity with the generic parameters in the system matrices [14]. This sensitivity has again been formulated and studied for the eigenparameters of the system matrices to detect structural damage [15]. By the matrix eigendecomposition and flexibility sensitivity analysis, Yang and Liu approach the damage identification problem in a decoupled fashion: determining the number of damaged elements, localizing the damaged elements, and quantifying the damage extents [16]. Li et al. proposed a generalized flexibility sensitivity method for structural damage detection [17]. Compared with the original flexibility matrix based approach, the effect of truncating higher-order modes can be considerably reduced in their method. Wong et al. proposed a perturbation method to detect damage of a multistorey building by combining the eigenvalue sensitivity with the eigenvector sensitivity [18]. Lam et al. presented a damage localization procedure based on the eigenvalue and eigenvector sensitivity analysis [19]. Using the Neumann series expansion, Yang derived the flexibility sensitivity and developed a mixed perturbation method to identify structural damage by combining the eigenvalue sensitivity with the flexibility sensitivity [20].

The sensitivity-based damage detection techniques generally require considerable computational expense for large damage case. It has been pointed out that when the change of structural parameter is more than 15%, the second order perturbation should be taken into account [21]. As an alternative, some researches [13] have used the iteration scheme to tackle the large damage case. It is anticipated that the computational cost of these existing sensitivity methods will be very expensive for large damage case, since a higher-order approximation should be performed or an iteration scheme must be used to estimate the damage extent more precisely. To combat this drawback, a universal fast algorithm is presented in this paper that can improve the calculation accuracy of the existing sensitivity-based technique without any high-order sensitivity analysis or multi-iterations, regardless of whether the damage is small or large. The key point of the fast algorithm lies in a simple accelerated formula, which is derived from the stiffness and flexibility matrix spectral decomposition theory in [22]. As will be shown in Section 4, with the introduction of the accelerated formula, the sensitivity-based method is able to accurately and quickly quantify structural damages without high-order sensitivity analysis or multi-iterations. The presentation of this work is organized as follows. In Section 2, the basis for the sensitivity-based damage detection methods is briefly reviewed. Then a fast algorithm is developed in Section 3 to quickly improve the calculation accuracy of the sensitivity-based technique. Moreover, the source of the accelerated formula is also discussed in detail in Section 3. Three examples are used in Section 4 to show the feasibility and the superiority of the proposed method. The conclusions of this work are summarized in Section 5. In the following theoretical development, it is assumed that structural damages only reduce the system stiffness matrix and structural refined FEM has been developed before damage occurrence.

## 2. Sensitivity-Based Methods

In this section, the basis for the sensitivity-based damage detection methods is briefly reviewed. And then three existing sensitivity methods are introduced in detail, namely, the eigenvalue sensitivity, the flexibility sensitivity, and the generalized flexibility sensitivity.

Consider the analytical model of a given structure, with  $n$  degrees of freedom (DOFs), whose modes of vibration can be obtained by solving the following generalized eigenvalue problem:

$$K\phi_j = \lambda_j M\phi_j, \quad (1)$$

where  $M$  and  $K$  are the mass and stiffness matrices and  $\lambda_j$  and  $\phi_j$  are the  $j$ th eigenvalue and eigenvector, respectively. Since it is assumed that the damage can only cause change of stiffness, the global stiffness matrix  $K$  can be expressed as a function of elemental stiffness parameters, that is,

$$K = \sum_{i=1}^N K_i = K(\{p\}), \quad (\{p\} = \{p_1, p_2, \dots, p_N\}^T), \quad (2)$$

where  $K_i$  is the  $i$ th elemental stiffness matrix,  $\{p\}$  is the vector consisting of the elemental stiffness parameters  $p_i$  ( $i = 1 \sim N$ ), and  $N$  is the total number of elements. Using Taylor or Neumann series expansion and keeping the first order item, we can obtain the following linear approximation expression:

$$S\alpha = \Delta d, \quad \alpha = \left\{ \frac{\Delta p_1}{p_1}, \frac{\Delta p_2}{p_2}, \dots, \frac{\Delta p_N}{p_N} \right\}^T, \quad (3)$$

where  $S$  is the sensitivity matrix representing the first order derivation of modal data  $\{d\}$  to  $\{p\}$ ,  $\Delta d$  is the change vector of modal data,  $\alpha$  is the change of the stiffness parameters before and after damage, and  $\alpha_i = \Delta p_i / p_i$  is the  $i$ th elemental stiffness perturbed parameter (i.e., the elemental damage parameter). The value of  $\alpha_i$  is 0 if the  $i$ th element is undamaged and  $\alpha_i$  is 1 or less than 1 if the corresponding element is completely or partially damaged. From (3), one has

$$\alpha = S^+ \Delta d, \quad (4)$$

where the superscript “+” denotes the generalized inverse. Equation (4) shows that the location and extent of damage ( $\alpha$ ) can be determined only if the changes of modal parameters  $\Delta d$  are available through modal test. The main differences between the various sensitivity-based schemes are the test parameters  $\Delta d$  used in (4) and the corresponding sensitivity matrix  $S$ . In the next section, three existing sensitivity methods are introduced, which will be used to demonstrate the merits of the proposed fast method.

**2.1. The Eigenvalue Sensitivity Method.** For the eigenvalue sensitivity analysis, the eigenvalues are measured in structural modal test and used in (4) to compute the stiffness perturbed parameters. The first order derivative of the  $j$ th eigenvalue can be computed by [9–12]

$$\frac{\partial \lambda_j}{\partial p_i} = \phi_j^T \frac{\partial K}{\partial p_i} \phi_j. \quad (5)$$

Then, the eigenvalue sensitivity matrix  $S_1$  can be derived from (5) as

$$S_1 = \begin{bmatrix} \frac{\partial \lambda_1}{\partial p_1} & \frac{\partial \lambda_1}{\partial p_2} & \dots & \frac{\partial \lambda_1}{\partial p_N} \\ \frac{\partial \lambda_2}{\partial p_1} & \frac{\partial \lambda_2}{\partial p_2} & \dots & \frac{\partial \lambda_2}{\partial p_N} \\ \vdots & \vdots & \ddots & \vdots \\ \frac{\partial \lambda_m}{\partial p_1} & \frac{\partial \lambda_m}{\partial p_2} & \dots & \frac{\partial \lambda_m}{\partial p_N} \end{bmatrix}. \quad (6)$$

If  $m$  eigenvalues are available through modal test,  $\alpha$ , that is, the structural damage, can be identified by (4).

**2.2. The Flexibility Sensitivity Method.** Using Neumann series expansion, the first-order sensitivity of structural flexibility matrix can be obtained as [14–17]

$$\frac{\partial F}{\partial p_i} = FK_iF, \quad (7)$$

where  $F$  ( $F = K^{-1}$ ) is the flexibility matrix of the intact structure. Then, the first-order sensitivity equation of structural flexibility matrix for all elemental damage parameters can be established as

$$\Delta F = \sum_{i=1}^N \alpha_i \frac{\partial F}{\partial p_i}. \quad (8)$$

With mode shapes normalized to unit mass, the flexibility matrix change can be obtained approximately by a few low-frequency modes as

$$\Delta F = \sum_{j=1}^m \frac{1}{\lambda_{dj}} \phi_{dj} \phi_{dj}^T - \sum_{j=1}^m \frac{1}{\lambda_j} \phi_j \phi_j^T, \quad (9)$$

where  $\lambda_{dj}$  and  $\phi_{dj}$  are the  $j$ th eigenvalue and eigenvector of the damaged structure and  $m$  is the number of measured modes in modal survey. From (8) and (9), the unknown damage parameters  $\alpha_i$  ( $i = 1 \sim N$ ) can be readily computed by manipulating the matrix equation (8) into a set of linear equations.

**2.3. The Generalized Flexibility Sensitivity Method.** The generalized flexibility matrix  $F^g$  for a structure with  $n$  degrees of freedom is defined as

$$F^g = FMF, \quad (10)$$

where  $F$  and  $M$  are the  $(n \times n)$  flexibility and mass matrices, respectively. The first order derivative of the generalized flexibility matrix can be computed by [17]

$$\frac{\partial F^g}{\partial p_i} = FK_iFMF + FMFK_iF. \quad (11)$$

Then the sensitivity equation of the generalized flexibility matrix for all elemental damage parameters can be established as

$$\Delta F^g = \sum_{i=1}^N \alpha_i \frac{\partial F^g}{\partial p_i}, \quad (12)$$

where  $\Delta F^g$  is the change of the generalized flexibility matrix. When damage is introduced,  $\Delta F^g$  can be approximately expressed by using only a few of the lower frequency modes as

$$\Delta F^g = F_d M F_d - F M F \approx \sum_{j=1}^m \frac{1}{\lambda_{dj}^2} \phi_{dj} \phi_{dj}^T - \sum_{j=1}^m \frac{1}{\lambda_j^2} \phi_j \phi_j^T, \quad (13)$$

where  $F_d$  is the damaged stiffness matrix. From (12) and (13), the unknown damage parameters  $\alpha_i$  ( $i = 1 \sim N$ ) can be computed by manipulating the matrix equation (12) into a set of linear equations.

### 3. The Universal Fast Algorithm

As stated in Section 1, the above sensitivity techniques generally require considerable computational expense for large damage case, since a higher order approximation should be performed or an iteration scheme must be used to estimate the damage extent more precisely. In this section, a universal accelerated formula is developed to quickly improve the calculation accuracies of the above original sensitivity methods without any high-order sensitivity analysis or multi-iterations.

The fast algorithm consists of the following steps. (1) Compute the elemental damage parameters  $\alpha_i$  ( $i = 1 \sim N$ ) by any one of the existing sensitivity methods. (2) Use the universal accelerated formula to obtain the new value ( $\alpha_i^{\text{new}}$ ) of damage parameter for those elements with  $\alpha_i \geq 0.176$ . The accelerated formula is as follows:

$$\alpha_i^{\text{new}} = \frac{\alpha_i}{1 + \alpha_i}. \quad (14)$$

Then the damage extent can be assessed again from the new result  $\alpha_i^{\text{new}}$  for those elements (i.e.,  $\alpha_i^{\text{new}} = \alpha_i/(1 + \alpha_i)$  if  $\alpha_i \geq 0.176$ ). (3) For those elements with  $\alpha_i < 0.176$ , the original calculation result  $\alpha_i$  will be as the final result  $\alpha_i^{\text{new}}$  (i.e.,  $\alpha_i^{\text{new}} = \alpha_i$  if  $\alpha_i < 0.176$ ). (4) In the end, structural damages can be evaluated by the resulting  $\alpha_i^{\text{new}}$  ( $i = 1 \sim N$ ). The above steps are described in Figure 1. As will be shown in the examples in Section 4, with the introduction of the accelerated formula, structural damage extents can be quickly and accurately calculated without any high-order sensitivity analysis or multi-iterations, regardless of whether the damage is small or large.

The source of the accelerated formula (14) is illustrated as follows. In [22], the author proposed a new flexibility perturbation technique based on matrix spectral decomposition, which has a unique advantage that it can accurately compute the stiffness perturbation parameter without any higher-order sensitivity analysis or iteration. In this study, we will prove that this new flexibility perturbation method can be seen as a combination of the original flexibility sensitivity method and the above accelerated formula.

The new flexibility perturbation theory in [22] begins with the disassembly of the  $(n \times n)$  global stiffness matrix,

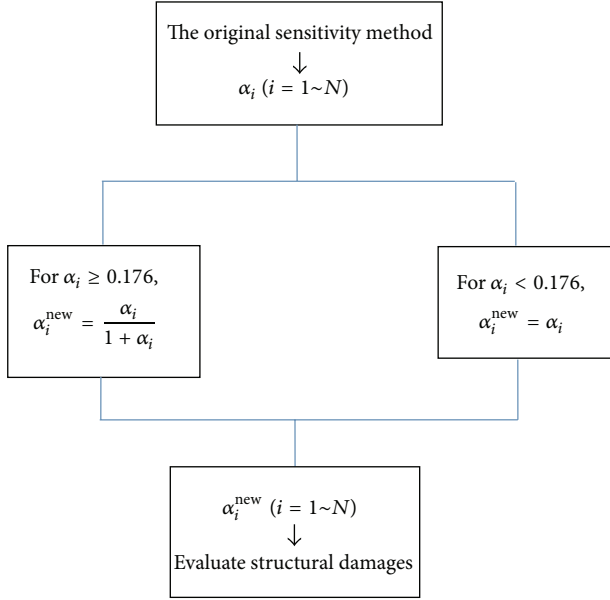


FIGURE 1: A graphical illustration of the universal fast algorithm.

which can be obtained by the spectral decomposition of each elemental stiffness matrix [15, 16]. Generally, the elemental stiffness matrix  $K_i$  is not of full rank in most cases. Without loss of generality, for convenience of the following derivation, all the ranks of elemental stiffness matrices are presumed to be 1 (other cases with the rank greater than 1 are also valid). Using the spectral decomposition, the disassembly of the undamaged global stiffness matrix can be obtained as

$$K = \sum_{i=1}^N K_i = C [p] C^T, \quad (15)$$

where

$$\begin{aligned} K_i &= c_i p_i c_i^T, \\ C &= [c_1, c_2, \dots, c_N], \end{aligned} \quad (16)$$

$$[p] = \begin{bmatrix} p_1 & p_2 & \ddots & p_N \end{bmatrix}.$$

The  $(n \times N)$  matrix  $C$  is defined as the stiffness connectivity matrix representation of the connectivity between DOFs. According to (15), it is important to note that  $N \geq n$  and the matrix  $C$  is of full rank ( $\text{rank}(C_{n \times N}) = n$ ), because  $K$  is of full rank ( $\text{rank}(K_{n \times n}) = n$ ). The matrix  $C$  is independent of  $[p]$

and unchanged as damage occurs. Then the global stiffness matrix of the damaged structure can be assembled as

$$\begin{aligned} K_d &= \sum_{i=1}^N p_i (1 - \alpha_i) K_i = C [p_d] C^T \\ [p_d] &= \begin{bmatrix} p_1 (1 - \alpha_1) & p_2 (1 - \alpha_2) & \ddots & \\ & & & p_N (1 - \alpha_N) \end{bmatrix}. \end{aligned} \quad (17)$$

For the case of  $n = N$ , the disassemblies of the  $(n \times n)$  global flexibility matrices  $F$  and  $F_d$ , for the undamaged and damaged structure, can be obtained by  $F \cdot K = F_d \cdot K_d = I_{n \times n}$  as

$$F = K^{-1} = (C^T)^{-1} [p]^{-1} C^{-1} \quad (18)$$

$$F_d = K_d^{-1} = (C^T)^{-1} [p_d]^{-1} C^{-1}. \quad (19)$$

Subtracting (18) from (19), the flexibility matrix perturbation  $\Delta F$  can be given as

$$\Delta F = (C^T)^{-1} [[p_d]^{-1} - [p]^{-1}] C^{-1}. \quad (20)$$

Equation (20) can be rewritten as

$$\Delta F = (C^T)^{-1} [p]^{-1} [\beta] C^{-1}, \quad (21)$$

where

$$[\beta] = \begin{bmatrix} \beta_1 & \beta_2 & \ddots & \\ & & & \beta_N \end{bmatrix} \quad (22)$$

$$\beta_i = \frac{\alpha_i}{1 - \alpha_i}, \quad (23)$$

where  $\beta_i$  is defined as the  $i$ th elemental flexibility perturbed parameter. According to the matrix theory, we have

$$(C^T)^{-1} [p]^{-1} = (C^T)^{-1} \cdot [p]^{-1} \cdot (C^{-1} C) = F C \quad (24)$$

$$\begin{aligned} C^{-1} &= [p] \cdot [p]^{-1} C^{-1} = [p] (C^T \cdot (C^T)^{-1}) [p]^{-1} C^{-1} \\ &= [p] C^T F. \end{aligned} \quad (25)$$

Substituting (22), (24), and (25) into (21), one has

$$\begin{aligned} \Delta F &= F C [\beta] [p] C^T F = \sum_{i=1}^N \beta_i F (c_i p_i c_i^T) F \\ &= \sum_{i=1}^N \beta_i F K_i F. \end{aligned} \quad (26)$$

Substituting (7) into (26) yields

$$\Delta F = \sum_{i=1}^N \beta_i \frac{\partial F}{\partial p_i}. \quad (27)$$

TABLE 1: Comparisons of the estimated damage parameters by the original flexibility sensitivity method and the fast algorithm (Example 1).

Damage case	Element no.	True damage reduction	Damage parameters computed by the original flexibility sensitivity method	Damage parameters computed by the universal fast algorithm
1	2	0.15	0.1765	0.15
2	2	0.8	4	0.8
3	2, 3	0.6, 0.5	1.5, 1	0.6, 0.5

TABLE 2: Damage scenarios studied in [13] (Example 2).

Case 1		Case 2		Case 3	
Element no.	Damage	Element no.	Damage	Element no.	Damage
16	30%	1	30%	7	15%
		2	20%	11	20%
				12	15%

The implication of (27) is very important. Compared with (8), (27) shows that the results obtained by (8) are not the stiffness perturbed parameters in a real sense, but the flexibility perturbed parameters. And the true stiffness perturbed parameter should be computed by using (23) as

$$\alpha_i = \frac{\beta_i}{1 + \beta_i}. \quad (28)$$

In view of the traditional sensitivity technique, (28) can be seen as an accelerated operation based on the results obtained by the original sensitivity method. Therefore, the accelerated formula (14) can be obtained by replacing  $\beta_i(\alpha_i)$  with  $\alpha_i(\alpha_i^{\text{new}})$  in (28). For the case of  $n = N$ , we can use the generalized inverse "+" instead of the inverse "-" in the above derivation and the same accelerated formula as (14) can be obtained. In addition, the critical value 0.15 in the traditional sensitivity method also changes to be 0.176 (according to (23), the new critical value is  $0.15/(1 - 0.15) = 0.176$ ).

#### 4. Numerical Examples

To illustrate the feasibility and superiority of the universal fast algorithm, three numerical examples are presented to show the improvement of the existing sensitivity methods by using the universal fast algorithm.

*Example 1.* The first example is a spring-mass system with 3 DOFs as shown in Figure 2, which is used to compare the performance of the universal fast algorithm and the original flexibility sensitivity method. Consider the nominal model of the system to have the parameters  $k_i = 1$  ( $i = 1 \sim 3$ ) and  $m_j = 1$  ( $j = 1 \sim 3$ ). Three damage cases are studied in the example. Case 1: element 2 is damaged with  $k_2 = 0.85$ . Case 2: element 2 is damaged with  $k_2 = 0.2$ . Case 3: elements 2 and 3 are damaged with  $k_2 = 0.4$  and  $k_3 = 0.5$ . Table 1 presented the results obtained by the original flexibility sensitivity method and the proposed fast algorithm. In Table 1, the results of the fast algorithm are calculated by

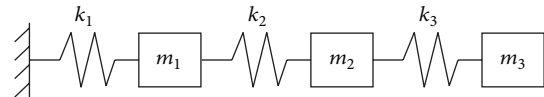


FIGURE 2: Spring-mass system (Example 1).

using (14). For example, in Table 1,  $\alpha_2^{\text{new}} = \alpha_2/(1 + \alpha_2) = 0.1765/(1 + 0.1765) = 0.15$  for damage case 1,  $\alpha_2^{\text{new}} = \alpha_2/(1 + \alpha_2) = 4/(1 + 4) = 0.8$  for damage case 2, and so on. Table 1 shows that the stiffness perturbed parameters (i.e., the damage parameters) can be exactly computed for this example by the universal fast algorithm if the complete and exact modes are given, regardless of whether the damage is small or large.

*Example 2.* The second example is the two-dimensional truss structure (shown in Figure 3) used by Shi et al. [13], which is employed to compare the performance of the universal fast algorithm and the iterative eigenvalue sensitivity method used in [13]. Three damage cases (listed in Table 2) are studied in [13]. Table 3 lists the values of damage parameters calculated by the original iterative sensitivity method in [13]. From Table 3, it is obvious that results obtained in the first iteration all have large errors compared to the true values, regardless of whether the noise is considered or not. Although more accurate results can be obtained with the iteration number increasing, the computational cost of this iterative sensitivity method is very expensive, because the sensitivity matrix must be recalculated in each iteration. Table 4 lists the results obtained by the proposed fast algorithm. The values in Table 4 are achieved by using the accelerated formula (14) on the basis of the values of the first iteration in Table 3. For example, the value 0.286 in Table 4 is obtained by  $\alpha_{16}^{\text{new}} = \alpha_{16}/(1 + \alpha_{16}) = 0.4/(1 + 0.4) = 0.286$ , the value 0.292 in Table 4 is obtained by  $\alpha_1^{\text{new}} = \alpha_1/(1 + \alpha_1) = 0.412/(1 + 0.412) = 0.292$ , and so on. The values 0.134, 0.172, and 0.154 in Table 3 are directly used as the final results in Table 4, because they are

TABLE 3: Results of the calculated damage parameters in [13] (Example 2).

Damage case	Element no.	True damage reduction	No noise			With noise		
			Iteration 1	Iteration 2	Iteration 1	Iteration 2	Iteration 3	
1	16	0.3	<b>0.400 (33.3%)</b>	0.311 (3.7%)	<b>0.482 (60.7%)</b>	0.421 (40.3%)	0.378 (26%)	
2	1	0.3	<b>0.412 (37.3%)</b>	0.317 (5.7%)	<b>0.452 (50.7%)</b>	0.342 (14%)	0.318 (6%)	
	2	0.2	<b>0.260 (30%)</b>	0.207 (3.5%)	<b>0.312 (56%)</b>	0.248 (24%)	0.241 (20.5%)	
3	7	0.15	<b>0.18 (20%)</b>	0.149 (0.7%)	<b>0.182 (21.3%)</b>	0.141 (6%)	0.140 (6.7%)	
	11	0.2	<b>0.236 (18%)</b>	0.205 (2.5%)	<b>0.172 (14%)</b>	0.194 (3%)	0.196 (2%)	
	12	0.15	<b>0.134 (10.7%)</b>	0.149 (0.7%)	<b>0.144 (4%)</b>	0.149 (0.7%)	0.147 (2%)	

\*The value in bracket denotes the comparative error between the calculated value and the true value.

TABLE 4: The results obtained by the universal fast algorithm (Example 2).

Damage case	Element no.	True damage reduction	No noise	With noise
1	16	0.3	0.286 (4.7%)↓	0.325 (8.3%)↓
2	1	0.3	0.292 (2.7%)↓	0.311 (3.7%)↓
	2	0.2	0.206 (3%)↓	0.238 (19%)↓
3	7	0.15	0.153 (2%)↓	0.154 (2.7%)↓
	11	0.2	0.191 (4.5%)↓	<b>0.172 (14%)</b>
	12	0.15	<b>0.134 (10.7%)</b>	<b>0.144 (4%)</b>

\*The value in bracket denotes the comparative error between the calculated value and the true value. “↓” denotes the decrease in error.

TABLE 5: Comparisons of the estimated damage parameters by the original generalized flexibility sensitivity method and the fast algorithm (Example 3).

Element no.	True damage reduction	Damage parameters obtained in [17]	Damage parameters computed by the universal fast algorithm
2	0.15	0.1777 (18%)	0.1509 (0.6%)↓
11	0.2	0.2564 (28.2%)	0.2041 (2.1%)↓
19	0.1	0.1120 (12%)	0.1120 (12%)

\*The value in bracket denotes the comparative error between the calculated value and the true value. “↓” denotes the decrease in error.

all less than 0.176. From Table 4, one can see that the result obtained by the proposed method is more accurate than the results in Table 3 achieved by the iterative sensitivity method after three iterations. It can be seen from Tables 3 and 4 that the results of the presented method have equivalent accuracy to that of the iterative scheme after two or three iterations. It has been shown that the proposed method can achieve satisfactory results without any higher-order approximation or multi-iterations.

*Example 3.* The third example is a simple supported beam (shown in Figure 4) used by Li et al. in [17], which is used to compare the performance of the universal fast algorithm and the generalized flexibility sensitivity method. In [17], multiple damages are simulated in elements 2, 11, and 19 with stiffness losses of 15%, 20%, and 10%, respectively. Results computed by the original generalized flexibility sensitivity method in [17] are listed in Table 5. Using the accelerated formula, results obtained by the universal fast algorithm are also listed in

Table 5 for comparison. As before, the new damage parameter  $\alpha_i^{\text{new}}$  is calculated by (14). For example, in Table 5,  $\alpha_2^{\text{new}} = \alpha_2 / (1 + \alpha_2) = 0.1777 / (1 + 0.1777) = 0.1509$ . It can be concluded from Table 5 that the universal fast algorithm can achieve more accurate results than that obtained by the original generalized flexibility sensitivity method.

## 5. Conclusions

A universal fast algorithm for sensitivity-based structural damage detection has been developed in this study, which can improve the calculation accuracy of the sensitivity-based technique without any high-order sensitivity analysis or multi-iterations, regardless of whether the damage is small or large. The key point of the fast algorithm lies in a simple accelerated formula, which is derived from the stiffness and flexibility matrix spectral decomposition theory. Three examples are used to exercise this process and measurement

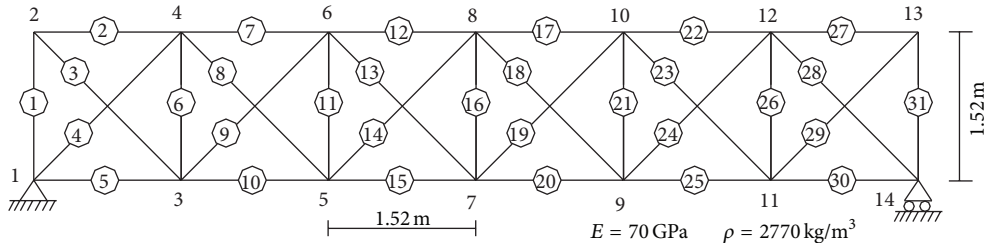


FIGURE 3: Thirty-one-bar truss structure (Example 2).

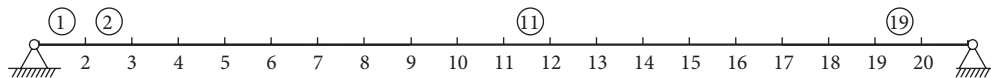


FIGURE 4: A simple supported beam (Example 3).

noise is also simulated in damage detection. The results show the superiority of the proposed method over the original sensitivity-based methods in the identification of structural damages. It has been shown that the proposed procedure may be a promising method in structural damage detection.

## Acknowledgments

This work is supported by National Natural Science Foundation of China (nos. 11202138 and 11272361) and Zhejiang Province Natural Science Foundation (no. Y1110949).

## References

- [1] J.-C. Chen and J. A. Carba, "On-orbit damage assessment for large space structures," *AIAA Journal*, vol. 26, no. 9, pp. 1119–1126, 1988.
- [2] D. C. Zimmerman and M. Kaouk, "Structural damage detection using a minimum rank update theory," *Journal of Vibration and Acoustics*, vol. 116, no. 2, pp. 222–231, 1994.
- [3] S. W. Doebling, "Minimum-rank optimal update of elemental stiffness parameters for structural damage identification," *AIAA Journal*, vol. 34, no. 12, pp. 2615–2621, 1996.
- [4] J. K. Liu and Q. W. Yang, "A new structural damage identification method," *Journal of Sound and Vibration*, vol. 297, no. 3–5, pp. 694–703, 2006.
- [5] Q. W. Yang and J. K. Liu, "Structural damage identification based on residual force vector," *Journal of Sound and Vibration*, vol. 305, no. 1–2, pp. 298–307, 2007.
- [6] G. James, D. Zimmerman, and T. Cao, "Development of a coupled approach for structural damage detection with incomplete measurements," *AIAA Journal*, vol. 36, no. 12, pp. 2209–2217, 1998.
- [7] Z. Y. Shi, S. S. Law, and L. M. Zhang, "Structural damage localization from modal strain energy change," *Journal of Sound and Vibration*, vol. 218, no. 5, pp. 825–844, 1998.
- [8] Z. Y. Shi, S. S. Law, and L. M. Zhang, "Structural damage detection from modal strain energy change," *Journal of Engineering Mechanics*, vol. 126, no. 12, pp. 1216–1223, 2000.
- [9] A. Messina, E. J. Williams, and T. Contursi, "Structural damage detection by a sensitivity and statistical-based method," *Journal of Sound and Vibration*, vol. 216, no. 5, pp. 791–808, 1998.
- [10] C. N. Wong, W. D. Zhu, and G. Y. Xu, "On an iterative general-order perturbation method for multiple structural damage detection," *Journal of Sound and Vibration*, vol. 273, no. 1–2, pp. 363–386, 2004.
- [11] L. Yu, L. Cheng, L. H. Yam, and Y. J. Yan, "Application of eigenvalue perturbation theory for detecting small structural damage using dynamic responses," *Composite Structures*, vol. 78, no. 3, pp. 402–409, 2007.
- [12] Q. W. Yang and J. K. Liu, "A coupled method for structural damage identification," *Journal of Sound and Vibration*, vol. 296, no. 1–2, pp. 401–405, 2006.
- [13] Z. Y. Shi, S. S. Law, and L. M. Zhang, "Damage localization by directly using incomplete mode shapes," *Journal of Engineering Mechanics*, vol. 126, no. 6, pp. 656–660, 2000.
- [14] D. Wu and S. S. Law, "Model error correction from truncated modal flexibility sensitivity and generic parameters—part I: simulation," *Mechanical Systems and Signal Processing*, vol. 18, no. 6, pp. 1381–1399, 2004.
- [15] W. Di and S. S. Law, "Eigen-parameter decomposition of element matrices for structural damage detection," *Engineering Structures*, vol. 29, no. 4, pp. 519–528, 2007.
- [16] Q. W. Yang and J. K. Liu, "Damage identification by the eigenparameter decomposition of structural flexibility change," *International Journal for Numerical Methods in Engineering*, vol. 78, no. 4, pp. 444–459, 2009.
- [17] J. Li, B. Wu, Q. C. Zeng, and C. W. Lim, "A generalized flexibility matrix based approach for structural damage detection," *Journal of Sound and Vibration*, vol. 329, no. 22, pp. 4583–4587, 2010.
- [18] C. N. Wong, J. C. Chen, and W. M. To, "Perturbation method for structural damage detection of multi-storey buildings," in *Proceedings of the International Conference on Structural Dynamics, Vibration, Noise and Control*, 1995.
- [19] H. F. Lam, J. M. Ko, and C. W. Wong, "Localization of damaged structural connections based on experimental modal and sensitivity analysis," *Journal of Sound and Vibration*, vol. 210, no. 1, pp. 91–115, 1998.

- [20] Q. W. Yang, "A mixed sensitivity method for structural damage detection," *Communications in Numerical Methods in Engineering*, vol. 25, no. 4, pp. 381–389, 2009.
- [21] S. H. Chen, *Matrix Perturbation Theory in Structure Dynamics*, International Academic Publishers, 1993.
- [22] Q. W. Yang, "A new damage identification method based on structural flexibility disassembly," *Journal of Vibration and Control*, vol. 17, no. 7, pp. 1000–1008, 2011.

## Research Article

# Detecting the Activation of a Self-Healing Mechanism in Concrete by Acoustic Emission and Digital Image Correlation

E. Tsangouri,<sup>1,2</sup> D. G. Aggelis,<sup>1</sup> K. Van Tittelboom,<sup>3</sup> N. De Belie,<sup>3</sup> and D. Van Hemelrijck<sup>1</sup>

<sup>1</sup> Department of Mechanics of Materials and Constructions, Vrije Universiteit Brussel, Pleinlaan 2, 1050 Brussels, Belgium

<sup>2</sup> SIM vzw—Program SHE, Technologiepark 935, 9052 Zwijnaarde, Belgium

<sup>3</sup> Magneil Laboratory for Concrete Research, Department of Structural Engineering, Faculty of Engineering, Ghent University, Technologiepark Zwijnaarde 904, 9052 Ghent, Belgium

Correspondence should be addressed to D. Van Hemelrijck; danny.van.hemelrijck@vub.ac.be

Received 8 September 2013; Accepted 29 October 2013

Academic Editors: R. Feng, T. Pan, and S.-Q. Yang

Copyright © 2013 E. Tsangouri et al. This is an open access article distributed under the Creative Commons Attribution License, which permits unrestricted use, distribution, and reproduction in any medium, provided the original work is properly cited.

Autonomous crack healing in concrete is obtained when encapsulated healing agent is embedded into the material. Cracking damage in concrete elements ruptures the capsules and activates the healing process by healing agent release. Previously, the strength and stiffness recovery as well as the sealing efficiency after autonomous crack repair was well established. However, the mechanisms that trigger capsule breakage remain unknown. In parallel, the conditions under which the crack interacts with embedded capsules stay black-box. In this research, an experimental approach implementing an advanced optical and acoustic method sets up scopes to monitor and justify the crack formation and capsule breakage of concrete samples tested under three-point bending. Digital Image Correlation was used to visualize the crack opening. The optical information was the basis for an extensive and analytical study of the damage by Acoustic Emission analysis. The influence of embedding capsules on the concrete fracture process, the location of capsule damage, and the differentiation between emissions due to capsule rupture and crack formation are presented in this research. A profound observation of the capsules performance provides a clear view of the healing activation process.

## 1. Introduction

The use of expansive healing agents encapsulated into tubular capsules and actuated when damage occurs, appears to be one of the most promising autonomous healing systems in concrete research [1]. Van Tittelboom studied in detail different healing agents and encapsulation approaches and selected tubular glass capsules placed in couples filled with a two-component polyurethane-based healing agent and embedded into concrete elements. In more details, the healing mechanism is activated when crack formation ruptures the pairs of glass capsules and the two-component healing agent is released filling the crack volume. The polyurethane healing agent polymerizes when both agents come into contact. After a few hours of curing the intended repair is achieved [2].

Recently, the mechanical performance of the aforementioned smart material was investigated under different dam-

age and loading conditions [2]. The recovery of cracked areas is confirmed under bending. In one of those studies, Acoustic Emission (AE) confirmed capsule breakage and was used to monitor crack formation and repair during two cycles of bending tests [3].

Preliminary results of our research on the Self-healing (SH) performance under bending load seemed promising [4], although obtaining accurate analyses on such a complicated material remains challenging. A clear indication of cracking damage and distinction from capsule fracture are required. Furthermore, profound analysis of the conditions under which SH activation occurs will improve the material manufacturing process. In this study, an attempt was made to monitor by optical and acoustic techniques the capsules performance during crack formation. The obtained results focus on the trigger mechanism of healing while the mechanical performance of the smart material system is also important.

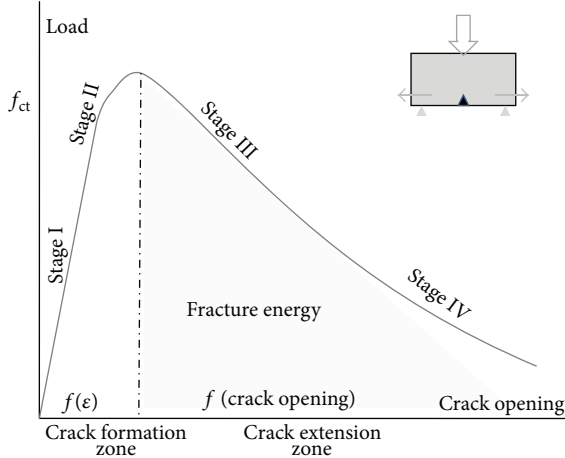


FIGURE 1: Fracture model of three-point bending crack opening test.

## 2. Three-Point Bending Damage

The study of materials damage, namely, fracture mechanics, provides analytical and experimental approaches in order to understand and prevent failure. Complicated multiple crack formation is initially simplified to a single notched crack analysis that provides the fundamental knowledge and crucial understanding of the damage process. Several methods approach the quasibrittle nature of plain concrete under mode-I bending fracture [5]. Common point between all is the five stages of crack formation under opening mode testing presented in the load versus crack opening curve shown in Figure 1. Initially, a linear elastic response of concrete (Stage I) is obtained. Stage I ends when the stress applied reaches the concrete tensile strength and a crack forms. At that moment, the crack initiation point, namely, the crack tip, concentrates the critical stresses that govern the crack evolution (Stage II). Crack propagation occurs as the loading capacity of the material decreases and crack deformation evolves (Stage III). The plastic fracture process zone around the crack tip propagates following the crack path and enclosing crucial microcracks. The final bending fracture stage (Stage IV) states local failure when the limit crack opening width is reached [6].

The energy balance approach is a well-established fracture model that predicts the crack formation mechanism [7]. In more detail, during mode-I cracking part of the elastic stored energy is absorbed to create free damaged surfaces and another part is released due to fracture [8]. The key of the crack propagation mechanism is the unstable energy equilibrium that leads to energy release during fracture [9].

The material response will potentially differentiate due to the presence of embedded capsule. It is well known in the literature that irregularities in material composition can induce stress concentrations. In that direction, research has been done on the influence of aggregates size and nature on cracking response of concrete samples. In this respect, tubular capsules filled by healing agent acting as distortions may affect the cracking process. An analytical study of capsule breakage phenomena during concrete crack opening is

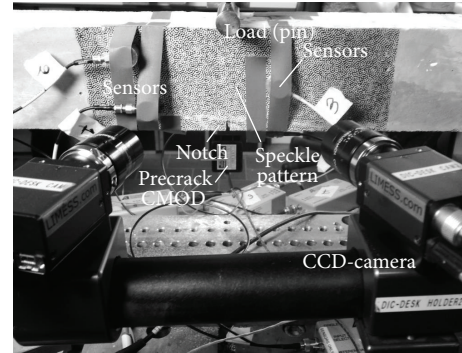


FIGURE 2: Experimental set-up.

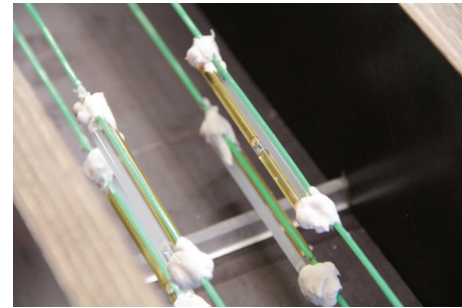


FIGURE 3: Series of capsules placed into the mold during casting.

required in order to clarify their impact on material fracture. The crucial stage of cracking at which capsule rupture occurs should be well defined since at that time healing repair is activated. More specifically, the healing triggering event should be characterized in time and accurately located within the material.

In this study, crack formation under three-point bending is investigated in the case of concrete samples with and without encapsulated healing material. Advanced optical and acoustic methods are used to monitor the performance of capsules and locate the healing activation. An analytical overview of acoustic signals captured by AE may provide experimental indications of capsules performance.

## 3. Materials

Plain concrete specimens were casted. The absence of reinforcement guarantees pure crack opening phenomena under bending. A water/cement/sand/coarse aggregate ratio of 1/2.07/4.28/4.52 was chosen. The maximum aggregate size was 13 mm.

After mixing the concrete was casted into wooden molds 840 mm long, 100 mm wide, and 100 mm high. At the bottom of the wooden mold a Teflon slice was positioned in order to create a notch in the concrete beams. The notch, shown in Figure 2, covers the width of the beam and its cross section is 3 mm wide and 10 mm high. The notch was created at the middle section of the beams and its presence was compulsory in order to induce crack formation at the middle of the beam. The sample dimensions were chosen according to the Rilem

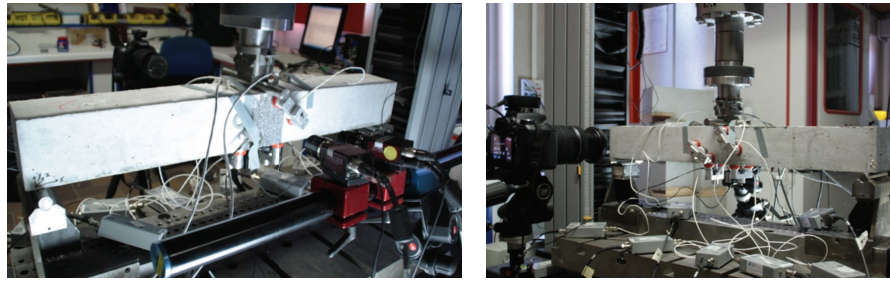


FIGURE 4: View of experimental setup configuration.

Technical Committee TC 50-FMC recommendation report on concrete fracture mechanics computations [10].

The beams were casted and consequently vibrated. Twenty-four hours after casting, the samples were demolded and stored under water for 14 days until testing time.

Reference samples did not contain any capsules in contrast to samples with self-healing properties within which couples of capsules were placed above the notch up to the neutral axis height.

Two-component polyurethane-based healing agent was embedded into borosilicate glass capillaries [1, 2]. The tubes, shown in Figure 3, are 50 mm long, the inner and outer diameters are 3.00 and 3.35 mm, respectively, and are sealed by glue at both sides. To prevent movement of the capsules during mixing, the capsules were attached to thin, poor in stiffness metallic wires crossing the length of the beam.

## 4. Methods

**4.1. Three-Point Bending Configuration.** The span between the test supports was fixed at 800.00 mm. An Instron load cell with a 20 kN capacity was used and the load was applied with a speed of 0.04 mm/min at the midsection of the sample.

A Crack Mouth Opening Displacement (CMOD) device, guided by EN 14651, was positioned over the notch to provide a precise display of the crack opening. Prior to testing, the CMOD gage was calibrated on 10.00 mm amplitude.

During testing, the load, the displacement, and the CMOD crack opening values were monitored and stored on a raw data file. Bending was applied until a crack opening of 0.40 mm was reached. Samples were subsequently unloaded, stored at room temperature for 72 hours of curing, and then reloaded following the same procedure.

The present study focuses on the initial crack formation and capsule activity. Digital Image Correlation (DIC) and AE full-field monitoring of the testing process crucially contributes to this goal. Indicatively, the experimental setting up combining the different techniques is shown in Figure 4.

**4.2. Digital Image Correlation Analysis.** DIC is an optical measuring technique that determines displacement fields and strain distribution profiles of a sample when movements due to loading occur.

TABLE 1: DIC test set-up features.

Hardware setup		
2 CCD-cameras	AVT Stingray	
Lenses	23 mm	
Aperture	3.4	
Software setup		
Resolution	2456 × 2058	
Area of interest	100 × 100 mm—20 px/mm	
Subset	27 × 27	
Subset spacing	5	
Strain field size	15	
Testing setup		
Time capture	Every 3 seconds or Δload = 0.1 kN	
Average speckle diameter	2.00 mm	

A 2-cameras system fixes an orthogonal coordinate system as shown in Figure 4—X, Y, Z (measured in mm or pixels)—and observes the random black-white speckle pattern painted at the surface of the sample. The stereoscopic cameras set-up captures periodically (every 3 seconds) high-resolution images and provides a series of virtual strain gauges fully covering the fractured area. Stereo-correlation between the images allows calculation of the sample position and deformation—U/V/W (measured in mm or pixels)—as crack opening occurs. Local derivative calculations provide Lagrangian strain tensor profiles— $e_{xx}/e_{yy}/e_{zz}$  (measured in  $\mu$ strain, mm/mm, or %)—across the entire surface under analysis. Also, the DIC software is able to calculate the maximum principal strains  $e_1$  and  $e_2$  obtained by the  $e_{xx}$  and  $e_{yy}$  combinations for  $e_{xy} = 0.00$  [11].

The cameras were positioned next to the INSTRON device and aligned on a metallic cylinder attached to a tripod. The DIC set-up was balanced and both cameras were oriented perpendicular to the concrete sample. The set-up parameters are shown at Table 1 and Figure 4.

Settling the focus of the cameras, a calibration table was positioned at the sample region, and a calibration analysis was finalized by the DIC software giving a projection error (standard deviation error) less than 0.035. Then, the sample was placed back to the testing position, the CMOD device was attached to the beam and balanced, the load cell was reset, and

TABLE 2: AE testing set-up features.

Analog filter		
Lower	100 kHz	
Upper	2 MHz	
Waveform setup		
Sample rate	1 MSPS	
Pretrigger	256	
Length	1 k	
Timing setup		
PDT	100 $\mu$ s	
HDT	200 $\mu$ s	
HLT	500 $\mu$ s	
Max duration	1000 $\mu$ s	

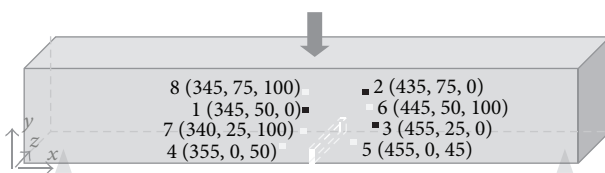


FIGURE 5: Coordinates system setup and sensors location.

three to four pictures were captured to insure that correlation could be done by DIC software for this set-up of testing.

**4.3. Acoustic Emission Analysis.** Acoustic Emission analysis can be used to detect crack initiation and to monitor crack propagation. Apart from that, the AE technique can be applied to locate and outline capsule rupture and to notice the interaction between concrete and capsule material [12–15]. As innovation in this research, the analysis of crack opening by AE is combined with the AE activity of embedded encapsulated healing agent.

Eight AE resonant R-15 PZT transducers were placed on both sides and the bottom of the sample. Stripe elastic tape and holding clamps with a magnetic base are applied to attach the sensors. The sensors named Channel 1, 2, 3, 6, 7, 8 were positioned antisymmetrically with respect to the depth of the beam at the sides of the beam. Channels 4 and 5 were placed symmetrically at the lower surface with respect to the notch. The sensors were attached to the surface by use of Vaseline coupling sealant and captured elastic waves arriving at the surface of the beam with amplitudes higher than 45 dB (AE threshold). Thereafter, gain of 40 dB was provided before the sensors activity reached a 32-bit digital signal processor. The analog bandwidth, the waveform, and timing parameters are shown in Table 2.

Hit-driven analysis was applied and it provided several waveform AE features. Some of them were selected representing and illustrating the damage process (amplitude, energy, duration, rise time, average frequency, counts, and counts to peak).

Apart from the AE hits evaluation, the origin of the signal can be detected in 3D by the source location algorithm. Being aware of the wave velocity (as calculated by the pencil lead

TABLE 3: AE localization setup.

Wave velocity	4.000 m/sec
Event definition time	150 mm
Event lockout time	180 mm
Overall time	20 mm
Hits/event	min: 4, max: 8
Max iterations	256

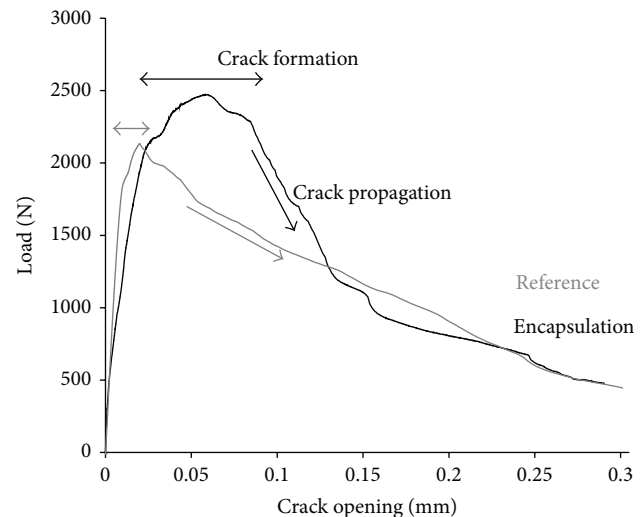


FIGURE 6: Load-crack opening graph for a representative sample of the reference and encapsulation series.

break test) and sensor position (as given in Figure 5), the source location can be determined by the time required for the wave to travel through the material and reach at least four sensors [16].

Taking into account the signal magnitude degradation due to attenuation effect, the localization analysis setup is given at Table 3.

## 5. Experimental Results

The evolution of the crack during performance of the three-point bending test provides primary information of the behaviour of samples with embedded capsules compared to reference samples. The load-crack opening displacement (measured by the CMOD device at the bottom of the beam) curves shown in Figure 6 are derived from a representative sample of the reference group of four beams (i.e., reference series) and another of the group of six beams into which healing system is embedded (i.e., encapsulation series).

Material properties of both test series as the initial stiffness, the load at crack formation, the maximum load, and the post peak load evolution can be derived from the graph in Figure 6. The values accounting for fracture response are quantitatively presented in Figure 7.

It is concluded that the initial stiffness (represented by the slope of the first part of the curves shown in Figure 7) is relatively similar for both series. As expected, the addition

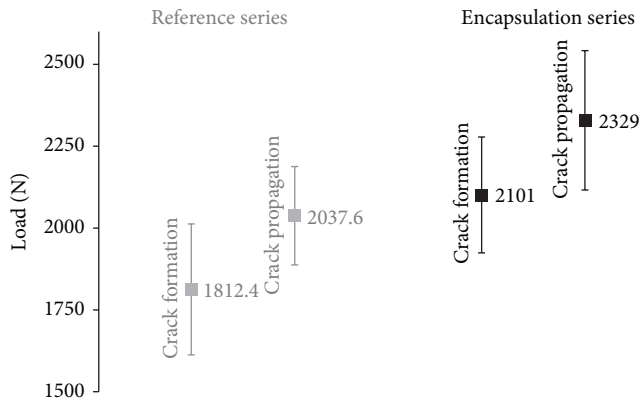


FIGURE 7: Material properties under bending: mean and standard deviation distribution for the sum of the beams.

of capsules does not influence the linear elastic behaviour of the concrete matrix. On the other hand, the load at the moment of crack formation is slightly increased in the case of encapsulation test series indicating potential influence of capsules on the loading performance of the samples [1]. Further on, the encapsulation series maximum load obtained is significantly elevated compared to the reference one. The behaviour of the encapsulation series during crack propagation is greatly diversified and in combination with the extended fracture energy release offers a clear evidence of the effect of capsules on the loading response and resistance of the concrete samples.

In the literature, different fracture models analyze the crack path morphology and crack tip performance under bending. For instance, the fictitious crack model, generalizing several quasibrittle fracture models, defines the linear elastic zone of loading as the stage at which loading depends on the strain capacity of the material and defines the postpeak zone as the stage at which crack opening controls the decrease in load. Graphically, the fracture theory splits the loading graph into two zones as shown in Figure 1. The energy release due to crack extension is analogous to the area under the curve of Figure 1.

Microcrack formation around the crack surfaces, stress concentration in front of the crack tip, and local redistribution of strains due to crack propagation are the crucial factors of the evolution of crack opening.

Apart from the aforementioned damage principle, it is assumed that encapsulated material probably gives enhanced energy release due to the capsule breakage process. The fracture process at the concrete matrix-capsule interface and sliding of the capsule leads to microcrack formation or debonding effects that may justify the enhanced crack extension energy release. Determination of the location and time of capsule breakage during bending is required to obtain a definite explanation.

**5.1. Crack Opening Activity Monitored by DIC: An Overview of Damage.** DIC strain and deformation profiles provide an overview of the damage evolution as the crack forms, propagates, and opens till failure. In Figure 8 a progressive view

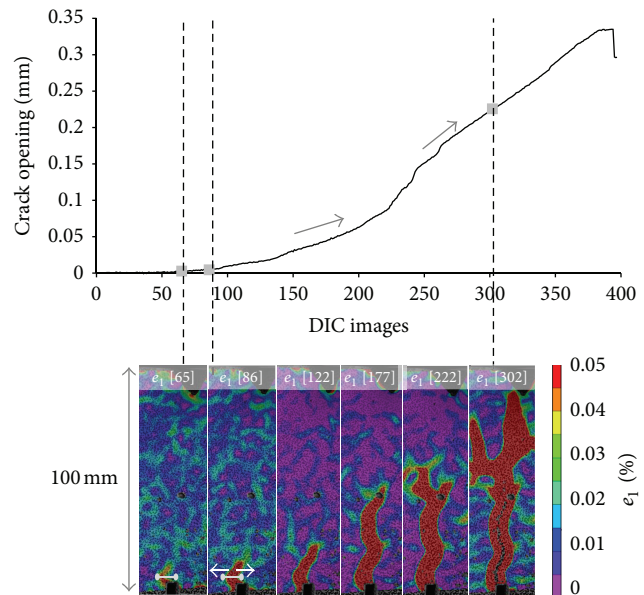


FIGURE 8: DIC monitoring strain and crack opening during bending.

of the crack morphology is presented and the continuously rising crack opening quantitatively measured at the bottom of the sample is shown. The position, at which the crack opening was calculated, is shown with a white mark in Figure 8.

In agreement with the fracture models analyzed above, at first, limited strain concentration appears at the edge of the notch. The principal— $e_1$ —strain profile of DIC image 65, corresponding to the end of Stage I of fracture indicates, the damage initiation before crack opening occurs. At the beginning of the experiment, the crack opening calculated at the concrete area above the notch remained negligible until that moment at which strain concentration locally appears, as shown at the strain profile  $e_1$  [65] graph of Figure 8.

The principal strain of DIC image 86 defines the end of crack formation and the beginning of crack extension. Crack initiation is confirmed by the limited crack opening shown at the crack displacement graph in Figure 8.

Subsequently, upon completion of stage II (visualized in images 122, 177, and 222), the crack propagates and gets wider in two different opening rates, indicated by arrows at the graph of Figure 8 up to the DIC strain profile of image 302 at which cracking propagates till the highest region across the height of the sample. That moment defines the end of fracture Stage III. Further on, mainly crack widening occurs leading to final failure (Stage IV of fracture).

It is shown on the strain profiles that the crack propagates above the precrack groove and reaches the top region of the beam. Capsules positioned orthogonal to the crack path are expected to break under bending. DIC optical observation of the cracked region leads to the next analysis focussing on the detection of tube breakage.

**5.2. Acoustic Emission Energy Classification of Damage.** An Acoustic Emission energy-based analysis was performed in order to distinguish capsule breakage from other damage

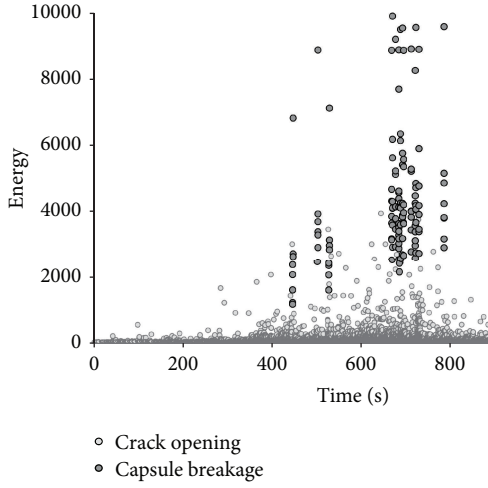


FIGURE 9: Hits energy activity during testing-detection of capsule breakage high energy hits.

events [17, 18]. Van Tittelboom et al. differentiate AE events due to capsule breakage, that provide high energy hits, from matrix cracking which releases lower energy-carrying hits [3]. Based on that ascertainment, in Figure 9 the energy of all AE hits captured during testing is shown. Analyzing the energy range, the presence of brittle instantaneous capsule breakage events is confirmed.

In more detail, every time a glass tube breaks, each of the AE sensors captures a waveform, represented by a set of descriptors analyzed in this research. Thereby, the AE hits energy derived from the area under the waveform shape is indicative to the released fracture energy and its magnitude and general characteristics are indicators of the damage mode. High energy hits correspond to discrete events of capsule breakage and are well differentiated from the rest of the AE events. Only in case of capsule breakage, the energy received by all the eight sensors placed at surface of the beam exhibits values ranging from 2000 to 12000 depending on the receiver's sensor distance from the event location (the energy of hits is relatively low in case of sensors placed far from capsules region and higher in case of sensors standing closer to the capsule fracture). Any other AE activity belongs to the second cluster as plotted in Figure 9 and its source is investigated below.

Regarding the bending mode crack formation, AE energy analysis may not differentiate the stages of crack evolution and the influence of capsules in the crack plane and the fracture process zone of the surroundings. Material damage optically based observation by DIC points out any diversity due to encapsulation.

**5.3. Detecting the Conditions under Which Capsule Breakage Activates Healing.** Localization of capsule breakage was successfully done by synchronizing the AE activity with the Instron load data and DIC periodically captured images. Subsequently, the loading stage and the coordinates in three directions for each AE capsule breakage event were detected. Capsule damage events are plotted on the already discussed

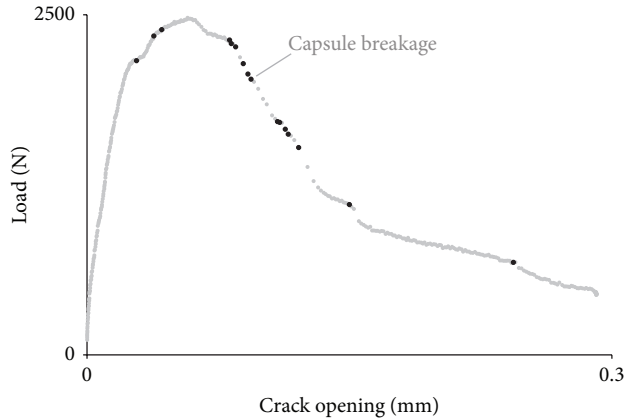


FIGURE 10: Capsules breakage events localization by AE at the load-crack opening graph.

load-crack opening graph and are shown in Figure 10. Primary capsule rupture is coincided with crack initiation. Further, crack formation and propagation lead to a series of capsule breakages well-distributed in the postpeak region of the load graph.

Consistent with the graph in Figure 10, the fact that capsules break after crack initiation is verified. Stress concentration at the notch during Stage I is not sufficient to rupture the glass tubes. On the contrary, primary deformation, visualized at DIC image 86 strain profile of Figure 9, is the trigger mechanism of autonomous crack healing. Furthermore, it is concluded that the extended crack formation stage for the encapsulation series compared to the reference series appears due to breakage of the capsules, as shown in Figure 8. The release of stresses concentrated at the interface between the tubes and the concrete matrix and the undistributed crack propagation due to capsule irregularities leads to the steep decrease in load as capsule rupture occurs.

For further information, the sum and the distribution of AE hits during testing for both series is included in this study. An augmentation of the number of hits due to capsule embedment is observed at the cumulative hits graph as presented in Figure 11. In more detail, linear loading response provides limited AE hits activity in both series. Crack formation leads to energy release due to crack deformations and gradually the number of AE hits increases. It is noticed that AE hits activity initiates earlier in the case of encapsulation beams. Local heterogeneity and stress concentration at the region of capsules placed above the notch can justify the prior AE activity. Building up of the fracture zone and crack expansion signifies the sharp rise of hits for both series of testing. In total, the AE activity of the encapsulation series at the end of the crack propagation stage is three times more extended than for the reference series. AE activity of the reference beam is related to crack opening and microcrack formation in the vicinity at both damaged sides of the beam. Well-distributed concrete material components may not arrest the crack propagation as it is shown already at the featureless postpeak region of the load-crack opening curve in Figure 6. On the other hand, crack opening of encapsulation series

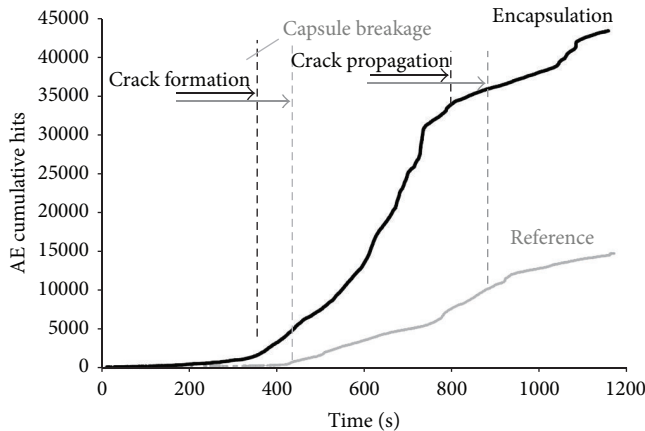


FIGURE 11: AE cumulative hits activity during testing for reference and encapsulation series.

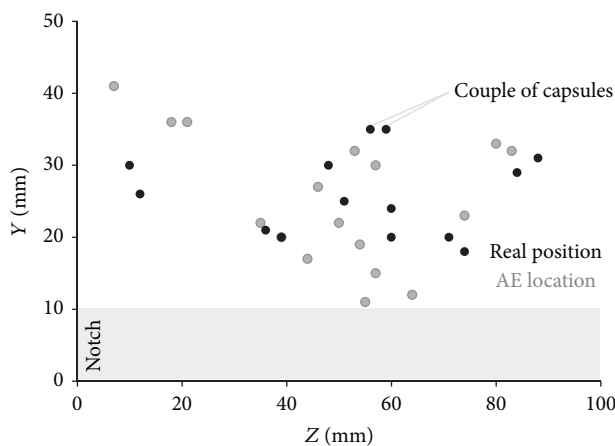


FIGURE 12: Real and AE located capsule breakage position at the crack plane.

is a combination of complex fracture phenomena. Capsules placed above the notch create stress concentration and increase of the energy required to form cracks. Furthermore, capsule rupture involves the high energy release due to brittle fracture of the tube, potential debonding at different places across the capsule length, and friction or sliding forces between concrete and glass tubes that provide continuous AE activity and constant low energy release. The fracture activity is marked also at the energy-based analysis graph discussed already in Figure 9.

**5.4. Further AE Postprocessing Analysis-Location of AE Capsule Events.** After completion of the two-cycle bending test, the sample is broken in two pieces and the capsule coordinates were determined. Probable shortage of precise AE analysis can be assessed when the real location of capsules measured at the crack plane is compared to the coordinates given by the 3D localization algorithm. In Figure 12 the two-dimensional ( $Y-Z$  coordinates in mm) map of capsule breakage events at the crack plane is presented. In different gray-scales the actual and AE calculated location of the

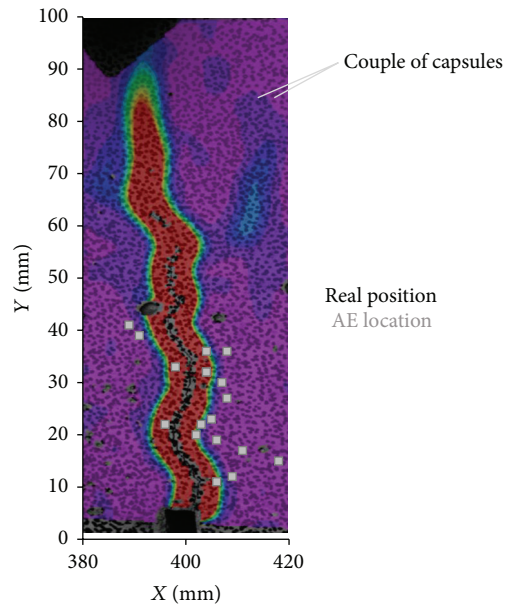


FIGURE 13: AE capsule location across the length of the beam and crack opening DIC fracture profile.

capsules is given. Slight variations—less than 8.00 mm—in the results observed fall within the accuracy limits of AE. In general, accurately located capsule rupture validates the localization approach and AE seems as a promising method to detect embedded healing systems in concrete.

Regarding the loading response of the sample, it is worth noticing that a big amount of capsule couples stand 20–30 mm above the notch. The heterogeneity of that zone justifies the accumulate stress applied at the postpeak stage of loading to break the concentrated glass tubes and let the crack propagate.

Careful observation of AE localization results points out a conflicting note. Inside the sample 7 couples of glass tubes are placed which entails that 14 capsule breakages are expected. Apparently, the AE algorithm locates 18 individual capsule breakages in the case of the beam analyzed. For all the other beams of the series 17–25 events of capsule rupture are captured. It is reasonable to conclude that some capsules break at multiple places as cracking propagates. Apparently, breakage of a tube on a specific point leads to local strength loss. Local discontinuity redistributes the loading across the capsule surface and rearranges microcrack effects on the concrete zone that covers the tube. In any case, the loading capacity under bending is maintained away from the damaged spot. Thereby, a capsule may break more than once in different sections as soon as the crack deformation applies unsustainable loading on them.

Apart from the crack plane observations, the capsule breakage phenomena are also located across the length of the sample. In Figure 13 the capsule rupture events are projected at the surface of one side of the beam. In parallel, a DIC strain profile is fixed to the same coordinate system and shown as background plot of the analysis. It is concluded that capsules

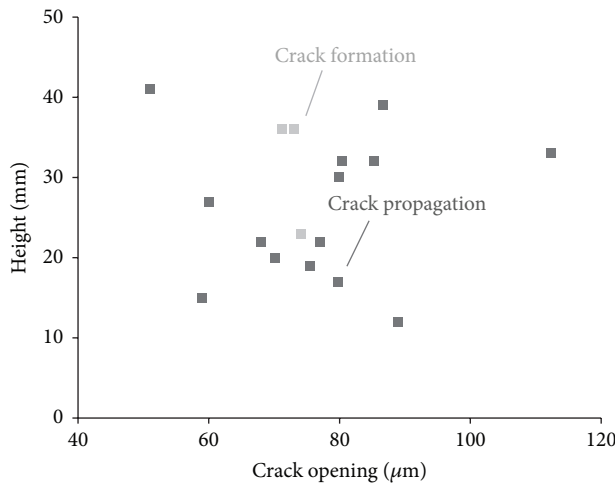


FIGURE 14: Local crack opening during capsules breakage.

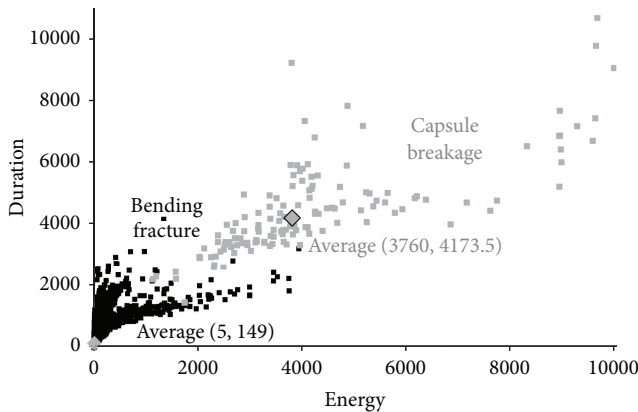


FIGURE 15: Clustering based on energy and duration features.

do not always break at the crack plane. It should be kept in mind that the DIC monitors surface strain profiles and that crack propagates in different paths across the thickness of the sample avoiding aggregates and capsule constraints.

This observation confirms the presence of substantial fracture mechanisms acting at the limits of cracking damage and further away into the concrete matrix. As the crack forms, concrete microcracks in the vicinity of damage and the glass tube receive the fracture energy released and redistribute the strain formation.

**5.5. Further AE Postprocessing Analysis: Measuring by DIC and AE the Crack Opening Whereby Capsules Break.** Accurate AE events localization and DIC deformation profiles were combined once again to quantify the crack opening which was sufficient to fracture the glass capsules. In practice, knowing the coordinates of capsule failure events and the loading stage at that time, full-field DIC displacement recording provides the displacement at different heights along the crack improving the measured CMOD values of crack opening. The associated results are presented in Figure 14. According to the damage evolution, it was chosen to allocate a different

color to the capsule breakages that appear at the stage of crack formation and those during crack propagation. For all cases, the crack opening ranges from 50 to 90  $\mu\text{m}$  proving that low crack opening may sufficiently trigger capsule breakage. The location of the tube at upper positions across the height of the crack plane appears not to delay the rupture nor to require higher values of crack opening. In parallel, it is observed that similar loading and stress conditions lead to capsule fracture throughout the entire bending test. Widening of the crack during loading does not further damage the tubes and after tube breakage the release of the agent should successively fill the crack plane.

**5.6. Further AE Postprocessing Analysis: Clustering of AE Features.** Clustering of cracking and capsule breakage AE hits according to their energy released, which was shown and discussed above, is the first approach in order to differentiate the global bending opening from local and instant capsule fraction. Retaining the energy clustering of hits, several other AE features are classified.

To start with, the signal duration was investigated since this is together with the energy values are the most representative waveform strength indicator. The plot of hits energy and duration captured during testing provides a clear evidence of clustering between material fracture and capsule breakage as shown in Figure 15.

In parallel, a concise summary of other AE features is presented in Figure 16. Energy and duration classification is reviewed providing the mean, the first, and the third quartile of their values. Box plots of median and spread values are also prepared for the amplitude population of hits. Even in this case, the amplitude of capsule breakage significant differentiation is evident.

In contrast, the classification of hits based on average frequency, counts to peak, and rise time is not as straightforward as above. The hits of capsule breakage are masked by the opening mode of damage as shown in Figure 17. It is worth noticing that the average frequency values of the second cluster (capsule breakage) are well concentrated around the mean value. On the other hand, the different fracture phenomena falling in the first cluster show a wide spread frequency range.

## 6. Conclusions

The aim of this study, to detect the mechanism that activates autonomous crack healing of concrete beams under bending, is achieved. The challenging task is accomplished by optical and acoustic monitoring of the damage evolved. Acoustic Emission provided an integrated overview of capsule brittle fracture. The location of failure inside the material and identification of the conditions (loading, time, crack width, and fracture evolution) under which capsule breakage occurred were done by analyzing the hits activity captured by eight sensors attached to the concrete surface.

Classification of matrix damage in combination with interplay to the glass tubes interface and the capsule breakage was successfully done for several AE features. The study

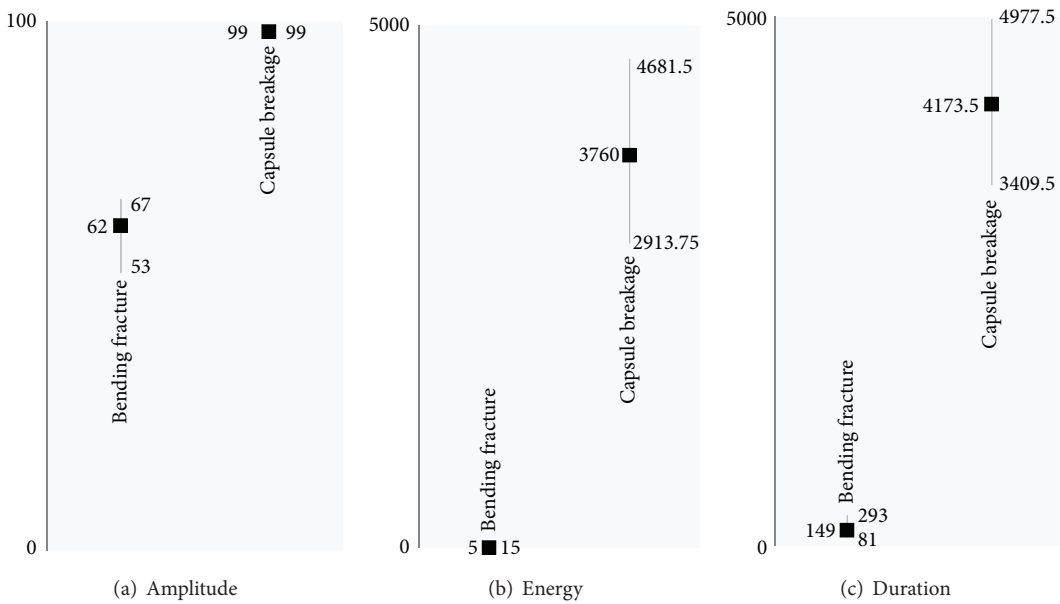


FIGURE 16: Clustering of AE features-part 1.

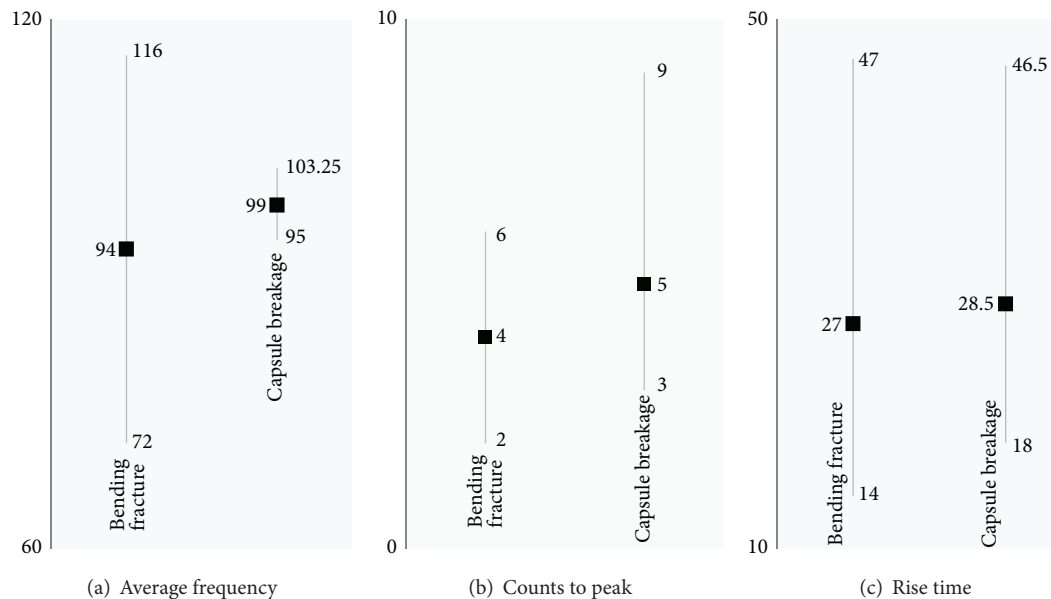


FIGURE 17: Clustering of AE features-part 2.

aims to showcase an experimental system that detects the behaviour of capsules in the material. On that approach, precisely settled AE appliance carries the leading role.

The efficiently fixed experimental setup of two DIC cameras, eight AE sensors, and a CMOD device may be applied to hereby confirm healing recovery when after curing crack reopens.

## Acknowledgments

The research described in this paper has been performed in the frame of the SIM program on Engineered Self-Healing

Materials (SHE). The authors are grateful to SIM (Strategic Initiative Materials Flanders) for providing financial support.

## References

- [1] K. Van Tittelboom, *Self-Healing Concrete through Incorporation of Encapsulated Bacteria- or Polymer-Based Healing Agents*, Department of Structural Engineering, Ghent University, 2012.
- [2] K. Van Tittelboom, N. De Belie, P. Zhang, and F. H. Wittmann, *Self-Healing of Cracks in Concrete*, Basic Research on Concrete and Applications, 2011.

- [3] K. Van Tittelboom, N. De Belie, F. Lehmann, and C. U. Grosse, "Acoustic emission analysis for the quantification of autonomous crack healing in concrete," *Construction and Building Materials*, vol. 28, no. 1, pp. 333–341, 2012.
- [4] E. Tsangouri, K. Van Tittelboom, D. Van Hemelrijck, and N. De Belie, "Visualization of the healing process on reinforced concrete beams by application of Digital Image Correlation," in *Proceedings of the 6th International Conference on High-Performance Structures and Materials*, pp. 1–12, New Forest, UK, 2012.
- [5] M. Modeer, "A fracture mechanics approach to failure analyses of concrete materials," Tech. Rep. TVBM-1001, Lund University, Lund, Sweden, 1979.
- [6] J. Roesler, G. H. Paulino, K. Park, and C. Gaedicke, "Concrete fracture prediction using bilinear softening," *Cement and Concrete Composites*, vol. 29, no. 4, pp. 300–312, 2007.
- [7] X. Z. Lu, J. G. Teng, L. P. Ye, and J. J. Jiang, "Bond-slip models for FRP sheets/plates bonded to concrete," *Engineering Structures*, vol. 27, no. 6, pp. 920–937, 2005.
- [8] J. Wang, "Cohesive zone model of intermediate crack-induced debonding of FRP-plated concrete beam," *International Journal of Solids and Structures*, vol. 43, no. 21, pp. 6630–6648, 2006.
- [9] M. Elices, G. V. Guinea, J. Gómez, and J. Planas, "The cohesive zone model: advantages, limitations and challenges," *Engineering Fracture Mechanics*, vol. 69, no. 2, pp. 137–163, 2002.
- [10] RILEM TC-50-FCM, "Determination of fracture energy of mortar and concrete by means of three-point bend tests on notched beams," *Materials and Structures*, vol. 18, no. 106, pp. 285–290, 1985.
- [11] M. A. Sutton, J. Orteu, and H. Schreier, *Image Correlation for Shape, Motion and Deformation Measurements: Basic Concepts, Theory and Applications*, Springer, 2009.
- [12] C. U. Grosse and M. Ohtsu, *Acoustic Emission Testing*, Springer, 2008.
- [13] D. G. Aggelis, T. Shiotani, S. Momoki, and A. Hirama, "Acoustic emission and ultrasound for damage characterization of concrete elements," *ACI Materials Journal*, vol. 106, no. 6, pp. 509–514, 2009.
- [14] M. Ohtsu, "Recommendation of RILEM TC 212-ACD: acoustic emission and related NDE techniques for crack detection and damage evaluation in concrete: test method for classification of active cracks in concrete structures by acoustic emission," *Materials and Structures*, vol. 43, no. 9, pp. 1187–1189, 2010.
- [15] K. Ohno and M. Ohtsu, "Crack classification in concrete based on acoustic emission," *Construction and Building Materials*, vol. 24, no. 12, pp. 2339–2346, 2010.
- [16] *E976—10 Standard Guide for Determining the Reproducibility of Acoustic Emission Sensor Response*, ASTM, Philadelphia, Pa, USA, 1988.
- [17] D. G. Aggelis, "Classification of cracking mode in concrete by acoustic emission parameters," *Mechanics Research Communications*, vol. 38, no. 3, pp. 153–157, 2011.
- [18] D. G. Aggelis, A. C. Mpalkas, and T. E. Matikas, "Investigation of different fracture modes in cement-based materials by acoustic emission," *Cement and Concrete Research*, vol. 48, pp. 1–8, 2013.

## Research Article

# The Sacred Mountain of Varallo in Italy: Seismic Risk Assessment by Acoustic Emission and Structural Numerical Models

**Alberto Carpinteri, Giuseppe Lacidogna, Stefano Invernizzi, and Federico Accornero**

*Department of Structural, Geotechnical and Building Engineering, Politecnico di Torino, 10129 Torino, Italy*

Correspondence should be addressed to Giuseppe Lacidogna; giuseppe.lacidogna@polito.it

Received 26 July 2013; Accepted 1 September 2013

Academic Editors: D. G. Aggelis, N. Alver, and H. K. Chai

Copyright © 2013 Alberto Carpinteri et al. This is an open access article distributed under the Creative Commons Attribution License, which permits unrestricted use, distribution, and reproduction in any medium, provided the original work is properly cited.

We examine an application of Acoustic Emission (AE) technique for a probabilistic analysis in time and space of earthquakes, in order to preserve the valuable Italian Renaissance Architectural Complex named “The Sacred Mountain of Varallo.” Among the forty-five chapels of the Renaissance Complex, the structure of the Chapel XVII is of particular concern due to its uncertain structural condition and due to the level of stress caused by the regional seismicity. Therefore, lifetime assessment, taking into account the evolution of damage phenomena, is necessary to preserve the reliability and safety of this masterpiece of cultural heritage. A continuous AE monitoring was performed to assess the structural behavior of the Chapel. During the monitoring period, a correlation between peaks of AE activity in the masonry of the “Sacred Mountain of Varallo” and regional seismicity was found. Although the two phenomena take place on very different scales, the AE in materials and the earthquakes in Earth’s crust, belong to the same class of invariance. In addition, an accurate finite element model, performed with DIANA finite element code, is presented to describe the dynamic behavior of Chapel XVII structure, confirming visual and instrumental inspections of regional seismic effects.

## 1. Introduction: The Historic Site of the Sacred Mountain of Varallo

The Sacred Mountain of Varallo is located in the Italian province of Vercelli. Built on a cliff above the town of Varallo, it is the oldest and most important Sacred Mountain of the Alps (Figure 1). This historical site is composed of a Basilica and 45 Chapels, some of which are isolated, while others are part of monumental groups. The Chapels contain over 800 life-size wooden and multicoloured terracotta statues, which represent the Life, Passion, and Death of Christ. The site is considered the most notable example in the group of Sacred Mountains of Piedmont, a complex that has been included in the UNESCO World Heritage List since 2003.

Its story began in the late fifteenth century when the Franciscan friar Bernardino Caimi of Milan, returning from the Holy Land where he was guardian of the Holy Sepulchre, decided to reproduce in Varallo the holy places of Palestine [1].

The “New Jerusalem,” as it was called the Sacred Mountain, initially intended to represent the distant sites of the Christian tradition for all those people who could never go there (Figure 2). Inside these places are, instead of pictures, paintings and sculptures to evoke the corresponding event in the history of the life of Christ. Already in the early sixteenth century, thanks to the work of the painter sculptor and architect Gaudenzio Ferrari, the scenes inside the chapels are represented in an ingenious and innovative merging of painting and sculpture, with a strong sense of reality, so that the devotee could feel himself deeply involved by the depicted scene of the Christ’s Life and almost part of it (Figure 3). The work of Gaudenzio Ferrari will be taken as a model in the construction of many other Sacred Mountains. In the era of the Counter-reformation, the Sacred Mountain of Varallo assumed the appearance of a path, real but at the same time mystical, that the pilgrim completes following the telling of the story of Christ’s Life [1].



FIGURE 1: The Sacred Mountain of Varallo, Italy. Overview.



FIGURE 2: The Sacred Mountain of Varallo. The Square of Tribunals.



FIGURE 3: Chapel XXXIII. *Ecce Homo*.



FIGURE 4: Chapel XVII. *The Transfiguration of Christ on Mount Tabor*.

## 2. Chapel XVII Monitoring Set-Up

The Acoustic Emission monitoring was conducted on the frescoed masonry walls of the Chapel XVII of the Sacred Mountain of Varallo: the Chapel of the Transfiguration of Christ on Mount Tabor (Figure 4). The construction of the Chapel XVII began in 1572, but the structure was completed only in 1647. In 1664 the lantern top was built as crowning.

One of the purposes of monitoring by means of AE sensors applied to the frescoed wall was to detect the AE signals from a region of the wall in which the frescos show a plaster detachment. Moreover, we used the collected data coming from the “*in situ*” monitoring in order to assess the seismic risk of artworks and possible collapses due to earthquake actions [2, 3].

As regards the structural integrity, the North wall of the Chapel XVII shows a vertical crack of about 3.00 m in length and a detachment of frescos. These phenomena were one of the objective of the monitoring campaign by means of AE technique. Six AE sensors were employed to monitor the damage evolution of the structural support of the decorated surfaces: four were placed around the vertical crack while two were positioned near the frescos detachment (Figure 5). In addition, the South wall of the Chapel XVII also shows a vertical crack, symmetric to the previous one with respect to the pronaos of the building.

For the sensor pasting on decorated surfaces, a suitable methodology was applied. The necessary operations for bonding the AE sensors to the wall were carried out by a group of restorers, which have prepared a film of Japanese paper, on the surface of which is coated a thin layer of “Paraloid”.

The “Paraloid” is an acrylic resin (methyl acrylate soluble in ketones, esters, hydrocarbons, and chlorinated hydrocarbons) and is used in the field of restoration as a consolidant at low concentrations (2,4%) or as an adhesive at higher concentrations. It allows an excellent waterproof performance and has the advantage of being reversible and long-term stable. The layer of “Paraloid” forms a good protective base for the AE sensors bonding with silicone glue. The sensors were applied to monitor both the vertical crack and the detachment of the plaster (Figure 5) [2, 3].

The Acoustic Emission acquisition system is shown schematically in Figure 6. The piezoelectric transducers (PZT) are calibrated over a range of frequency between 50 kHz and 800 kHz. The USAM acquisition system consists of 6 preamplified sensors, 6 units of data storage provided of triggers, a central unit for the synchronization operations, an internal clock, and a trigger threshold. The obtained data are the cumulative counting of each mechanical wave considered as acoustic emission events, the acquisition time, the measured amplitude in Volt, the duration, and the number of oscillations over the threshold value for each wave [4, 5].

The monitoring time started from May 9, 2011, and finished on September 5, 2011. Regarding the monitoring results on the chapel structural integrity, they are reported in [2]. We interpreted the AE data by means of statistical analysis, considering the amplitude and time distribution of AE signals during the cracking phenomena. From this



FIGURE 5: Chapel XVII. View of the monitored areas. Left side: sensors 5, 6, and the frescos detachment. Right side: sensors 1–4 and the vertical crack.

analysis, we found that the vertical crack monitored on the North wall of the chapel is in a stable condition during the acquisition period, while the process of detachment of the frescos is evolving cyclically. It appears that the frescos degradation could be mainly related to the diffusion of moisture in the mortar substrate [2].

### 3. AE and Seismic Events

Nondestructive testing methods are currently used to evaluate structural damage phenomena and to predict their development over time. It is worth noting that the evaluation of damage in historic buildings is often a complex task. It is essential to distinguish between stable damage patterns and damage in evolution towards a catastrophic collapse. Some structural damage can be triggered by events such as earthquakes. Furthermore, the limited ductility of the masonry, combined with the large size of this type of construction, provides a rather fragile structural behavior. Fortunately, the damage evolution in time can be effectively evaluated by means of the AE technique [4–10].

Moreover, the statistical distribution of earthquakes shows a complex nonlinear space-time behavior, that reflects the heterogeneities of the Earth's crust. Despite this complexity, a scaling law is universally valid: the earthquakes frequency-magnitude statistical distribution provided by the Gutenberg-Richter (GR) law [11].

On the other hand, AE in materials and earthquakes in the crust are very similar from many aspects and correlated in time, even though they occur at very different scales [12]. In both cases, there is a release of elastic energy from a source located in the medium, respectively, the tip of opening

microcracks and the seismic hypocenter [13]. This similarity suggests that the seismic events and the AE events can be related in space and time. Therefore, it is possible to search for a correlation between the AE parameters related and the regional seismicity. In our opinion, this approach can be used to identify some warning signals that anticipate a catastrophic collapse of a structure. In fact, in many cases, the warning signals can be detected well in advance with respect to the time at which the unrecoverable damage event will occur [14, 15].

Most earthquakes have precursors, that are phenomena that in the short or long term change their activity before the earthquake. In the literature, many precursors have been proposed, but there is still no clear evidence about their reliability. In addition, any operative warning procedure must be based on the acquisition of a combination of several precursor clues. Recently, major efforts in the field of earthquake prediction have focused on the fluctuations of the physical parameters of the crustal rocks of the seismically active continental areas, and on regular intervals in the space-time distribution of earthquakes [16]. The variation in the rate of the regional seismicity is considered as a precursor in the long term. A region which had a small earthquake activity for a remarkable number of years is called “seismic gap.” The “seismic gaps” are considered as potential sites for major earthquakes. On the other hand, the increasing pressure in the rock surface in the region of the epicenter produces numerous cracks before the final collapse and, as a result, it causes changes in the properties of rocks. Therefore, the drop in speed of seismic waves caused by the expansion of the rock becomes a significant precursor. Other precursors linked to the expansion of the rocks and the opening of cracks are the crustal tilt and elevation changes, the decrease of the electrical resistivity of the rocks, and the release of radon gas in the atmosphere, which requires small pores to propagate. As the process of damage develops, the water diffuses from the surrounding rocks in pores and microcracks of increasing size, which in the meantime are forming. The moment the water fills the cracks, the speed of seismic waves grows, the soil lifting stops, the emission of radon from the new cracks is relieved, and the electrical resistivity decreases. The next stage is the beginning of the earthquake, which is immediately followed by several aftershocks in the surrounding area [7, 16].

When a crack in the Earth's crust increases (i.e., a fault propagates), the corresponding AE show, progressively lower frequencies, eventually decreasing from the ultrasound field down to the sonic range: as it occurs during the well-known phenomenon of seismic roar. Thus, AE techniques can be effectively put into relation with the spread of tensions through the Earth's crust. Some Italian researchers collected continuously, for many years, the AE signals from below the Gran Sasso massif [14, 15]. The progressive decrease of detected AE frequencies reveals that the damage localization is taking place, while AE high-frequency can be associated with the increase of small lesions more uniformly distributed in the crust. Therefore, the potential of earthquake prediction related to the AE monitoring appears promising [14].

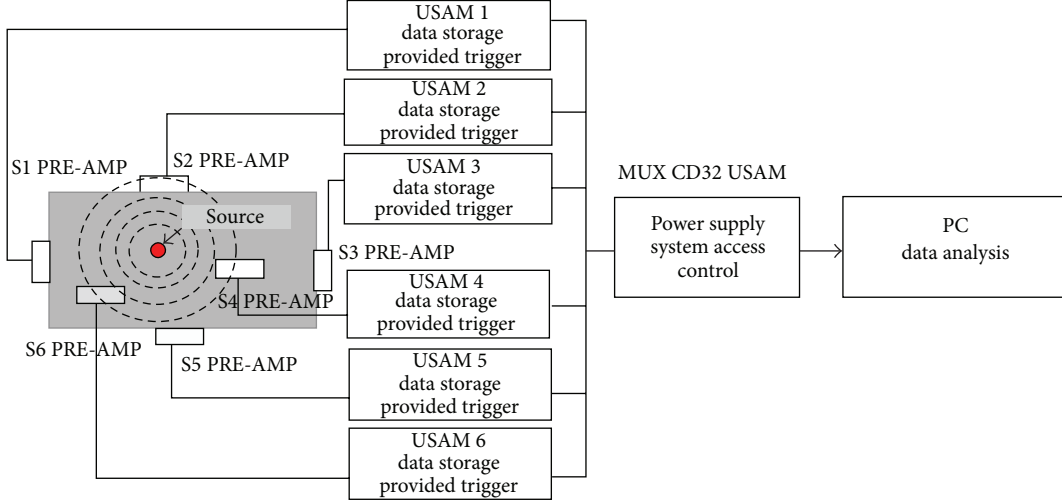


FIGURE 6: AE acquisition system.

**3.1. Correlation Algorithms between AE and Seismic Events.** Among the various studies on the earthquakes space-time correlation, there is a statistical method that allows to calculate the degree of correlation both in space and time between a series of AE and the local seismic recordings, collected in the same period. This analysis is based on the generalization of the space-time correlation known as the integral of Grassberger-Procaccia [17], defined as follows:

$$C(r, \tau) \equiv \frac{1}{N_{EQ} N_{AE}} \sum_{k=1}^{N_{EQ}} \sum_{j=1}^{N_{AE}} \Theta(r - |x_k - x_j|) \Theta(\tau - |t_k - t_j|), \quad (1)$$

where  $N_{AE}$  is the number of peaks of AE activity registered in site, in this case Chapel XVII, and in a defined time window,  $N_{EQ}$  is the number of earthquakes recorded in the surrounding area during the same time window and  $\Theta$  is the step function of Heaviside ( $\Theta(x) = 0$  if  $x \leq 0$ ,  $\Theta(x) = 1$  if  $x > 0$ ). The index  $k$  refers to the recorded seismic events  $\{x_k, t_k\}$ , while the index  $j$  refers to the recorded AE events  $\{x_j, t_j\}$ .

Therefore, between all possible pairs of recorded AE and seismic events, the sum expressed by the integral of Grassberger-Procaccia can be calculated for those having the epicentral distance  $|x_k - x_j| \leq r$  and the temporal distance  $|t_k - t_j| \leq \tau$ . Hence,  $C(r, \tau)$  is the probability of occurrence of two events, an earthquake and an AE event, whose mutual spatial distances are smaller than  $r$  and mutual temporal distances are smaller than  $\tau$ .

Note that, in order to evaluate (1), the numbers of  $N_{AE}$  and  $N_{EQ}$  are not required to assume the same value, and that  $x_j$  correspond to the geographic position of the Chapel.

Anyway, this approach does not consider the chronological order of the two types of events. Since the AE time series and the earthquake sequences are closely intertwined in the time domain, the problem of the predictive ability of the AE peaks is still open. The records of AE could be

TABLE 1: AE as precursor from May 9, 2011 to June 16, 2011. Cumulative probability  $C^+(r, \tau)$  for radius  $r$  ranging between 60 and 100 km, and time  $\tau$  varying from 1 week to 5 weeks.

	60 km	80 km	100 km
1 week	0.0339	0.1121	0.2018
2 weeks	0.0772	0.2130	0.3661
3 weeks	0.1228	0.3018	0.4875
4 weeks	0.1487	0.3661	0.5549
5 weeks	0.1630	0.4321	0.6210

both the consequences of the progressive development of microdamage or the effect of widespread microseismicity. Therefore, a probabilistic analysis can be carried out discriminating between the AE events prior to the earthquake, which are precursors, and the AE following the earthquake, which are aftershocks. This analysis can be performed adopting a modified correlation integral [7] as follows:

$$C^\pm(r, \tau) \equiv \frac{1}{N_{EQ} N_{AE}} \sum_{k=1}^{N_{EQ}} \sum_{j=1}^{N_{AE}} \Theta(r - |x_k - x_j|) \Theta(\pm(t_k - t_j)), \quad (2)$$

where “+” and “-” in the Heaviside function are used to take into account that the AE events could be, respectively, seismic precursors and aftershocks.

In this way, the function  $C^+(r, \tau)$  gives the probability that a peak of AE, detected at a certain time, will be followed by an earthquake in the subsequent days within a radius of  $r$  kilometers from the AE monitoring site. Varying the thresholds  $r$  and  $\tau$  in (2), two cumulative probability distributions can be constructed, one for each condition (sign “+” or “-”) and then the corresponding probability density functions can be derived and represented (see Figure 7 and Tables 1–6, in which the radius  $r$  ranges between 60 and 100

TABLE 2: AE as aftershock from May 9, 2011 to June 16, 2011. Cumulative probability  $C^-(r, \tau)$  for radius  $r$  ranging between 60 and 100 km, and time  $\tau$  varying from 1 week to 5 weeks.

	60 km	80 km	100 km
1 week	0.0254	0.0732	0.1437
2 weeks	0.0357	0.1196	0.2629
3 weeks	0.0371	0.1509	0.3362
4 weeks	0.0371	0.1652	0.3732
5 weeks	0.0371	0.1665	0.3768

TABLE 3: AE as precursor from July 5, 2011 to September 5, 2011. Cumulative probability  $C^+(r, \tau)$  for radius  $r$  ranging between 60 and 100 km, and time  $\tau$  varying from 1 week to 9 weeks.

	60 km	80 km	100 km
1 week	0.0075	0.0278	0.0846
2 weeks	0.0184	0.0552	0.1896
3 weeks	0.0239	0.0833	0.3222
4 weeks	0.0346	0.1040	0.3841
5 weeks	0.0498	0.1210	0.4435
6 weeks	0.0557	0.1268	0.5130
7 weeks	0.0557	0.1268	0.5497
8 weeks	0.0557	0.1268	0.5607
9 weeks	0.0557	0.1268	0.5657

TABLE 4: AE as aftershocks from July 5, 2011 to September 5, 2011. Cumulative probability  $C^-(r, \tau)$  for radius  $r$  ranging between 60 and 100 km, and time  $\tau$  varying from 1 week to 9 weeks.

	60 km	80 km	100 km
1 week	0.0045	0.0298	0.1192
2 weeks	0.0132	0.0465	0.1916
3 weeks	0.0234	0.0717	0.2592
4 weeks	0.0301	0.0970	0.3251
5 weeks	0.0313	0.1114	0.3737
6 weeks	0.0313	0.1246	0.4164
7 weeks	0.0313	0.1299	0.4283
8 weeks	0.0313	0.1336	0.4333
9 weeks	0.0313	0.1341	0.4338

kilometers, and the time interval  $\tau$  varies from 1 week up to a maximum of 9 weeks).

#### 4. AE as Seismic Precursors in the Sacred Mountain of Varallo

**4.1. AE Monitoring Periods.** For this analysis, the AE collected data are grouped into two different time windows. The first time window started May 9, 2011, and finished June 16, 2011. The second time window started July 5, 2011, and finished September 5, 2011. Both time windows involved the monitoring of the vertical crack and of the frescos detachment [2].

TABLE 5: Filtered AE as precursor from July 5, 2011 to September 5, 2011. Cumulative probability  $C^+(r, \tau)$  for radius  $r$  ranging between 60 and 100 km, and time  $\tau$  varying from 1 week to 9 weeks.

	60 km	80 km	100 km
1 week	0.0080	0.0290	0.0829
2 weeks	0.0197	0.0592	0.1969
3 weeks	0.0252	0.0866	0.3288
4 weeks	0.0364	0.1081	0.3920
5 weeks	0.0517	0.1248	0.4538
6 weeks	0.0577	0.1308	0.5267
7 weeks	0.0577	0.1308	0.5625
8 weeks	0.0577	0.1308	0.5731
9 weeks	0.0577	0.1308	0.5776

TABLE 6: Filtered AE as aftershocks from July 5, 2011 to September 5, 2011. Cumulative probability  $C^-(r, \tau)$  for radius  $r$  ranging between 60 and 100 km, and time  $\tau$  varying from 1 week to 9 weeks.

	60 km	80 km	100 km
1 week	0.0042	0.0294	0.1149
2 weeks	0.0117	0.0464	0.1889
3 weeks	0.0203	0.0681	0.2521
4 weeks	0.0278	0.0935	0.3142
5 weeks	0.0292	0.1074	0.3604
6 weeks	0.0292	0.1202	0.4041
7 weeks	0.0292	0.1253	0.4151
8 weeks	0.0292	0.1292	0.4213
9 weeks	0.0292	0.1297	0.4218

**4.2. Recognizing Impending Earthquakes by means of AE.** In this section, we obtain a correlation between seismic and acoustic events through the application of the modified integral of Grassberger-Procaccia.

The data series of analyzed AE are shown in Figures 8 and 9, and are related to the abovementioned time intervals. The seismic events are taken from the website <http://iside.rm.ingv.it/iside/standard/result.jsp?rst=1&page=EVENTS#result> (seismic catalog of INGV, National Institute of Geophysics and Volcanology), selecting the events comprised in a circle of 100 km radius around the site of the Sacred Mountain of Varallo, during the defined AE monitoring periods (Figure 8).

Looking at the temporal distribution of earthquakes in relation to the cumulative AE trend, a quite good correspondence between AE peaks and earthquake events can be observed (Figures 9 and 10). By applying the modified correlation integral of Grassberger-Procaccia to the data series, we obtain the cumulative probabilities, as a function of the radius of interest  $r$  and of the interval of occurrence  $\tau$ , both considering the peak of Acoustic Emission as earthquake precursor or as aftershock (Tables 1–4).

The probability values obtained for the period May–June show that, regardless of the distance and of the correlation time, the probability of a seismic event following a peak of Acoustic Emission (AE Precursor) is always greater than the probability of the same AE peak being an effect of the damage caused by the earthquake (AE Aftershock) (Tables 1 and 2).

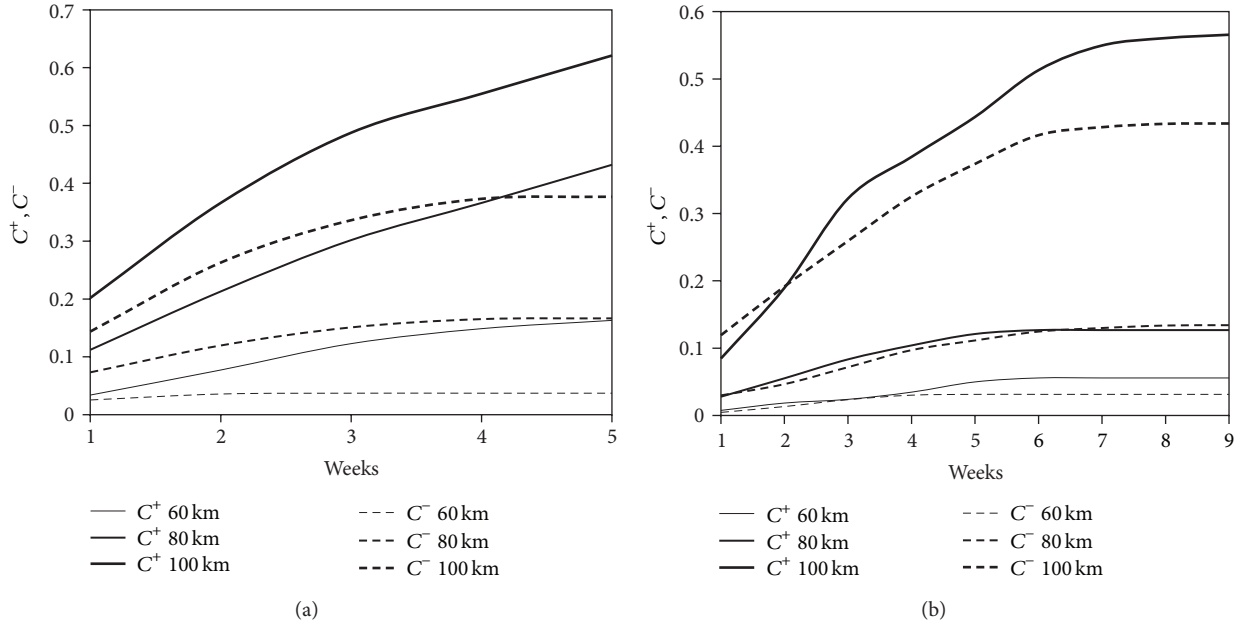


FIGURE 7: Evolution of the modified correlation integral for different time windows, during the two monitoring period. (a) Monitoring time from May 9, 2011 to June 16, 2011, see Tables 1 and 2. (b) Monitoring time from July 5, 2011 to September 5, 2011, see Tables 5 and 6.

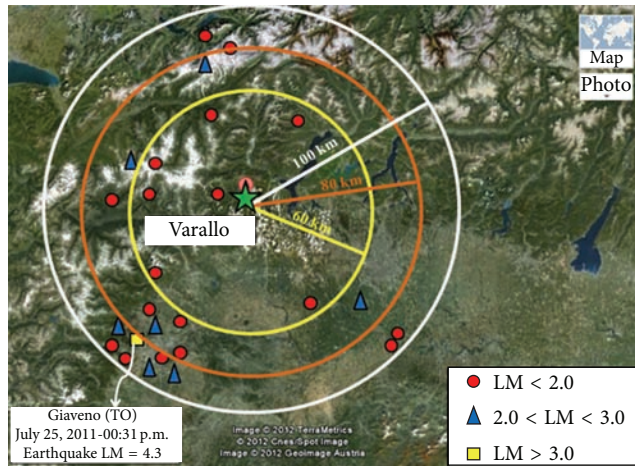


FIGURE 8: Seismic events around Varallo (Italy) from May, 2011 to September, 2011 (LM: local magnitude).

In practice, we see that the monitored structure behaves as a sensitive seismic receptor.

It is interesting to note that, for both monitoring periods, within a radius of 60 km from the monitored site, the AE signals still play their role as seismic precursors, as it can be assessed observing the values of the cumulative probability  $C^+$ . On the contrary, at distances of 80 km and 100 km, the character of AE occurrence is different (see Tables 3 and 4). In particular, we observe a clear reversal of the AE signal character from precursor to aftershock for the second monitoring period (July–September).

More in detail, within a radius of 60 km, there is a clear tendency of AE signals to anticipate earthquakes, and behave as precursors. At a distance of 80 km, AE are precursor signals

only in the time window comprised between 2 and 6 weeks, were  $C^+ > C^-$ . At a distance of 100 km, all the AE signals behave as aftershocks, being always  $C^+ < C^-$ .

In any case, it is worth distinguishing between the environmental contributions due to crustal trembling (external source), and the structural damage contributions (inner source) to AE activity on the Chapel XVII.

To better analyze the results from the second monitoring period (Tables 3 and 4), it is useful to discriminate the recorded signals assigning thresholds both in frequency and amplitude, which are consistent with the physical nature of Acoustic Emissions detected by the sensors. Looking at the USAM data stored, a good choice to discriminate the recorded signals is setting a frequency threshold equal to

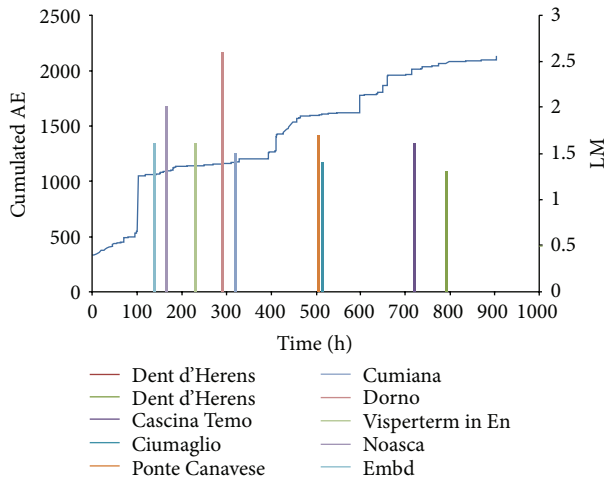


FIGURE 9: Sacred Mountain of Varallo: cumulated AE and seismic events from May 9, 2011 to June 16, 2011 (LM: local magnitude).

30 kHz, which divides the field VLF (Very Low Frequency) from the field LF (Low Frequency), and a signal amplitude threshold equal to 1 mV. The choice of the thresholds (amplitude and frequency) was based upon empirical considerations in order to emphasize the signals coming farther from the structure, which were characterized by lower frequencies and amplitudes.

The results are shown in Tables 5 and 6, where it can be easily recognized that filtered AE signals actually behave like seismic precursor. From a theoretical point of view, lower frequencies allow for the diffusion of the elastic waves in the masonry bulk, either intact or damaged, while higher frequency waves can propagate only through small heterogeneities [18–20]. Moreover, if constant velocity is assumed, the Lamb ratio [21] implies that the AE wavelength has to be larger than the size of the maximum inhomogeneity in order to travel through the ground up to the structure without significant modifications in its waveform [22]. On the other side, low amplitudes are reasonably related to the fact that an event captured by AE sensors on the monitored structure may have originated from a source that is physically distant from the monitored site (surrounding microseismicity that shakes the whole structure) and therefore is subject to the laws of amplitude damping [20].

## 5. Finite Element Modeling: Spectral Dynamic Analysis of the Chapel XVII

The Chapel XVII was discretized with three-dimensional linear pyramid elements, accounting for the accurate geometry of the stone masonry structure. The shapes of the cylindrical chapel and of the above spherical dome are precisely discretized, taking into account the various apertures, the inside internal vault supporting the Mount Tabor installation, and the outside pronao with columns. On the contrary, the wooden roof structure was considered only as an external load. The mesh of the structure is shown in Figure 11.

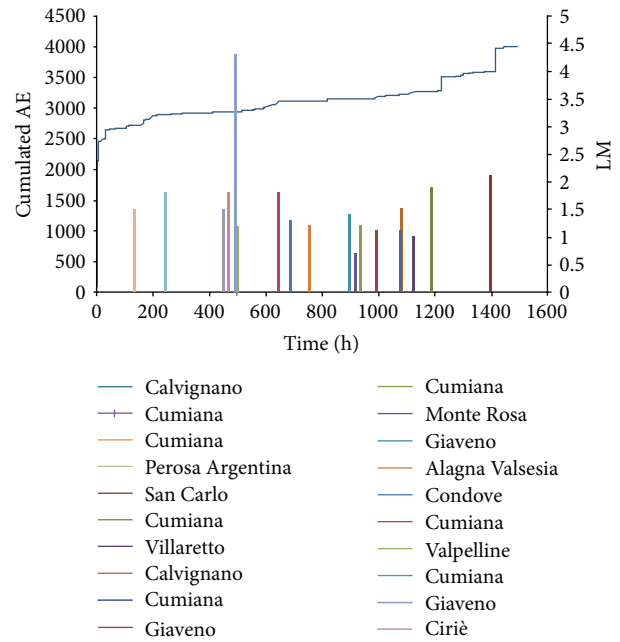


FIGURE 10: Sacred Mountain of Varallo: cumulated AE and seismic events from July 5, 2011 to September 5, 2011 (LM: local magnitude).

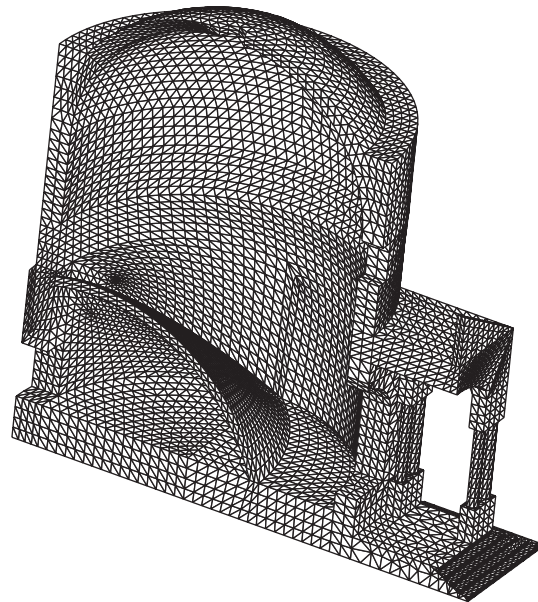


FIGURE 11: Finite element mesh of Chapel XVII: half of the model.

The finite element model is discretized using 30271 nodes, connected by 129689 elements, and is characterized by 86076 degrees of freedom. The elastic properties assumed for the masonry and the density, where, respectively, equal to  $E = 2 \times 10^9$  Pa;  $\nu = 0.3$ ;  $\gamma = 20$  kN/m<sup>3</sup>. For the dynamic analysis, the Elastic Response Spectrum of Acceleration  $S_d$  (g) is shown in Figure 12. It is obtained considering the geographic coordinates of the site of investigation, the soil

TABLE 7: Natural frequencies of the first 20 calculated modes of vibration of Chapel XVII and percentages of mass involved in each mode of vibration for directions X and Y in the horizontal plane.

Mode	Frequency (Hz)	Period (s)	X direction		Y direction	
			%	Cumulated%	%	Cumulated%
1	4.737	0.211	5.31E + 01	5.31E + 01	5.89E - 05	5.89E - 05
2	5.162	0.194	5.82E - 05	5.31E + 01	4.97E + 01	4.97E + 01
3	8.570	0.117	5.94E - 02	5.32E + 01	2.61E - 07	4.97E + 01
4	9.891	0.101	1.20E - 01	5.33E + 01	1.43E - 05	4.97E + 01
5	10.087	0.099	1.50E - 05	5.33E + 01	1.95E - 01	4.99E + 01
6	13.192	0.076	3.37E + 00	5.67E + 01	4.59E - 06	4.99E + 01
7	13.373	0.075	1.68E - 04	5.67E + 01	2.85E - 01	5.02E + 01
8	13.881	0.072	6.60E + 00	6.33E + 01	5.39E - 06	5.02E + 01
9	14.479	0.069	6.48E - 05	6.33E + 01	9.44E + 00	5.96E + 01
10	14.616	0.068	1.13E - 04	6.33E + 01	3.83E + 00	6.35E + 01
11	15.633	0.064	2.65E - 05	6.33E + 01	3.31E - 01	6.38E + 01
12	17.402	0.057	2.36E - 02	6.33E + 01	5.14E - 06	6.38E + 01
13	17.612	0.057	3.66E - 06	6.33E + 01	5.25E - 02	6.38E + 01
14	18.031	0.055	5.02E - 01	6.38E + 01	1.91E - 05	6.38E + 01
15	18.677	0.054	2.45E - 04	6.38E + 01	1.28E - 01	6.40E + 01
16	18.750	0.053	9.08E - 02	6.39E + 01	1.67E - 04	6.40E + 01
17	19.165	0.052	6.71E - 02	6.40E + 01	1.91E - 05	6.40E + 01
18	19.874	0.050	3.13E - 09	6.40E + 01	2.02E - 01	6.42E + 01
19	20.545	0.049	4.58E - 01	6.44E + 01	7.58E - 06	6.42E + 01
20	21.578	0.046	5.79E - 06	6.44E + 01	5.48E - 01	6.47E + 01

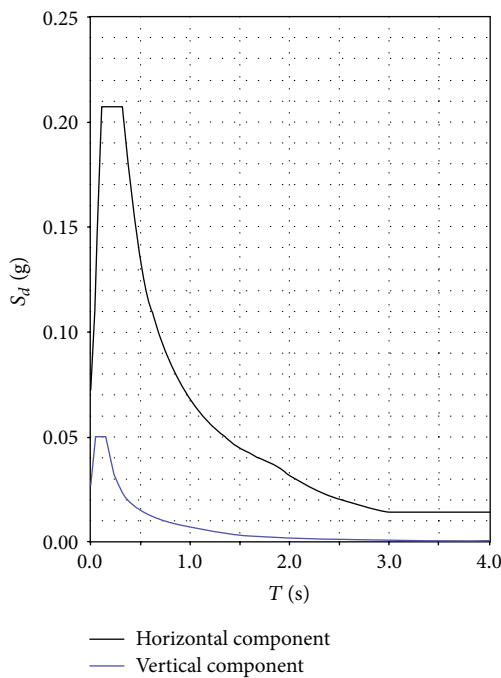


FIGURE 12: Elastic response spectrum of acceleration  $S_d$  (g).

characteristics, a nominal life of the structure equal to 400 years, and a probability to exceed the acceleration spectrum equal to 5% in 400 years. The structural damping of masonry

is considered to be equal to 5%. The vertical component of the Spectrum is neglected [23].

The dynamic analysis, performed with the commercial finite element code DIANA [24] allows for a preliminary assessment of the modal behavior of the structure. Table 7 shows natural frequencies and periods of the first 20 calculated modes of vibration of Chapel XVII, and percentages of mass involved in each mode of vibration for directions X and Y in the horizontal plane. The first 3 modes of vibration of the structure are shown in Figure 13.

Figure 14 shows the contour of the principal tensile stress during simulated earthquake, reported on the deformed shape of the structure. The total combination of the seismic effects is performed using the Square Root of the Sum of the Squares (SRSS) method. The tensile stresses calculated on the internal wall of the chapel, subjected to dead loads and an earthquake in the X direction, justify the presence of the two symmetric dominant cracks detected by a visual inspection. Figure 15 shows the deformed shape of the structure compared to the initial shape under the effect of the dead loads only. The deformation clearly shows the opening mechanism due to the effect of the pronao settlement, as well as to the thrust of the internal vault that supports the Mount Tabor installation.

The FEM analysis provides stress levels under dead loads near to the vertical cracks that are not so high for a stone masonry with mortar joints (see Figures 14 and 15). Therefore, the stability assessment derived by AE monitoring, reported in Section 2, is confirmed and a stable behavior of fractures is

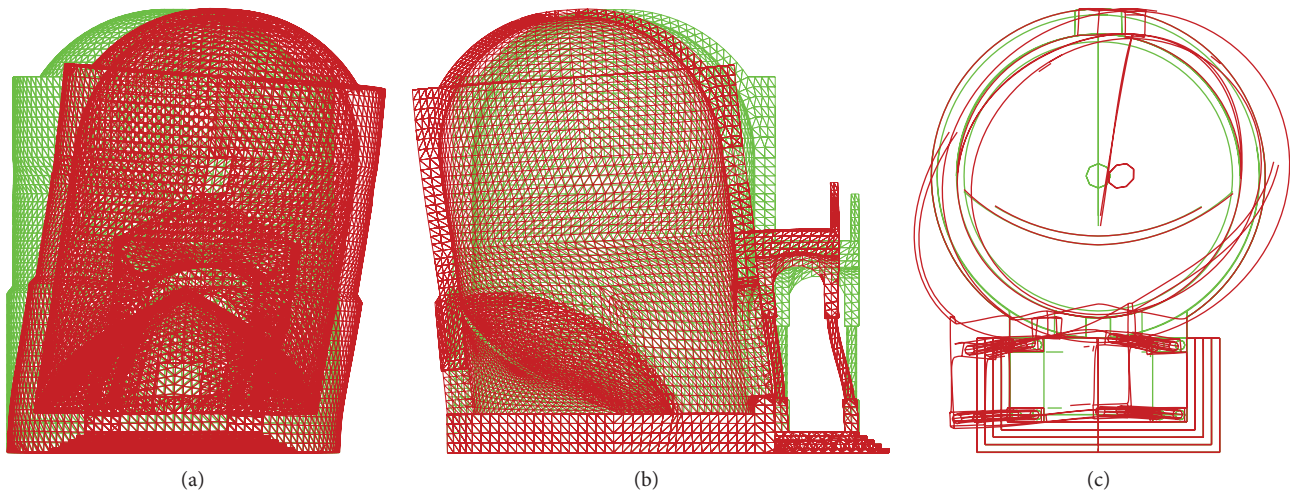


FIGURE 13: Chapel XVII mode 1 of vibration (a); Chapel XVII mode 2 of vibration (b); Chapel XVII mode 3 of vibration (c).

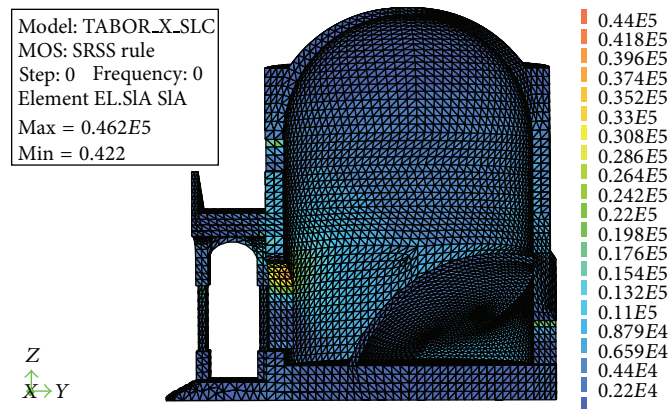


FIGURE 14: Chapel XVII principal SRSS stress contour, measured in Pa, during simulated earthquake in the X direction.

identified. On the other hand, the dynamic FEM analysis, in correspondence to the main seismic events, locally identifies levels of stress that agree well with the nucleation of microcracks after the arrival of the main seismic shockwave, which is detected as the AE aftershocks as described in Section 4.

A more detailed mechanical characterization of the masonry is currently under development to perform the subsequent nonlinear analysis.

## 6. Conclusions

Besides the canonical use in nondestructive tests, the heuristic potential of AE monitoring of civil structures for earthquakes prediction appears very intriguing. Starting from the assumption that any structure should not be regarded as separated from its environment, a method of correlating AE activity on the Renaissance Complex of the Sacred Mountain of Varallo subjected to a long-term monitoring with regional seismicity is investigated. Two qualitatively very similar phenomena such as Acoustic Emission and

earthquakes become two aspects of a unique phenomenon, which looks self-similar.

Furthermore, in this work, by applying the modified Grassberger-Procaccia correlation algorithm, with the aim of explaining the correlation between regional seismicity and Acoustic Emission emerging from the Chapel XVII of the Sacred Mountain of Varallo, it is observed that the structure behaves as sensitive receptors for earthquakes occurring within a radius of about 100 km, distinguishing environmental contributions to AE activity on the Chapel XVII due to crustal trembling (external source) from contributions due to structural damage (inner source). An accurate finite element model, performed with DIANA finite element code for the dynamic analysis of Chapel XVII structure, is utilized to confirm visual inspections and monitoring the results of the earthquakes' effects.

### Acknowledgments

The financial support that is provided by the Piedmont Region (Italy) to the Project “*Preservation, Safeguard, and*

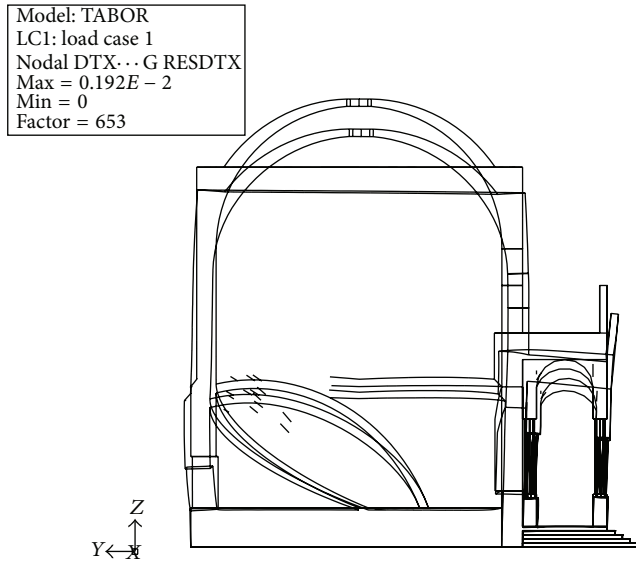


FIGURE 15: Chapel XVII deformed shape.

*Valorisation of Masonry Decorations in the Architectural Historical Heritage of Piedmont*” (RE-FRESCOS) is gratefully acknowledged.

## References

- [1] E. de Filippis, *Sacro Monte of Varallo*, Borgosesia, 2009.
- [2] G. Lacidogna, A. Manuello, G. Niccolini, and A. Carpinteri, “Acoustic emission monitoring of Italian historical buildings and the case study of the Athena temple in Syracuse,” *Architectural Science Review*, 2012.
- [3] A. Carpinteri, S. Invernizzi, G. Lacidogna, and F. Accornero, “Acoustic emission monitoring of frescos degradation in a XVIIIth century chapel of the “Sacred Mountain of Varallo” (Italy),” in *Proceedings of the 8th International Conference on Structural Analysis of Historical Constructions*, J. Jasinko, Ed., Wroclaw, Poland, 2012.
- [4] A. Anzani, L. Binda, A. Carpinteri, G. Lacidogna, and A. Manuello, “Evaluation of the repair on multiple leaf stone masonry by acoustic emission,” *Materials and Structures*, vol. 41, no. 6, pp. 1169–1189, 2008.
- [5] A. Carpinteri, G. Lacidogna, S. Invernizzi, A. Manuello, and L. Binda, “Stability of the vertical bearing structures of the Syracuse Cathedral: experimental and numerical evaluation,” *Materials and Structures*, vol. 42, no. 7, pp. 877–888, 2009.
- [6] A. Carpinteri and G. Lacidogna, “Structural monitoring and integrity assessment of medieval towers,” *Journal of Structural Engineering*, vol. 132, no. 11, pp. 1681–1690, 2006.
- [7] A. Carpinteri, G. Lacidogna, and G. Niccolini, “Acoustic emission monitoring of medieval towers considered as sensitive earthquake receptors,” *Natural Hazards and Earth System Science*, vol. 7, no. 2, pp. 251–261, 2007.
- [8] A. Carpinteri, G. Lacidogna, and N. Pugno, “Structural damage diagnosis and life-time assessment by acoustic emission monitoring,” *Engineering Fracture Mechanics*, vol. 74, no. 1-2, pp. 273–289, 2007.
- [9] A. Carpinteri and G. Lacidogna, “Damage evaluation of three masonry towers by acoustic emission,” *Engineering Structures*, vol. 29, no. 7, pp. 1569–1579, 2007.
- [10] G. Niccolini, A. Carpinteri, G. Lacidogna, and A. Manuello, “Acoustic emission monitoring of the Syracuse Athena temple: scale invariance in the timing of ruptures,” *Physical Review Letters*, vol. 106, no. 10, Article ID 108503, 2011.
- [11] C. Richter, *Elementary Seismology*, W. H. Freeman, San Francisco, Calif, USA, 1958.
- [12] A. Carpinteri, G. Lacidogna, and N. Pugno, “Richter’s laws at the laboratory scale interpreted by acoustic emission,” *Magazine of Concrete Research*, vol. 58, no. 9, pp. 619–625, 2006.
- [13] C. H. Scholz, “The frequency-magnitude relation of microfracturing in rock and its relation to earthquakes,” *Bulletin of the Seismological Society of America*, vol. 58, pp. 399–415, 1968.
- [14] G. P. Gregori and G. Paparo, “Acoustic emission: a diagnostic tool for environmental sciences and for non destructive tests (with a potential application to gravitational antennas),” in *Meteorological and Geophysical Fluid Dynamics*, Schroeder, Bremen, Germany, 2005.
- [15] G. P. Gregori, G. Paparo, M. Poscolieri, and A. Zanini, “Acoustic emission and released seismic energy,” *Natural Hazards and Earth System Science*, vol. 5, no. 6, pp. 777–782, 2005.
- [16] B. A. Bolt, *Earthquakes*, W. H. Freeman, San Francisco, Calif, USA, 1978.
- [17] P. Grassberger and I. Procaccia, “Characterization of strange attractors,” *Physical Review Letters*, vol. 50, no. 5, pp. 346–349, 1983.
- [18] D. G. Aggelis, “Classification of cracking mode in concrete by acoustic emission parameters,” *Mechanics Research Communications*, vol. 38, no. 3, pp. 153–157, 2011.
- [19] D. G. Aggelis, A. C. Mpaskas, D. Ntalakas, and T. E. Matikas, “Effect of wave distortion on acoustic emission characterization of cementitious materials,” *Construction and Building Materials*, vol. 35, pp. 183–190, 2012.
- [20] D. G. Aggelis, T. Shiotani, A. Papacharalampopoulos, and D. Polyzos, “The influence of propagation path on elastic waves as measured by acoustic emission parameters,” *Structural Health Monitoring*, vol. 11, no. 3, pp. 359–366, 2012.
- [21] H. Lamb, “On waves in an elastic plate,” *Proceedings of the Royal Society A*, vol. 93, no. 648, pp. 114–128, 1917.
- [22] E. N. Landis and S. P. Shah, “Frequency-dependent stress wave attenuation in cement-based materials,” *Journal of Engineering Mechanics*, vol. 121, pp. 737–743, 1995.
- [23] Decreto del Ministero delle Infrastrutture 14 Gennaio 2008, Norme Tecniche per le Costruzioni. Gazzetta Ufficiale della Repubblica Italiana no. 29 del 4 Febbraio 2008 (Italian).
- [24] J. Maine, *DIANA. Finite Element Analysis User’s Manual. Release 9.4.4*, TNO DIANA bv, Delft, The Netherlands, 2012.

## Research Article

# Unsupervised Performance Evaluation Strategy for Bridge Superstructure Based on Fuzzy Clustering and Field Data

**Yubo Jiao, Hanbing Liu, Peng Zhang, Xianqiang Wang, and Haibin Wei**

*College of Transportation, Jilin University, Changchun 130025, China*

Correspondence should be addressed to Haibin Wei; [weihb@jlu.edu.cn](mailto:weihb@jlu.edu.cn)

Received 8 July 2013; Accepted 1 September 2013

Academic Editors: D. G. Aggelis and N. Alver

Copyright © 2013 Yubo Jiao et al. This is an open access article distributed under the Creative Commons Attribution License, which permits unrestricted use, distribution, and reproduction in any medium, provided the original work is properly cited.

Performance evaluation of a bridge is critical for determining the optimal maintenance strategy. An unsupervised bridge superstructure state assessment method is proposed in this paper based on fuzzy clustering and bridge field measured data. Firstly, the evaluation index system of bridge is constructed. Secondly, a certain number of bridge health monitoring data are selected as clustering samples to obtain the fuzzy similarity matrix and fuzzy equivalent matrix. Finally, different thresholds are selected to form dynamic clustering maps and determine the best classification based on statistic analysis. The clustering result is regarded as a sample base, and the bridge state can be evaluated by calculating the fuzzy nearness between the unknown bridge state data and the sample base. Nanping Bridge in Jilin Province is selected as the engineering project to verify the effectiveness of the proposed method.

## 1. Introduction

With the sustained growth of road traffic and influence of external environment such as temperature, carbonation, and corrosion, the number of deteriorated bridges has increased dramatically. Their safe operation and service life are seriously threatened [1–3]. Therefore, the maintenance and repair management become particularly important. However, the human and financial resources are limited in many countries. How to determine the optimal maintenance program is critical in practice. With the development of systems theory and computer technology, bridge management system has been widely used. In order to achieve an appropriate management, the performance condition for deteriorated bridge must be evaluated [4–8].

The methods that are used for condition evaluation include existing national evaluation norms, analytic hierarchy process (AHP), and neural networks and fuzzy logic. The most widely used code in China for bridge condition assessment is “Code for maintenance of highway bridges and culvers” [9]. This code divides the bridge components into seventeen parts. Based on severity, influence degree, and changes of damage condition, the grade can be evaluated for each substructure using cumulative scores. The technical condition

of entire bridge can be assessed by considering weights of seventeen parts. Sasmal and Ramanjaneyulu [10] developed a systematic procedure and formulations for condition evaluation of existing bridges using analytic hierarchy process in a fuzzy environment. Kawamura et al. [11] presented a novel approach for developing a performance evaluation system for concrete slabs of existing bridges based on neural networks and fuzzy inference. The numerical examples and conclusions reveal that the proposed approach demonstrates real potential for practical applications. Tarighat and Miyamoto [12] introduced a new fuzzy method to deal with uncertainties from inspection data, which was practically based on both subjective and objective results of existing inspection methods and tools. Wang and Elhag [13] proposed a fuzzy group decision making (FGDM) approach for bridge risk assessment. Case study revealed that the FGDM approach was a flexible, practical, and effective way of modeling bridge risks.

However, there are some drawbacks for these methods in practical application. Firstly, the adoption of evaluation index system and selection of indicators are not specific. Secondly, the scoring process for indicators is affected by subjective factors especially in existing norms. Thirdly, the determination of membership function for widely applied fuzzy logic system is difficult. Therefore, reduction of uncertainties from

subjective factors is significant for improving the effectiveness in the process of evaluation.

Since state assessment methods of the existing bridge are easily influenced by subjective factors, this paper proposes an unsupervised bridge superstructure state assessment method based on fuzzy clustering according to bridge field measured data. Practical engineering is presented to verify its feasibility.

## 2. Theoretical Background

**2.1. Theory of Fuzzy Clustering.** Traditional sample classification method belongs to supervised learning style which realizes the classification through specific standards. However, fuzzy clustering method can conduct the process based on properties of the sample characteristics, and it is unsupervised. The criterion for classification is not consistent and possesses apparent dynamic characteristics. It can establish the uncertainty description of samples and more precisely reveals the actual situation [14–16].

(1) *Standardization for Clustering Data.*  $x = \{x_1, x_2, \dots, x_n\}$  is the vector of data for classification, and each data possesses  $m$  properties, and  $x_i$  can be represented by

$$x_i = [x_{i1}, x_{i2}, \dots, x_{im}]. \quad (1)$$

An original data matrix can be constructed as follows:

$$X = \begin{bmatrix} x_{11} & x_{12} & \cdots & x_{1m} \\ x_{21} & x_{22} & \cdots & x_{2m} \\ \cdots & \cdots & \cdots & \cdots \\ x_{n1} & x_{n2} & \cdots & x_{nm} \end{bmatrix}, \quad (2)$$

where  $x_{ij}$  is the  $j$ th property of the  $i$ th classification object.

The normalized matrix  $X'$  can be calculated from the following equation:

$$x'_{ij} = \frac{x_{ij} - \min_{1 \leq i \leq n}(x_{ij})}{\max_{1 \leq i \leq n}(x_{ij}) - \min_{1 \leq i \leq n}(x_{ij})} \quad j = 1, 2, \dots, m. \quad (3)$$

(2) *Construction of Fuzzy Similarity Matrix.*  $r_{ij}$  is the similarity degree between  $x_i$  and  $x_j$ ; it can be calculated as

$$r_{ij} = \frac{\sum_{k=1}^m (x_{ik} - \bar{x}_i)(x_{jk} - \bar{x}_j)}{\sqrt{\sum_{k=1}^m (x_{ik} - \bar{x}_i)^2 \sum_{k=1}^m (x_{jk} - \bar{x}_j)^2}}, \quad (4)$$

where  $\bar{x}_i = (1/m) \sum_{k=1}^m x_{ik}$ ,  $\bar{x}_j = (1/m) \sum_{k=1}^m x_{jk}$ .

(3) *Clustering Analysis.* The fuzzy similarity matrix calculated by (4) only satisfies the reflexivity and symmetry but not with transitivity. In order to conduct clustering analysis, the corresponding fuzzy equivalent matrix must be obtained. In this paper, successive square method is used to calculate the equivalent matrix as shown in

$$R^* = t(R) = R^{2k}, \quad R^{2k} = R^{2k-1}, \quad (5)$$

where  $R^* = t(R)$  and  $t(R)$  are the fuzzy equivalent matrices  $R^*$ .

By selecting appropriate thresholds  $\lambda \in [0, 1]$ , the dynamic clustering map can be obtained through its truncated matrix  $R_\lambda^* = t_\lambda(R)$ .

(4) *Determination of Best Classification Threshold.*  $X = \{x_1, x_2, \dots, x_n\}$  is the objects for classification,  $x_j = [x_{j1}, x_{j2}, \dots, x_{jm}]$ , and  $x_{jk}$  is the  $k$ th feature of  $x_j$  ( $k = 1, 2, \dots, m$ ).  $r$  is the classification number corresponding to  $\lambda$ , and  $n_i$  is the number for the  $i$ th category. The average value for  $k$ th eigenvalue of  $i$ th category can be calculated as follows

$$\bar{x}_{ik} = \frac{1}{n_i} \sum_{j=1}^{n_i} x_{jk}, \quad k = 1, 2, \dots, m. \quad (6)$$

The average value for  $k$ th eigenvalue of all data can be calculated using

$$\bar{x}_k = \frac{1}{n} \sum_{j=1}^n x_{jk}, \quad k = 1, 2, \dots, m. \quad (7)$$

Assuming that  $P$  ( $P \leq n$ ) is the scheme number for classification,  $F$ -statistics analysis is used for determining the best classification threshold; it can be calculated by (8). The bigger  $F$  is, the better it is for classification. Consider the following equation:

$$F = \frac{\sum_{i=1}^r n_i \sum_{k=1}^m (\bar{x}_{ik} - \bar{x}_k)^2 / (r-1)}{\sum_{i=1}^r \sum_{j=1}^{n_i} \sum_{k=1}^m (x_{ik} - \bar{x}_{jk})^2 / (n-r)} \sim F(r-1, n-r). \quad (8)$$

## 2.2. Theory of Fuzzy Nearness and Approaching Principle

(1) *Fuzzy Nearness.* Given that  $A$  and  $B$  are fuzzy sets in domain  $F(U)$ , denoted by  $A, B \in F(U)$ , the inner and outer products between  $A$  and  $B$  are defined by [17]

$$A \bullet B = \bigvee_{i=1}^n (A(i) \wedge B(i)),$$

$$A \otimes B = \bigwedge_{x \in U} (A(x) \vee B(x)),$$

where  $A \bullet B$  and  $A \otimes B$  are, respectively the inner and outer products, symbols  $\vee$  and  $\wedge$  are, respectively, used to obtain maximum and minimum values.

The fuzzy nearness between  $A$  and  $B$  is defined by

$$(A, B) = \frac{1}{2} [A \bullet B + A \otimes B], \quad (10)$$

where  $(A, B)$  is the fuzzy nearness between  $A$  and  $B$ .  $0 \leq (A, B) \leq 1$ ; the bigger  $(A, B)$  is, the better the nearness between  $A$  and  $B$  is.

(2) *Approaching Principle.* Given  $A_1, A_2, \dots, A_n \in F(U)$  are the fuzzy sets. For fuzzy set  $B$ , if  $\exists i \in \{1, 2, \dots, n\}$ ,  $(B, A_i) = \max_{1 \leq j \leq n} (B, A_j)$ , then the nearness between  $A_i$  and  $B$  is much better, and fuzzy set  $B$  can be classified into fuzzy set  $A_i$ .

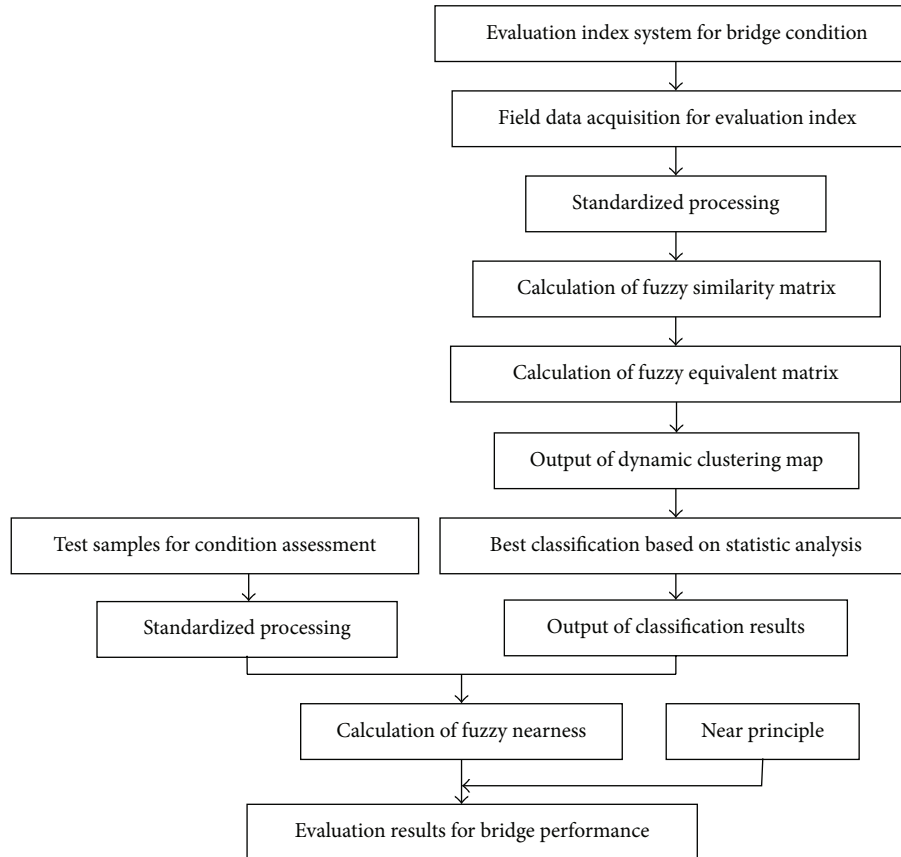


FIGURE 1: Calculation process of bridge condition evaluation based on fuzzy clustering and field data.

### 3. Technical Route of Bridge Condition Evaluation Using Fuzzy Clustering

The technical route used in this paper for condition evaluation of bridge by fuzzy clustering is shown in Figure 1.

### 4. Fuzzy Clustering-Based Method for Bridge Condition Evaluation

**4.1. Construction of Index System for Bridge Condition Evaluation.** In the process of condition evaluation, the index system must scientifically, rationally, and objectively reflect the actual working status of the bridge. The index system for medium and small span bridge is determined based on the principle of integrity, simplicity, objectivity, and representativity in this paper, and it is shown in Figure 2.

**4.2. Construction of Evaluation System Based on Fuzzy Clustering.** The relative depth of carbonation calculated by (11) is used as evaluation index for degree of concrete carbonation

$$C_d = \frac{x_c}{x}, \quad (11)$$

where  $x_c$  is the average depth of carbonation for bridge members,  $x$  is the average thickness of the reinforced protective layer.

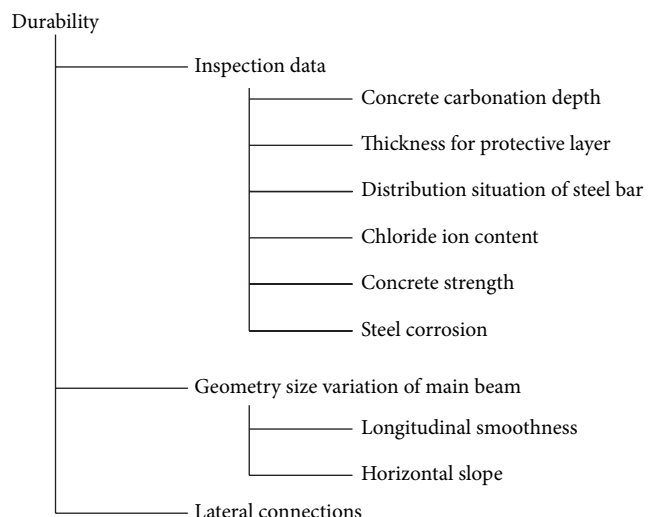


FIGURE 2: Index system for condition evaluation of bridge superstructure.

Relative value of the protective layer thickness calculated by (12) is treated as evaluation index of protective layer thickness parameter

$$P_t = \frac{P_m}{P_d}, \quad (12)$$

where  $P_m$  is measured value, while  $P_d$  is design value.



FIGURE 3: Overview of Nanping Bridge.

The evaluation index for distribution situation of steel bar is shown in (13). The spacing between the rebars can be measured through electromagnetic induction technology

$$S_d = \frac{s_m}{s_d}, \quad (13)$$

where  $s_m$  is the measured value for steel bar spacing, while  $s_d$  is design value.

The percentage of chloride ion content in cement content is used as evaluation index of chlorine ion parameters; it is denoted by  $C_l$ .

The evaluation index for concrete strength is calculated by

$$K_{bm} = \frac{R_{im}}{R}, \quad (14)$$

where  $R_{im}$  is average value which can be measured by core testing, while  $R$  is the design strength of concrete.

Minimum value of steel corrosion potential is treated as evaluation index of steel corrosion parameters; it is denoted by  $R_c$ .

The percentage of deviated measured points in the total points ( $L_R$ ) is used as evaluation index for longitudinal smoothness.

The percentage of offset value that exceeds  $\pm 0.3\%$  in the total points ( $T_R$ ) is used as evaluation index for transverse slope.

Crack width of joint concrete ( $C_w$ ) is adopted as the evaluation index for lateral connections.

The inspection data for ten bridges are selected as clustering samples for condition evaluation; these samples should possibly cover every bridge condition. They are listed in Table 1.

The calculated fuzzy equivalence matrix based on fuzzy clustering theory is listed in Table 2.

Different thresholds  $\lambda$  are adopted for clustering analysis; its dynamic process is listed in Table 3.

Firstly, we determined the effective classification quantity (3, 4, 5, and 6), and  $F$ -statistics analysis is used to determine the best classification. The calculation results of  $F_{0.05}$  and  $F$  are listed in Table 4.

TABLE 1: Field data for bridge durability evaluation.

	$C_d$	$P_t$	$S_d$	$C_l$	$K_{bm}$	$R_c$	$L_R$	$T_R$	$C_w$
1	1.2	0.79	0.97	0.52	0.93	-305	15	5	0.31
2	0.1	1.0	0.98	0.02	1.1	-12	05	0	0
3	0.7	0.87	0.96	0.31	0.97	-205	5	3	0.16
4	0.2	0.98	1.0	0.05	1.08	-35	0	0	0.02
5	0.3	0.98	0.99	0.08	1.1	-56	2	0	0.06
6	0.7	0.86	0.96	0.26	0.99	-182	6	2	0.12
7	1.8	0.62	0.95	0.88	0.90	-369	18	9	0.45
8	1.3	0.81	0.97	0.61	0.95	-256	14	7	0.36
9	0.8	0.87	0.96	0.28	0.98	-212	7	2	0.13
10	2.1	0.55	0.96	0.92	0.84	-356	20	12	0.52

As can be seen from Table 4, when  $\lambda = 0.9684$ , the gap between  $F$  and  $F_{0.05}$  is the largest. Therefore, four categories are the best classification; the detailed results are {2, 4, 5}, {3, 6, 9}, {1, 8}, and {7, 10}.

The durability condition can be determined combined with service time of bridge; the year of opening for each bridge are listed in Table 5.

As can be seen from Table 5, the service time for {2, 4, 5} is the shortest; therefore, its condition is “very good”. Similarly, {3, 6, 9} is “good,” {1, 8} is “ordinary,” and {7, 10} is “poor.”

**4.3. Engineering Verification.** Ten samples for durability evaluation are classified into four categories, and their conditions are determined through service time. The clustering results can be treated as database for assessment; the average value corresponding to each index is regarded as the center of this category as shown in Table 6, and the other bridges can be evaluated based on approaching principle through calculation of fuzzy nearness.

Nanping Bridge was built in 2005; there are totally eight spans, and they are simply supported T-beam bridges. Its overview is shown in Figure 3. The inspection data are listed in Table 7.

The calculation results of fuzzy nearness between field data of Nanping Bridge and category center for durability evaluation are listed in Table 8.

TABLE 2: Fuzzy equivalence matrix for durability evaluation index system.

1	0.5732	0.5732	0.5732	0.5732	0.5732	0.9059	0.9737	0.5732	0.9059
0.5732	1	0.8836	0.9885	0.9920	0.8836	0.5732	0.5732	0.8836	0.5732
0.5732	0.8836	1	0.8836	0.8836	0.9933	0.5732	0.5732	0.9933	0.5732
0.5732	0.9885	0.8836	1	0.9885	0.8836	0.5732	0.5732	0.8836	0.5732
0.5732	0.9920	0.8836	0.9885	1	0.8836	0.5732	0.5732	0.8836	0.5732
0.5732	0.8836	0.9933	0.8836	0.8836	1	0.5732	0.5732	0.9942	0.5732
0.9059	0.5732	0.5732	0.5732	0.5732	0.5732	1	0.9059	0.5732	0.9684
0.9737	0.5732	0.5732	0.5732	0.5732	0.5732	0.9059	1	0.5732	0.9059
0.5732	0.8836	0.9933	0.8836	0.8836	0.9942	0.5732	0.5732	1	0.5732
0.9059	0.5732	0.5732	0.5732	0.5732	0.5732	0.9684	0.9059	0.5732	1

TABLE 3: Dynamic clustering results using different thresholds.

$\lambda$	Clustering results									
	1	2	3	4	5	6	7	8	9	10
0.5732	{1, 2, 3, 4, 5, 6, 7, 8, 9, 10}									
0.8836		{2, 3, 4, 5, 6, 9}, {1, 7, 8, 10}								
0.9059			{2, 4, 5}, {3, 6, 9}, {1, 7, 8, 10}							
0.9684				{2, 4, 5}, {3, 6, 9}, {1, 8}, {7, 10}						
0.9737					{2, 4, 5}, {3, 6, 9}, {1, 8}, {7}, {10}					
0.9885						{2, 4, 5}, {3, 6, 9}, {1}, {8}, {7}, {10}				
0.9920							{2, 5}, {4}, {3, 6, 9}, {1}, {8}, {7}, {10}			
0.9933								{2}, {4}, {5}, {3, 6, 9}, {1}, {8}, {7}, {10}		
0.9942									{2}, {3}, {4}, {5}, {6, 9}, {1}, {8}, {7}, {10}	

TABLE 4:  $F$ -statistics calculation results for each program.

Classification quantity	3	4	5	6
$\lambda$	0.9059	0.9684	0.9737	0.9885
$F$	7.44	107.3	66.28	74.86
$F_{0.05}$	4.74	4.76	5.19	6.26
$F - F_{0.05}$	2.7	102.54	61.09	68.6

TABLE 5: Opening data for bridge.

No.	1	2	3	4	5	6	7	8	9	10
Date	1996	2011	2001	2009	2006	1999	1985	1994	1996	1980

TABLE 6: Category center for durability evaluation.

Category	$C_d$	$P_t$	$S_d$	$C_l$	$K_{bm}$	$R_c$	$L_R$	$T_R$	$C_w$
Very good	0.2	0.99	0.99	0.05	1.09	-34	2.33	0	0.03
Good	0.73	0.87	0.96	0.28	0.98	-200	6	2.33	0.14
Ordinary	1.25	0.80	0.97	0.57	0.94	-281	14.5	6	0.34
Poor	1.95	0.59	0.96	0.9	0.87	-363	19	10.5	0.49

TABLE 7: Field data for durability evaluation of Nanping Bridge.

Index	$C_d$	$P_t$	$S_d$	$C_l$	$K_{bm}$	$R_c$	$L_R$	$T_R$	$C_w$
Field data	1.2	0.92	0.90	0.8	0.92	-286	10	10	0.96

As shown in Table 8, the fuzzy nearness between field data and “poor” is the largest. Therefore, the durability of Nanping Bridge can be evaluated as “poor”, and it needs

TABLE 8: Fuzzy nearness between field data and category center of Nanping Bridge.

Category	Very good	Good	Ordinary	Poor
Fuzzy nearness	0.6611	0.6184	0.6816	0.8171



FIGURE 4: Traffic volume of Nanping Bridge.

enhancement of the conservation and maintenance. This bridge bears heavy traffic load through investigation and analysis of the traffic (Figure 4), and the evaluation result is consistent with the actual situation. It reveals that the proposed method possesses satisfactory results.

## 5. Conclusions

A fuzzy clustering-based condition assessment method is proposed in this paper. Firstly, this method builds the durability evaluation index system of bridges based on field measured parameters. And then, a certain number of bridge health monitoring data is selected as clustering samples to obtain the fuzzy similarity matrix and fuzzy equivalent matrix of samples by calculation. Finally, different thresholds are used to form dynamic clustering map and determine the best classification based on statistic analysis. The clustering result is regarded as a sample base of bridge durability state assessment. Taking the average of the corresponding indicators of the same type bridges as the approximate center of this category, this method can analyze and evaluate the bridge state for assessment on the basis of selecting the near principle by calculating the fuzzy nearness between the

unknown bridge state data and the center's. Nanping Bridge is used as the physical works of the bridge durability assessment to verify the effectiveness.

The fuzzy clustering method proposed in this paper is convenient to implement. However, the disproportionality of index system is not considered. In practical engineering, each index does not have the same effect for the durability assessment of the bridge. In future work, index weight will be considered in the process of fuzzy clustering-based condition assessment of bridge.

## Acknowledgement

The authors express their appreciation for the financial support of National Natural Science Foundation of China under Grant nos. 51378236 and 51278222.

## References

- [1] M. Chandrashekhar and R. Ganguli, "Uncertainty handling in structural damage detection using fuzzy logic and probabilistic simulation," *Mechanical Systems and Signal Processing*, vol. 23, no. 2, pp. 384–404, 2009.
- [2] R. Palma, G. Rus, and R. Gallego, "Probabilistic inverse problem and system uncertainties for damage detection in piezoelectrics," *Mechanics of Materials*, vol. 41, no. 9, pp. 1000–1016, 2009.
- [3] E. P. Carden and P. Fanning, "Vibration based condition monitoring: a review," *Structural Health Monitoring*, vol. 3, no. 4, pp. 355–377, 2004.
- [4] J. De Brito, F. A. Branco, P. Thoft-Christensen, and J. D. Sørensen, "An expert system for concrete bridge management," *Engineering Structures*, vol. 19, no. 7, pp. 519–526, 1997.
- [5] P.-Q. Xia and J. M. W. Brownjohn, "Bridge structural condition assessment using systematically validated finite-element model," *Journal of Bridge Engineering*, vol. 9, no. 5, pp. 418–423, 2004.
- [6] Y.-M. Wang and T. M. S. Elhag, "Evidential reasoning approach for bridge condition assessment," *Expert Systems with Applications*, vol. 34, no. 1, pp. 689–699, 2008.
- [7] Y.-M. Wang and T. M. S. Elhag, "An adaptive neuro-fuzzy inference system for bridge risk assessment," *Expert Systems with Applications*, vol. 34, no. 4, pp. 3099–3106, 2008.
- [8] N.-F. Pan, T.-C. Lin, and N.-H. Pan, "Estimating bridge performance based on a matrix-driven fuzzy linear regression model," *Automation in Construction*, vol. 18, no. 5, pp. 578–586, 2009.
- [9] *Code for Maintenance of Highway Bridges and Culvers*, China Communications Press, 2004.
- [10] S. Sasmal and K. Ramanjaneyulu, "Condition evaluation of existing reinforced concrete bridges using fuzzy based analytic hierarchy approach," *Expert Systems with Applications*, vol. 35, no. 3, pp. 1430–1443, 2008.
- [11] K. Kawamura, A. Miyamoto, D. M. Frangopol, and R. Kimura, "Performance evaluation of concrete slabs of existing bridges using neural networks," *Engineering Structures*, vol. 25, no. 12, pp. 1455–1477, 2003.
- [12] A. Tarighat and A. Miyamoto, "Fuzzy concrete bridge deck condition rating method for practical bridge management system," *Expert Systems with Applications*, vol. 36, no. 10, pp. 12077–12085, 2009.
- [13] Y.-M. Wang and T. M. S. Elhag, "A fuzzy group decision making approach for bridge risk assessment," *Computers & Industrial Engineering*, vol. 53, no. 1, pp. 137–148, 2007.
- [14] Y. M. Sebzalli and X. Z. Wang, "Knowledge discovery from process operational data using PCA and fuzzy clustering," *Engineering Applications of Artificial Intelligence*, vol. 14, no. 5, pp. 607–616, 2001.
- [15] L. Podofillini, E. Zio, D. Mercurio, and V. N. Dang, "Dynamic safety assessment: scenario identification via a possibilistic clustering approach," *Reliability Engineering and System Safety*, vol. 95, no. 5, pp. 534–549, 2010.
- [16] S. Y. Li, *Engineering Fuzzy Mathematics with Application*, Harbin Institute of Technology Press, 2004.
- [17] H. B. Liu, Y. B. Jiao, Y. C. Cheng, and Y. F. Gong, "Reduction of uncertainties for damage identification of bridge based on fuzzy nearness and modal data," *Journal of Applied Mathematics*, vol. 2012, Article ID 812932, 13 pages, 2012.

## Research Article

# Static Testing of a Bridge Using an Interferometric Radar: The Case Study of “Ponte degli Alpini,” Belluno, Italy

**Devis Dei, Daniele Mecatti, and Massimiliano Pieraccini**

*Department of Information Engineering, University of Florence, Via Santa Marta 3, 50139 Firenze, Italy*

Correspondence should be addressed to Massimiliano Pieraccini; massimiliano.pieraccini@unifi.it

Received 18 July 2013; Accepted 25 August 2013

Academic Editors: D. G. Aggelis, N. Alver, and H. K. Chai

Copyright © 2013 Devis Dei et al. This is an open access article distributed under the Creative Commons Attribution License, which permits unrestricted use, distribution, and reproduction in any medium, provided the original work is properly cited.

Ground-based radar interferometry is an increasingly popular technique for monitoring civil infrastructures. In this paper, the static testing of a bridge is reported. It was an 8-span bridge, 297 m long, named “Ponte degli Alpini,” crossing the valley of the Ardo River. The radar has been used for testing a lateral span and a central span. The obtained results present elements of novelty not previously reported in the literature. In fact, some displacement measurements of the lateral span have been affected by a horizontal shift that has to be taken into account for a correct interpretation of the measured data. Furthermore, the measurements of the central span have been carried out with the radar positioned transversally with respect to the bridge deck; this unusual arrangement has allowed for obtaining displacement maps less geometrically distorted with respect to other cases reported in the literature.

## 1. Introduction

The static load test of a bridge is part of a process aimed to verify the capability of a structure to support heavy loads. This test is always associated with the analysis of the materials and the design of the structure. The conventional instrument for measuring the deformation of a bridge under static loads is the optical level sensor. It can measure the relative displacement of some points by referring their movement to a reference point off the loaded span, which is supposed steady during the measurement time. This method does not measure directly the deformation of the beams (the bearing structural elements of the span) but the deformation of the slab, supposing it should be strictly joined to the beams. Unfortunately, the accuracy of the optical level sensor decreases rapidly with the distance. Therefore, in case of a long bridge like the structure under investigation, the reference point for measuring the deformation of the central spans cannot be located off the bridge, but it has to be located on another span near the loaded one. In this case, the assumption of the stability of the reference point may not be verified, as the residual effect of the deformation of the loaded span can be transferred to the neighbouring ones.

The interferometric radar is a sensor increasingly used mainly in dynamic testing of infrastructures [1–10].

Nevertheless, it can be used even for static tests as reported in several papers [11–15]. The unique advantages of this technique are (1) measurement of the displacement component along the direction of view; therefore, its accuracy does not depend on distance alike for optical level sensor and (2) capability to provide a displacement map.

In the case study we have reported in this paper, both were important issues, so radar has been selected for integrating the conventional sensors.

## 2. The Bridge

The bridge under test is named “Ponte degli Alpini,” located in Belluno, Italy. Large reinforcement works were implemented in order to make the bridge compliant with the most recent antiseismic law. The works finished in 2009, the year after a load test was planned before to open the bridge to heavy traffic (over 3.5 tons).

The “Ponte degli Alpini” is an 8-span bridge, 297 m long. Each span has 4 longitudinal reinforced concrete beams, 37 m long, and a slab. The beams are supported by concrete piers (see Figure 1).

The bridge is 13.40 m large, with a central roadway 9 m large with two sidewalks 2.2 m large as shown in the picture of Figure 2.

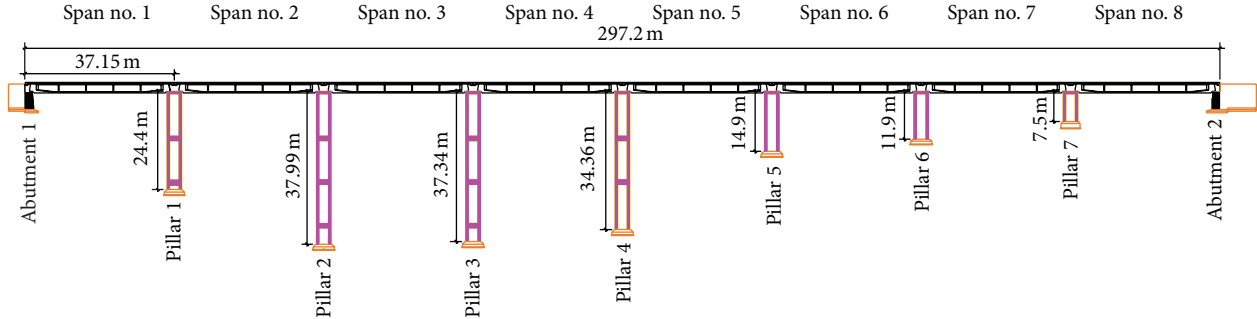


FIGURE 1: Scheme of "Ponte degli Alpini."



FIGURE 2: Deck of "Ponte degli Alpini."

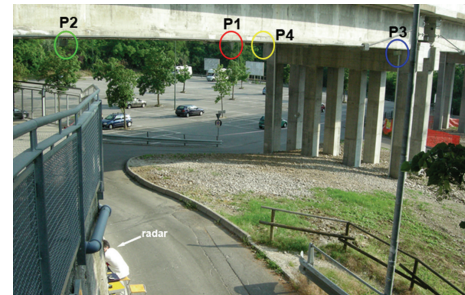


FIGURE 4: Radar measurement of the lateral span no. 8 in Figure 1.



FIGURE 3: Interferometric radar in only-range configuration.

### 3. The Lateral Span

For testing one of the lateral span (labelled with no. 8 in Figure 1), the radar has been used in only-range modality (see Figure 3). It means that it is able to discriminate the target points only for their different distances from the radar head.

Four dihedral corner reflectors (P1, P2, P3, and P4) have been installed on the lower side of the deck positioned as in Figures 4 and 5. These high reflectivity targets give peaks in the radar plot clearly detectable on the background. Figure 6 shows the measured radar plot where the 4 corner reflectors are labelled with their numbers.

The load test was carried out by loading the span with 8 trucks. Each truck had 4 axes and was completely filled with sand for a total weight of about 40 tons. The loading procedure is sketched in Figure 7.

In the first loading phase, two trucks were stopped at the centre of the span near the north side, as shown in

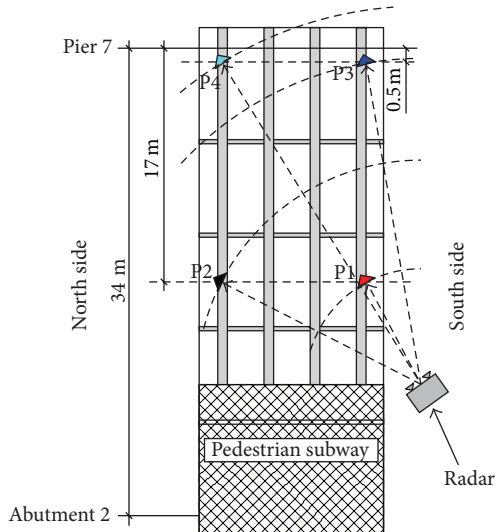


FIGURE 5: Measurement setup for the span no. 8.

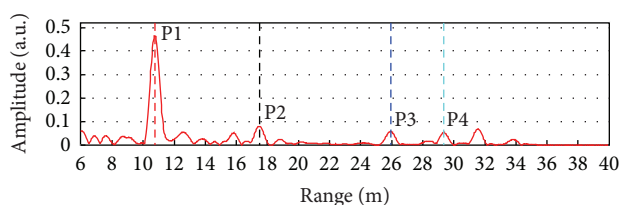


FIGURE 6: Radar plot relative to the measurement of span no. 8.

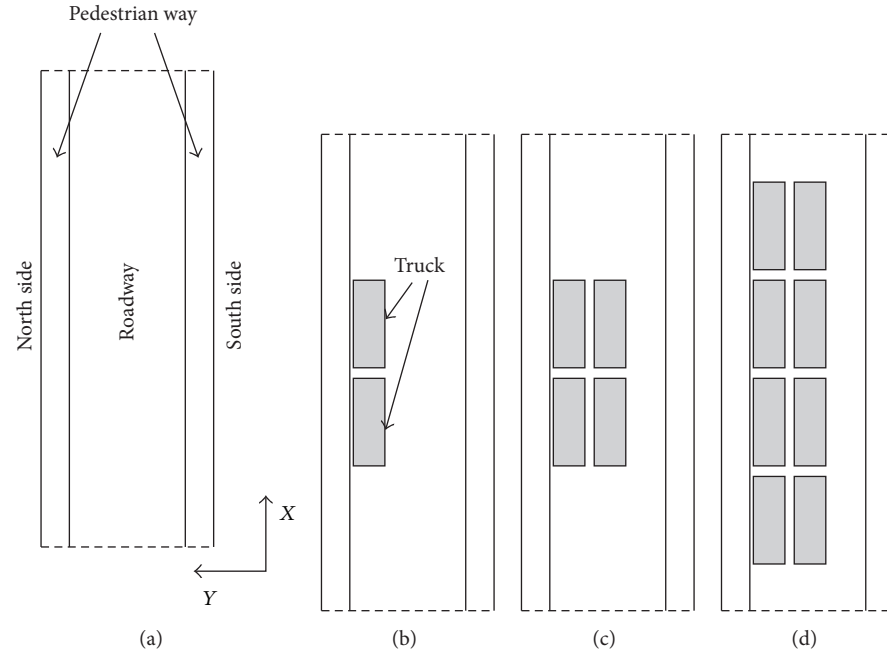


FIGURE 7: Upward view of the span which illustrates the sequence and the placing of the loads: (a) unloaded; (b) 2 trucks; (c) 4 trucks; and (d) 8 trucks.

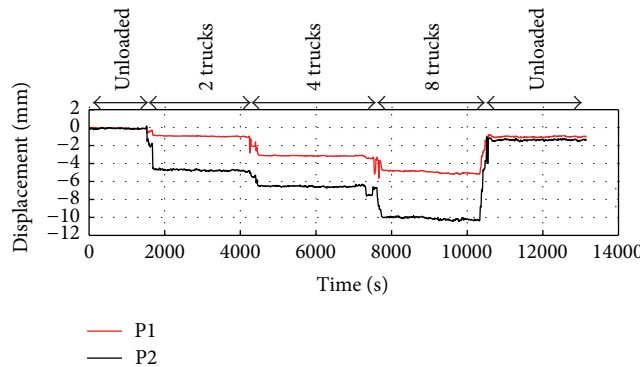


FIGURE 8: Measured displacements of P1 and P2 during the load test.

Figure 7(b). The load was disposed asymmetrically in order to concentrate the effort on one of the external beams. In the second phase, two other trucks were positioned as in Figure 7(c), and in the third phase, the span was loaded with eight trucks (see Figure 7(d)). Finally, the load was removed, and the residual displacement was measured. The radar was set up for acquiring 10 samples per second, so it was able to follow even the dynamic behaviour of the bridge during the different phases of the test. The maximum measured displacement was  $10.30 \text{ mm} \pm 0.1 \text{ mm}$  (at the P2 point). The relative residual displacement was 1.4 mm (see Figure 8). Both are consistent with the expected values for this kind of bridge.

A more interesting behaviour has been observed for points P3 and P4; they gave apparent positive displacements as shown in Figure 9. It is due to the fact that they are not at the centre of the span but close to the piers. Therefore, during

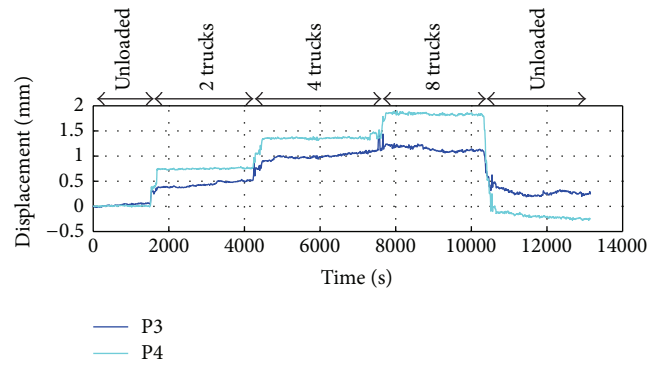


FIGURE 9: Measured displacements of P3 and P4 during the load test.

the loading, they move both vertically and horizontally, as shown in the sketch of Figure 10. But the radar see the bridge from a grazing angle, so a horizontal displacement can give a component in view direction larger than the component due to the vertical displacement. This effect is not present for the points P1 and P2 that are close to the span centre, where there is no horizontal displacement as shown in the sketch in Figure 11.

#### 4. The Central Span

For testing the central span (labelled with no. 4 in Figure 1), the radar has been used in cross-range modality. It means that the radar head has been moved during each single measurement on a mechanical linear guide (as shown in Figure 12), in order to acquire a bidimensional image of the

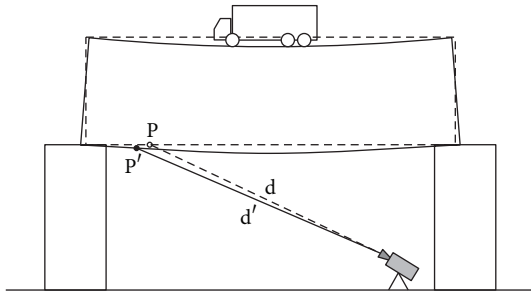


FIGURE 10: Sketch of the measurement geometry of the points P3 and P4 during the deformation of the deck.

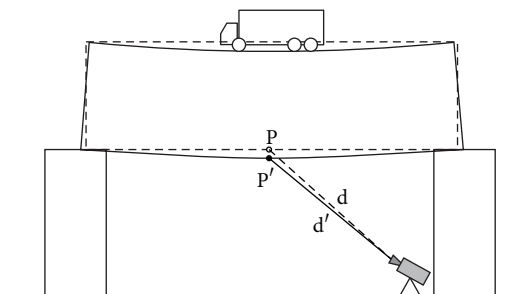


FIGURE 11: Sketch of the measurement geometry of the points P3 and P4 during the deformation of the deck.

deck. In this modality, the radar requires several minutes for a single acquisition.

As the riverbed was accessible, the radar was placed on a concrete basement at ground, 34.5 m below the bridge and 15 m off the span southwards, as shown in Figure 13. The antennas were rotated upward, and they were able to illuminate the whole lower surface of the span. During each measurement, the radar front-end was moved on the mechanical guide with 381 steps of 5 mm to cover the whole guide length of 1.9 m. The radar was set to generate 3057 equally spaced frequency tones sampling a 400 MHz bandwidth, starting from 16.55 GHz. This setting provides 0.37 m range resolution and 0.19 m cross-range resolution at 40 m.

The static test was carried out with the loading procedure in 4 phases sketched in Figure 7. A first reference measurement was collected when the bridge was unloaded, aftermath, and image has been acquired at each phase. The radar is able to provide a complete displacement image of the lower surface of the bridge, but in order to locate precisely the vertical movement of the points of interest, six trihedral corner reflectors were installed on the external beams as shown in Figure 14.

The interferometric radar in this configuration provides a two-dimensional complex radar cross-section (RCS) images, with amplitude and phase information. The amplitude information is used to identify and select the pixels corresponding to the point of interest. The phase information gives the differential displacement of the identified targets.

The amplitude image of the span is shown in Figure 15. It is an image on the XY plane, sampled with increments  $\Delta x = 12.5$  mm and  $\Delta y = 12.5$  mm. The Y axis is the range, and



FIGURE 12: Radar installation on the riverbed.



FIGURE 13: The radar (red circle) placed on a basement under the span.

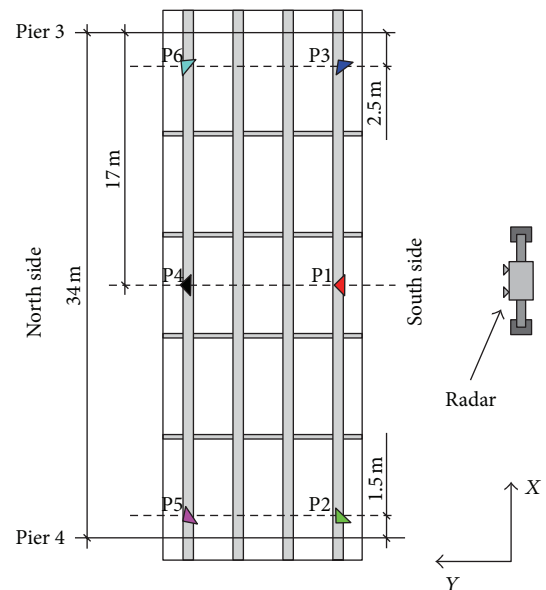


FIGURE 14: Positions of the corner reflectors (named from P1 to P6).

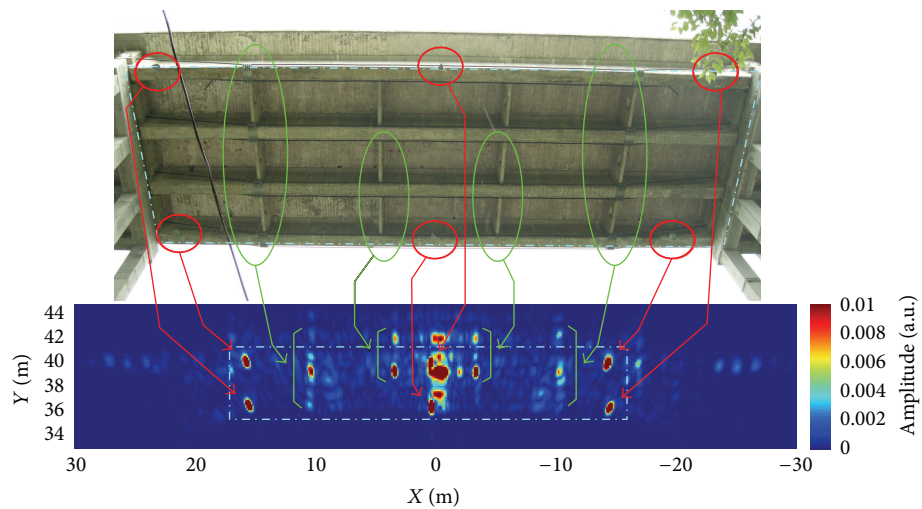


FIGURE 15: Amplitude radar image with the targets highlighted in the corresponding picture of the span.

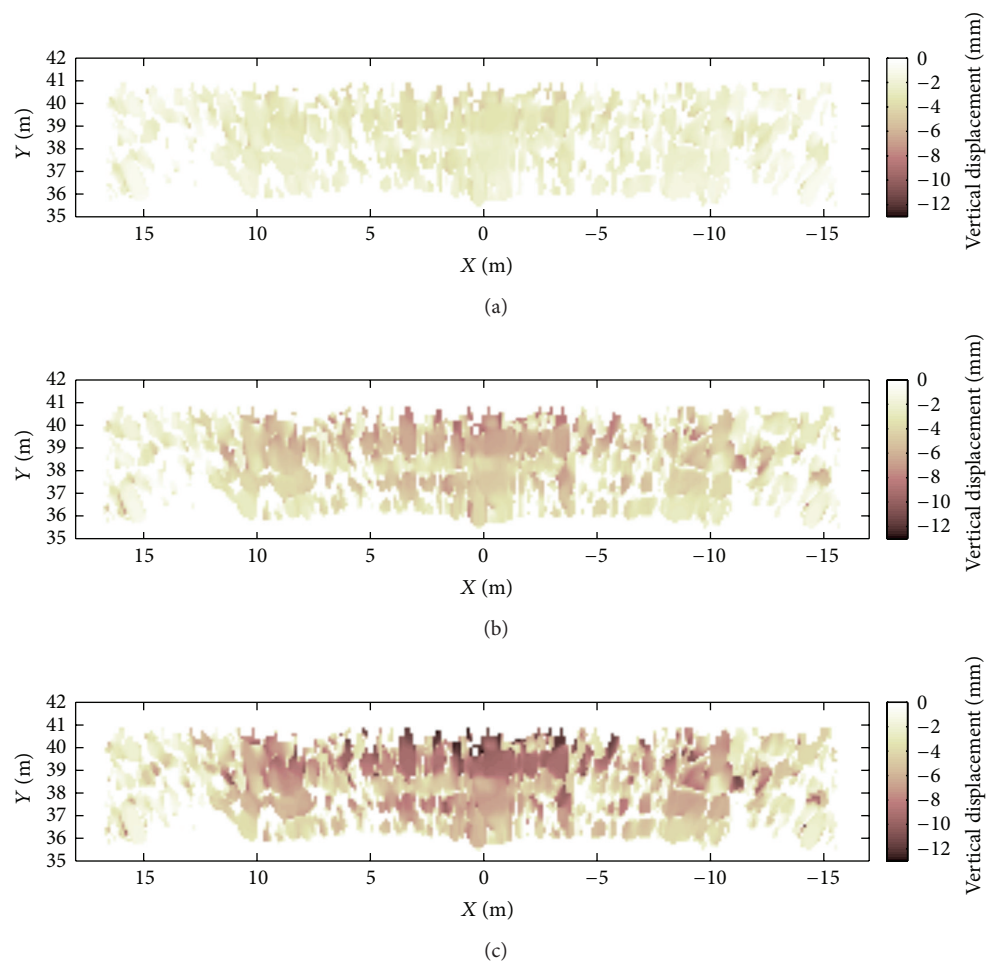


FIGURE 16: Displacement maps: (a) 2 trucks; (b) 4 trucks; and (c) 8 trucks.

TABLE 1

P1	P2	P3	P4	P5	P6
$0.10 \pm 0.05$	$0.40 \pm 0.05$	$0.47 \pm 0.05$	$0.34 \pm 0.05$	$0.44 \pm 0.05$	$0.57 \pm 0.05$

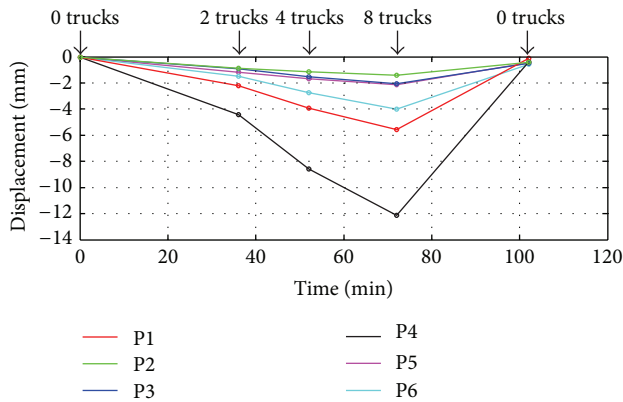


FIGURE 17: Vertical displacement of the corner reflectors during the loading and the unloading of the bridge: labels from P1 to P6 are referred to in Figure 14.

the  $X$  axis is the cross-range. The targets highlighted with red circles refer to the corner reflectors and other structural characteristics of the surface.

The displacement maps (interferograms) between the reference image, before the loading of the span, and the three following loading phases of 2, 4, and 8 trucks are shown in Figure 16.

The radar image has been masked selecting the pixels with two criteria: (1) a geometrical mask which removes all the pixels scattered out of the surface of the span and (2) an amplitude mask which removes the pixels where the signal is lower than 0.2% of the maximum amplitude of the image. The last one is an empirical method for cutting out the noisy pixels with low backscattered signal. As the radar only detects the displacement component along the line of sight, the vertical displacement has to be calculated by supposing the horizontal component negligible. On the other part, it should be noted that usually the radar is positioned close to a pier with view direction nearly parallel to the bridge span [1, 2, 11, 12]. But in this measurement geometry, a possible horizontal displacement has a large component in the view direction, so it could not be correct to neglect it, as well-evident in the case of the testing of the lateral span reported above. On the contrary, by positioning the radar transversally and at great distance, any possible horizontal displacement in the direction of the length of the bridge has a very small component along the view direction.

Finally, Figure 17 shows the calculated vertical displacement of the points corresponding to the corner reflectors installed on the beams, which coordinates have been identified in the amplitude image. The time between a radar acquisition and the next one was as such to allow the structure to settle.

The largest displacement was measured on the beam northward, which was the most loaded, and a residual

deformation remains after the final unloading phase as expected. The residual displacement of the six points is reported in Table 1.

## 5. Conclusions

The ground-based radar interferometry has been confirmed as a useful tool for measuring the deformation of a bridge during a static load test. This test is always a key step for assessing the health of a structure and its compliance with the safety guidelines and laws.

Radar interferometry offers some advantages in comparison with the traditional optical level sensors. The radar can be installed on the ground below the bridge (when it is accessible), and it can detect directly the vertical displacement of the beams. As it overcomes the limit of the optical sensors regarding the accuracy of the measurement when used on long bridge, it can effectively integrate the traditional equipment.

## Conflict of Interests

The authors declare that they have been involved in the development and design of the commercial interferometric radar named IBIS, manufactured by IDS Company of Pisa, Italy.

## References

- [1] M. Pieraccini, M. Fratini, F. Parrini, and C. Atzeni, "Dynamic monitoring of bridges using a high-speed coherent radar," *IEEE Transactions on Geoscience and Remote Sensing*, vol. 44, no. 11, pp. 3284–3288, 2006.
- [2] C. Gentile and G. Bernardini, "Output-only modal identification of a reinforced concrete bridge from radar-based measurements," *NDT and E International*, vol. 41, no. 7, pp. 544–553, 2008.
- [3] C. Gentile, "Deflection measurement on vibrating stay cables by non-contact microwave interferometer," *NDT and E International*, vol. 43, no. 3, pp. 231–240, 2010.
- [4] M. Pieraccini, M. Fratini, F. Parrini, G. Pinelli, and C. Atzeni, "Dynamic survey of architectural heritage by high-speed microwave interferometry," *IEEE Geoscience and Remote Sensing Letters*, vol. 2, no. 1, pp. 28–30, 2005.
- [5] M. Pieraccini, D. Dei, M. Betti, G. Bartoli, G. Tucci, and N. Guardini, "Dynamic identification of historic masonry towers through an expeditious and no-contact approach: application to the "Torre del Mangia" in Siena (Italy)," *Cultural Heritage*, 2013.
- [6] C. Atzeni, A. Bicci, D. Dei, M. Fratini, and M. Pieraccini, "Remote survey of the leaning tower of pisa by interferometric sensing," *IEEE Geoscience and Remote Sensing Letters*, vol. 7, no. 1, pp. 185–189, 2010.

- [7] M. Pieraccini, F. Parrini, M. Fratini, C. Atzeni, and P. Spinelli, "In-service testing of wind turbine towers using a microwave sensor," *Renewable Energy*, vol. 33, no. 1, pp. 13–21, 2008.
- [8] D. Beben, "Experimental study on the dynamic impacts of service train loads on a corrugated steel plate culvert," *Journal of Bridge Engineering*, vol. 18, no. 4, pp. 339–346, 2013.
- [9] M. Fratini, M. Pieraccini, C. Atzeni, M. Betti, and G. Bartoli, "Assessment of vibration reduction on the Baptistry of San Giovanni in Florence (Italy) after vehicular traffic block," *Journal of Cultural Heritage*, vol. 12, no. 3, pp. 323–328, 2011.
- [10] C. Negulescu, G. Luzi, M. Crosetto et al., "Comparison of seismometer and radar measurements for the modal identification of civil engineering structures," *Engineering Structures*, vol. 51, pp. 10–22, 2013.
- [11] M. Pieraccini, F. Parrini, M. Fratini, C. Atzeni, P. Spinelli, and M. Micheloni, "Static and dynamic testing of bridges through microwave interferometry," *NDT and E International*, vol. 40, no. 3, pp. 208–214, 2007.
- [12] M. Pieraccini, D. Tarchi, H. Rudolf et al., "Structural static testing by interferometric synthetic radar," *NDT and E International*, vol. 33, no. 8, pp. 565–570, 2000.
- [13] D. Tarchi, H. Rudolf, M. Pieraccini, and C. Atzeni, "Remote monitoring of buildings using a ground-based SAR: application to cultural heritage survey," *International Journal of Remote Sensing*, vol. 21, no. 18, pp. 3545–3551, 2000.
- [14] S. Rödelsperger, G. Läufer, C. Gerstenecker, and M. Becker, "Monitoring of displacements with ground-based microwave interferometry: IBIS-S and IBIS-L," *Journal of Applied Geodesy*, vol. 4, no. 1, pp. 41–54, 2010.
- [15] M. Pieraccini, G. Luzi, D. Mecatti et al., "Remote sensing of building structural displacements using a microwave interferometer with imaging capability," *NDT and E International*, vol. 37, no. 7, pp. 545–550, 2004.

## Research Article

# Ambient Vibration Testing for Story Stiffness Estimation of a Heritage Timber Building

**Kyung-Won Min, Junhee Kim, Sung-Ah Park, and Chan-Soo Park**

*Department of Architectural Engineering, Dankook University, Yongin 448-701, Republic of Korea*

Correspondence should be addressed to Junhee Kim; [junheekim@dankook.ac.kr](mailto:junheekim@dankook.ac.kr)

Received 26 July 2013; Accepted 1 September 2013

Academic Editors: D. G. Aggelis, N. Alver, and H. K. Chai

Copyright © 2013 Kyung-Won Min et al. This is an open access article distributed under the Creative Commons Attribution License, which permits unrestricted use, distribution, and reproduction in any medium, provided the original work is properly cited.

This paper investigates dynamic characteristics of a historic wooden structure by ambient vibration testing, presenting a novel estimation methodology of story stiffness for the purpose of vibration-based structural health monitoring. As for the ambient vibration testing, measured structural responses are analyzed by two output-only system identification methods (i.e., frequency domain decomposition and stochastic subspace identification) to estimate modal parameters. The proposed methodology of story stiffness is estimation based on an eigenvalue problem derived from a vibratory rigid body model. Using the identified natural frequencies, the eigenvalue problem is efficiently solved and uniquely yields story stiffness. It is noteworthy that application of the proposed methodology is not necessarily confined to the wooden structure exemplified in the paper.

## 1. Introduction

Vibration-based structural health monitoring (SHM) is based on vibration testing of structures which requires high capacity actuators. However, exciting structures in a controlled and repeatable manner is rather limited in practice. In addition, the forced vibration testing is not preferred for heritage building structures where artificial loading might induce significant damage to the tested structures. Thus, monitoring of structural responses from ambient vibration is preferred, since dynamic properties can be identified by analyzing ambient responses of the buildings, for example, heritage court building [1], bell tower of the Monza's Cathedral [2], three representative monuments in Rome [3] (i.e., the Colosseum, Trajan's Column, and Aurelian Walls), and the historic Morca suspension footbridge [4]. All of these studies are exclusively for masonry or stony structures.

In Northeast Asia (i.e., Korea, China, Japan, etc.), timber buildings had been traditionally constructed for majestic superstructures on gates of stony castle walls and then have been preserved as heritages so far. These days, portions of the heritage buildings are exposed to rather strong ambient vibration sources. Excitation induced by passage of traffics propagates to the structures. The repeated support

excitation might induce functional problems to sensitive equipments or structural damage at the structures. Structural vibration might trigger damage especially for the structures with weathered structural members and weakened structural integrity. In the context, analytical and experimental studies on structural behaviors of historic timber buildings have been conducted: analytical procedure of finite element method was applied to ancient Chinese timber architecture [5]; shaking table and static tests were carried out with scaled models of Japanese temples [6].

Structural vibrations derived from support excitations can be used to characterize the structure [7]. The structural vibratory responses depend on both spectral content of the excitations and dynamic characteristics of the structure. Assuming that the support excitations are random, structural responses represent directly the structural dynamic characteristics which are useful to understand behavior of the structure and further assess structural integrity. For example, natural frequencies and mode shapes can be used for examining overall structural stiffness. The structural stiffness is important especially for the heritage timber structures. At the typical timber framing, all connections between columns and beams are neither rigid nor pinned, since the structural members are fitted with joints secured by wooden pegs.

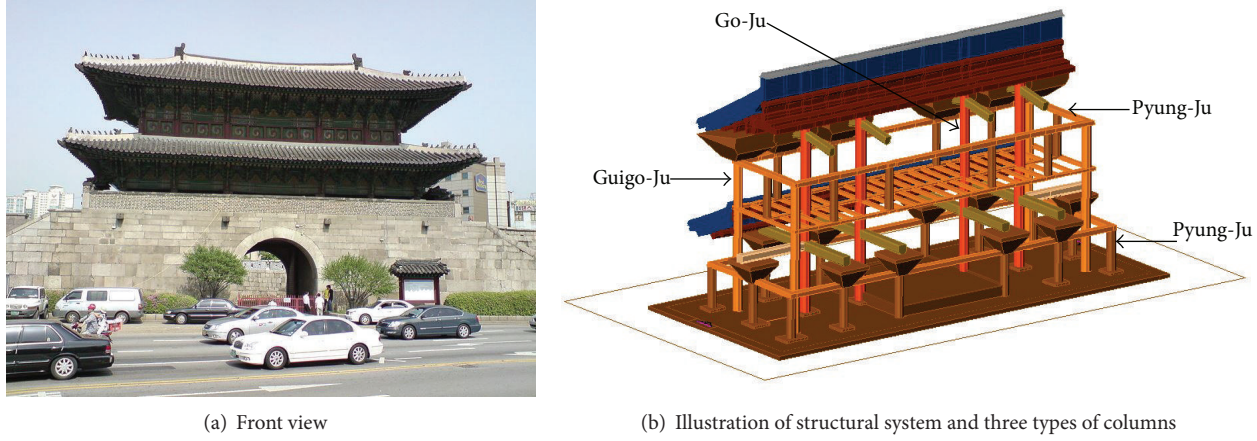


FIGURE 1: The Dongdaemun (great gate in the East).

Therefore, estimation of structural stiffness of the timber structures has been considered challenging so far.

The Dongdaemun, designated as the Korean treasure no. 1, is a historic timber structure: it is a two-story wooden building on the platform of stone foundations. It is located at an intersection of busy roads in downtown Seoul being exposed to traffic vibrations. In this study, ambient vibration testing is conducted for the Dongdaemun for the purpose of story stiffness evaluation. The structural responses of ambient vibrations are measured and then analyzed by output-only system identification for estimation of the modal parameters. A simplified rigid body model is adopted to efficiently model the Dongdaemun based on the identified mode shapes. Then, using the identified natural frequencies, an eigenvalue problem of the rigid body model is solved for estimating story stiffnesses of the structure.

## 2. Ambient Vibration Testing of a Historic Structure

**2.1. The Dongdaemun, Korea.** Castle walls surrounding Hanyang (the old capital of Korea, now the downtown area of Seoul) were built in Joseon (the final ruling dynasty of Korea, lasted from 1392 to 1910). Among eight gates along the castle walls, the one located at the East is the Dongdaemun, which stands for great gate in the East. The Dongdaemun was originally constructed in 1396, repaired in 1453, and finally rebuilt in 1869. It has two types of distinct structures, as shown in Figure 1(a). The upper structure is a timber frame consisting of beams and supporting columns (i.e., postings), and the lower structure is a massive platform foundation made with stones. The columns and beams of the two-story wooden structure are fitted with joints secured by mortise and tenon without metallic fasteners supporting eaves, bracket complexes and roofs, and so forth.

Three types of columns (Figure 1(b)) support the structure: (1) four core columns (termed Go-Ju) are located along the center line in a row connecting foundations and roof beams; (2) four corner columns (termed Goigo-Ju) are located at four edges of the structure connecting foundations and the second floor; (3) numerous interstory columns

(termed Pyung-Ju) are built up along the four sides at each floor delivering dead load to the floor beams. The three types of columns are also illustrated at each floor plan in Figure 2. Because of the rectangular footprint of the structure, it has two directions of motion: a flexurally strong axis along the long side of the rectangle is referred to as the longitudinal direction in the paper; the orthogonal direction is a flexurally weak axis and referred to as the lateral direction.

**2.2. Ambient Vibration Testing.** The Dongdaemun is located at an intersection of roads and above two subway lines. Excitation by ambient vibration sources (i.e., passages of vehicles and trains) is conveniently utilized as input to the structure. However, monitoring of structural responses with a high density of sensor array is necessitated due to the unique characteristics of timber frame and complex structural system of the Dongdaemun. To provide a high nodal density using a limited number of sensor nodes, reconfiguration of sensor installation is selected in the ambient vibration testing.

A reconfiguring strategy with up to ten sensor nodes is adopted with the system redeployed six times after the initial deployment with two nodes overlapped. Pairs of accelerometers deployed along longitudinal and lateral directions are installed at each setup. For example, four pairs of sensors are installed at the first Go-Ju (Figure 3(a)) with the elevations of 0.5, 4.0, 5.8, and 8.8 m. Once the installation is complete, monitoring of ambient vibration is conducted. Then, sensors except the nodes 5 and 6 at the first Go-Ju highlighted are reinstalled at another Go-Ju, and two more sensors are installed at the nodes 5 and 6 at the Go-Ju. Similarly, testing and reinstallation are sequentially conducted twice for the remaining Go-Ju's. After completion of ambient vibration testing at Go-Ju's, the four pairs of moving sensors are installed twice at four Guigo-Ju's with the elevations of 5.8, and 8.8 m, respectively for each setup (Figure 3(b)). Finally, ambient vibration testing at Pung-Ju's is once conducted with sensor installation at the elevation of 8.8 m (Figure 3(c)). It should be noted that sensors at nodes 5 and 6 at the first Go-Ju collected data during the ambient vibration testing at Guigo-Ju's and Pyung-Ju's. This reconfiguring strategy realized

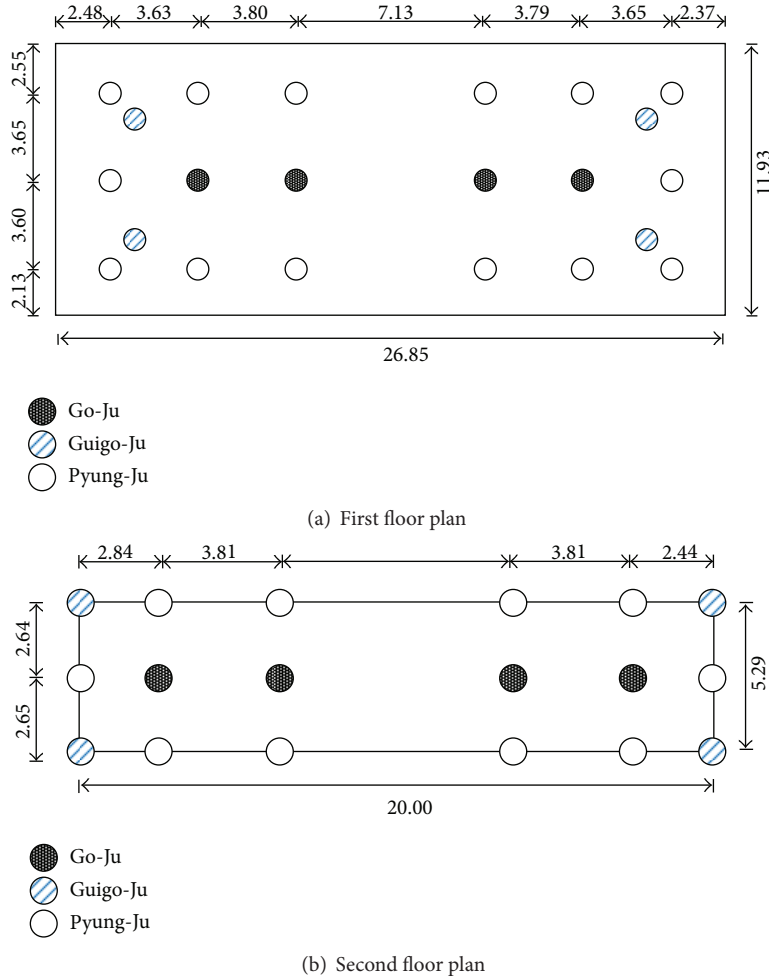


FIGURE 2: Layout of columns (unit: m).

a dense nodal configuration with 10 sensors installed in 48 nodes at the tested structure.

For measurement of weak ambient vibration in the seven tests, a multichannel high resolution data acquisition system interfaced by accelerometers with high sensitivity is adopted: a National Instruments 16-bit data acquisition system (NI USB-6210) is used with PCB Piezotronics 393B12 integrated circuit piezoelectric (ICP) accelerometers interfaced. The accelerometer measurement range is  $\pm 0.5$  g, and its spectral noise floor of 100 Hz bandwidth is  $0.07 \mu\text{g}/\sqrt{\text{Hz}}$ . The accelerometer is well suited for civil structural monitoring because of its high sensitivity (10 V/g). The data is collected for 480 sec using a 30 Hz sampling frequency.

### 3. Output-Only Modal Analysis

**3.1. Output-Only Modal Analysis Theory Revisited.** Output-only modal parameter estimation techniques are categorized into two distinct groups depending on their analysis domains: frequency domain methods dealing with output spectra or power spectral density (PSD) and time domain methods using correlation (i.e., projection in subspace) of past and future outputs. In this study, a frequency domain technique

called frequency domain decomposition (FDD) [1] is adopted to estimate the modal parameters of the Dongdaemun. The FDD is basically an output-only version of the conventional complex mode indicator function (CMIF) method [8]. PSD relationship between the system input,  $\mathbf{u}$ , and the measured output,  $\mathbf{y}$ , is expressed in continuous-time frequency domain as follows:

$$\mathbf{G}_{yy}(j\omega) = \mathbf{H}(j\omega) \mathbf{G}_{uu}(j\omega) \mathbf{H}^H(j\omega), \quad (1)$$

where  $\mathbf{G}_{uu}(j\omega)$  is the PSD matrix of the input;  $\mathbf{G}_{yy}(j\omega)$  is the PSD matrix of the output;  $\mathbf{H}(j\omega)$  is frequency response function (FRF) matrix;  $\mathbf{H}^H(j\omega)$  is its complex transpose conjugate. If the system input is assumed as white noise,  $\mathbf{G}_{uu}(j\omega)$  will simply be a constant matrix in frequency axis; hence,  $\mathbf{G}_{yy}(j\omega)$  is directly proportional to the product of FRFs,  $\mathbf{H}(j\omega)\mathbf{H}^H(j\omega)$ . By applying singular value decomposition (SVD) to (1), the output PSD matrix can be decomposed into singular vectors (mode shapes) and singular values of dominant frequencies.

As a counterpart of the frequency domain method of FDD, this study also adopts the stochastic subspace identification (SSI) [8, 9] as a time domain alternative. The output

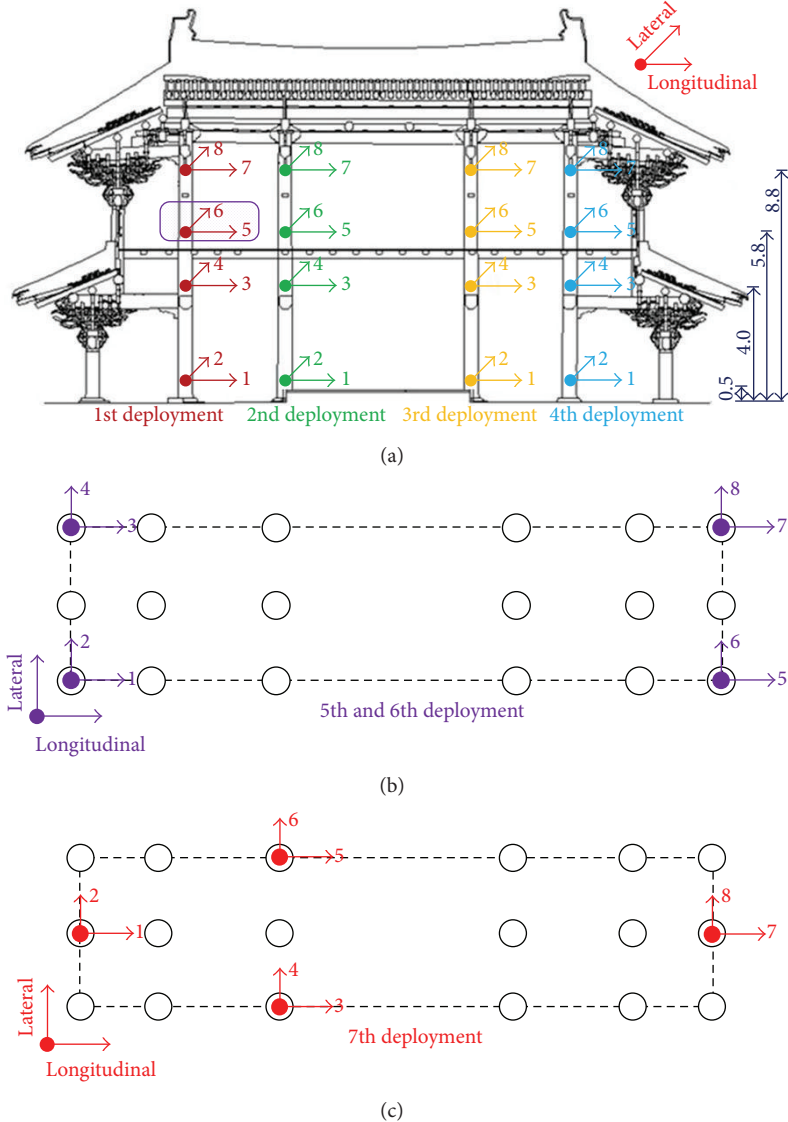


FIGURE 3: Schematics of multiple deployments of accelerometers. (a) Four sensor deployments at Go-Ju's with elevations noted (unit: m); the fixed reference sensor pairs are highlighted. (b) Two sensor deployments at Guigo-Ju's (elevations of 5.8 and 8.8 m). (c) A sensor deployment at Pyung-Ju's (elevation of 8.8 m).

block Hankel matrix is constructed from the measured  $2i + j - 1$  structural output vector sequence and partitioned as past output and future output as follows:

$$\mathbf{Y}_{0|2i-1} = \begin{bmatrix} \mathbf{y}_0 & \mathbf{y}_1 & \cdots & \mathbf{y}_{j-1} \\ \vdots & \vdots & \ddots & \vdots \\ \mathbf{y}_{i-1} & \mathbf{y}_i & \cdots & \mathbf{y}_{i+j-2} \\ \hline \mathbf{y}_i & \mathbf{y}_{i+1} & \cdots & \mathbf{y}_{i+j-1} \\ \vdots & \vdots & \ddots & \vdots \\ \mathbf{y}_{2i-1} & \mathbf{y}_{2i} & \cdots & \mathbf{y}_{2i+j-2} \end{bmatrix} \quad (2)$$

$$= \begin{bmatrix} \mathbf{Y}_{0|i-1} \\ \mathbf{Y}_{i|2i-1} \end{bmatrix} = \begin{bmatrix} \mathbf{Y}_p \\ \mathbf{Y}_f \end{bmatrix}.$$

The main role of the partitioned output block Hankel matrix is preparing orthogonal projection where the past

output works as instrumental variables for elimination of bias estimates due to colored noise output [10]. Two orthogonal projections of the row space of the future output,  $\mathbf{Y}_f$ , on the row space of the past output,  $\mathbf{Y}_p$ , can be determined through LQ decomposition of the output block Hankel matrix:

$$\mathbf{P}_i := \frac{\mathbf{Y}_f}{\mathbf{Y}_p}; \quad \mathbf{P}_{i-1} := \frac{\mathbf{Y}_f^-}{\mathbf{Y}_p^-}, \quad (3)$$

where  $\mathbf{Y}_f^-$  and  $\mathbf{Y}_p^-$  are defined as a one block row downshift in (2) as  $\mathbf{Y}_{0|i}$  and  $\mathbf{Y}_{i+1|2i-1}$ , respectively. SVD is applied to factorize the projection  $\mathbf{P}_i$ :

$$\mathbf{P}_i = \mathbf{U}\mathbf{S}\mathbf{V}^T \cong [\mathbf{U}_1 \quad \mathbf{U}_2] \begin{bmatrix} \mathbf{S}_1 & \mathbf{0} \\ \mathbf{0} & \mathbf{0} \end{bmatrix} \begin{bmatrix} \mathbf{V}_1^T \\ \mathbf{V}_2^T \end{bmatrix} = \mathbf{U}_1 \mathbf{S}_1 \mathbf{V}_1^T. \quad (4)$$

Since the projection is equal to the product of the extended observability matrix and the nonstationary Kalman filter state sequence [9], the extended observability matrix and the nonstationary Kalman filter state sequence are calculated respectively as

$$\mathcal{O}_i = \mathbf{U}_1 \mathbf{S}_1^{1/2}; \quad \widehat{\mathbf{X}}_i = \mathbf{S}_1^{1/2} \mathbf{V}_1^T. \quad (5)$$

The one-step shifted state sequence is also calculated as

$$\widehat{\mathbf{X}}_{i+1} = (\mathcal{O}_{i-1})^\dagger \mathbf{P}_{i-1}, \quad (6)$$

where  $\mathcal{O}_{i-1}$  is equivalent to  $\mathcal{O}_i$  with the last block row omitted. Furthermore,  $\dagger$  is the pseudoinverse operator. Finally, estimates of system matrices of  $\mathbf{A}$  and  $\mathbf{C}$  are calculated by a least-squares solution:

$$\begin{bmatrix} \widehat{\mathbf{A}} \\ \widehat{\mathbf{C}} \end{bmatrix} = \begin{bmatrix} \widehat{\mathbf{X}}_{i+1} \\ \mathbf{Y}_{i|i} \end{bmatrix} \widehat{\mathbf{X}}_i^\dagger. \quad (7)$$

Modal parameters can be estimated from the estimated system matrices. The estimated system matrix  $\widehat{\mathbf{A}}$  can be decomposed by eigen decomposition as  $\widehat{\mathbf{A}} = \Psi \Lambda \Psi^{-1}$ , where diagonal matrix  $\Lambda = \text{diag}(\lambda_{di})$  consists of the discrete-time complex eigenvalues.  $\Psi$  contains eigenvectors in each column. The discrete-time eigenvalues are first converted to continuous-time eigenvalues  $\lambda_{ci}$  as  $\lambda_{ci} = \ln(\lambda_{di})/\Delta t$ , where  $\Delta t$  is the time step of the digital data acquisition system. The natural frequencies  $\omega_{ni}$  and damping ratios  $\zeta_i$  can then be easily calculated from the conjugate pair of complex-valued eigenvalues:  $\lambda_{ci}, \lambda_{ci}^* = -\zeta_i \omega_{ni} \pm j\omega_{ni} \sqrt{1 - \zeta_i^2}$ . The mode shape vector for the  $i$ th mode  $\Phi_i$  can be calculated as  $[\Phi_1 \dots \Phi_i \dots \Phi_n] = \widehat{\mathbf{C}} \Psi$ .

**3.2. Modal Parameter Estimation.** The measured acceleration data are analyzed to identify the modal characteristics of the Dongdaemun without known input loading. The quality of the estimated modal parameters by the FDD method is governed by the estimated PSD functions. The PSD function calculated for each sensor location is improved by using a Hanning window on the time-history data prior to the use of the fast Fourier transform (FFT) algorithm. In addition, repeated Fourier spectra calculated from time-history records with 50% overlap between them in the time domain are averaged. This approach to improving the PSD spectra provides a good tradeoff between the reduction of noise and the distinctive qualities of the modal peaks [11].

Figure 4 presents the PSD spectra of the measured longitudinal accelerations at sensor nodes 5, 1, and 1, respectively, for the 1st, 6th, and 7th sensor deployments as representatives of Go-Ju, Guigo-Ju, and Pyung-Ju. A dominant frequency of 1.51 Hz is observed at the three cases. The PSD spectra of the measured lateral accelerations at the sensor nodes 6, 2, and 2, respectively, for the 1st, 6th, and 7th sensor deployments are given in Figure 5. Sharp peaks at 1.13, 1.34, and 4.23 Hz seen at the three cases imply modal frequencies in lateral direction revealing complex vibratory behavior of the structure in the lateral direction.

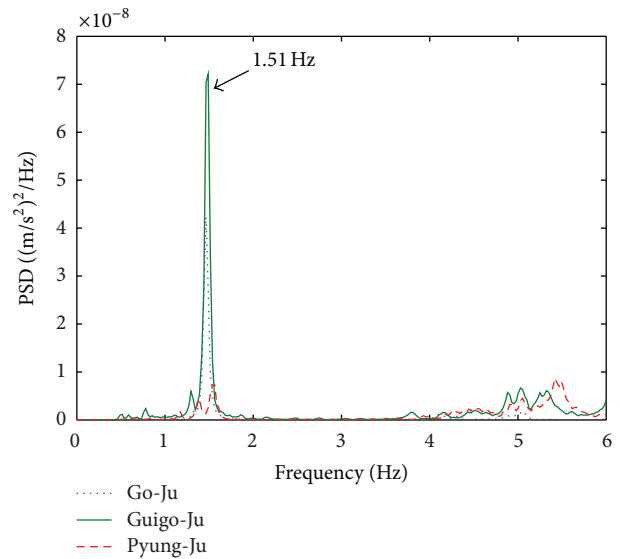


FIGURE 4: PSD spectra in longitudinal direction.

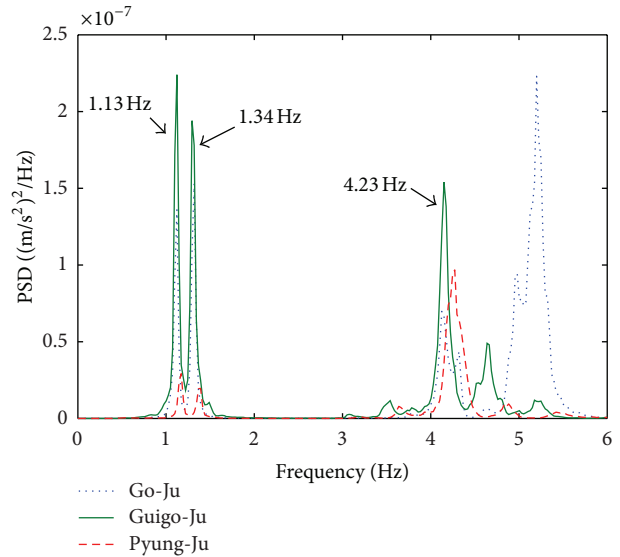


FIGURE 5: PSD spectra in lateral direction.

Two output-only system identifications are conducted by the frequency-domain FDD and time-domain SSI with the collected ambient vibration data. As for the FDD method, by selecting dominant peaks in the previously calculated PSDs of Figures 4 and 5, natural frequencies are determined, and mode shapes are automatically acquired from the corresponding first singular vector. For the purpose of damping estimation, a variation of half power method, so-called enhanced FDD [12], is adopted using the PSD spectra in lieu of frequency response function. The time-domain SSI is independently conducted with the identical data, and modal parameters are determined. Results of the estimated modal parameters by FDD and SSI are tabulated in Table 1.

Table 1 shows natural frequencies and damping ratios in the lateral and longitudinal directions. Overall, the natural

TABLE 1: Identified natural frequencies and damping ratios.

Modes	Descriptions	$\omega_{\text{FDD}}$ (Hz)	$\omega_{\text{SSI}}$ (Hz)	$\zeta_{\text{FDD}} (\%)$	$\zeta_{\text{SSI}} (\%)$
1	Transversal (1st lateral mode)	1.13	1.11	2.35	3.07
2	Torsional	1.34	1.35	2.04	3.50
3	Transversal (1st longitudinal mode)	1.51	1.51	1.38	2.00
4	Transversal (2nd lateral mode)	4.23	4.20	1.56	2.32

Note: The descriptions of each mode are illustrated in Figure 6.

frequencies identified by the two methods are very close. However, the damping ratios are a little different, which implies the uncertainty of damping estimation from output-only system identification in the literature [13]. Damping ratios in the lateral direction are larger than those in the longitudinal direction. As a result, flexible and deformable behavior is expected in lateral direction.

The mode shapes calculated for each subsection of the structure are stitched together using the collocated sensors to yield the full global modes of the structure respectively for the two FDD and SSI methods. For quantitative comparison, the modal assurance criterion (MAC) [14] is adopted in this study. The MAC is a scholar index to correlate two sets of mode vectors, defined as

$$\text{MAC}_i(\Phi_{\text{FDD},i} \cdot \Phi_{\text{SSI},i}) = \frac{(\Phi_{\text{FDD},i}^T \cdot \Phi_{\text{SSI},i})^2}{(\Phi_{\text{FDD},i}^T \cdot \Phi_{\text{FDD},i})(\Phi_{\text{SSI},i}^T \cdot \Phi_{\text{SSI},i})}, \quad (8)$$

where  $\Phi_{A,i}$  is the  $i$ th mode from the method  $A$ . The MAC ranges from 0 to 1: the value of 1 implies perfect correlation of two mode shape vectors, while the value close to 0 means the uncorrelated vectors. In general, it is accepted that the MAC greater than 0.80 to 0.85 is considered a good match [4]. The MACs calculated with the identified mode shapes in this study are listed in Table 2: the lowest MAC of 0.9855 implies an excellent match between the mode shapes from the two methods. Since the two sets of mode shapes are very close, the mode shapes derived from the FDD are presented in Figure 6, where original shapes of the structure are superimposed by dotted lines. As seen, very clear mode shapes which are noticeable amplitudes in the directions of motion are almost identical at all nodes. Thus, it can be concluded that the structure behaves as an integrated body in the vibratory motion.

#### 4. Model-Based Story Stiffness Estimation

*4.1. Simplified Rigid Body Model.* Finite element model updating [15, 16] and data-driven structural parameter estimation [17, 18] can be applied to identify structures. However, these approaches are deemed to be rather challenging for its direct application to this study, since the tested structure is a complex timber frame with numerous structural elements. In

TABLE 2: MACs for corresponding two sets of mode shapes.

Modes	1	2	3	4
MAC	0.9965	0.9855	0.9976	0.9940

this regard, a different identification approach of model based data fitting is sought in this study.

The estimated modal characteristics of the Dongdaemun aforementioned in Section 3.2 confirm that identical dominant frequencies are noticed in the PSD spectra regardless of sensor deployments and sensor nodes, which leads to the speculation that the structure behaves as an integrated body. Therefore, a simplified rigid body model with two lumped masses is suggested to idealize the structure under the assumption that sum of flexural rigidities of beam-columns can be replaced equivalently with story stiffness at each mass. In the model, all connections between masses can be considered rotation-free hinges.

As seen in Figure 7, two degrees of freedom are considered for translational motions at each floor.  $m_1$  and  $m_2$  present lumped masses, respectively, for the first and second floors;  $k_1$  and  $k_2$  are equivalent story stiffnesses, respectively, for the first and second floors;  $P_1$  and  $P_2$  are weights of each floor acting in the direction of gravity; inter-story heights are  $l_1$  and  $l_2$ , respectively, for each floor; rigid body motions are described as displacements of  $Y_1$  and  $Y_2$ , respectively, for each floor.

The equation of motion for the model can be derived using an instant deformed shape of the model with displacements  $Y_1$  and  $Y_2$ , respectively, for the first and second stories shown in Figure 6(b). Considering dynamic moment equilibriums at points  $A$  and  $B$  and ignoring structural damping phenomena [19] leads to

$$\begin{aligned} P_2 l_2 \sin(\alpha + \beta) &= k_2 Y_2 l_2 \cos(\alpha + \beta) \\ &\quad + m_2 \ddot{Y}_2 l_2 \cos(\alpha + \beta), \\ P_2 (l_2 \sin(\alpha + \beta) + l_1 \sin \beta) + P_1 l_1 \sin \beta &= (k_2 Y_2 + m_2 \ddot{Y}_2) \\ &\quad \times (l_2 \cos(\alpha + \beta) + l_1 \cos \beta) \\ &\quad + (k_1 Y_1 + m_1 \ddot{Y}_1) l_1 \cos \beta. \end{aligned} \quad (9)$$

Assuming rotational angles  $\alpha$  and  $\beta$  are small, the trigonometric functions in (9) can be simplified. Then, combining (9), a linear equation for dynamic motion of the model is written in matrix expression as

$$\begin{bmatrix} m_1 & 0 \\ 0 & m_2 \end{bmatrix} \begin{Bmatrix} \ddot{Y}_1 \\ \ddot{Y}_2 \end{Bmatrix} + \begin{bmatrix} k_1 - \frac{P_1}{l_1} - \frac{P_2(l_1 + l_2)}{l_1 l_2} & \frac{P_2}{l_2} \\ \frac{P_2}{l_2} & k_2 - \frac{P_2}{l_2} \end{bmatrix} \begin{Bmatrix} Y_1 \\ Y_2 \end{Bmatrix} = \begin{Bmatrix} 0 \\ 0 \end{Bmatrix}. \quad (10)$$

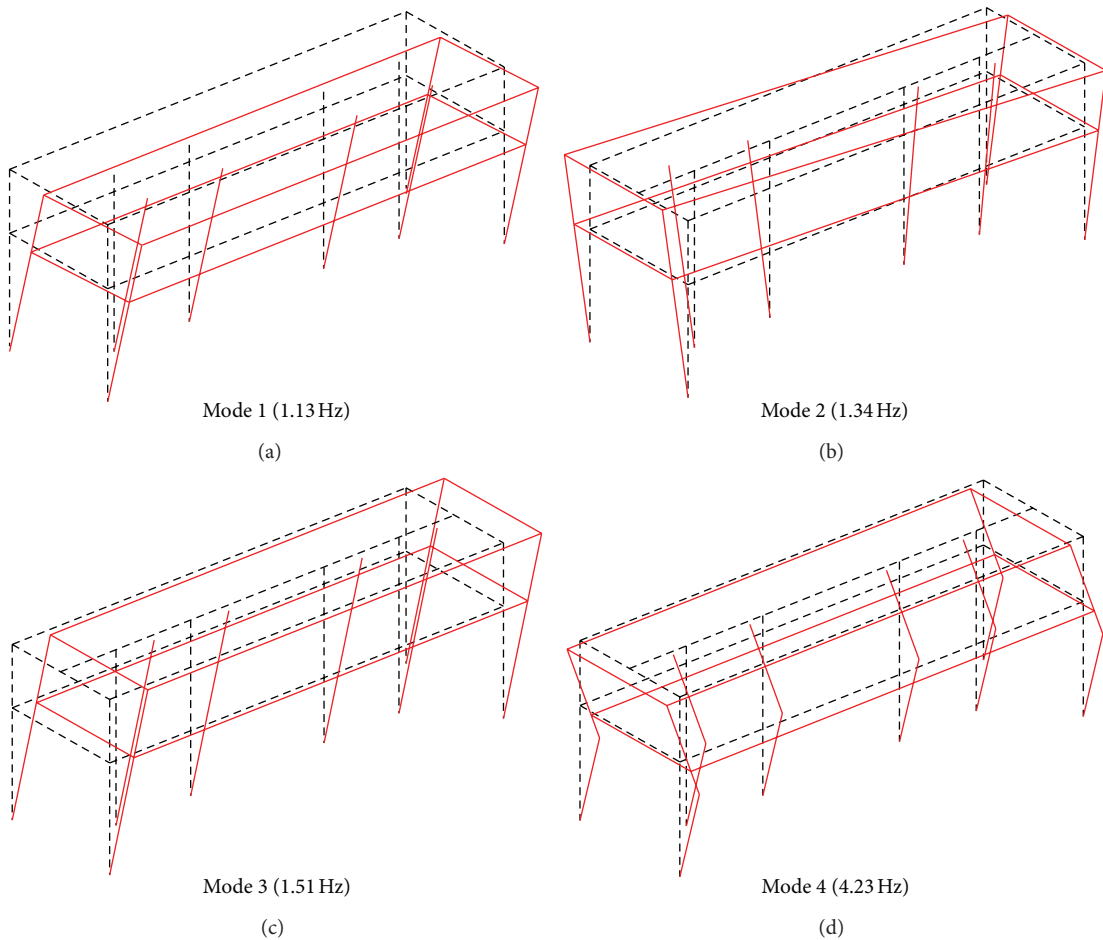


FIGURE 6: FDD derived mode shapes.

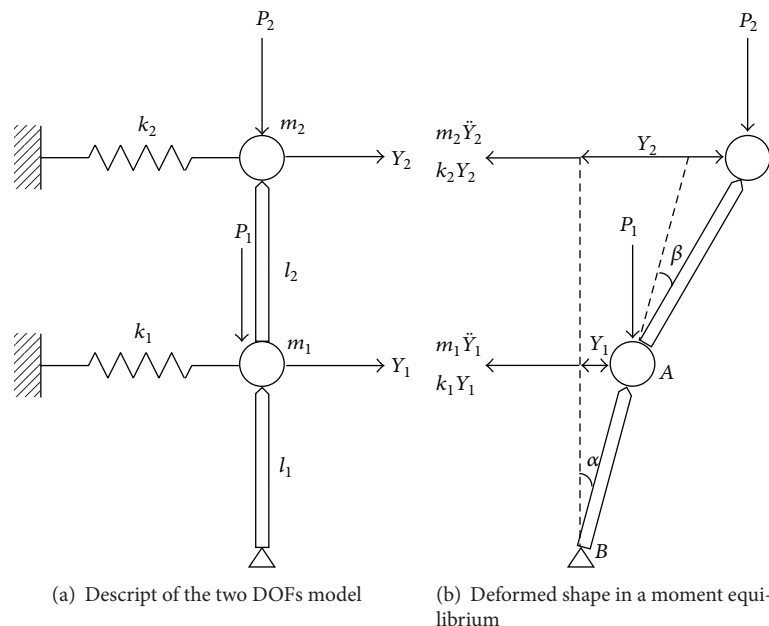


FIGURE 7: Simplified rigid body model.

Equation (10) can be further symbolized as

$$\mathbf{M}\ddot{\mathbf{Y}} + \mathbf{K}\mathbf{Y} = \mathbf{0}, \quad (11)$$

which stands for an eigenvalue problem, provided that a harmonic motion is considered. Namely, the eigenvalue problem of (11) captures vibratory behavior of the Dongdaemun.

**4.2. Story Stiffness Estimation.** Structural integrity of the Dongdaemun is assessed by story stiffness estimation of the simplified rigid body model: the story stiffnesses are estimated using the vibration model derived as (10) and the modal parameters estimated from the ambient vibration testing. The other parameters in (10) should be known in advance based on geometrical and material properties regarding the structure; referring to the report on field examination of Dongdaemun issued by the authority [20], the parameters are given as  $m_1 = 290\text{ t}$ ,  $m_2 = 315\text{ t}$ ,  $l_1 = 5.84\text{ m}$ ,  $l_2 = 7.69\text{ m}$ ,  $P_1 = 5,934\text{ kN}$ , and  $P_2 = 3,082\text{ kN}$ . The eigenvalue problem of (11) can be easily solved by setting determinant of the matrix equation to zero:

$$\det \begin{vmatrix} k_1 - \frac{P_1}{l_1} - \frac{P_2(l_1 + l_2)}{l_1 l_2} & \frac{P_2}{l_2} \\ \frac{P_2}{l_2} & k_2 - \frac{P_2}{l_2} \end{vmatrix} - \omega^2 \begin{bmatrix} m_1 & 0 \\ 0 & m_2 \end{bmatrix} = 0. \quad (12)$$

Substituting the given parameters and natural frequencies identified previously into (12), story stiffnesses are uniquely calculated for each vibratory direction of the Dongdaemun. As a result, the story stiffnesses in the lateral direction are calculated as 15.1 and 15.2 kN/mm, respectively, for  $k_1$  and  $k_2$ . In the longitudinal direction, 27.1 and 28.0 kN/mm are yielded, respectively, for  $k_1$  and  $k_2$ .

## 5. Conclusions

A Korean heritage property of the Dongdaemun is a historic wooden structure surrounded by lots of traffic such as subway trains, cars, and buses. In this study, a series of ambient vibration tests were conducted to identify the modal parameters of the structure. A dense sensor array was achieved by the virtue of multiple deployments of sensors sharing a small number of fixed reference sensors. Using time-history response data collected from the structure exposed to ambient excitation, offline output-only modal analysis was conducted by frequency domain decomposition and stochastic subspace identification methods. The four modes (i.e., two lateral, one longitudinal, and one torsional modes) were successfully identified. The modal parameters estimated from the two methods were also in a strong agreement.

Based on the experimental findings, a simplified rigid body model was derived for story stiffness estimation. Using the identified natural frequencies and vibration equation described as eigenvalue problem, the story stiffness was calculated. Future work is focused on development of methodology to track structural deterioration for heritage structures

based on the proposed story stiffness estimation; schedule-based monitoring of story stiffness of structures investigated gives a means for structural condition assessments along time line.

## Acknowledgment

The present research was conducted by the research fund of Dankook University in 2011. The authors gratefully acknowledge the financial support.

## References

- [1] R. Brincker and P. Andersen, "Ambient response analysis of the heritage court tower building structure," in *Proceedings of the 18th International Modal Analysis Conference (IMAC '00)*, Antonio, Tex, USA.
- [2] C. Gentile and A. Saisi, "Ambient vibration testing of historic masonry towers for structural identification and damage assessment," *Construction and Building Materials*, vol. 21, no. 6, pp. 1311–1321, 2007.
- [3] A. Pau, A. De Sortis, R. Marzellotta, and F. Vestroni, "Health monitoring of cultural heritage using ambient and forced vibration," in *Proceedings of the 1st International Conference on Safety and Security Engineering (SAFE '05)*, Rome, Italy, 2005.
- [4] C. Gentile and N. Gallino, "Ambient vibration testing and structural evaluation of an historic suspension footbridge," *Advances in Engineering Software*, vol. 39, no. 4, pp. 356–366, 2008.
- [5] W. Xin and M. Zhaobo, "Research on dynamic response of historic timber structure with platform-foundation under metro-induced loads," in *Proceedings of the 14th International Conference on Computer Supported Cooperative Work in Design (CSCWD '10)*, pp. 574–578, Shanghai, China, April 2010.
- [6] Y. Suzuki and M. Maeno, "Structural mechanism of traditional wooden frames by dynamic and static tests," *Structural Control and Health Monitoring*, vol. 13, no. 1, pp. 508–522, 2006.
- [7] J. Kim and J. P. Lynch, "Subspace system identification of support-excited structures-part I: theory and black-box system identification," *Earthquake Engineering and Structural Dynamics*, vol. 41, no. 15, pp. 2235–2251, 2012.
- [8] B. Peeters and C. E. Ventura, "Comparative study of modal analysis techniques for bridge dynamic characteristics," *Mechanical Systems and Signal Processing*, vol. 17, no. 5, pp. 965–988, 2003.
- [9] P. Van Overschee and B. De Moor, *Subspace Identification for Linear Systems*, Kluwer Academic Publishers, Dordrecht, Netherlands, 1996.
- [10] M. Verhaegen and V. Verdult, *Filtering and System Identification, A least square Approach*, Cambridge University Press, Cambridge, UK, 2007.
- [11] A. V. Oppenheim and R. W. Schafer, *Discrete-Time Signal Processing*, Prentice-Hall, Upper Saddle River, NJ, USA, 1999.
- [12] R. Brincker, C. E. Ventura, and P. Andersen, "Damping estimation by frequency domain decomposition," in *Proceedings of the 19th International Modal Analysis Conference (IMAC '01)*, Orlando, Fla, USA.
- [13] J. Kim and J. P. Lynch, "Subspace system identification of support excited structures-part II: gray-box interpretations and damage detection," *Earthquake Engineering and Structural Dynamics*, vol. 41, no. 15, pp. 2253–2271, 2012.

- [14] R. J. Allemand and D. L. Brown, "Correlation Coefficient for Modal Vector Analysis," in *Proceedings of the 1th International Modal Analysis Conference (IMAC '83)*, Orlando, Fla, USA, 1983.
- [15] E. Yu, E. Taciroglu, and J. W. Wallace, "Parameter identification of framed structures using an improved finite element model-updating method—part I: formulation and verification," *Earthquake Engineering and Structural Dynamics*, vol. 36, no. 5, pp. 619–639, 2007.
- [16] Q. W. Zhang, C. C. Chang, and T. Y. P. Chang, "Finite element model updating for structures with parametric constraints," *Earthquake Engineering and Structural Dynamics*, vol. 29, pp. 927–944, 2000.
- [17] J. Kim, K. Kim, and H. Sohn, "Data-driven physical parameter estimation for lumped mass structures from a single point actuation test," *Journal of Sound and Vibration*, vol. 132, no. 18, pp. 4390–4402, 2013.
- [18] H. Xiao, O. T. Bruhns, H. Waller, and A. Meyers, "An input/output-based procedure for fully evaluating and monitoring dynamic properties of structural systems via a subspace identification method," *Journal of Sound and Vibration*, vol. 246, no. 4, pp. 601–623, 2001.
- [19] K. J. Bathe, *Finite Element Procedures*, Prentice-Hall, Upper Saddle River, NJ, USA, 2007.
- [20] "The Report on Field Examination of Dongdaemun," Jongno-gu Office of Seoul Metroplitan Goverment: Jongno-gu, Seoul, 2006.

## Research Article

# Investigation of Time Series Representations and Similarity Measures for Structural Damage Pattern Recognition

Wenjia Liu,<sup>1</sup> Bo Chen,<sup>2</sup> and R. Andrew Swartz<sup>3</sup>

<sup>1</sup> Elektrobit Automotive Inc. Detroit, Farmington Hills, MI 48331, USA

<sup>2</sup> Department of Mechanical Engineering—Engineering Mechanics, Department of Electrical and Computer Engineering, Michigan Technological University, Houghton, MI 49931, USA

<sup>3</sup> Department of Civil and Environmental Engineering, Department of Electrical and Computer Engineering, Michigan Technological University, Houghton, MI 49931, USA

Correspondence should be addressed to Bo Chen; bochen@mtu.edu

Received 20 July 2013; Accepted 25 August 2013

Academic Editors: D. G. Aggelis, N. Alver, and H. K. Chai

Copyright © 2013 Wenjia Liu et al. This is an open access article distributed under the Creative Commons Attribution License, which permits unrestricted use, distribution, and reproduction in any medium, provided the original work is properly cited.

This paper investigates the time series representation methods and similarity measures for sensor data feature extraction and structural damage pattern recognition. Both model-based time series representation and dimensionality reduction methods are studied to compare the effectiveness of feature extraction for damage pattern recognition. The evaluation of feature extraction methods is performed by examining the separation of feature vectors among different damage patterns and the pattern recognition success rate. In addition, the impact of similarity measures on the pattern recognition success rate and the metrics for damage localization are also investigated. The test data used in this study are from the System Identification to Monitor Civil Engineering Structures (SIMCES) Z24 Bridge damage detection tests, a rigorous instrumentation campaign that recorded the dynamic performance of a concrete box-girder bridge under progressively increasing damage scenarios. A number of progressive damage test case datasets and damage test data with different damage modalities are used. The simulation results show that both time series representation methods and similarity measures have significant impact on the pattern recognition success rate.

## 1. Introduction

Time series is one of the most commonly used data formats in real world. It is being generated in a tremendous speed from almost every application area. Processing raw time series data is expensive due to its high dimension. Two key aspects for achieving effectiveness and efficiency when managing time series data are representation methods and similarity measures [1]. In the last decades, a number of representation methods and similarity measures have been proposed to extract features from time series data for indexing, classification, and clustering. The objective of feature extraction is to find a representation at a lower dimensionality that preserves the fundamental characteristics of the original time-series data [2]. The time series representation methods can be classified as shape-based method, structure-based (or model-based) method, and dimensionality reduction. For long time series data, model-based and dimensionality reduction methods are more effective.

Model-based time series representation methods extract global features from time series, create feature vectors, and use these feature vectors to measure similarity of time series for classification and clustering. Time series data are usually fitted into models, such as Box Jenkins model or Markov Model, and the parameters of the model are used to form feature vectors. The dimensionality reduction methods are typically based on data transformation. Many dimensionality reduction methods have been reported in the literature, such as discrete Fourier transformation (DFT) [3, 4], single value decomposition (SVD) [5], discrete wavelet transformation (DWT) [6], piecewise approximation [7], and Chebyshev polynomials (CHEB) [8].

Similarity measure is important for both evaluating feature extraction methods and time series classification. Feature extraction process consists of following steps: establishing a distance metric, producing a dimensionality reduction technique that reduces the dimensionality of the data from

$n$  to  $N$  (where  $N < n$ ), and producing a distance measure defined on the  $N$ -dimensional representation of the data. There are over a dozen distance measures that have been reported in the literature for mining and indexing time series. These similarity measures include Euclidean distance [4], Mahalanobis distance, Cosine distance, Standardized Euclidean (Seuclidean) distance, Correlation distance, and Dynamic Time Warping (DTW) [9, 10].

This paper examines several time series representation methods and similarity measures for structural damage feature extraction and pattern recognition. Smart sensors have been widely used for structural health monitoring, and sensor data-based structural damage detection has received increased attention recently [11–13]. In this paper, pattern-recognition-based structural damage detection and classification are based on the similarity measure of damage feature vectors with normal feature vectors. The goal of the feature extraction is to select features which will result in the separation of damage feature vectors and normal feature vectors in the feature space. This will allow us to distinguish damage and normal patterns. The performance of representation methods and similarity measures are evaluated utilizing acceleration data collected from the Z24 Bridge as part of the System Identification to Monitor Civil Engineering Structures (SIMCES) project.

The rest of the paper is organized as follows. Section 2 introduces the Z24 bridge datasets which are used for the validation. Section 3 presents feature representation methods studied in this paper for structural damage feature extraction from time series sensor data. Section 4 evaluates the effects of multiple similarity measures and the length of time series data on the performance of structural damage pattern recognition. Section 5 concludes the work.

## 2. Validation Structural Data: Z24 Bridge Datasets

To investigate the effectiveness of time series representation methods and similarity measures applied to structural damage pattern recognition, the Z24 Bridge test datasets are used as validation data in this paper [14]. The Z24 Bridge datasets are especially appealing because the progressive damage scenarios include scenarios of the same type of damage but varying levels (support settlement) as well as radically distinct damage modalities (support settlement versus concrete spalling versus damage to pretension elements). These features of the damage scenarios allow us to differentiate between damage patterns that differ based on damage modality versus damage patterns that differ based on damage severity.

Sensors collecting global level vibrational data (e.g., displacements or accelerations in frequency ranges consistent with global modes of the structure) are capable of capturing dynamic effects that can give an indication of the overall health of the structure. The Z24 Bridge datasets are global level vibrational data that are well known within the civil structural health monitoring community and that have been made widely available for other health monitoring studies.

TABLE 1: Description of progressive damage tests.

Test	Description
Pattern 1	No damage (missing/corrupted data)
Pattern 2	No damage, pier hinge added (baseline)
Pattern 3	Pier 3 settlement: 20 mm
Pattern 4	Pier 3 settlement: 40 mm
Pattern 5	Pier 3 settlement: 80 mm
Pattern 6	Pier 3 settlement: 95 mm
Pattern 7	Pier 3 foundation tilt
Pattern 8	No damage, pier 3 restored
Pattern 9	Concrete spalling: 12 m <sup>2</sup>
Pattern 10	Concrete spalling: 24 m <sup>2</sup>
Pattern 11	Landslide at abutment
Pattern 12	Concrete hinge failure
Pattern 13	Anchor head failure (2)
Pattern 14	Anchor head failure (4)
Pattern 15	Tendon wire failure (54/2)
Pattern 16	Tendon wire failure (100/4)

The SIMCES project began in 1997 with a goal to collect real-world data from an operational bridge under realistic damage scenarios. The Z24 Bridge, crossing Bern to Zurich highway and located between Koppigen and Utzenstorf, Switzerland, was heavily instrumented and tested under a systematic program of progressive damage scenarios before it was demolished to make way for a new railway line [14]. Extensive acceleration measurements were made both from the undamaged bridge (correlated with environmental effects) and during the progressive damage scenarios. Data from this project has been used in a number of published studies on the properties of the structure [15–20] as well as damage detection strategies [20–25].

The bridge itself was a three-span, medium-span pre-stressed concrete, two-cell, closed box-girder bridge with concrete columns. Global level acceleration data were recorded in both ambient vibration test (AVT) and forced vibration test (FVT). Two vertical shakers were used to excite the bridge for the forced tests. The distribution of bridge surface accelerometers is shown in Figure 1. A series of progressive damage cases were applied beginning with the most reversible cases (including multiple levels of support settlement) and progressing to irreversible cases (e.g., concrete spalling, damage to prestressing tendons, anchor heads, etc.). Table 1 provides a list of damage scenarios. In the presented study, the data collected from these damage scenarios are divided into training and test subsets. The training subset was used to generate representative feature vectors for damage patterns, and the test subset was used to find the success rate of the pattern recognition.

## 3. Feature Representation of Time Series Sensor Data

Many high-level representations of time series data have been proposed for similarity search and data mining as shown in

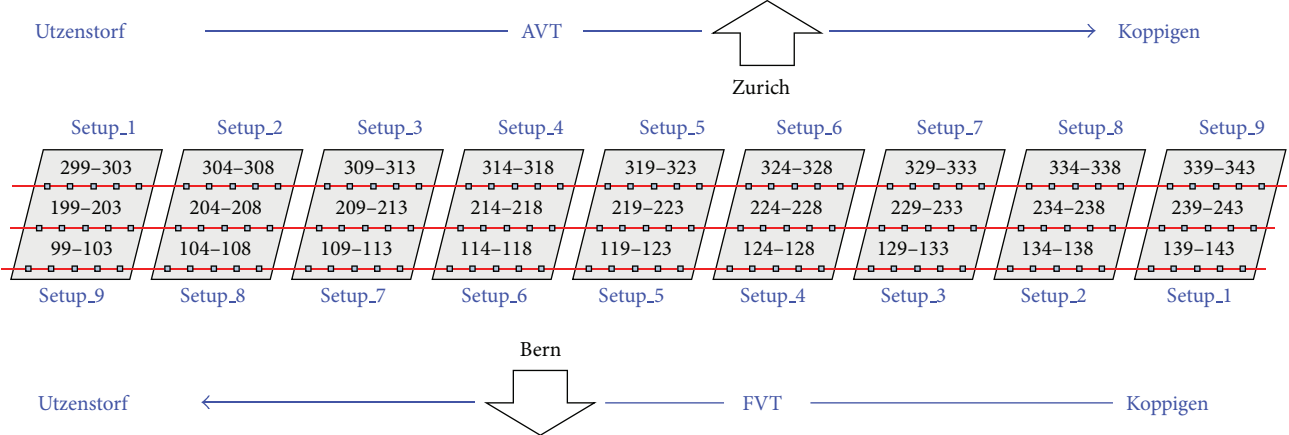


FIGURE 1: Measurement setup for vibration test on Z24 bridge [26].

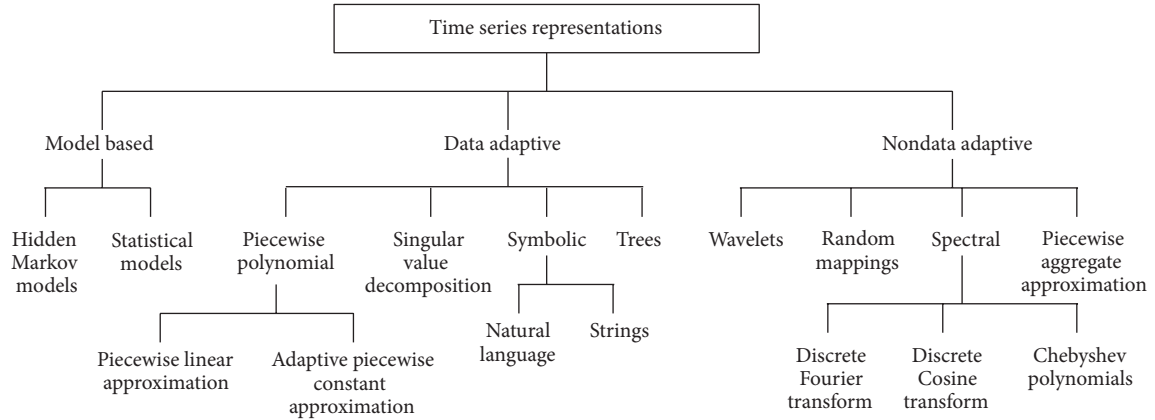


FIGURE 2: Time series representations [27].

Figure 2, including single value decomposition (SVD) [5], discrete Fourier transformation [3, 4], discrete wavelet transformation [6], adaptive piecewise constant approximation [7], discrete cosine transformation [5], Chebyshev polynomials [8], piecewise aggregate approximation [29], and symbolic aggregate approximation [30]. In this paper, autoregressive (AR) model-based and dimensionality reduction (DFT and DWT) feature extraction methods are investigated.

**3.1. Model-Based Feature Extraction Methods.** In this paper, autoregressive model is used to model a time series sensor data. The AR model-based feature extraction method fits time series into an AR model and uses the coefficients of the AR model as members of the feature vector. For a time series sensor data  $x$ , it can be fitted into an AR model of order  $p$  as shown by

$$x_k = \sum_{i=1}^p \alpha_i x_{k-i} + r_k, \quad k = p+1, \dots, n, \quad (1)$$

Where  $\alpha_i$ ,  $i = 1, 2, \dots$ , and  $p$  are the coefficients of the AR model. The order of AR model is 20 in this paper. The feature

vector of the time series sensor data  $x$ ,  $F(X)$ , is formed by the coefficients of the AR model as shown by

$$F(X) = (\alpha_1, \alpha_2, \dots, \alpha_p)^T. \quad (2)$$

To reduce noise effects, the measurement sensor data  $Z$  are standardized by

$$x_i = \frac{z_i - \mu_i}{\sigma_i}, \quad i = 1, 2, \dots, n, \quad (3)$$

where  $\mu_i$  and  $\sigma_i$  are the mean and standard deviation of the time series  $Z$ .

### 3.2. Dimensionality Reduction Methods

**3.2.1. Discrete Fourier Transform.** The Discrete Fourier Transform (DFT) is one type of discrete transforms which transforms a function in the time domain into another in the frequency domain. Given a time series  $x$  with the length of  $n$ , the DFT of  $x$  is defined to be  $X$  consisting of  $n$  complex numbers  $X_k$ ,  $k = 1, 2, \dots, n$  as shown by

$$X_k = \sum_{i=1}^n x_i e^{-j(2\pi/n)(k-1)(i-1)}, \quad k = 1, 2, \dots, n. \quad (4)$$

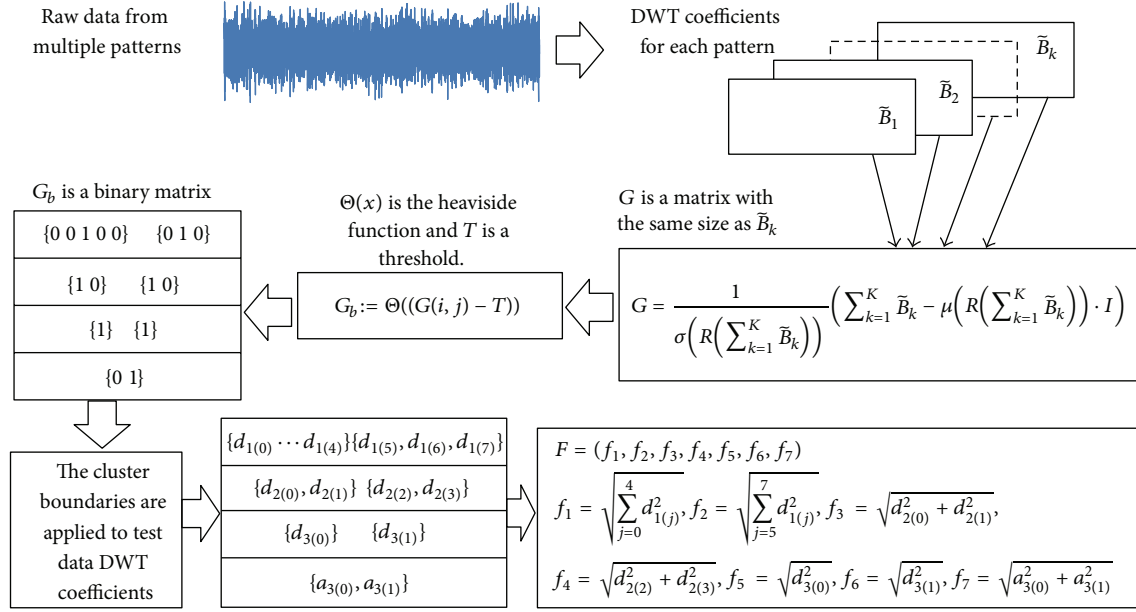


FIGURE 3: Feature extraction from DWT coefficients [28].

To perform the dimensionality reduction of the time series  $X$  into a reduced feature space of dimensionality  $R$ , two feature selection methods are compared. The first method uses the first  $R$  number of DFT coefficients to form an  $R$ -dimensional feature vector to represent the time series  $X$  in the  $R$ -dimensional feature space [4]. The second method uses first 8 model frequencies and corresponding signal amplitudes to form feature vectors. Model frequencies of the bridge presented in [31] are used as references in the search of real modal frequencies and signal amplitudes in sensor time series. Assume that the first 8 model frequencies and amplitudes of a time series signal are  $f_1, f_2, f_3, f_4, f_5, f_6, f_7$ , and  $f_8$  and  $a_1, a_2, a_3, a_4, a_5, a_6, a_7$ , and  $a_8$ , the feature vector of the time series is defined as

$$\begin{aligned} F(X) = & (f_1, k \times a_1, f_2, k \times a_2, f_3, k \times a_3, f_4, k \times a_4, \\ & f_5, k \times a_5, f_6, k \times a_6, f_7, k \times a_7, f_8, k \times a_8), \end{aligned} \quad (5)$$

where  $k$  is the weight factor of the amplitudes.

**3.2.2. Discrete Wavelet Transform.** Discrete wavelet transform decomposes a signal into layers of coefficients. These coefficients contain both frequency and time domain information. Discrete wavelet transform has been applied for feature extraction in different fields [32–34]. Given a time series  $x$  with the length of  $n$ , the discrete wavelet transform (DWT) of  $x$  is calculated by passing the time series signal through a series of low pass and high pass filters as shown by

$$\begin{aligned} y_l[n] &= x[n] * g[n] = \sum_{k=-\infty}^{\infty} x[k] g[n-k], \\ y_h[n] &= x[n] * h[n] = \sum_{k=-\infty}^{\infty} x[k] h[n-k], \end{aligned} \quad (6)$$

where  $g[n]$  and  $h[n]$  are low pass filter and high pass filter, respectively. The outputs of the high pass filter are detail coefficients, while the outputs of the low pass filter are approximation coefficients. The approximation coefficients are further decomposed in the next iteration while the detail coefficients are kept as the current level wavelet coefficients.

To form feature vectors from wavelet coefficients, feature extraction method proposed in [28] is employed. This feature extraction method consists of two steps: cluster determination and feature extraction. The cluster determination process divides the wavelet coefficients into a number of clusters  $c_1, c_2, \dots, c_k$ , and the feature extraction process calculates the feature vector for a time series of sensor data. The elements of a feature vector are Euclidean norms of each cluster  $F = (\|c_1\|_2, \|c_2\|_2, \dots, \|c_k\|_2)$ . The clusters  $c_1, c_2, \dots, c_k$  are determined as row vectors such that each cluster contains a significant wavelet coefficient near the midpoint of each cluster.

Figure 3 shows the process of cluster determination and feature extraction from the sensor data of multiple data patterns. First, the DWT coefficient matrices of sensor data from multiple patterns are calculated. The dimensions of these coefficient matrices are the same if time series sensor data have the same length. To find significant wavelet coefficients, the Central Limit Theorem [35] is applied to the elements of the DWT coefficient matrices to generate a new matrix  $G$  as shown by

$$G = \frac{1}{\sigma(R(\sum_{k=1}^K \tilde{B}_k))} \left( \sum_{k=1}^K \tilde{B}_k - \mu \left( R \left( \sum_{k=1}^K \tilde{B}_k \right) \right) \cdot I \right), \quad (7)$$

where  $R$  is the operator to reduce a matrix by its last row and  $I$  is a matrix which has the same size as  $\tilde{B}_k$  and has all the elements of 1. The members of the  $G$  matrix are then compared with a threshold and save the comparison

results to the corresponding location in a matrix  $G_b$ . The comparison result is 1 when the member of the  $G$  matrix is greater than the threshold and 0 when the member of the  $G$  matrix is less than the threshold. Pittner and Kamarthi [28] prove that the 1s in the matrix  $G_b$  occur at the same locations where the significant wavelet coefficients occur in the matrices  $\tilde{B}_k$ . Based on the  $G_b$  matrix, the clusters are then formed with the following rules: (1) each cluster contains one “1” element and (2) if one row contains no “1” element, this row is treated as one cluster. After the boundaries of each cluster are determined from the  $G_b$  matrix, the wavelet coefficients in the  $\tilde{B}_k$  matrices are grouped into clusters using the cluster boundary information obtained from the  $G_b$  matrix. The feature vector of the  $\tilde{B}_k$  matrix is calculated with the Euclidean norms of each cluster as shown in Figure 3.

#### 4. Performance Evaluation

Performance evaluation was conducted to test the effectiveness of the feature extraction methods. Two test scenarios were designed: (1) same type of structural damage with different extents (patterns 2–6 in Table 1) and (2) different damage modalities (patterns 6, 10, 11, 12, 14, and 16 in Table 1). We adopted sensor data collected by sensor node 232 in the forced vibration test. Data points in the sensor data files were divided into two groups: training data and test data. Feature vectors generated from training data were used to find the representative feature vectors for each damage pattern using  $K$ -means method. The feature vectors created from test data were used to test the effectiveness of feature extraction methods for damage pattern recognition using  $K$ -nearest neighbor (KNN-1) classification method.

To find good similarity measures for structural damage pattern recognition, a number of commonly used similarity measures are evaluated using Z24 bridge datasets. The tested similarity measures include Manhattan distance, Euclidean distance, L-infinity (Maximum) norm, Mahalanobis distance, cosine distance, standardized Euclidean (Seuclidean) distance, and correlation distance. Let  $X$  and  $Y$  be two feature vectors with dimension  $n$ . The definitions of these similarity measures are given as follows.

(i) Manhattan distance:

$$d_{XY} = \sum_{i=1}^n |X_i - Y_i|. \quad (8)$$

(ii) Euclidean distance:

$$D = \sqrt{(X - Y)(X - Y)^T}. \quad (9)$$

(iii) L-infinity:

$$d_{XY} = \max(|X_i - Y_i|), \quad i \in n. \quad (10)$$

(iv) The Mahalanobis distance of a multivariate vector  $X = (x_1, x_2, \dots, x_n)^T$  from a group of values with

mean  $\mu = (\mu_1, \mu_2, \dots, \mu_n)^T$  and covariance matrix  $S$  is defined as

$$D = \sqrt{(X - \mu)^T S^{-1} (X - \mu)}. \quad (11)$$

(v) Cosine distance:

$$d_{XY} = 1 - \frac{XY^T}{(XX^T)^{1/2} (YY^T)^{1/2}}. \quad (12)$$

(vi) Standardized Euclidean (Seuclidean) distance:

$$d_{XY}^2 = (X - Y) D^{-1} (X - Y)^T, \quad (13)$$

where  $D$  is a diagonal matrix with diagonal elements given by  $v_j^2$ , which denotes the variance of the  $j$ th-feature over all the features vectors contained by  $X$  and  $Y$ .

(vii) Correlation distance:

$$d_{XY} = 1 - \frac{(X - \bar{X})(Y - \bar{Y})^T}{\left((X - \bar{X})(X - \bar{X})^T\right)^{1/2} \left((Y - \bar{Y})(Y - \bar{Y})^T\right)^{1/2}}, \quad (14)$$

where  $\bar{X} = (1/p) \sum_j X_j$ ,  $\bar{Y} = (1/p) \sum_j Y_j$ .

**4.1. The Effects of Similarity Measures and the Length of Time Series on the Performance of Pattern Recognition Using AR-Based Feature Extraction.** To test the performance of feature extraction methods, the Z24 Bridge datasets described in Section 2 are used. In the Z24 bridge datasets, each sensor data file contains 65536 acceleration data points. To avoid unstable measurement data in the beginning of each test, the first 4999 data points are abandoned. The rest of the measurement data in data files are used for feature extraction. The first time series starts from 5000th data point. The next time series is formed by shifting 100 data points from previous time series. For example, the second time series starts from 5100th data point and the third time series starts from 5200th data point. Various lengths of time series are formed to test the impact of time series length on the performance of pattern recognition. The selected time series lengths include 100, 200, 300, 500, 700, 1000, 1500, 2000, 3000, and 5000.

The success rate of classifying test data to corresponding damage patterns using AR-based feature extraction method was evaluated for different damage modalities and progressive damage patterns. Figure 4 shows the average success rate of pattern recognition in first scenario (pattern 2–6 in Table 1) using similarity measures defined above. Five data patterns defined in the first scenario are No damage, pier 3 settlement—20 mm, pier 3 settlement—40 mm, pier 3 settlement—80 mm, and pier 3 settlement—95 mm. The  $x$ -axis stands for the length of time series for feature extraction; the  $y$  axis stands for the type of similarity measures; and the  $z$  axis is the average success rate of AR-based feature extraction method. From Figure 4, we can see that the Mahalanobis

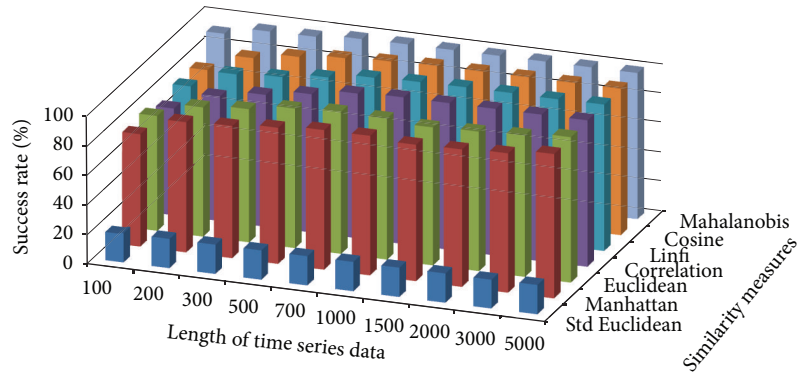


FIGURE 4: Average success rate of pattern recognition with different similarity measures and the length of time series in first scenario.

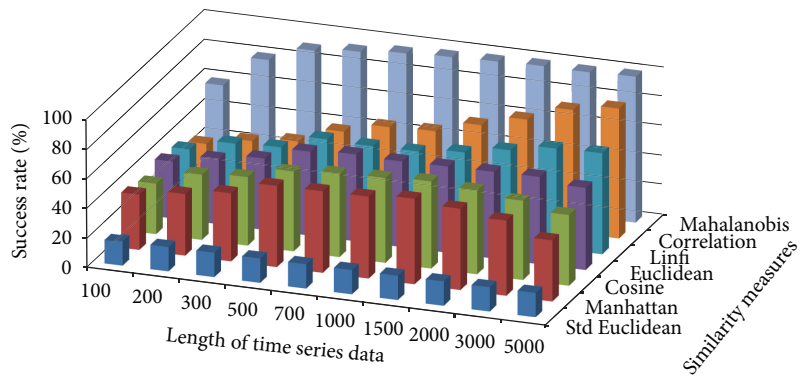


FIGURE 5: Average success rate of pattern recognition with different similarity measures and the length of time series in second scenario.

distance outperforms over other similarity measures. For each similarity measure, the success rate increases as the length of time series gets longer.

Figure 5 shows the average success rate of pattern recognition for Patterns 6, 10, 11, 12, 14, and 16 in Table 1 (pier 3 settlement—95 mm, concrete spalling— $24 \text{ m}^2$ , landslide at abutment, concrete hinge failure, anchor head failure (4), and tendon wire failure (100/4)). Figure 5 presents similar trends as Figure 4 with regard to the effects of similarity measures on the pattern recognition success rate for AR-based feature extraction method. The success rate in Figure 5, however, is generally lower than in Figure 4. This is due to the separation of feature vectors in first scenario is better than that of the second scenario. This can be observed from Figures 6 and 7. These two figures show the distribution of AR feature vectors of data patterns in the first and second scenarios from the sensor node 232 using Mahalanobis distance. To display high dimensional feature vectors in 2D space, 20-dimensional feature vectors are reduced to 2-dimensional feature vectors using principal component analysis (PCA). The  $x$ -axis is the first component after PCA and the  $y$ -axis is the second component after PCA.

The impact of the length of time series on pattern recognition success rate using Mahalanobis distance as similarity measure was also investigated. Figure 8 shows the success rates of pattern recognition in first scenario and Figure 9 shows the success rates of pattern recognition in second

scenario. Figure 8 indicates that the success rate increases as the length of time series increases. In addition, the severity of damage affects the pattern recognition success rate. Pattern 6, with largest settlement, has the highest pattern recognition success rate. Figure 9 shows the success rate of pattern recognition performed on different damage modalities. Similarly, the success rates go up as the lengths of time series increases.

The success rate is also affected by the separation of feature vectors in feature space. Figures 6 and 7 show the distribution of feature vectors in the first and second scenarios. The length of time series is 5000 in both plots. In Figure 6, the feature vectors of pattern 6 are located far away from feature vectors of other patterns. As a result, pattern 6 is easy to be recognized. The success rate of pattern 6 is the highest one compared with other patterns. Figure 7 shows the distribution of the feature vectors from different damage modalities. As we can see from Figure 7, feature vectors of pattern 14 are located far away from feature vectors of other patterns, so the success rates of pattern 14 is higher than the success rate of other patterns. In general, the separation of feature vectors in first scenario is better than that of the second scenario. The overall success rate in first scenario is also higher than that of the second scenario.

#### 4.2. The Effects of Similarity Measures on the Performance of Pattern Recognition Using DFT-Based Feature Extraction.

Figures 10 and 11 show the average success rate of DFT-based

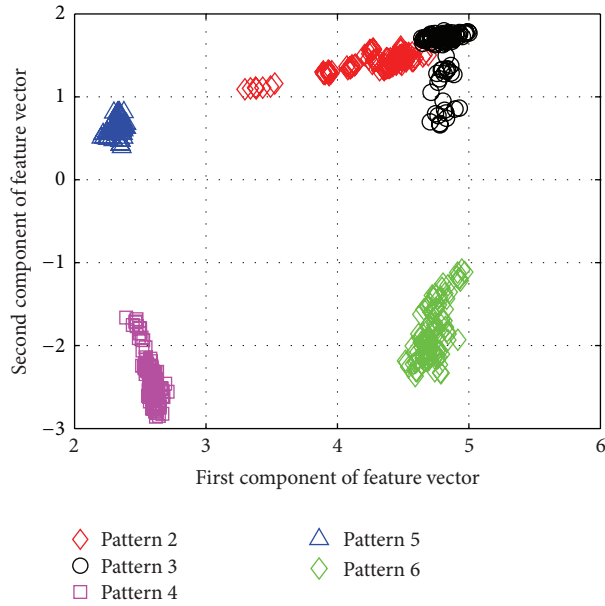


FIGURE 6: The AR feature vectors of data patterns in first scenario from sensor node 232 using Mahalanobis distance.

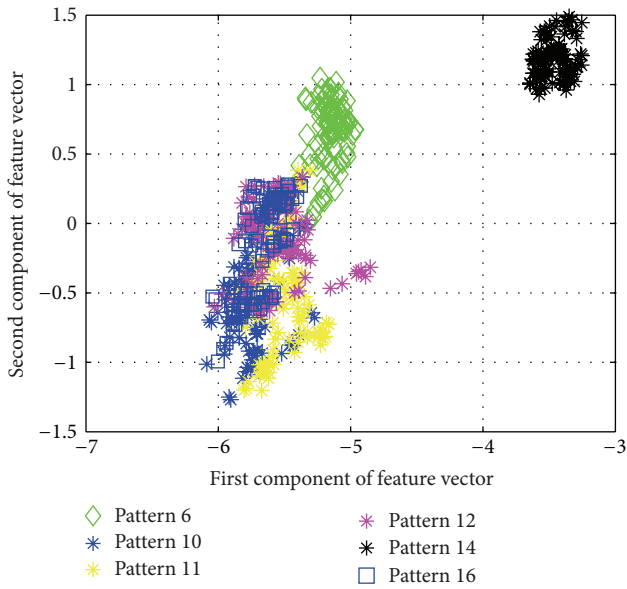


FIGURE 7: The AR feature vectors of data patterns in second scenario from sensor node 232 using Mahalanobis distance.

feature extraction method for structural damage pattern recognition with different similarity measures. In general, the success rate of DFT-based feature extraction is lower than that of AR-based feature extraction method. Compare with two test scenarios, the first scenario has relatively high success rate. In both test scenarios, the dissimilarity measure—Mahalanobis distance again showing better performance than other similarity measures.

#### 4.3. The Effects of Time Series Length on Success Rate Using DFT-Based Feature Extraction.

Figures 12 and 13 show the

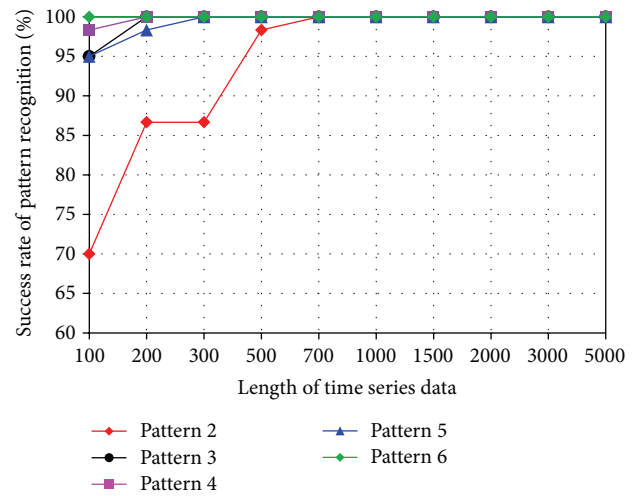


FIGURE 8: Success rate of pattern recognition for first scenario (pattern 2–6) using Mahalanobis distance.

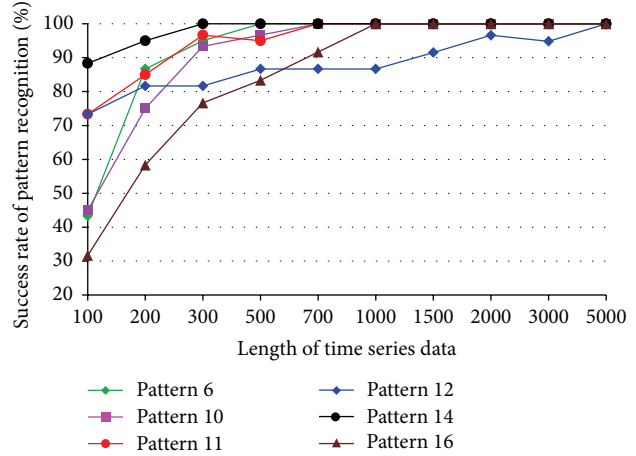


FIGURE 9: Success rate of pattern recognition for second scenario (patterns 6, 10, 11, 12, 14, and 16) using Mahalanobis distance.

success rates of pattern recognition for each damage pattern with different lengths of time series. The similarity measure used in the tests is the Mahalanobis distance. For most damage patterns, the success rate increases as the length of time series increases. In general, the success rate of pattern recognition in first scenario is better than that of the second scenario. Figures 14 and 15 show the distribution of the feature vectors in two scenarios using DFT-based feature extraction method. The length of time series is 5000 in both plots. The separation of feature vectors using AR-based feature extraction method (Figures 6 and 7) is better than that of the DFT-based feature extraction method (Figures 14 and 15). As a result, the success rates of pattern recognition using AR-based feature extraction (Figures 8 and 9) are higher than that of the DFT-based feature extraction (Figures 12 and 13).

#### 4.4. The Effects of Similarity Measures on the Performance of Pattern Recognition Using DWT-Based Feature Extraction.

Figures 16 and 17 show the average success rate of

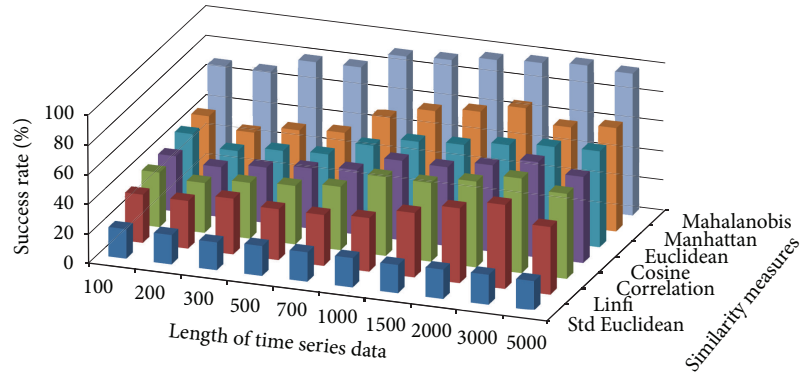


FIGURE 10: Average success rate of pattern recognition using DFT-based feature extraction in first scenario.

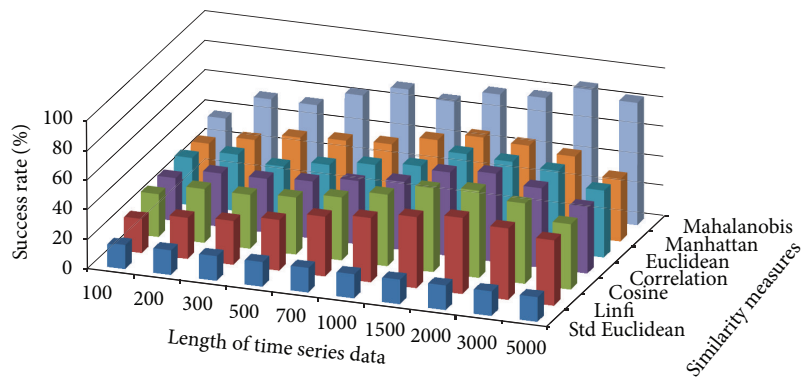


FIGURE 11: Average success rate of pattern recognition using DFT-based feature extraction in second scenario.

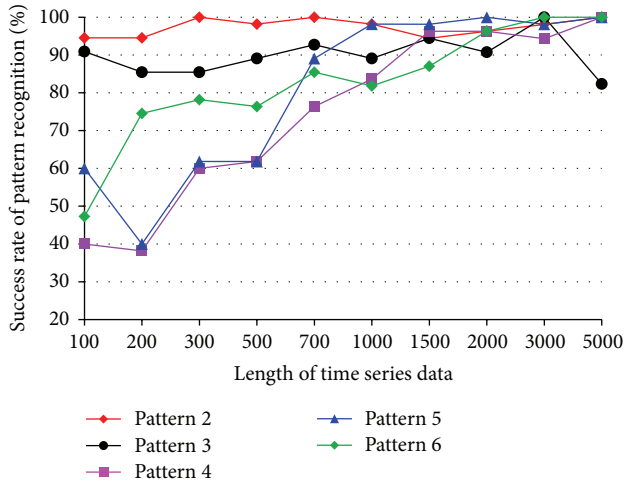


FIGURE 12: Success rate of pattern recognition using DFT-based feature extraction in first scenario.

DWT-based feature extraction method for structural damage pattern recognition with different similarity measures. In general, the success rate of DWT-based feature extraction is lower than that of AR-based feature extraction method but higher than that of the DFT-based feature extraction method. Compare with two test scenarios, the first scenario has relatively high success rate. In both test scenarios, the

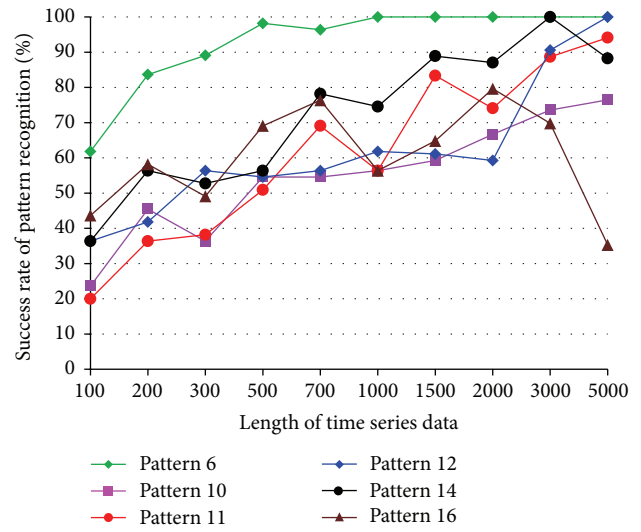


FIGURE 13: Success rate of pattern recognition using DFT-based feature extraction in second scenario.

dissimilarity measure—Mahalanobis distance again showing better performance than other similarity measures.

**4.5. The Effects of Time Series Length on Success Rate Using DWT-Based Feature Extraction.** Figures 18 and 19 show the

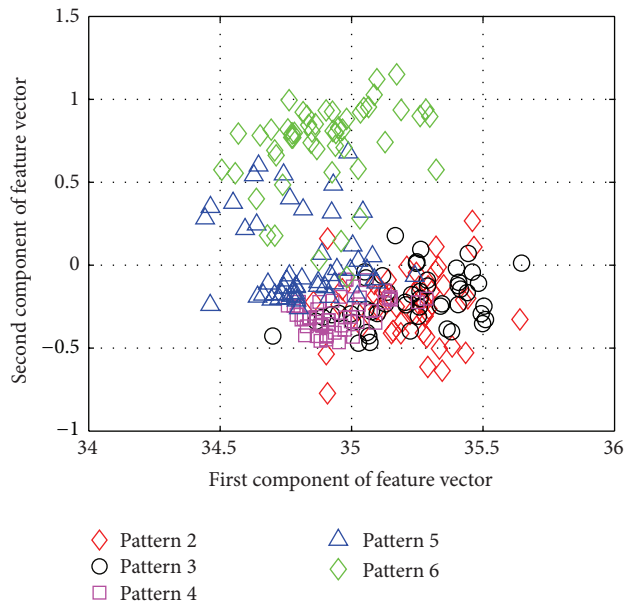


FIGURE 14: The DFT feature vectors of data patterns in first scenario from sensor node 232.

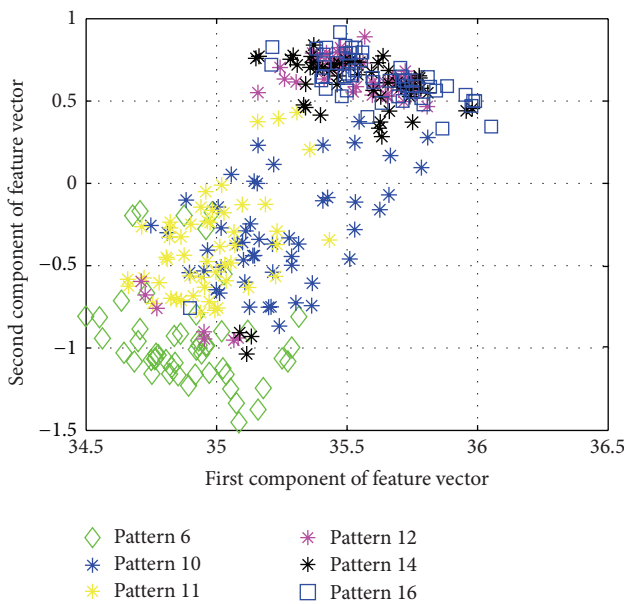


FIGURE 15: The DFT feature vectors of data patterns in second scenario from sensor node 232.

success rates of pattern recognition for each damage pattern with different lengths of time series. The similarity measure used in the tests is the Mahalanobis distance. For most damage patterns, the success rate increases as the length of time series increases. Figures 20 and 21 show the distribution of the feature vectors in two scenarios. The length of time series is 5000 in both plots. Comparing the success rate plot with feature distribution in both test scenarios, the impact of the separation of feature vectors on the success rate can clearly be seen again. The success rates of patterns 2 and 3 in the first

scenario are much higher compared with other patterns, and the success rates of patterns 6 and 14 in the second scenario are much higher compared with other patterns.

**4.6. Damage Localization Analysis Using Pattern Recognition Approach.** Damage localization is important when the damage is detected. To investigate the applicability of pattern recognition approach for structural damage localization, the numerical analysis study has been conducted to examine the shift of the representative feature vectors of the damage patterns from the normal pattern in the feature space using damage pattern 6 data of Z24 Bridge. To find out the potential relationship between damage location and the feature vectors of sensor data, the distances between normal pattern feature vectors and damage pattern 6 feature vectors are calculated. The similarity measure used in the calculation is Mahalanobis distance as

#### Feature shift distance

$$= \text{Mahalanobis}(\text{damage feature vectors}, \text{normal feature vectors}). \quad (15)$$

Figure 22 shows the feature vector shift of damage pattern 6 from the normal pattern on the sensor nodes 120–320. The distribution of these sensor nodes on the bridge is indicated by numbers corresponding to their IDs as shown in Figure 22. There are three rows of sensor nodes. The sensor nodes 120–135 form the first row and are located in the front edge of the bridge; the sensor nodes 220–235 form the second row and are located in the middle of the bridge; the sensor nodes 320–335 form the third row of sensor arrays. The sensor data used for the numerical analysis are chosen from the forced vibration tests with vertical directionality. The length of the sensor data time series is 5000. The shifted distances are measured by the centroids of the normal feature vectors and the damage pattern 6 feature vectors. From Figure 22, we can see that the closer the sensor nodes to the damage location (pier 3), the larger the shifted distance from pattern 6 feature vectors to the normal feature vectors. This result shows the potential of using pattern recognition approach for damage localization analysis.

**4.7. The Effects of Time Series Length on Computing Time.** To investigate the impact of the time series length on computing time, simulation tests were performed using different feature extraction methods and with various time series lengths. The evaluation tests were conducted using a Dell computer with Intel Core2 Quad 2.4 GHz CPU and 4 GB of RAM. Figure 23 shows the computing time for three feature extraction methods when the length of the time series changes. For the DFT- and DWT-based feature extraction methods, the length of the time series does not have significant impact on the computing time. For the AR-based feature extraction method, the computing time increases when the length of the time series increases.

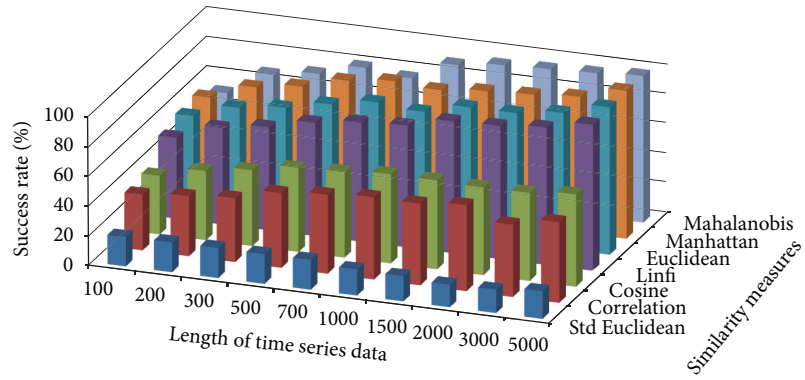


FIGURE 16: Average success rate of pattern recognition using DWT-based feature extraction in first scenario.

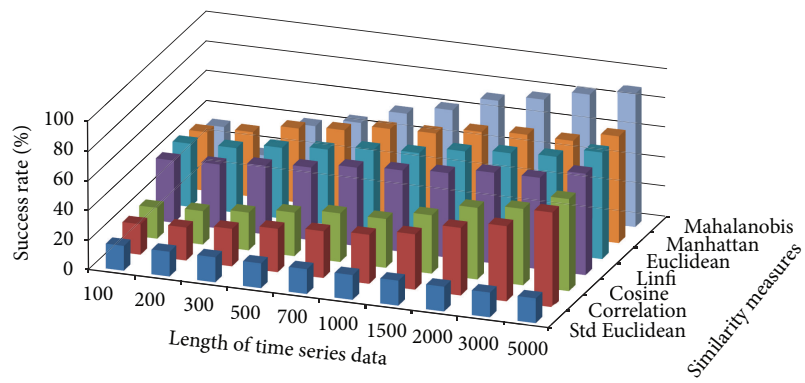


FIGURE 17: Average success rate of pattern recognition using DWT-based feature extraction in second scenario.

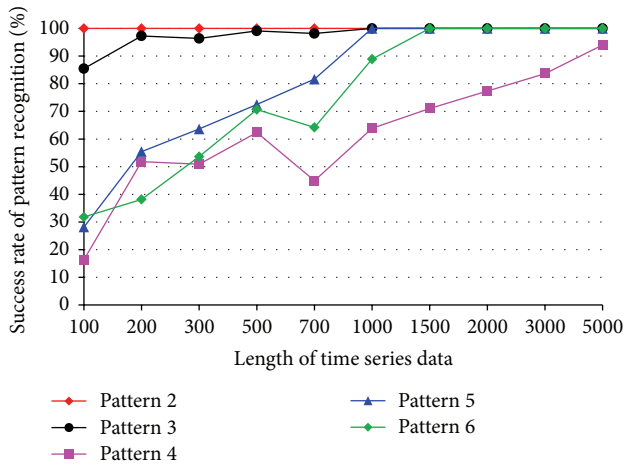


FIGURE 18: Success rate of pattern recognition using DWT-based feature extraction in first scenario (sensor 232).

## 5. Conclusions

This paper presents the research results of three feature extraction methods: autoregressive model, discrete Fourier transform, and discrete wavelet transform, for structural damage pattern recognition. The performance of a number of dissimilarity measures for feature extraction and pattern recognition is also investigated. The test data for evaluating

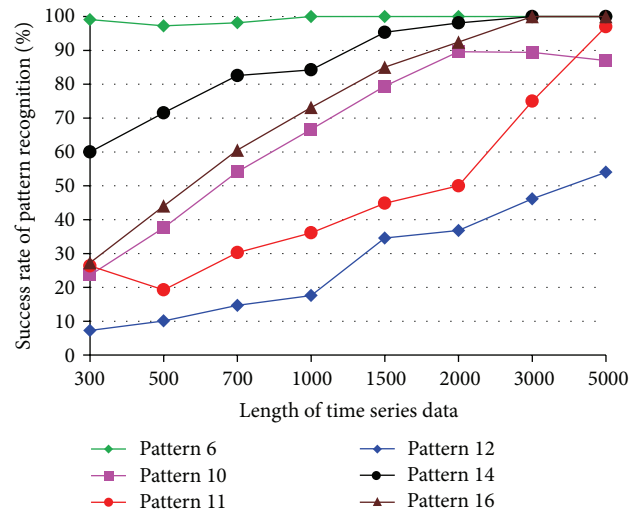


FIGURE 19: Success rate of pattern recognition using DWT-based feature extraction in second scenario (sensor 232).

the performance of feature extraction methods and dissimilarity measures are chosen from the Z24 bridge test. The Z24 bridge test data include the progressive damage data of the same type but varying levels as well as radically distinct damage modalities. These features of the damage data allow us to evaluate the performance of feature extraction methods and

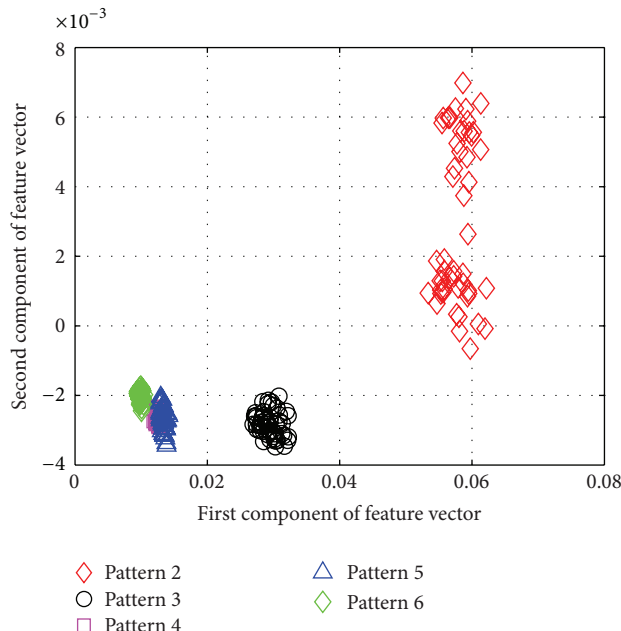


FIGURE 20: The DWT feature vectors of data patterns in first scenario from sensor node 232.

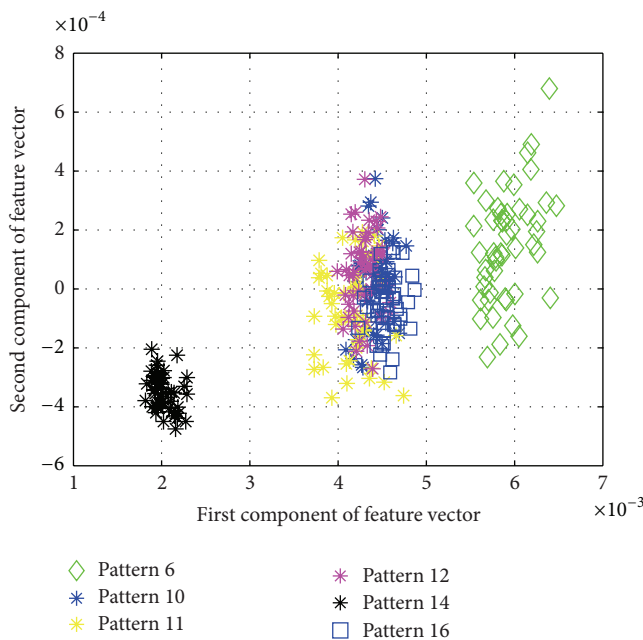


FIGURE 21: The DWT feature vectors of data patterns in second scenario from sensor node 232.

dissimilarity measures for different damage modalities and different levels of damage severity. The comparison results show that the combination of AR-based feature extraction and the Mahalanobis distance presents better performance compared with other feature extraction methods and dissimilarity measures. Although the computing time of AR-based feature extraction will increase when the length of a time series is longer than 1,000 data points, this will not

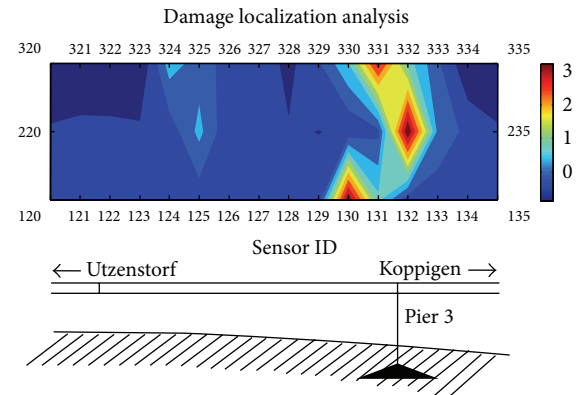


FIGURE 22: The shifted distances of damage pattern 6 feature vectors from normal pattern feature vectors.

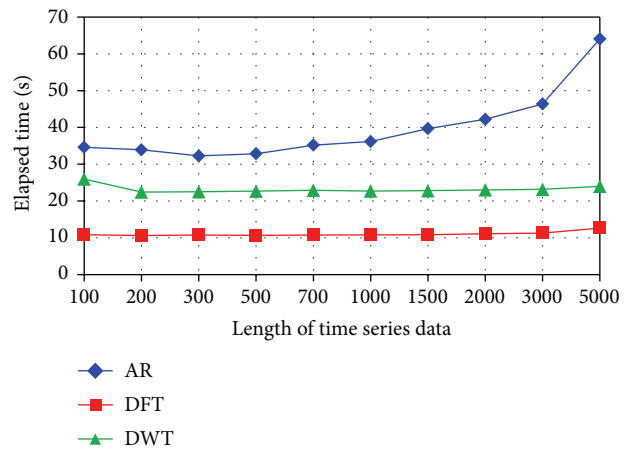


FIGURE 23: The impact of the time series length on the computing time for different feature extraction methods.

impede the application of AR method. The reason is that the success rate of AR-based pattern recognition is already high when the length of a time series is 700 data points for both scenarios 1 and 2. The success rate does not improve too much when the length is further increased. In addition to feature extraction and pattern recognition, the feasibility of using pattern recognition approach for damage localization analysis is also studied in this paper. The simulation result shows that the closer the sensor nodes to the damage location, the larger the distances of damage feature vectors shift from the normal pattern feature vectors.

## Acknowledgments

This material is based upon work supported by the National Science Foundation under Grant no. CMMI-1049294. Any opinions, findings, and conclusions or recommendations expressed in this material are those of the author(s) and do not necessarily reflect the views of the National Science Foundation.

## References

- [1] H. Ding, G. Trajcevski, P. Scheuermann, X. Wang, and E. Keogh, "Querying and mining of time series data: experimental comparison of representations and distance measures," *Proceedings of the VLDB Endowment*, vol. 1, no. 2, pp. 1542–1552, 2008.
- [2] J. Lin, M. Vlachos, E. Keogh, and D. Gunopulos, "Iterative incremental clustering of time series," in *Advances in Database Technology—EDBT 2004*, pp. 106–122, Springer, Berlin, Germany, 2004.
- [3] R. Agrawal, C. Faloutsos, and A. Swami, "Efficient similarity search in sequence databases," in *Proceedings of the 4th Conference on Foundations of Data Organization and Algorithms*, 1993.
- [4] C. Faloutsos, M. Ranganathan, and Y. Manolopoulos, "Fast subsequence matching in time-series databases," in *Proceedings of the ACM SIGMOD International Conference on Management of Data*, vol. 23, pp. 419–429, May 1994.
- [5] F. Korn, H. V. Jagadish, and C. Faloutsos, "Efficiently supporting ad hoc queries in large datasets of time sequences," in *Proceedings of the ACM SIGMOD International Conference on Management of Data*, vol. 26, pp. 289–300, June 1997.
- [6] C. Kin-Pong and F. Ada Wai-Chee, "Efficient time series matching by wavelets," in *Proceedings of the 15th IEEE International Conference on Data Engineering*, pp. 126–133, Sydney, Australia, 1999.
- [7] E. Keogh, K. Chakrabarti, S. Mehrotra, and M. Pazzani, "Locally adaptive dimensionality reduction for indexing large time series databases," in *Proceedings of the ACM SIGMOD International Conference on Management of Data*, vol. 30, pp. 151–162, May 2001.
- [8] Y. Cai and R. Ng, "Indexing spatio-temporal trajectories with Chebyshev polynomials," in *Proceedings of the ACM SIGMOD International Conference on Management of Data (SIGMOD '04)*, pp. 599–610, Paris, France, June 2004.
- [9] D. J. Berndt and J. Clifford, "Using dynamic time warping to find patterns in time series," in *Proceedings of the AAAI Workshop on Knowledge Discovery in Databases*, pp. 359–370, Seattle, Wash, USA, 1994.
- [10] E. Keogh and C. A. Ratanamahatana, "Exact indexing of dynamic time warping," *Knowledge and Information Systems*, vol. 7, no. 3, pp. 358–386, 2005.
- [11] D. Bernal, D. Zonta, and M. Pozzi, "ARX residuals in damage detection," *Structural Control & Health Monitoring*, vol. 19, no. 4, pp. 535–547, 2012.
- [12] J. A. Rice, K. A. Mechitov, S. H. Sim, B. F. Spencer Jr., and G. A. Agha, "Enabling framework for structural health monitoring using smart sensors," *Structural Control & Health Monitoring*, vol. 18, no. 5, pp. 574–587, 2011.
- [13] A. Mita, H. Sato, and H. Kameda, "Platform for structural health monitoring of buildings utilizing smart sensors and advanced diagnosis tools," *Structural Control & Health Monitoring*, vol. 17, no. 7, pp. 795–807, 2010.
- [14] Institute for Research in Computer Science and Random Systems, "Health monitoring of a concrete three-span bridge," 2013, <http://www.irisa.fr/prive/lmevel/bridge/test.html>.
- [15] L. Garibaldi, S. Marchesiello, and E. Bonisoli, "Identification and up-dating over the Z24 benchmark," *Mechanical Systems and Signal Processing*, vol. 17, no. 1, pp. 153–161, 2003.
- [16] A. Fasana, L. Garibaldi, E. Giorcelli, and D. Sabia, "Z24 bridge dynamic data analysis by time domain methods," in *Proceedings of the 19th International Modal Analysis Conference (IMAC '01)*, pp. 852–856, Kissimmee, Fla, USA, 2001.
- [17] D. J. Luscher, J. M. W. Brownjohn, H. Sohn, and C. R. Farrar, "Modal parameter extraction of Z24 bridge data," in *Proceedings of the 19th International Modal Analysis Conference (IMAC '01)*, pp. 836–841, Kissimmee, Fla, USA, 2001.
- [18] S. Marchesiello, B. A. D. Piombo, and S. Sorrentino, "Application of the CVA-BR method to the Z24 bridge vibration data," in *Proceedings of the 19th International Modal Analysis Conference (IMAC '01)*, pp. 864–869, Kissimmee, Fla, USA, 2001.
- [19] K. Womack and J. Hodson, "System identification of the Z24 Swiss bridge," in *Proceedings of the 19th International Modal Analysis Conference (IMAC '01)*, pp. 842–845, Kissimmee, Fla, USA, 2001.
- [20] L. Mevel, M. Goursat, and M. Basseville, "Stochastic subspace-based structural identification and damage detection and localisation—application to the Z24 bridge benchmark," *Mechanical Systems and Signal Processing*, vol. 17, no. 1, pp. 143–151, 2003.
- [21] R. A. Swartz and J. P. Lynch, "Damage characterization of the Z24 bridge by transfer function pole migration," in *Proceedings of the 26th International Modal Analysis Conference (IMAC '08)*, Orlando, Fla, USA, 2008.
- [22] C. Krämer, C. A. M. de Smet, and G. de Roeck, "Z24 bridge damage detection tests," in *Proceedings of the 17th International Modal Analysis Conference (IMAC '99)*, pp. 1023–1029, Kissimmee, Fla, USA, February 1999.
- [23] J. Kullaa, "Damage detection of the Z24 bridge using control charts," *Mechanical Systems and Signal Processing*, vol. 17, no. 1, pp. 163–170, 2003.
- [24] J. Maeck and G. de Roeck, "Damage assessment using vibration analysis on the Z24-bridge," *Mechanical Systems and Signal Processing*, vol. 17, no. 1, pp. 133–142, 2003.
- [25] A. Teughels and G. de Roeck, "Structural damage identification of the highway bridge Z24 by FE model updating," *Journal of Sound and Vibration*, vol. 278, no. 3, pp. 589–610, 2004.
- [26] G. de Roeck, B. Peeters, and J. Maeck, "Dynamic monitoring of civil engineering structures," in *Proceedings of the 4th International Colloquium on Computation of Shell & Spatial Structures*, Chania, Greece, 2000.
- [27] A. Bagnall, C. Ratanamahatana, E. Keogh, S. Lonardi, and G. Janacek, "A bit level representation for time series data mining with shape based similarity," *Data Mining and Knowledge Discovery*, vol. 13, no. 1, pp. 11–40, 2006.
- [28] S. Pittner and S. V. Kamarthi, "Feature extraction from wavelet coefficients for pattern recognition tasks," *IEEE Transactions on Pattern Analysis and Machine Intelligence*, vol. 21, no. 1, pp. 83–88, 1999.
- [29] E. Keogh, K. Chakrabarti, M. Pazzani, and S. Mehrotra, "Dimensionality reduction for fast similarity search in large time series databases," *Knowledge and Information Systems*, vol. 3, no. 3, pp. 263–286, 2001.
- [30] J. Lin, E. Keogh, L. Wei, and S. Lonardi, "Experiencing SAX: a novel symbolic representation of time series," *Data Mining and Knowledge Discovery*, vol. 15, no. 2, pp. 107–144, 2007.
- [31] B. Peeters and C. E. Ventura, "Comparative study of modal analysis techniques for bridge dynamic characteristics," *Mechanical Systems and Signal Processing*, vol. 17, no. 5, pp. 965–988, 2003.
- [32] A. Subasi, "EEG signal classification using wavelet feature extraction and a mixture of expert model," *Expert Systems with Applications*, vol. 32, no. 4, pp. 1084–1093, 2007.
- [33] N. Saravanan and K. I. Ramachandran, "Fault diagnosis of spur bevel gear box using discrete wavelet features and Decision Tree

- classification," *Expert Systems with Applications*, vol. 36, no. 5, pp. 9564–9573, 2009.
- [34] S.-C. Huang and T.-K. Wu, "Integrating GA-based time-scale feature extractions with SVMs for stock index forecasting," *Expert Systems with Applications*, vol. 35, no. 4, pp. 2080–2088, 2008.
- [35] P. K. Sen and J. M. Singer, *Large Sample Methods in Statistics: An Introduction with Applications*, Chapman and Hall, New York, NY, USA, 1994.

## Review Article

# Monitoring of Civil Infrastructures by Interferometric Radar: A Review

**Massimiliano Pieraccini**

*Department of Information Engineering, University of Florence, Via Santa Marta, 3, 50139 Firenze, Italy*

Correspondence should be addressed to Massimiliano Pieraccini; [massimiliano.pieraccini@unifi.it](mailto:massimiliano.pieraccini@unifi.it)

Received 19 July 2013; Accepted 8 August 2013

Academic Editors: D. G. Aggelis, N. Alver, and H. K. Chai

Copyright © 2013 Massimiliano Pieraccini. This is an open access article distributed under the Creative Commons Attribution License, which permits unrestricted use, distribution, and reproduction in any medium, provided the original work is properly cited.

Ground-based radar interferometry is an increasingly popular technique for monitoring civil infrastructures. Many research groups, professionals, and companies have tested it in different operative scenarios, so it is time for a first systematic survey of the case studies reported in the literature. This review is addressed especially to the engineers and scientists interested to consider the applicability of the technique to their practice, so it is focused on the issues of the practical cases rather than on theory and principles, which are now well consolidated.

## 1. Introduction

Radar interferometry is a powerful remote sensing technique, able to detect small displacement at great distance. The scientific background is derived from space technology. Since 1990s [1], satellite-based radar has been able to exploit the phase information of images for detecting ground displacements of a few millimetres at a distance of hundreds of km. These developments had an early followup in analogue ground-based radar systems in the late '90s. In 2000 Tarchi et al. [2] proposed for the first time exploiting the ground-based interferometry principles for monitoring buildings. In 2004, Pieraccini et al. [3] designed and tested in field the first interferometric radar for dynamic monitoring of bridges. Since those early days, the technique and the equipment have been continuously developed and tested in different operative scenarios until their diffusion in the community of structural engineers and scientists.

## 2. Working Principle of Radar Interferometry

An interferometric radar is a sensor able to detect differential displacements of the targets in its cone of view by exploiting the phase information of the backreflected microwave signal. In Figure 1 its working principle is sketched.

If we consider a monochromatic wave impinging a single point scatter, the backreflected wave has a phase difference (with respect to the transmitted one) depending on the distance between radar and target. This phase information cannot be exploited directly for distance measurement, as it is affected by an ambiguity equal to half a wavelength (i.e., distances that differ by a multiple of a half a wavelength give the same detected phase), but if the target moves of a fraction of wavelength, the differential displacement can be detected as a phase shift with a precision depending on the capability of the electronic device to appreciate small phase rotation. In practice, by using 17.6 mm as wavelength (corresponding to the central frequency of the microwave band licensed for this kind of applications), with an integration time of 10  $\mu$ s, the displacement precision is in the order of 0.1 mm. Better precision (up to tens of  $\mu$ m) can be obtained with longer integration time, which can be set when the motion to be detected can be considered stationary (this is the norm when the purpose is to detect the natural frequency of the stationary modes of a structure).

The same working principle is applicable when the radar transmits a modulated signal that gives to the sensor the capability to detect separately the displacements of different targets (or portions of targets) at different distances from

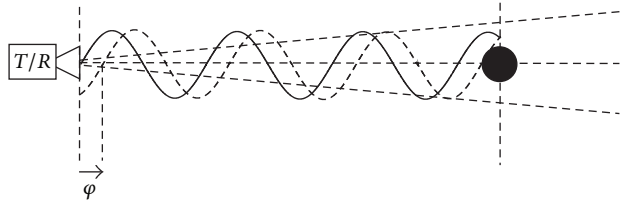


FIGURE 1: Working principle of interferometry  $T/R$ : transmit/receive equipment,  $\varphi$ : phase.

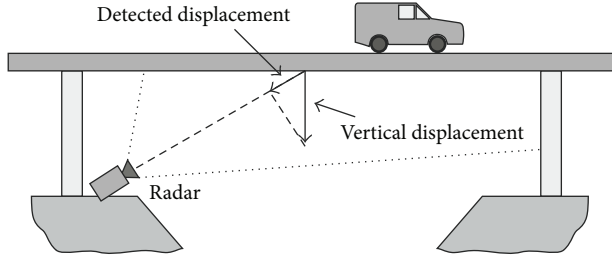


FIGURE 3: Interferometric radar for monitoring a bridge.

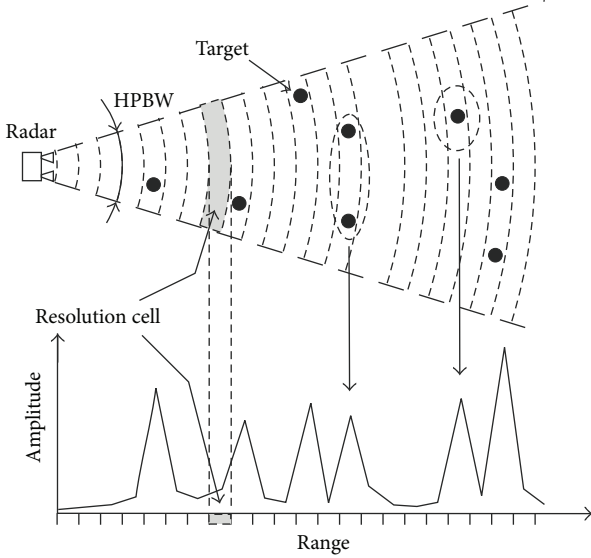


FIGURE 2: Interferometric radar. HPBW: half-power beamwidth.

the radar head, which provided that they are spaced more than the resolution of the radar (Figure 2).

Only-range resolution could be not enough in any application. In order to provide angular resolution too, it is necessary for rotating or moving the radar head. In this way it is possible to obtain a bidimensional image in which the responses of targets at the same distance from the radar can be discriminated in azimuth [2, 4]. In other words, moving the radar head, it is possible to obtain a bidimensional image of the displacement pattern and not only a plot of its projection in the view direction. This is an important capability, but obviously it makes the sensor rather slow, heavier, and bulky, so it is an option not so commonly implemented.

Generally speaking, an interferometric radar can be used both for dynamic and static tests of engineering structures, but aims and scopes of the two modalities are quite different. In the first case the engineer is interested mainly in the frequency spectrum of the displacement. In the second case, the structure is in static condition, and the aim of the measurement is to detect precisely the displacement in relationship to a dead load. But, while frequency spectrum measurement does not present critical issues (at least in certain conditions, as we shall see), the measurement of the absolute displacement by radar interferometry is affected by a systematic and deterministic error that can be kept small but

cannot ever be entirely eliminated. Indeed, the target is never a single electromagnetic scatter (an ideal isotropic reflector) but a complex structure. Its movement changes slightly the geometric shape altering its interaction with the impinging electromagnetic wave. This does not affect the measurement of frequency, but it could affect the absolute measurement of displacement with an error that can range from a few percent to even 10–20% depending on particular shape and movement of the structure under test. As rule of thumb, the larger the displacement, the greater the percentage error. Another essential operative difference between dynamic and static tests is that in the second case the measurement time is long enough to allow to rotate or move the radar head, so it is possible to obtain a bidimensional image of the displacement pattern.

### 3. Dynamic Monitoring

As mentioned above, a radar used for dynamic monitoring of an infrastructure cannot provide a bidimensional map of the displacement but only a plot in view direction. Therefore, the engineering structures more suitable for this kind of sensor are those with a prevalent dimension, such as bridges (that span mainly in horizontal direction) or towers (that span mainly in vertical direction).

**3.1. Bridges.** The standard arrangement for monitoring a bridge using an interferometric radar is sketched in Figure 3 [3].

The instrument is positioned at the base of a pier in order to image the lower part of the deck. The antenna's lobe (HPBW: half-power beamwidth) is large enough to illuminate a significant part of the arcade, so different sections of the bridge arcade can be discriminated by their different distances from the sensor. The radar gives a plot of the back-reflected amplitude (as in Figure 1), which shows a series of peaks. Each of these corresponds to a geometrical feature of the arcade able to reflect electromagnetic waves, and it can be a transversal beam, a corner, or even just a bolt. In correspondence of each peak the sensor is able to detect the displacement component along the view direction. The deformation curve can be obtained by interpolation [6]. As mentioned above, the correspondence between peaks and points on the bridge relies on the measured distance from the radar, but in particular application a more precise location of the measurement point can be necessary. In these cases,



FIGURE 4: Corner reflector installed on a bridge.

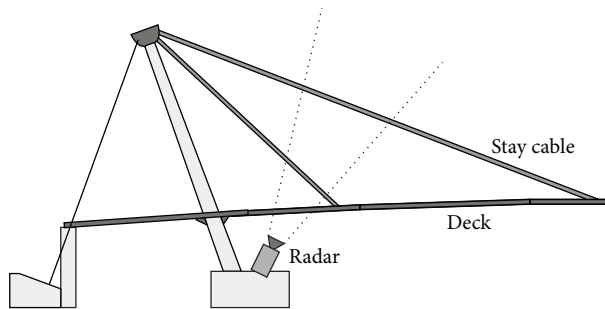


FIGURE 5: Monitoring of stay cable with interferometric radar.

a special reflectors should be installed on the bridge arcade. These are metallic trihedrons (named “corner reflectors”) with a side typically of 20–50 cm (see Figure 4).

Their particular shape has the property to reflect an impinging wave at the same direction from which it had come. As their reflectivity is very high, they are clearly identifiable in the radar plot. The evident drawback in the use of corner reflectors is that they have to be installed on the structure, while a key advantage of the radar is just the capability to operate remotely.

In order to assess the health of an infrastructure, the detected movement of a bridge has to be correlated to its vibration modes, and it can be done using the standard mathematical procedures developed for the accelerometers [7].

In cable-stayed bridges the radar can be used for monitoring even the stay cables. Indeed, the tensional state of the cables affects their oscillation frequency, which can be detected by the radar without installing any device on the cable [8], as shown in Figure 5 where the radar is pointed to the cables from a ground installation.

It is important to note that the possible torsional movements of the deck are not detectable by radar in standard configuration. This can be a severe drawback of the technique. Nevertheless, Dei et al. [9] proposed a method for detecting even possible torsional modes. The basic idea is to use a radar able to acquire a radar image of the deck by moving it along a mechanical guide [4] or by rotating the head [32]. This radar image is used as reference for fitting the measured dynamic data with a model that takes into account even possible torsional movements. The main drawback of this procedure

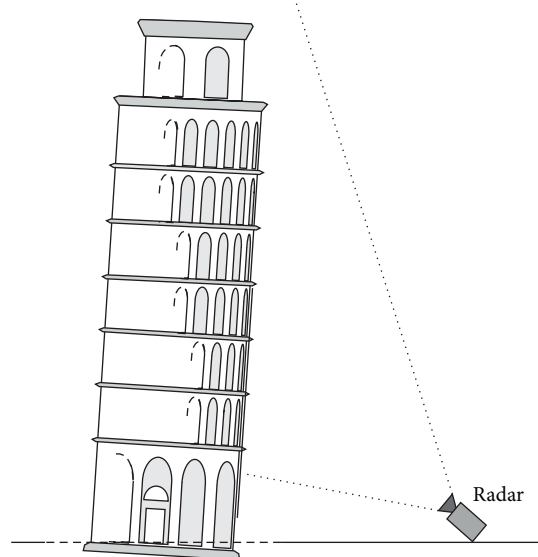


FIGURE 6: Radar measurement of Leaning Tower of Pisa.

is the need of a radar with imaging capability (that is much more heavy and expensive than a radar head mounted on a tripod) and even the complexity of the two-phase measurement. Furthermore, the robustness of the inversion algorithm should be proven in a larger number of cases.

**3.2. Masonry Towers.** The towers are structures rather vulnerable that need constant surveillance. Ancient bell towers, minarets, and lighthouses, are often part of World Heritage and so their conservation is a priority. Aging of materials, long-term ground subsiding, and accumulation of the effects of earthquakes and strong winds, as well as vibrations induced by today’s vehicular traffic, are all causes of possible deterioration. Dynamic characterization is recognized as a powerful method for testing the conservation status of structures, and in planning maintenance or repairs [33]. Indeed, as the resonance frequency of a structure is directly related to its rigidity, its measured value can highlight a damage that may compromise the structure’s integrity [34, 35]. In effect, the interferometric radar has been successfully tested in famous historic monuments as the Giotto’s tower [13] in Florence (Italy), Mangia’s tower [14] in Siena (Italy), and the Leaning Tower of Pisa [15] (Italy). As an example, Figure 6 shows the measurement geometry in the radar monitoring of the Pisa Tower.

Due to the asymmetric shape of the tower produced by its inclination, four different positions of observation were chosen. The radar was oriented empirically at an elevation angle such that the antenna half-power beamwidth illuminated most of the tower surface. The vibration frequencies were evaluated separately from each radar position. Each single measurement spanned 1800 s. It has been revealed a resonance frequency of 1.04 Hz along the west-to-east direction, slightly different from the frequency of 1.01 Hz along the north-to-south direction. These values coincide substantially with the frequencies 1.06 Hz (W-E) and 0.98 Hz (N-S)



FIGURE 7: Radar measurement of a wind tower.

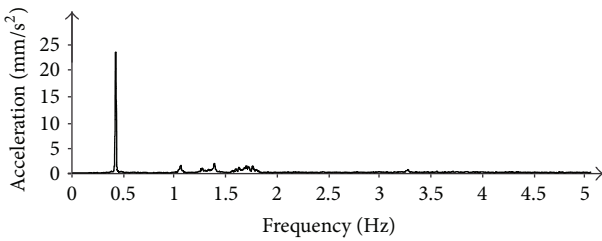


FIGURE 8: Spectral power distribution of the movement of a wind tower.

measured by other authors using microtremor measurements [36]. The case of Pisa's Tower is emblematic, but the presence of two resonances (i.e., two first modal frequencies) is rather common. A perfectly symmetric base (a circle, a square, an hexagon) is rare, as a small difference between the side lengths, or even an external constrain as a building leaning against, can break the symmetry.

**3.3. Wind Turbines.** The number of wind turbine towers installed worldwide is over several hundreds of thousands and is fast growing [37]. All these structures have to be tested after installation, and they need a periodical monitoring. The key requirements for this kind of in-field testing are (1) in-service operation, (2) equipment portable and fast, and (3) direct measurement of the deflection of the structure under test. These requirements are fulfilled by the interferometric radar, which has been extensively used in this application [17–19]. The movement of the blade is not a problem if the measurement is limited to the points of the tower lower than the blade edges or if the blades are stopped. As an example, Figure 7 shows an interferometric testing of a wind tower. The joints between the sections (one of 3–4 meters) are good point scatters for the electromagnetic wave impinging the structure. Each of these gives a well-detectable signal so it acts as a sort of “virtual sensor” installed on the tower.

Figure 8 shows the spectral power distribution of the acceleration measured by radar in a point at 72 m height of a wind tower. The speed of wind was about 11 m/s as measured

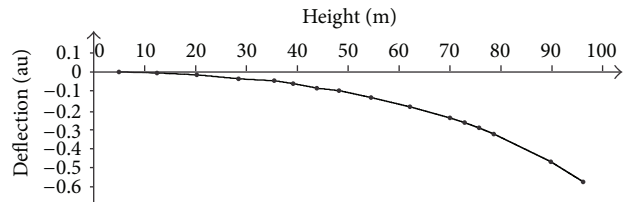


FIGURE 9: Modal shape at 0.43 Hz.

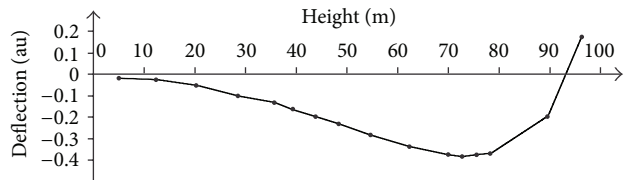


FIGURE 10: Modal shape at 1.06 Hz.

by the anemometer of the wind turbine. The radar was installed at 14 m from the base of the tower.

As the radar is able to provide simultaneously the movement of several points on the tower, it is possible to estimate the modal shape of the main modes as shown in Figures 9 and 10.

In a wind field there could be even 50–100 towers, therefore Pieraccini et al. [17] proposed an operative modality (named “landscape”) for measuring at the same time several towers, and provided that they can be seen from a single point. Nevertheless in this modality the movement of the blades give additional frequencies (due to the rotation speed) which can be confused with the frequencies of the structural modes.

**3.4. Chimneys.** The chimneys of industrial plants are high and thin structures sensible to the wind, that can give severe problems when it triggers the detachment of von Kármán vortices. Several authors [10, 20–22] reported the use of the interferometric radar for detecting the oscillation of chimneys. Although these structures are often already instrumented with an accelerometer, the radar can provide the additional capability to detect the whole modal shape sampled in many points.

**3.5. Antenna Masts, Lighting Towers, and Streetlight.** Antenna masts, lighting towers, pylons, and streetlights are all steel structures that are potentially dangerous if they are not periodically monitored. Currently they are occasionally inspected, but there are no satisfactory monitoring tools for expeditious and affordable operations. In this context, the interferometric radar can offer a fast no-contact measurement device already successfully used for this kind of applications [11, 23].

**3.6. Culverts.** The railway culverts are routinely tested to validate structural specifications or to provide diagnostic surveys for planning maintenance. Beben [24] used the interferometric radar to study deeply the dynamic impacts of

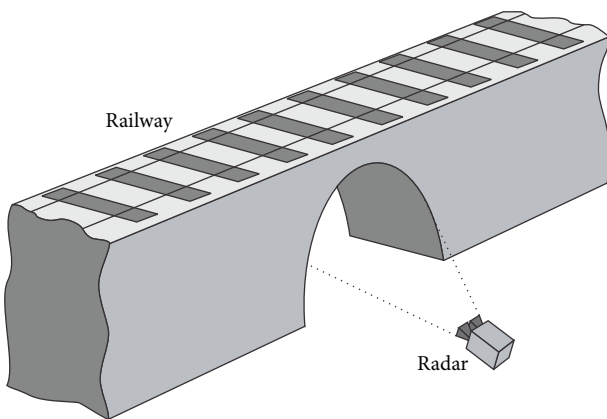


FIGURE 11: Railway culvert monitored by interferometric radar.



FIGURE 12: Testing of a bridge.

the service loads (kinematic excitations during passage of the real trains) on the corrugated steel plate culverts. A sketch of the experimental setup is shown in Figure 11.

Measurements were made for all trains passing over the culvert during a 24 h period. Finally a comparison between the dynamic amplification factor (DAF) obtained from tests and the dynamic coefficients, as reported in three design bridge standards, has been presented.

**3.7. Buildings.** A microwave interferometer has been employed to remotely detect the oscillations induced by vehicular traffic on the dome of the Baptistry of S. Giovanni in Firenze (Italy) [30]. The measurement has been carried out to assess the reduction of the structure oscillations after the ordinance issued by the Major of Florence forbidding all kind of vehicular traffic in the square around the Baptistry. The estimation of the structural vibrations was performed by using the recommendations of Italian UNI9916, and it resulted that “peak component particle velocity” had a decrease of about 33% from before to after the traffic block.

Recently (2013), Negulescu et al. [31] used the radar interferometry in a large architectonic complex. The building includes a double basement, a ground floor, and 10 storeys. It has a curved form comprised of a central building with two asymmetric wings with different lengths and inclinations. In such an articulated structure, the identification of the vibration modes required particular care in data analysis.

#### 4. Static Monitoring

The static test is a routine procedure for bridges and floors. Its scope is to detect the displacement in relationship to a dead load. These kinds of measurements are critical issues for the dams that are equipped with numerous and even redundant instrumentation. As it is not necessary for sampling time to be short enough to detect vibration and transient events, the interferometric radar can be used in both modalities: only-range (i.e., able to provide only a plot in view direction) and cross-range (i.e., able to provide a bidimensional map of the displacement).

**4.1. Bridges.** Normally the radar is positioned at the base of a pillar in order to image the lower part of the deck as shown in Figure 3. Statistic tests require to load and unload the deck (using trucks for road bridge, train for railway bridge, or bins full of water for pedestrian bridge), and these operations can require minutes or hours, so a critical question is the stability in time both of the radar equipment and environmental conditions. A temperature change, for example, between morning and evening, can give a sensible perturbation of (a) the target (bridge); (b) the air between radar and target; (c) the electronic equipment. Only the latter can be compensated with a suitable calibration procedure. Another possible source of perturbation is the movement of vehicles or other metallic objects in proximity of the view cone of the radar. This can produce phase rotation detectable as false displacements. Pieraccini et al. [5] reported a case study where the radar is used in only-range modality for testing a railway bridge before the entry into service. The case in [4] is relative to the first application of radar interferometry (by imaging both in range and cross-range) aimed to carry out a static test of a pedestrian bridge.

Static testing and dynamic testing of a bridge can be carried out even in a single measurement session as for the case shown in the picture of Figure 12. Four trucks loaded with inert materials were used as stimulus. Each weighted 44000 Kg, so the maximum applied static load was 176000 Kg.

The displacement was measured by an interferometric radar that operated continuously during two load/unload cycles. The radar pointed the central part of the arcade. The measured displacement in time (Figure 13) shows that the full static load gives a displacement of about 5 mm.

During the load phase, one of the trucks passed three times on a beam of wood of 15 cm side (as shown in Figure 14) soliciting the bridge with a mechanical beat.

The measured response relative to a single beat is shown in Figure 15. As pulse duration is short with respect to typical movements of a bridge, the plot in Figure 15 can be considered as the pulse response in time domain of the deck, that is a function of great importance for assessing the dynamic characteristics of a bridge.

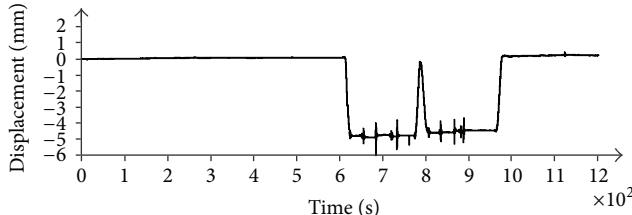


FIGURE 13: Displacement in time.



FIGURE 14: Dynamic stimulus of the bridge deck.

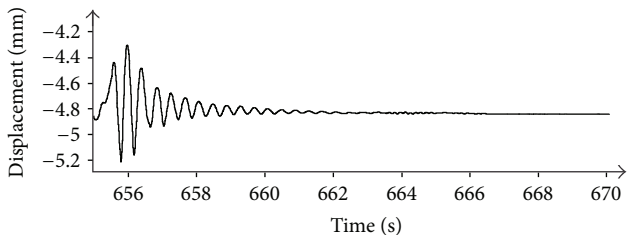


FIGURE 15: Measured pulse response in time domain of the bridge in Figure 11.

**4.2. Dams.** Dams are critical infrastructures that need continuous monitoring. In effect, one of the first applications of ground-based radar interferometry was just in a dam [25]. Many other cases are reported in literature [26–28]. The radar is able to give a displacement image projected on a horizontal (or vertical) plane. This is of valuable interest for obtaining the strain pattern of the structure.

**4.3. Multistorey Buildings.** Static testing by radar has been assessed even in structure like multistorey buildings. As a significant example, we mention the case of a test-building already intentionally damaged. The radar has been able to detect the inelastic behaviour of the structure [29].

## 5. Summary and Discussion

Table 1 rearranges the references of this paper by dividing them by applications. Although the bibliographic research is, of course, not exhaustive, it clearly highlights the greatest

TABLE 1

	Static testing	Dynamic testing
Bridges	[4, 5]	[3, 5–12]
Masonry towers		[13–16]
Wind turbines		[17–19]
Chimneys		[10, 20–22]
Antenna masts		[20, 23]
Lighting towers		[11]
Culverts		[24]
Dams	[25–28]	
Buildings	[29]	[30, 31]

number of works that has been published on the dynamic testing of bridges. In the field of static testing, the dams are the structures more often equipped with interferometric radars.

As resumed even in Table 1, the application fields of ground-based radar interferometry are varied and numerous. Nevertheless, the practitioner should be aware of some limits and warnings. First of all, when the radar is used in only-range modality, it should be always taken in mind that the radiation lobe of a radar antenna is not a laser beam: single pixel in the radar plot could not correspond to a physical point in the structure, so it could be affected by static clutter and dynamic clutter due to disturbing targets at the same distance. A careful setup of the measurement geometry is essential for a successful use of this technique. Furthermore, a frequent cause of misunderstanding of the measurement data is due to the fact that even the radar with its tripod is a mechanical structure with its movement. It could be even greater of the displacement to be detected, if the ground or the floor where the radar is installed is not stable. In these cases, a possible solution is to integrate a seismic accelerometer in the radar head [16] with the aim to remove its own movement in data processing.

The application field of interferometric radar could be even larger if it could be able to provide bidimensional images of the displacement pattern in dynamic conditions, that is, if it could be able to provide bidimensional images with a frame rate of a few of milliseconds. At the state of art, this is not possible, but a step in the right way seems to be done by Tarchi et al. [38]. They designed a coherent radar based on multiple inputs multiple outputs (MIMO) technology. Finally, a critical issue for a wide popularity of this technique, as well as of any advanced equipment, is the cost. Currently interferometric radars, also in the simplest configuration, are relatively expensive for the market of the structural testing. For this reason, a downgraded version of the device, without range discrimination capability has been proposed [12] and successfully tested in comparison with a standard interferometric radar. This solution is potentially very low in cost.

## 6. Conclusion

Ground-based radar interferometry is a measurement technique recently proposed for static testing and dynamic testing

of infrastructures. It has the unique advantage to provide global information on the structure under test, with the drawback that it is often not easy to localize with precision in the structure the measured displacement as all the points in the same resolution cell can contribute to it.

The technique has been demonstrated effective in bridges, culverts, dams, towers, chimneys, pylons, antenna masts, lighting towers, streetlight, and even multistorey buildings. For all these application the radar is a valuable tool for contributing to assess the health of the structure; nevertheless it should be clearly stated that the measurements of displacements and natural frequencies, as well as the modal shapes, never give directly structural information. The health evaluation of a civil structure always depends essentially on the reliability of the specific (static or dynamic) model. The instrumental data are only possible inputs, as well as the survey and the materials tests.

## Disclosure

The author declares that he has been involved in development and design of the commercial interferometric radar named IBIS, manufactured by IDS Company of Pisa (Italy).

## References

- [1] M. Borgeaud, J. Noll, and A. Bellini, "Multi-temporal comparisons of ERS-1 and JERS-1 SAR data for land applications," in *Proceedings of the International Geoscience and Remote Sensing Symposium (IGARSS '94)*, vol. 3, pp. 1603–1605, August 1994.
- [2] D. Tarchi, H. Rudolf, M. Pieraccini, and C. Atzeni, "Remote monitoring of buildings using a ground-based SAR: application to cultural heritage survey," *International Journal of Remote Sensing*, vol. 21, no. 18, pp. 3545–3551, 2000.
- [3] M. Pieraccini, M. Fratini, F. Parrini, G. Macaluso, and C. Atzeni, "High-speed CW step-frequency coherent radar for dynamic monitoring of civil engineering structures," *Electronics Letters*, vol. 40, no. 14, pp. 907–908, 2004.
- [4] M. Pieraccini, D. Tarchi, H. Rudolf, D. Leva, G. Luzi, and C. Atzeni, "Interferometric radar for remote monitoring of building deformations," *Electronics Letters*, vol. 36, no. 6, pp. 569–570, 2000.
- [5] M. Pieraccini, F. Parrini, M. Fratini, C. Atzeni, P. Spinelli, and M. Micheloni, "Static and dynamic testing of bridges through microwave interferometry," *NDT and E International*, vol. 40, no. 3, pp. 208–214, 2007.
- [6] M. Pieraccini, M. Fratini, F. Parrini, and C. Atzeni, "Dynamic monitoring of bridges using a high-speed coherent radar," *IEEE Transactions on Geoscience and Remote Sensing*, vol. 44, no. 11, pp. 3284–3288, 2006.
- [7] C. Gentile and G. Bernardini, "Output-only modal identification of a reinforced concrete bridge from radar-based measurements," *NDT and E International*, vol. 41, no. 7, pp. 544–553, 2008.
- [8] C. Gentile, "Deflection measurement on vibrating stay cables by non-contact microwave interferometer," *NDT and E International*, vol. 43, no. 3, pp. 231–240, 2010.
- [9] D. Dei, M. Pieraccini, M. Fratini, C. Atzeni, and G. Bartoli, "Detection of vertical bending and torsional movements of a bridge using a coherent radar," *NDT and E International*, vol. 42, no. 8, pp. 741–747, 2009.
- [10] V. Gikas, "Ambient vibration monitoring of slender structures by microwave interferometer remote sensing," *Journal of Applied Geodesy*, vol. 6, no. 3-4, pp. 167–176, 2012.
- [11] P. Kuras, T. Owerko, and M. Strach, "Application of interferometric radar to examination of engineering objects vibration," *Reports on Geodesy*, vol. 2, no. 87, 2009.
- [12] G. Grazzini, M. Pieraccini, D. Dei, and C. Atzeni, "Simple microwave sensor for remote detection of structural vibration," *Electronics Letters*, vol. 45, no. 11, pp. 567–569, 2009.
- [13] M. Pieraccini, M. Fratini, F. Parrini, G. Pinelli, and C. Atzeni, "Dynamic survey of architectural heritage by high-speed microwave interferometry," *IEEE Geoscience and Remote Sensing Letters*, vol. 2, no. 1, pp. 28–30, 2005.
- [14] M. Pieraccini, D. Dei, M. Betti, G. Bartoli, G. Tucci, and N. Guardini, "Dynamic identification of historic masonry towers through an expeditious and no-contact approach: application to the "Torre del Mangia" in Siena (Italy)," *Cultural Heritage*, 2013.
- [15] C. Atzeni, A. Bicci, D. Dei, M. Fratini, and M. Pieraccini, "Remote survey of the leaning tower of pisa by interferometric sensing," *IEEE Geoscience and Remote Sensing Letters*, vol. 7, no. 1, pp. 185–189, 2010.
- [16] M. Pieraccini, D. Dei, D. Mecatti, and F. Parrini, "Dynamic testing of historic towers using an interferometric radar from an unstable measurement position," *Journal of Nondestructive Evaluation*, 2013.
- [17] M. Pieraccini, F. Parrini, M. Fratini, C. Atzeni, and P. Spinelli, "In-service testing of wind turbine towers using a microwave sensor," *Renewable Energy*, vol. 33, no. 1, pp. 13–21, 2008.
- [18] H. Ruediger, S. Lachmann, and D. Hartmann, "Conceptual study on instrumentation for displacement-based service strength checking of wind turbines," in *Proceedings of the 14th International Conference on Computing in Civil and Building Engineering*, 2012.
- [19] A. J. Chen and G. J. He, "Wind-induced vibration analysis and remote monitoring test of wind turbine power tower," *Advanced Materials Research*, vol. 639–640, pp. 293–296, 2013.
- [20] T. Owerko, L. Ortyl, R. Kocierz, and P. Kuras, "Novel technique of radar interferometry in dynamic control of tall slender structures," *Journal of Civil Engineering and Architecture*, vol. 6, no. 8, pp. 1007–1013, 2012.
- [21] S. Rödelsperger, G. Läufner, C. Gerstenecker, and M. Becker, "Monitoring of displacements with ground-based microwave interferometry: IBIS-S and IBIS-L," *Journal of Applied Geodesy*, vol. 4, no. 1, pp. 41–54, 2010.
- [22] P. Kuras, R. Oruba, and R. Kocierz, "Application of IBIS microwave interferometer for measuring normal-mode vibrational frequencies of industrial chimneys," *Geomatics and Environmental Engineering*, vol. 4, no. 1/1, pp. 83–89, 2010.
- [23] C. Gentile and F. Ubertini, "Radar-based dynamic testing and system identification of a guyed mast," in *Proceedings of the 10th International Conference on Vibration Measurements by Laser and Noncontact Techniques*, vol. 1457, pp. 318–325, AIP Conference Proceedings, Ancona, Italy, June 2012.
- [24] D. Beben, "Experimental study on the dynamic impacts of service train loads on a corrugated steel plate culvert," *Journal of Bridge Engineering*, vol. 18, no. 4, pp. 339–346, 2013.
- [25] D. Tarchi, H. Rudolf, G. Luzi, L. Chiarantini, P. Coppo, and A. J. Sieber, "SAR interferometry for structural changes detection: a

- demonstration test on a dam,” in *Proceedings of the IEEE International Geoscience and Remote Sensing Symposium (IGARSS ’99)*, vol. 3, pp. 1522–1524, Hamburg, Germany, July 1999.
- [26] W. Jenkins, B. Rosenblad, F. Gomez, J. Legarsky, and E. Loehr, “Deformation measurements of earth dams using a ground based interferometric radar,” in *Proceedings of the 2012 ASDSO Annual Conference on Dam Safety*, p. 15, (GBIR) Association of State Dam Safety Officials-Dam Safety, Denver, Colo, United States, September 2012.
- [27] G. Luzi, M. Crosetto, and O. Monserrat, “Advanced techniques for dam monitoring, dam maintenance and rehabilitation II,” in *Proceedings of the 2nd International Congress on Dam Maintenance and Rehabilitation*, pp. 1103–1108, Zaragoza, Spain, November 2010.
- [28] M. Alba, G. Bernardini, A. Giussani et al., “Measurement of dam deformations by terrestrial interferometric techniques,” in *Proceedings of the International Archives of the Photogrammetry, Remote Sensing and Spatial Information Sciences. Part B1*, vol. 37, pp. 133–139, Beijing, China, 2008.
- [29] M. Pieraccini, G. Luzi, D. Mecatti et al., “Remote sensing of building structural displacements using a microwave interferometer with imaging capability,” *NDT and E International*, vol. 37, no. 7, pp. 545–550, 2004.
- [30] M. Fratini, M. Pieraccini, C. Atzeni, M. Betti, and G. Bartoli, “Assessment of vibration reduction on the Baptistry of San Giovanni in Florence (Italy) after vehicular traffic block,” *Journal of Cultural Heritage*, vol. 12, no. 3, pp. 323–328, 2011.
- [31] C. Negulescu, G. Luzi, M. Crosetto et al., “Comparison of seismometer and radar measurements for the modal identification of civil engineering structures,” *Engineering Structures*, vol. 51, pp. 10–22, 2013.
- [32] C. Werner, A. Wiesmann, T. Strozzi, A. Kos, R. Caduff, and U. Wegmuler, “The GPRI multi-mode differential interferometric radar for ground-based observations,” in *Proceedings of the 9th European Conference on Synthetic Aperture Radar (EUSAR ’12)*, pp. 304–307, April 2012.
- [33] A. Zingoni, Ed., “Special issue on structural health monitoring, damage detection and long-term performance (selected papers of SEMC, 2004 Conference),” *Engineering Structures*, vol. 27, no. 12, pp. 1713–1834, 2005.
- [34] D. J. Yu and W. X. Ren, “EMD-based stochastic subspace identification of structures from operational vibration measurements,” *Engineering Structures*, vol. 27, no. 12, pp. 1741–1751, 2005.
- [35] G. Hearn and R. B. Testa, “Modal analysis for damage detection in structures,” *Journal of Structural Engineering*, vol. 117, no. 10, pp. 3042–3063, 1991.
- [36] Y. Nakamura, E. D. Gurler, and J. Saita, “Dynamic characteristics of leaning tower of Pisa using microtremor-preliminary results,” in *Proceedings of the 25th JSCE Earthquake Engineering Symposium*, vol. 2, pp. 921–924, Tokyo, Japan, July 1999.
- [37] T. Ackermann and L. Söder, “An overview of wind energy-status 2002,” *Renewable and Sustainable Energy Reviews*, vol. 6, no. 1-2, pp. 67–128, 2002.
- [38] D. Tarchi, F. Oliveri, and P. F. Sammartino, “MIMO radar and ground-based SAR imaging systems: equivalent approaches for remote sensing,” *IEEE Transactions on Geoscience and Remote Sensing*, vol. 51, no. 1, pp. 425–435, 2013.